First Principles Design of Non-Centrosymmetric Metal Oxides

A Thesis

Submitted to the Faculty

of

Drexel University

by

Joshua Aaron Young

in partial fulfillment of the

requirements for the degree

of

Doctor of Philosophy

April 2016

Dedications

This thesis is dedicated to my wife Nicole, my parents Amy and Harvey, my brother Nathan, my parents-in-law LaDonna and Bill, and my sister-in-law Kristin. The constant love, support, and encouragement from my family has made this work possible.

If you wish to make an apple pie from scratch, you must first invent the universe.

Carl Sagan

Acknowledgements

I would first and foremost like to thank my research advisor, Professor James Rondinelli. It has been a privilege to work with him, and I owe him a great gratitude for everything he has done for me over the past five years. He pushed me to become the best scientist I could be, and much of my success is due to his guidance. From him, I have learned how to construct scientific arguments, write compelling articles, present my research effectively, teach and mentor students, and so much more. Because of his unending advice, encouragement, and mentorship, I have accomplished far beyond what I ever imagined I would as a graduate student.

Next, I can not overstate how much the other members of the Materials Theory and Design Group, both past and present, have helped me. Although publications seemingly appear as simple and polished products, the process of research is messy and fraught with uncertainty; discussions with them have been invaluable in guiding my work. Many special thanks go to Antonio Cammarata for teaching and training me when I was beginning my graduate studies, Nenian Charles for his friendship, support, and discussions (both scientific and not), Danilo Puggioni for his insights and humor, and Prasanna Balachandran, for our collaborations and for teaching me how to talk about my work in a way that makes people want to listen. I would also like to recognize Nicholas Wanger, Emrys Tennessen, Liang-Feng Huang, Kurt Gu, Xuezeng Lu, Jaye Harada, Nathan Koocher, Yongjin Shin, and Parth Lalkiya. Although our time together at Northwestern was short, our interactions improved me as both a scientist and a teacher. I am certain all of you will go far in anything you

choose to pursue.

I would also like to thank several other professors for their support. This includes Professor Steve May for his tireless encouragement, guidance, and collaboration, Professor P. Shiv Halasyamani for many successful joint efforts and his letters of recommendation, and Professors Nasim Alem and Venkatramam Gopalan for their experimental expertise. I would also like to thank my other dissertation committee members, Professors Karin Rabe, Jonathan Spanier, and Karl Sohlberg; their advice and suggestions during my proposal and pre-defense greatly improved the quality of my work.

I owe so many thanks to my parents Amy and Harvey, who have supported, encouraged, and guided me more than I ever could have imagined. I would also like to thank my brother Nathan, my grandparents Guybo and Gamma, Papaw and Mamaw, Aunt Nay, Uncle David, and my in-laws Bill, LaDonna, and Kristin, all of whose influences throughout my life provided the foundation for my accomplishments. Finally, and beyond all else, I am infinitely thankful for the constant love and support of my wife, Nicole. She was the first one to suggest I pursue my doctorate, and has been by my side the whole way. Graduate school is stressful, time-consuming, and daunting, but during it all I had her to lift me up when I was down and help me believe in myself when everything seemed overwhelming. She has been my rock to keep me steady and my shelter to weather the storm. No matter what the future holds, I know I would not be where I am now but for her. For this, I am forever grateful.

Table of Contents

List of Tables

List of Figures

Abstract

First Principles Design of Non-Centrosymmetric Metal Oxides

Joshua Aaron Young

Advisor: James M. Rondinelli, Ph.D.

The lack of an inversion center in a material's crystal structure can result in many useful material properties, such as ferroelectricity, piezoelectricity and non-linear optical behavior. Recently, the desire for low power, high efficiency electronic devices has spurred increased interest in these phenomena, especially ferroelectricity, as well as their coupling to other material properties. By studying and understanding the fundamental structure-property relationships present in non-centrosymmetric materials, it is possible to purposefully engineer new compounds with the desired "acentric" qualities through crystal engineering. The families of $AB\mathrm{O}_3$ perovskite and $AB\mathrm{O}_{2.5}$ perovskite-derived brownmillerite oxides are ideal for such studies due to their wide range of possible chemistries, as well as ground states that are highly tunable owing to strong electron-lattice coupling. Furthermore, control over the B-O-B bond angles through epitaxial strain or chemical substitution allows for the rapid development of new emergent properties. In this dissertation, I formulate the crystal-chemistry criteria necessary to design functional non-centrosymmetric oxides using first-principles density functional theory calculations. Recently, chemically ordered $(AA')B_2\mathrm{O}_6$ oxides have been shown to display a new form of rotation-induced ferroelectric polarizations. I now extend this property-design methodology to alternative compositions and crystal classes and show it is possible to induce a host of new phenomena. This dissertation will address: 1) the formulation of predictive models allowing for *a priori* design of polar oxides, 2) the optimization of properties exhibited by these materials through chemical substitution and cation ordering, and 3) the use of strain to control

the stability of new phases. Completion of this work has led to a deeper understanding of how atomic structural features determine the physical properties of oxides, as well as the successful elucidation of new design principles to help guide experimental synthesis of novel materials.

1. INTRODUCTION

1.1 Motivation

The technological requirements for electronic devices are constantly rising as the need to solve grand scientific challenges and satiate consumer demand for new products both continue to grow; the design of new materials with superior properties is key to generating solutions for these problems and has become increasingly important over the past few decades. Although standard engineering techniques rely on the often slow and laborious individual identification of materials, it is possible to accelerate these discoveries by understanding and then purposefully engineering the atomic scale structural features and mechanisms leading to the desired properties. For example, piezoelectricity, ferroelectricity, and non-linear optical behavior can only arise in materials with a non-centrosymmetric crystal structure (i.e., those lacking an inversion center).[1] Furthermore, they are used in a wide array of applications, such as memory, tunnel junctions, capacitors, sensors, actuators, and solid state lasers.[2–18] If methods can be developed to deterministically lift inversion through structural modifications,[19–22] these electronic properties can be induced independently of knowledge about a material's chemistry, allowing for rapid integration into novel types of electronic devices. Computational first-principles methods are some of the most viable techniques for the identification of new materials in this manner, as their speed and accuracy allows for the probing and disentangling of underlying physical mechanisms in complex systems on the atomic and molecular level.

One promising area of condensed matter research relating to materials discovery is interfacial phenomena. In materials where two or more chemically distinct compounds are interweaved on an atomic level, novel effects can arise from interactions

that may only manifest at their interface.[23,24] This includes interesting physics such as orbital reconstruction and exotic magnetic orderings,[25,26] in addition to potentially functionalizable properties such as two dimensional electron gases, superconductivity, and ferroelectricity.[27–30] Complex oxides (oxygen-containing compounds that also contain at least two non-oxygen elements) are especially fruitful families for studies of this nature, as their vast assortment of structure types and chemical compositions can support a wide variety of interactions between spin, orbital, magnetic, and lattice degrees of freedom, giving rise to a rich and diverse set of physics and properties.[31] While theoretical work (such as that based on density functional theory) has previously predicted the appearance of these so-called emergent phenomena in ultrashort period oxide superlattices, fundamental advances in layer-controlled synthesis techniques such as molecular beam epitaxy (MBE) or pulsed laser deposition (PLD) are beginning to allow detailed experimental investigation and verification.[32–35] Computation-based materials design is now poised to help further guide these synthesis endeavors and facilitate new discoveries. Finally, first principles calculations are not only an ideal method for modeling complex interactions, but also investigating their response to chemical substitution and external parameters such as lattice strain.[36,37]

These ideas lead to the overarching goal of my thesis, which is to utilize *ab initio* calculations to elucidate design strategies for lifting inversion symmetry, predict new materials for experimental synthesis, and enhance the resulting functional electronic properties (such as ferroelectricity) using external stimuli. The culmination of this work has the potential to spawn numerous ferroic discoveries from mechanisms based on functionalities that emerge in layered oxide structures that are otherwise not possible in simpler structures and chemistries. Combining these theoretical predictions with experimental procedures can help guide the materials development process in

useful directions and greatly accelerate the discovery of new, highly functional advanced materials.

1.2 Organization

This thesis is divided into eight chapters with each one focusing on a given topic as described below. Chapters 2, 3, and 4 constitute reviews of the literature; chapters 5, 6, and 7 describe new research; chapter 8 provides a summary and outlook.

Chapter 2 – **First Principles Electronic Structure Methods**: In this chapter, I discuss the theoretical underpinnings of the electronic structure methods used in this thesis. Beginning with the Schrödinger equation and the Born-Oppenheimer approximation, I introduce the various approximations used in modern implementations of density functional theory (DFT) that make computational investigations of real materials feasible, including density functionals, Bloch's theorem, and pseudopotentials. I end with a discussion of computing band gaps and lattice dynamics within the DFT framework.

Chapter 3 – **Structure and Chemistry of Perovskite and Perovskite-Related Compounds**: Here, I focus on the crystal-chemistry of the ABX_3 perovskite and the $ABX_{2.5}$ brownmillerite families. The underlying anion sublattice in these materials can undergo many different types of cooperative distortions, which manifest as "rotations" of the extended three dimensional corner connected BX_6 octahedral network. I first consider how these ubiquitous structural distortions modify the presence of various symmetry operations in the perovskite crystal structure, and then introduce the idea of chemically ordering the A- and B-site cations and discuss the factors necessary for stabilizing various ordering schemes. Finally, I show how ordered anion vacancies in the perovskite-derived brownmillerites control the symmetry of these compounds and add new degrees of structural complexity.

Chapter 4 – **Physics of Acentric Properties**: The focus of this chapter is the underlying physics of ferroelectricity and piezoelectricity. I first describe the modern theory of polarization, which revolutionized scientists' understanding of spontaneous polarization as a bulk property by defining it in terms of geometric Berry phases. This is followed by a discussion of ferroelectric phase transitions, which includes soft mode theory and Landau-Ginzberg-Devonshire theory. I then review the second order Jahn-Teller effect, which is the primary chemical mechanism driving many ferroelectric distortions. Finally, I end with an overview of improper and hybrid improper ferroelectrics, or those in which the appearance of a spontaneous polarization is driven by *non-polar* lattice distortions with polar displacements arising as a side effect.

Chapter 5 – **Predictive Models for Inversion Symmetry Lifting**: In this chapter, I put forth two new models to facilitate the identification of new types of ferroelectric materials. In both cases I begin by considering symmetry principles and lattice distortions independently of chemical makeup and only introduce the effect of composition after developing an understanding of these microscopic mechanisms.

The first model divides geometric improper ferroelectrics into different categories based on the number and type of cooperative atomic displacement patterns (*i.e.*, lattice modes) driving the polar phase transition. I then provide a review of the improper ferroelectric literature and demonstrate how previous experimentally synthesized or theoretically predicted compounds fit into this newly proposed scheme.

The second model is grounded in crystal engineering principles and describes how the shape, chemical composition, and arrangement of basic building units in a one, two, and three dimensional lattice can either preserve or destroy inversion centers. I then show how these guidelines can be applied to a real family of materials by systematically determining what combinations of 15 octahedral rotation patterns and 10

cation ordering schemes provide the previously identified structural features necessary to produce non-centrosymmetric compounds in ABX_3 perovskites. Finally, I use simple descriptors such as the tolerance factor and global instability index to identify the chemical species most likely to result in the desired structural distortions.

Chapter 6 – **Design and Investigation of New Ferroelectric Materials**: Here I use the inversion-lifting structural criteria identified in the previous chapter to design and investigate new ferroelectric and piezoelectric perovskite oxides with DFT. I begin by examining the effect of different cation ordering schemes on the inversion symmetry breaking and ferroelectric properties in a series of three chemically distinct orthorhombic $(AA')B_2O_6$ superlattices. Next, I look at the result of chemically ordering the A-sites in a different crystal structure by investigating three rhombohedral aluminate heterostructures; while this slightly diminishes the ferroelectric properties, I identify a new phase with a large piezoelectric response that persists up to high temperature. Finally, I show how chemical substitution on the A-sites in $(AA')(BB')O_6$ compounds can greatly enhance the magnitude of the ferroelectric polarization, as well as allow for the incorporation of magnetically active cations on the B-sites.

Chapter 7 – **Effect of Epitaxial Strain on the Crystal Structure and Electronic Properties of Acentric Compounds**: Because the flexible cation-anion network in complex oxide materials allows for significant control over their properties via external stimuli, in this chapter I investigate the effect of epitaxial strain on the crystal structure and properties of brownmillerites. I show how epitaxial strain can control the crystal structure and orientation of anion vacancies in brownmillerite oxides, as well as demonstrate how the band gap can be effectively tuned.

Chapter 8 – **Conclusions and Outlook**: I end this dissertation with a summary of the investigations performed and discuss new opportunities enabled by my work for this burgeoning field.

2. FIRST PRINCIPLES ELECTRONIC STRUCTURE METHODS

The fundamental goal of *ab initio* techniques is to describe and predict the properties of materials without the use of empirical parameters (or, more realistically, using as few as possible). This chapter presents a brief and historically contextualized review of the foundations of the electronic structure calculation methods used in this thesis. In particular, I discuss several of the approximations utilized to make first principles calculations tractable for real complex systems. Finally, I present a qualitative review of these methods and implement mathematical equations when they serve an illustrative purpose; a more complete review of the formalism of density functional theory and related subjects can be found in the following textbooks and review articles: Refs. 38, 39, 40.

2.1 The Schrödinger Equation

From the Schrödinger equation,[41] given in its simplest form as

$$H\Psi = E\Psi, \tag{2.1}$$

the ground state energy E of a system can found by operating on its many-particle wavefunction Ψ with the appropriate Hamiltonian H. Theoretically, any property of the system can then be determined from this result by taking the corresponding expectation values; in practice, however, solving this equation exactly is impossible for all but the simplest systems. Despite this, several approximations can be used to estimate the solutions to this problem, allowing for the modeling of more complex and interesting systems such as crystalline solids. First, the Hamiltonian describing a system of interacting electrons (e) and nuclei (n) can be decomposed into a series

of kinetic (T) and potential (V) energy terms:

$$H = T_e + T_n + V_{nn} + V_{en} + V_{ee}, \tag{2.2}$$

where the kinetic energy terms are given as:

$$T_e = -\frac{\hbar^2}{2m_e}\sum_{i=1}\nabla_i^2, \;\; T_n = -\frac{\hbar^2}{2m_A}\sum_{A=1}\nabla_i^2, \tag{2.3}$$

and the potential energy terms (describing electrostatic or Coulombic interactions between nuclei, between nuclei and electrons, and between electrons, respectively) are:

$$V_{nn} = \frac{e^2}{2}\sum_{A\neq B}\frac{Z_A Z_B}{r_{AB}}, \;\; V_{en} = -e^2\sum_{i,A=1}\frac{Z_A}{r_{iA}}, \;\; V_{ee} = \frac{e^2}{2}\sum_{i\neq j}\frac{1}{r_{ij}}. \tag{2.4}$$

Here, Z is the charge on an ion, m is its mass, and r is the separation between two particles; A and B denote nuclei, while i and j denote electrons.

Because the nuclei are much heavier than the electrons, the electrons can be thought of as moving in an external field while the nuclei remain fixed; the nuclear kinetic energy (T_n) is therefore approximately zero and the nuclear potential energy (V_{nn}) reduces to a simple classical interaction. This simplification is known as the "Born-Oppenheimer" or "adiabatic" approximation.[42] The remaining terms make up the so-called *electronic* Hamiltonian (H_{elec}), which consists of the kinetic energy of the electrons (T_e) and their interactions with the nuclei (V_{en}) and with each other (V_{ee}). Yet, while this represents a significant reduction in complexity, these simplifications are still not sufficient to allow for useful calculations of complex systems. First, three spatial coordinates for each of the approximately 10^{23} electrons in a real system must be specified; furthermore, the fact that each of these electrons interact with each other make determination of the electronic correlation term (*i.e.*, V_{ee}) completely

intractable. It is from this impasse that we now turn our attention to the formulation of density functional theory.

2.2 Density Functional Theory

Following the early attempts of Thomas and Fermi, the first breakthrough leading to density functional theory came from two theories proposed by Pierre Hohenberg and Walter Kohn in a 1964 paper.[43] First, they proposed that the external potential $V(r)$ affecting the electrons, and thus the total energy, is a unique functional of the electron density $n(r)$; this further implies that all of a system's properties can be determined from the electron density, which is a function of only the three spatial dimensions. This is easily demonstrated by showing that because application of the variational principle to two different external potentials with the same electron density gives a non-sensible result (*reductio ad absurdum*), the electron density *must* uniquely define the ground state energy $E[n(r)]$ (to within a constant term). Their second theorem defined a "universal" (in that it holds for any system of electrons and is valid for any choice of external potential) but unknown functional $F[n(r)]$ which contains all electronic kinetic and potential energy terms. The total energy $E[n(r)]$ for a unique $V(r)$ can now be written as:

$$E[n(r)] = \int V(r)n(r)dr + F[n(r)]. \tag{2.5}$$

Importantly, they then showed (again from the variational principle) that the exact ground state is that which minimizes Equation 2.5 and thus the ground state total energy. Although these two theorems represent extremely powerful insights and allow for practical and accurate calculations, they say nothing about *how* to determine $F[n(r)]$.

In 1965, Walter Kohn and Lu Sham published a seminal work (for which Kohn was awarded the 1998 Nobel Prize in Chemistry) showing that it is possible to re-write the interacting many-electron problem onto a system of *non-interacting* electrons that results in the exact same ground state density.[44] The various contributions to the total energy can be separated, and Equation 2.5 can be re-formulated as:

$$E[n(r)] = \int V(r)n(r)dr + T[n(r)] + E_H[n(r)] + E_{XC}[n(r)], \tag{2.6}$$

where $T[n(r)]$ is the non-interacting kinetic energy of the electrons. To account for the interactions, two terms are added. First, $E_H[n(r)]$ (called the Hartree energy) describes the interaction of the charge density with itself, and is given by the equation:

$$E_H[n(r)] = \frac{e^2}{2} \int \int \frac{n(r)n(r')}{|r - r'|} dr dr'. \tag{2.7}$$

Second, the rest of the electron-electron interactions are described by the exchange-correlation energy, $E_{XC}[n(r)]$.

Now that we have an explicit form for the total energy $E[n(r)]$ (given that we now know the universal functional $F[n(r)]$), we can obtain a potential that acts on the non-interacting system of electrons. This is called the Kohn-Sham potential, and is given by $V_{KS}(r)$. Because the same electron density $n(r)$ must minimize the total energy of both the interacting and non-interacting system, $V_{KS}(r)$ can be obtained via the partial derivatives of the Hartree and exchange-correlation energy:

$$V_{KS}(r) = V(r) + \frac{\partial E_H[n(r)]}{\partial n(r)} + \frac{\partial E_{XC}[n(r)]}{\partial n(r)}. \tag{2.8}$$

Using this, an associated Kohn-Sham Hamiltonian (H_{KS}) can now be defined as:

$$H_{KS} = -\frac{\hbar^2 \bigtriangledown^2}{2m} + V_{KS}(r). \tag{2.9}$$

Qualitatively, this Hamiltonian characterizes a system of non-interacting electrons that are affected by the external potential $V_{KS}(r)$ which, as shown previously, contains all of the information about the electron-electron interactions. The Schrödinger equation (Equation 2.1) for such a system is therefore given by:

$$[-\frac{\hbar^2 \bigtriangledown^2}{2m} + V_{KS}(r)]\Psi_i(r) = E_i \Psi_i(r), \tag{2.10}$$

where $\Psi_i(r)$ are single particle wave functions whose square modulus, when combined with the Fermi-Dirac distribution f_i, gives the interacting charge density via

$$n(r) = \sum_{i}^{N} f_i |\Psi_i(r)|^2. \tag{2.11}$$

Starting from a trial electron density and single particle wavefunction, the Kohn-Sham equations (Equations 2.8, 2.10, and 2.11) can be solved iteratively until self-consistency is achieved; from this, the ground state electron density and total energy are obtained.

2.3 The Exchange-Correlation Energy

The formulation of density functional theory laid out by Hohenburg, Kohn, and Sham has allowed for the mapping of a system of interacting electrons to that of a non-interacting one, putting us well on the way towards tractable quantum mechanical calculations of real materials. However, nothing has been said of the exchange-correlation energy $E_{XC}[n(r)]$, for which no analytical solution is provided; this poses

a problem due to the fact that it contains the many-particle interactions, including (as the name suggests) the *exchange interaction* (related to the fact that wavefunctions of fermions are anti-symmetric and giving rise to the Pauli exclusion principle) and the *electron correlation* (the interaction among electrons). So while density functional theory up to this point is an exact theory, we now must introduce assumptions about the form of the exchange-correlation functional and approximate its solution. A wide variety of such density functionals exist, ranging from those using very simple approximations to those which add in additionally complex contributions; climbing this so-called "Jacob's ladder of density functional approximations" generally allows for more accurate results but for greater computational expense.[45,46] In this section, I review several of these functionals, especially those used to produce the results presented in this thesis.

One of the first proposals to this end was to assume that the electron density in real system *locally* behaves as a homogenous electron gas (or HEG, the simplest possible model of interacting electrons), the exchange and correlation terms of which are known exactly from Hartree-Fock theory and quantum Monte Carlo methods, respectively.[47,48] From here, the "true" exchange-correlation energy $E_{XC}[n(r)]$ can be replaced with that of the HEG and be recast as:

$$E_{XC}^{LDA}[n(r)] = \int n(r) E_{XC}^{HEG}[n(r)] dr. \tag{2.12}$$

This is known as the Local Density Approximation (or LDA),[49] and is still one of the most used approximate functionals.[50] Perhaps surprisingly, this simple approximation works rather well for predicting the properties of a wide range of materials.[38] However, by overestimating the binding energy between atoms in a solid, LDA underestimates bond lengths and thus structural parameters such as lattice parameters and cell volume.[51]

The next rung up "Jacob's ladder" are semi-local functionals, such as the Generalized Gradient Approximation (or GGA).[52] As the name suggests, these functionals incorporate information about the gradient of the charge density, $\bigtriangledown n(r)$; the exchange-correlation energy now takes the form:

$$E_{XC}^{GGA}[n(r)] = \int n(r) E_{XC}[n(r), \bigtriangledown n(r)] dr. \tag{2.13}$$

Unlike LDA, there are numerous varieties of GGA functionals, one of the most common being that developed by Perdew, Burke, and Ernzerhof (PBE);[53] the PBE functional as revised for solids (called PBEsol) is the primary one used for this thesis.[54] While GGA functionals are more computationally expensive than LDA because they include the electron density gradient, the increase is basically negligible in return for the increased accuracy provided.

The final type of functionals that will be discussed are hybrids, which represent another step up the ladder in terms of complexity. Furthermore, while LDA and GGA functionals are non-empirical, hybrids are not; the fundamental idea is to combine some percentage of completely non-local exact exchange (as derived from Hartree-Fock theory) with the previously discussed *ab initio* approximations.[55,56] Although there are, again, many different implementations of hybrid functionals, I will only discuss those proposed by Heyd, Scuseria, and Ernzerhof in 2006 (called HSE, with two implementations known as HSE03 and HSE06).[57] This is a so-called "range separated" functional, due to the fact that it divides the electron exchange into short range (SR) and long range (LR) contributions. The short range exchange interactions are then described by a combination of exact exchange and that described by the PBE functional; the long range exchange and correlation contributions to E_{XC} also come

from PBE. This can be represented in the following manner:

$$E_{XC}^{HSE}[n(r)] = \alpha E_{X,SR}^{exact}[n(r)] + (1-\alpha)E_{X,SR}^{PBE}[n(r)] + E_{X,LR}^{PBE}[n(r)] + E_{C}^{PBE}[n(r)]. \quad (2.14)$$

As mentioned previously, this functional is empirical due to the α term, which can be tuned based upon the needs of the system under study. Although hybrid functionals can drastically improve the description of parameters such as the band gap, it must be applied carefully; not only is it much more computationally expensive than LDA or GGA, the selection of α can have a dramatic effect on the electronic properties, leading to either large over- or underestimation.[58]

2.4 Bloch's Theorem and the Irreducible Brillouin Zone

We have now reduced the complex and unsolvable system of interacting electrons to that of non-interacting electrons in an effective potential. Although this theory provides incredible insight, a real material will have somewhere on the order of 10^{23} electrons, still far too many to handle in reasonable calculations; further simplifications are once again needed to produce computationally tractable systems. To solve this problem, we now take advantage of the lattice periodicity of crystals to reduce the number of atoms, and therefore electrons, under consideration.

Application of Bloch's theorem[59] is our first step towards the further reduction of complexity. This states that in any periodic system (*i.e.*, atoms in a crystal), the single particle wavefunction Ψ can be written as:

$$\Psi(r) = e^{ik\cdot r}u(r). \quad (2.15)$$

Here, k is the wave vector of the crystal, while $e^{ik\cdot r}$ is a plane wave; $u(r)$ is a periodic function that, importantly, matches the period of the crystal lattice. Expanding $u(r)$

as a three dimensional Fourier series summed over the reciprocal lattice vector G results in:

$$u(r) = \sum_{G} Ce^{iG\cdot r}, \tag{2.16}$$

which, when combined with Equation 2.15, gives:

$$\Psi(r) = \sum_{G} Ce^{i(k+G)\cdot r}. \tag{2.17}$$

The Kohn-Sham equations and the wavefunction can now be easily solved using this plane wave expansion. One last caveat, however, is that we must truncate the sum at some G-vector or energy (such that $\frac{\hbar}{2m}|k+G|^2 \leq E_{cutoff}$) in order to not have an infinite expansion. This cutoff energy is a tunable input parameter that must be selected carefully so as to ensure converge of the calculations with respect to the properties of interest.

Given this plane wave representation of the Kohn-Sham equations derived from Bloch's theorem, the energy and charge density can now be determined from integrals over the Brillouin zone (BZ) rather than an infinite integral over all of real space. Furthermore, the BZ size can be further decreased by applying all of the symmetry elements of the point group of the crystal under consideration; this area is known as the irreducible Brillouin zone (IBZ). Despite the fact that the integrals now have to be evaluated only in a certain area of space, the integration still technically must be performed over an infinite number of k-points in the IBZ. However, by evaluating the functions at specifically determined points and interpolating the rest, the integrals can once again be reduced from an infinite one to a sum only over a few specially weighted k-points. While a number of methods for selection of these points have been proposed, in this thesis I exclusively use that put forth by Monkhorst and Pack in 1976, which sets up an evenly space grid throughout the BZ.[60] Like the cutoff

energy described above, the number of k-points along each reciprocal space direction is typically a manually chosen input parameter that can differ based on the accuracy required for the specific system under study; again, judicious selection must be made so as to again ensure convergence.

2.5 Pseudopotentials

Yet another way to reduce the complexity of a system is to decrease the number of electrons *per atom* under consideration. Because the electrons near the core of an atom (*i.e.*, the "core" electrons) are highly localized and their wavefunctions oscillate rapidly owing to the strong potential of the nucleus and orthogonality constraints, an accurate representation requires an immense number of plane waves in the basis set. While some so-called "all-electron" codes attempt to consider these due to the fact that the core is not always independent of its surroundings,[61] these electrons are not especially useful to study in terms of material properties and mainly serve only to slow down calculations (I note, however, that some processes do require core electrons). Instead, the core is "frozen" and replaced with an effective potential, greatly reducing the amount of plane waves required and allowing the chemically active valence electrons, which determine most of a compound's properties, to have much smoother wavefunctions (further decreasing the number of plane waves needed) and to be considered explicitly. Here I will discuss two types of approaches used to construct pseudopotentials for DFT calculations: norm-conserving and projector augmented wave (or PAW) methods. For the full details of these two methods (of which this summary is based), see Refs. 62 and 63, respectively. While I only use the PAW method in this thesis, the norm-conversing method serves as a simple but valuable illustration of the ideas behind pseudopotential generation.

To generate norm-conserving pseudopotentials, we first start from the all-electron

wavefunction of an atom. As mentioned previously, the highly fluctuating wavefunctions near the ion core are replaced up to a chosen cutoff radius r_c by a function that varies much more smoothly, and, importantly, is nodeless; beyond this radius, the function is required to exactly match the all-electron wavefunction. Consider the $2s$ and $2p$ state of oxygen as an example. Here, the all-electron wavefunction of the $2s$ orbital is localized close to the core and exhibits one node; the pseudopotential removes this node and smoothes out the wavefunction below $r_c \sim 0.7$ Bohr, while matching it exactly above r_c. On the other hand, the $2p$ all-electron wavefunction and pseudopotential are nearly equivalent. Finally, it should be noted that often "semi-core" states, such as the $4s$ states in $3d$ transition metals or fully filled d-shells in rare earth elements, must also be treated explicitly due to the fact that they are often not well separated from the true valence states.

As alluded to previously, loss of the information about the core states in norm-conserving pseudopotentials can have an effect on the calculation of certain properties. The projector augmented wave method provides a means to reduce computational complexity while still retaining the details of the all-electron approach; it has often been said that the PAW method is "pseudopotentials done right." While this may be a slight hyperbole, the PAW approach allows for smooth and nodeless wavefunctions, low numbers of plane waves, and access to the full all-electron wavefunction and density. In general, the area closest to the core is represented as an "augmentation sphere," while the region outside is represented by well-defined, smooth "envelope" functions; these are then matched at the boundary of the sphere. Inside the sphere, it is possible to map the all-electron wavefunctions to a "pseudo-" or "atomic-like" wavefunction, Here, I summarize the derivation of this mapping which was presented by Blöchl in 1994;[63] I use the compact Dirac notation to express his results.

We first define the all-electron and pseudo-wavefunctions as $|\Psi\rangle$ and $|\tilde{\Psi}\rangle$, respec-

tively; it is important to note that $|\Psi\rangle$ is the Kohn-Sham single particle wavefunction, as opposed to the many-body. As stated previously, we seek to map $|\Psi\rangle$ onto $|\tilde{\Psi}\rangle$; this is accomplished via some transformation operator $\mathcal{T}$ as so:

$$|\Psi\rangle = \mathcal{T}|\tilde{\Psi}\rangle. \tag{2.18}$$

In order to smooth out the wavefunction only near the nucleus, the $\mathcal{T}$ is rewritten as the sum of atomically centered transformation operators ($\mathcal{T}^a$) that act only inside non-overlapping augmentation spheres, each of radius r_c^a:

$$\mathcal{T} = 1 + \sum_a \mathcal{T}^a \tag{2.19}$$

Inside the sphere, we can now decompose the total wavefunction $|\Psi\rangle$ into a sum of atomic wavefunctions $|\phi^a\rangle$, each weighted by an expansion coefficient c_i, by:

$$|\Psi\rangle = \sum_i c_i^a |\phi_i^a\rangle, \tag{2.20}$$

and, using the transformation operator, map these onto the pseudo-wavefuctions:

$$|\phi_i^a\rangle = (1 + \mathcal{T}^a)|\tilde{\phi}_i^a\rangle. \tag{2.21}$$

From this, the transformation operator is now known in terms of the atomic wavefunctions:

$$\mathcal{T}^a|\tilde{\phi}_i^a\rangle = |\phi_i^a\rangle - |\tilde{\phi}_i^a\rangle \tag{2.22}$$

The expansion coefficients are given by:

$$c_i^a = \langle p_i^a|\tilde{\Psi}\rangle, \tag{2.23}$$

where p_i^a are projection operators that are orthonormal to the pseudo-atomic waves (*i.e.* they must satisfy the condition $\sum_i |\tilde{\phi}_j^a\rangle\langle p_i^a| = 1$). By combining this condition with Equations 2.19 and 2.22, we can rewrite the transformation operator as a double sum:

$$\mathcal{T} = 1 + \sum_a \sum_i (|\phi_i^a\rangle - |\tilde{\phi}_i^a\rangle)\langle p_i^a|, \tag{2.24}$$

and, finally, rewrite the full Kohn-Sham wavefunction as:

$$|\Psi\rangle = |\tilde{\Psi}\rangle + \sum_a \sum_i (|\phi_i^a\rangle - |\tilde{\phi}_i^a\rangle)\langle p_i^a|\tilde{\Psi}\rangle. \tag{2.25}$$

While this series of equations may seem rather obtuse, Equation 2.25 represents an extremely important result, as we now have the total wavefunction written in terms of atomic wavefunctions, pseudo-wavefunctions, and the projector functions. However, care must be taken in selection of an appropriate form for the projector, as different functions can result in different levels of accuracy. To summarize, we know that a very fine grid is needed to capture the information of the oscillating core states; in the original Kohn-Sham formalism, however, this means a very fine grid would be applied to the smooth functions as well, adding unneeded computational complexity. In the norm-conversing approach, the core states were simply removed, at the expense of losing knowledge about them. Qualitatively, what the PAW approach presented here has done is divide the original all-electron Khon-Sham wavefunction $|\Psi\rangle$ into two parts: one that contains functions that are smooth everywhere (*i.e.* both inside and outside the augmentation sphere), and one which contains highly oscillatory functions. The key innovation is that the smooth functions and oscillatory functions can now be treated separately by a very rough and very fine grid, respectively, allowing for retention of the core state information while significantly speeding up calculations. Finally, because atomic wavefunctions have been used, pseudopotentials generated

from this approach are independent of the chemistry of the system, as only one pseudopotential per atomic species (which can then be concatenated) is needed.

2.6 The Band Gap "Problem" and DFT+U

Although density functional theory provides an amazing degree of accuracy and predicts many material properties well, one of its major problems is a failure to properly describe excited state properties; a primary manifestation of this problem is a severe underestimation of the band gap, often by up to 50%.[64] This is a particular issue in oxides containing so-called strongly correlated metals, or those with whose ground states contain highly localized electrons, such as Mn, Co, Fe, and Ni compounds.[65] On a fundamental level, this stems from the fact that density functional theory tends to "over-delocalize" electrons due to the exchange-correlation functional (*i.e.* LDA or GGA) not fully canceling the self-interaction term. The electronic band gap is therefore reduced because an electron (or, more specifically, the charge density associated with it) repels itself, causing an exaggerated delocalization, which imparts greater metallic character to a system. While several methods have been proposed to deal with this problem, such as dynamical mean field theory (DMFT)[66] or GW,[67] their computational expense is often prohibitive. One of the most successful approaches has been to supplement DFT calculations with model Hamiltonians based on the Hubbard model,[68] which significantly improves the accuracy of the band gap while only slightly increasing the cost of a calculation.[69]

The central idea of the Hubbard model is that electrons in a lattice can be characterized by two terms: one which allows for a transfer between atoms (this is related to the electrons kinetic energy, and is often referred to as "hopping" or "tunneling"), and one which describes their on-site interaction (related to a potential energy). An insulating ground state then occurs when electrons from one atom cannot transfer

because of the repulsion from those on neighboring atoms. By applying an energetic penalty (henceforth called U) to the "hopping," electrons can be forced to be in certain orbitals in DFT calculations. The total energy of a system can now be written as:

$$E^{DFT+U} = E^{DFT} + E^{U} - E^{dc}, \tag{2.26}$$

where E^{DFT} is the total energy computed from density functional theory, E^{U} is the aforementioned penalty, and E^{dc} is a double counting term removing the interaction energy that is already accounted for in E^{DFT}. It is important to keep in mind that this Hubbard correction is selected by the user and only applied to the orbitals which contain the strongly correlated electrons, such as the d states in transition metals or f states in rare earth elements; the rest of the electrons are treated by standard density functional theory.

2.7 Lattice Dynamics and Instabilities

The final first principles computational methods covered in this chapter are lattice dynamical calculations. Lattice dynamics are key to understanding a wide variety of phenomena, including, but not limited to, phase transitions, thermal properties, and superconductivity.[70–74] From the viewpoint of density functional theory, computation of the phonon band structures is an indispensable tool when attempting to determine the ground state of a given system from first principles. The calculations in this thesis rely on the harmonic approximation and on the determination and solving of the dynamical matrix.[75,76] Because atoms move very little around their equilibrium positions at low temperature, we can expand the energy of a crystal as:

$$E(\Delta\vec{R}) = E(\vec{R}_0) + \sum_{ls\alpha} \frac{\partial E(\vec{R}_0)}{\partial \vec{R}_{ls\alpha}} \Delta\vec{R}_{ls\alpha} + \frac{1}{2} \sum_{ls\alpha} \sum_{l's'\beta} \frac{\partial^2 E(\vec{R}_0)}{\partial \vec{R}_{ls\alpha} \partial \vec{R}_{l's'\beta}} \Delta\vec{R}_{ls\alpha} \Delta\vec{R}_{l's'\beta} + ..., \tag{2.27}$$

where $\Delta\vec{R}$ describes the displacement of atom s in unit cell l from its equilibrium position along a given Cartesian direction (indicated by the Greek subscripts). The truncation of this expression after the second order term (as shown above) is called the harmonic approximation. Given this, any particular atom feels a force of:

$$F_{ls\alpha} = -\frac{\partial E(\vec{R}_0)}{\partial \vec{R}_{ls\alpha}} = -\sum_{l's'\beta} \Phi_{ls\alpha,l's'\beta} \Delta\vec{R}_{l's'\beta}, \tag{2.28}$$

where Φ is the so-called matrix of interatomic force constants and has the form of a Hessian:

$$\Phi_{ls\alpha,l's'\beta} = \frac{\partial^2 E(\vec{R}_0)}{\partial \vec{R}_{ls\alpha} \partial \vec{R}_{l's'\beta}}. \tag{2.29}$$

The solution to this second order differential equation takes the form of a traveling wave:

$$\vec{R}_{ls\alpha}(\vec{r}, t) = \sum_k \vec{R}_{ls\alpha}(k) e^{i\vec{k}\vec{r}} e^{i\omega_k t}, \tag{2.30}$$

and substitution of this solution into Equation 2.28 allows us to obtain the dynamical matrix:

$$D_{s\alpha,s'\beta}(\vec{k}) = \frac{1}{\sqrt{M_s M'_s}} \sum_{l'} \Phi_{ls\alpha,l's'\beta} e^{i\vec{k}(\vec{R}_{l's'} - \vec{R}_{0,ls})}. \tag{2.31}$$

Finally, solutions of this matrix yield the phonon frequencies $\omega_{m\vec{k}}$ (corresponding to mode m and wave vector $\vec{k}$) and their eigenvectors $\epsilon_{m\vec{k}}$:

$$\sum_{s',\beta} D_{s\alpha,s'\beta}(\vec{k}) \epsilon_{m\vec{k}}(s'\beta) = \omega^2_{m\vec{k}} \epsilon_{m\vec{k}}(s\alpha). \tag{2.32}$$

There are two main methods for computing the phonon band structure: the frozen phonon method and density functional perturbation theory (DFPT).[77] Here, a small displacement is applied to each atom, and the forces felt by all atoms in the system is calculated by using the Hellmann-Feynman theorem. This process is repeated until

the entire force constant matrix $\Phi_{ls\alpha,l's'\beta}$ is generated. Within this approach, large supercells must often be generated in order to access certain parts of the Brillouin zone; depending on the size of the system, this method can be quite time intensive. However, because each set of atomic displacements can be considered independently, the frozen phonon method is trivially parallelizable.

In DFPT, the variation in the electron density and wavefunctions is obtained from first-order perturbation theory, which generates a set of equations to be solved self-consistently (analogous to the Kohn-Sham equations of DFT). Furthermore, because the perturbations of different wavelengths are decoupled, the phonons at any arbitrary $\vec{q}$ can be obtained. However, DFPT can take large amounts of time. In principle, the two methods produce the exact same results, and the choice of method is generally based on time constraints and the size of the system under study.

As alluded to previously, phonon calculations are highly useful for determining the ground state of a system owing to the information about stability it can provide. If imaginary frequencies appear in the phonon band structure, it indicates that the system is unstable to the pattern of atomic displacements characterized by that mode and that their insertion into the crystal structure will lower the energy. If all the phonon frequencies are positive (*i.e.*, real), any further distortions will raise the energy of the system, indicating that this structure is in a minimum of the potential energy surface.

As an example, consider the perovskite $LaAlO_3$; phonon calculations on the high symmetry cubic $Pm\bar{3}m$ phase of this material indicate the presence of triply degenerate unstable modes at the R-point in the Brillouin zone (Figure 2.1).[78] An analysis of the displacement eigenvector indicates that this linear combination of these modes represents rotations of the AlO_6 octahedra about the three axes. Once this distortion is frozen in, re-computing the phonons shows no unstable modes; this rhombohedral

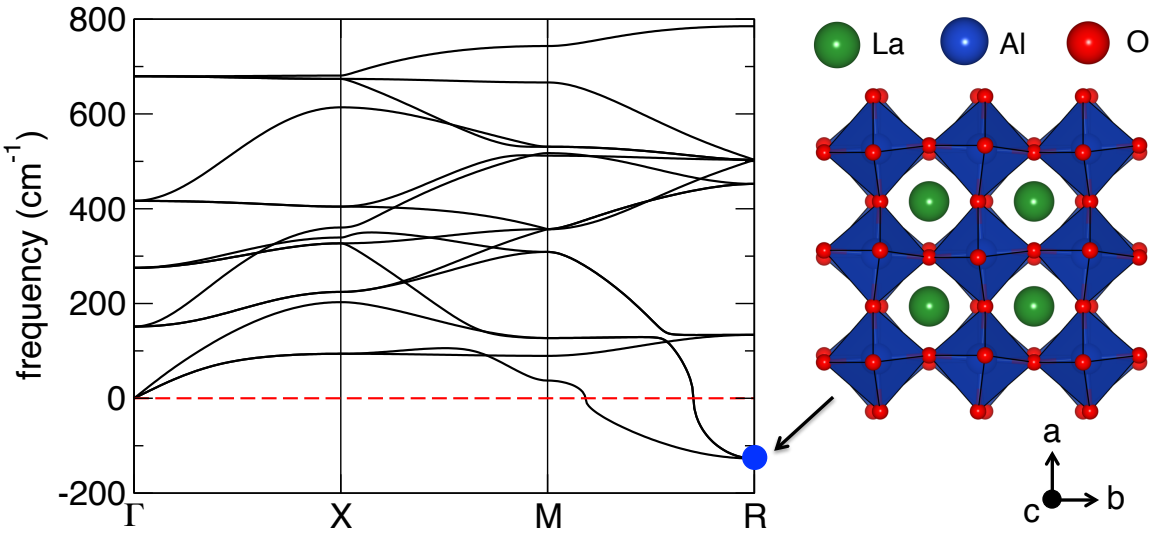

Figure 2.1: Phonon band structure of cubic $Pm\bar{3}m$ $LaAlO_3$ computed using density functional theory. The imaginary frequency at the R point represents a mode to which the high symmetry phase is unstable; in this case, it corresponds to out-of-phase AlO_6 octahedral rotations along the three Cartesian axes. Freezing in these displacements takes $LaAlO_3$ from its high symmetry $Pm\bar{3}m$ phase to a $R\bar{3}m$ ground state.

$R\bar{3}m$ phase can therefore be considered dynamically stable and a local ground state.

2.8 Specific Computational Details

Unless otherwise specified, all investigations presented in this dissertation were performed using density functional theory as implemented in the Vienna *Ab-initio* Simulation Package (`VASP`),[43,79,80] a plane-wave based code. Furthermore, projector augmented-wave (PAW) potentials[63] with the PBEsol functional[54] were chosen because they are adjusted to give better agreement with lattice parameters and bond angles specifically in solids. The k-point meshes for all systems were generated using the Monkhorst-Pack scheme.[60] If a Hubbard U correction was necessary, it was applied using the Dudarev formalism to treat the appropriate correlated states.[81] Symmetry-adapted mode decompositions were performed using the ISODISTORT tool, part of

the ISOTROPY software suite,[82] and all atomic structures were visualized using the Visualization for Electronic and Structural Analysis software (VESTA).[83]

3. STRUCTURE AND CHEMISTRY OF PEROVSKITE AND PEROVSKITE-RELATED COMPOUNDS

The family of ABX_3 perovskites is one of the most chemically diverse of all materials, as they are able to accommodate most of the elements of the periodic table. Because of this, the electronic character of different members can range from metallic to semiconducting to insulating (while also being able to transition between them), and they can exhibit exotic magnetic orderings, colossal magnetoresistance, superconductivity, multiferroicity, and piezoelectricity (among many other properties).[84–90] Furthermore, the flexibility of the characteristic corner-connected network of BX_6 octahedra makes these properties highly tunable via epitaxial strain or chemical substitution. In this chapter, I discuss the crystal-chemistry of perovskites, including common chemical descriptors and structural distortions, as well as cation ordering possibilities. I also review the closely related $ABX_{2.5}$ brownmillerite phases, which are perovskite derivatives exhibiting ordered channels of anion vacancies.

3.1 Perovskite Crystal Structure and Chemistry

A prototypical member of the perovskite family has the general chemical formula ABX_3, where A and B are cations and X are anions. These materials can support a vast array of chemistries, with the A- and B-site able to accept most of the metallic or semi-metallic elements of the periodic table (Figure 3.1a), as well as small organic molecules (such as methylammonium, CH_3NH_3). Furthermore, although the majority of perovskites are oxides (X = O), there are also halides (X = F, Cl, Br, I), sulfides (X = S), and nitrides (X = N), with multi-anion chemistries also possible.[91–100] The B-site atoms are coordinated by six X anions, which can be imagined as BX_6 octahedra

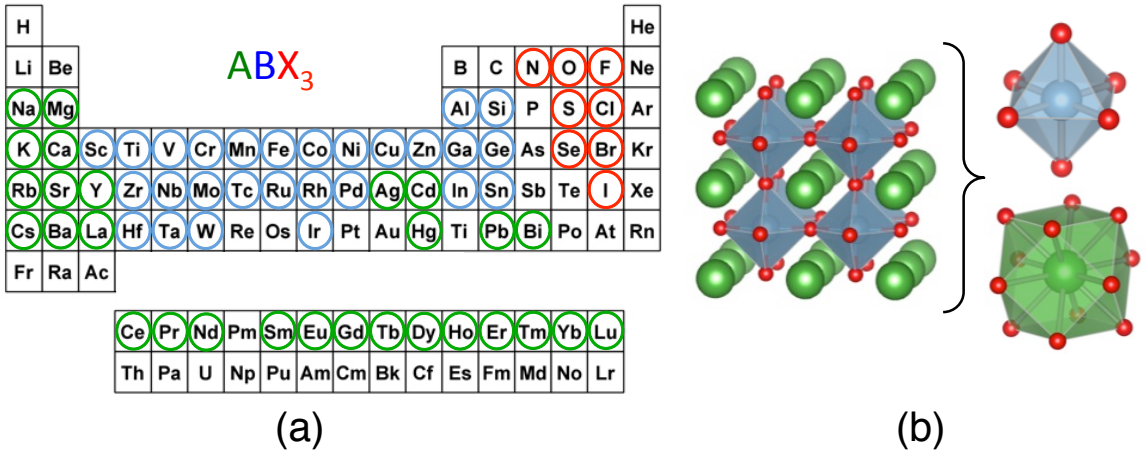

Figure 3.1: (a) The ABX_3 perovskite family can accommodate a wide variety of elements from the periodic table on the A-site (green), B-site (blue), and X-site (red). (b) The perovskite structure consists of corner-connected BX_6 octahedra (blue), with A-site cations filling the interstices and forming AX_{12} cuboctahedra (green).

that form a three-dimensionally corner-connected network extending throughout the crystal; the A-site atoms sit in the interstices and are coordinated by 12 anions, forming AX_{12} cuboctahedra (Figure 3.1b). While this ideal structure exhibits cubic space group symmetry $Pm\bar{3}m$ (no. 221), the vast majority of perovskites do not form in this undistorted phase, but instead undergo displacive distortions, the most common of which are cooperative displacements of the anion sublattice manifesting as "rotations" of the BX_6 units.[101–103]

The standard notation for describing these octahedral rotations was introduced by Glazer in the 1970's[104,105] and later refined with group theoretical insights from Aleksandrov[106] as well as Howard and Stokes.[107] A given octahedral rotation pattern is indicated by $a^X b^X c^X$, where a, b, and c denote the Cartesian a, b, and c axes, respectively. The X superscript is then replaced depending on the type of rotation present; along a Cartesian direction, the BX_6 units can either remain unrotated (indicated by $X = 0$, Figure 3.2a), or they can rotate in-phase ($X = +$, Figure 3.2b) or out-of-phase ($X = -$, Figure 3.2c). Finally, if the magnitude of the rotations are

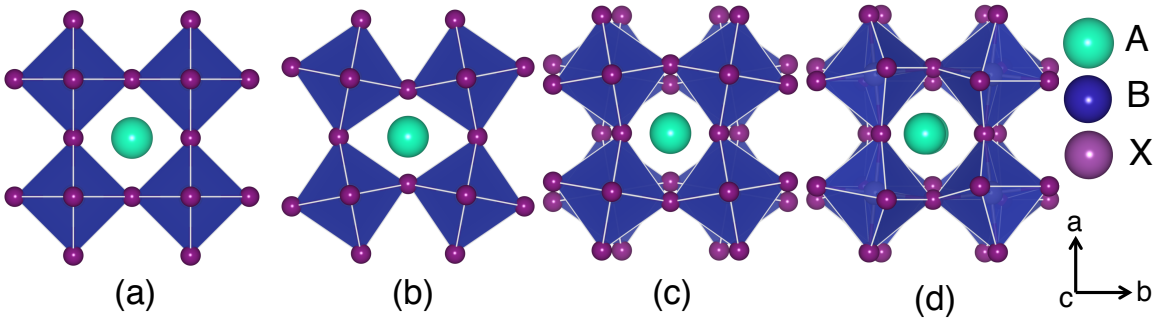

Figure 3.2: Cooperative anion displacement patterns result in "rotations" of the flexible corner-connected network of BX_6 octahedra in perovskites. Octahedral rotations patterns can consist of (a) no rotations, (b) in-phase rotations, or (c) out-of-phase rotations along different Cartesian axes; combinations of each result in (d) mixed tilt patterns.

equal along two different axes, they are replaced by the same letter. Given these rules, the undistorted perovskite shown in Figures 3.1b and 3.2a exhibits the $a^0a^0a^0$ rotational pattern, while those in Figure 3.2b and 3.2c exhibit $a^0a^0c^+$ and $a^0a^0c^-$, respectively; Figure 3.2d shows an example of a perovskite with a mixture of both in-phase and out-of-phase tilts ($a^-a^-c^+$). After taking all possible combinations into account, there are 15 distinct octahedral rotation patterns that retain the corner-connectivity of the BX_6 network (Table 3.1), which can be divided based on whether the pattern exhibits no rotations, only in-phase rotations, only out-of-phase rotations, or both in-phase and out-of-phase rotations ("mixed"). Each distortion modifies the point symmetry of different Wyckoff positions, resulting in the 15 different space groups listed (Table 3.1).

The most common qualitative descriptor parameterizing the propensity for a given perovskite to undergo octahedral rotations is the Goldschmidt tolerance factor,[108] given by:

$$\tau = \frac{r_A + r_X}{\sqrt{2}(r_B + r_X)}, \tag{3.1}$$

where r_A, r_B, and r_X are the ionic radii of the A-site, B-site, and X-site ions, re-

spectively. Although Shannon's ionic radii[109] are often used to compute τ, it is often better to utilize the tabulated A-X and B-X bond lengths from the bond valence model, which does not require knowledge of the cation coordination environment.[110] This quantity is a measure of the ability of the A-site cations to comfortably fit inside the interstices of the BX_6 lattice. For τ close to 1, the A-site is the ideal size to fill these spaces, and the undistorted cubic phase is predicted to form. A tolerance factor below 1 indicates that the A-site cation is too small and is underbonded by the X-site anions; to improve the A-site coordination and enhance A-X covalency, the compound typically undergoes octahedral rotations. This heuristic measure holds until $\tau \approx 0.7$, below which value the perovskite structure is highly unlikely to form. Finally, if τ is greater than 1.1, the A-site atom is too large, and non-perovskite hexagonal polymorphs are the most commonly observed phases.[111,112]

Although the tolerance factor is a useful measure of determining the stability of a given perovskite chemistry and whether a compound will undergo octahedral rotations, predicting what *type* of rotations (Table 3.1) it will undergo is a much more difficult task. Although the resulting tilt pattern(s) exhibited by a perovskite are the result of complex ionic and covalent interactions not easily condensed into simple rules, it is possible to identify some heuristic guidelines and chemical arguments for the observation of different tilt patterns. The first observation to note is that because the octahedra are assumed to remain nearly rigid while rotating (in the absence of other electronic instabilities), optimization of the A-X coordination environment is generally what drives these structural distortions.[102] The two most common tilt patterns are by far orthorhombic $a^-a^-c^+$ ($Pnma$) and rhombohedral $a^-a^-a^-$ ($R\bar{3}c$), which together represent nearly 75% of perovskites.[103] In the case of $a^-a^-c^+$, the BX_6 rotations are stabilized primarily by the ability of the A-site to off-center and create strong A-X bonds. While the cations are not allowed to off-center in the $a^-a^-a^-$ case,

Table 3.1: The 15 distinct BX_6 rotational pattern can be divided into groups based on whether the pattern contains no rotations (1 variant), in-phase rotations only (4 variants), out-of-phase rotations only (6 variants), or a mixture of in-phase and out-of-phase rotations (4 variants).

Rotation Pattern	Glazer Notation	Space Group
None	$a^0a^0a^0$	$Pm\bar{3}m$ (221)
In-phase	$a^0a^0c^+$	$P4/mbm$ (127)
	$a^0b^+b^+$	$I4/mmm$ (139)
	$a^+a^+a^+$	$Im\bar{3}$ (204)
	$a^+b^+c^+$	$Immm$ (71)
Out-of-phase	$a^0a^0c^-$	$I4/mcm$ (140)
	$a^0b^-b^-$	$Imma$ (74)
	$a^-a^-a^-$	$R\bar{3}c$ (167)
	$a^0b^-c^-$	$C2/m$ (12)
	$a^-b^-b^-$	$C2/c$ (15)
	$a^-b^-c^-$	$P\bar{1}$ (2)
Mixed	$a^0b^+c^-$	$Cmcm$ (63)
	$a^+b^-b^-$	$Pnma$ (62)
	$a^+b^-c^-$	$P2_1/n$ (11)
	$a^+a^+c^-$	$P4_2/nmc$ (37)

this tilt pattern is stabilized by the fact that it allows for maximum ionic interaction (*i.e.* Coulombic attraction of cations and anions). Finally, the undistorted $a^0a^0a^0$ pattern is also fairly common, and $a^+a^+a^+$ is often exhibited by double perovskites of the form $AA'_3B_4O_{12}$;[113] while other types of rotations are possible, many of them are exceedingly rare or have never been seen in bulk.[103]

One useful descriptor for comparing different octahedral rotation patterns in perovskites is the global instability index (GII),[114] which is given by:

$$\mathrm{GII} = \sqrt{\frac{1}{N}\sum_{i=1}^{N} d_i^2}, \tag{3.2}$$

where N is the number of atoms in the unit cell. The variable d_i is called the "discrepancy factor," and is simply the difference between the formal oxidation state of atom i and its computed bond valence sum in the structure under study. This implies that the closer an atom is to its ideal valence, the smaller d_i will became, and the GII will be minimized; the smaller the GII, the more stable the structure is predicted to be. Previous work has determined that the ground state of a typical perovskite will have GII < 0.1, and nearly always < 0.2.[115] By freezing in different tilt patterns and seeing which one minimizes the GII, we can obtain a rough measure of which one a given ABX_3 chemistry has the greatest propensity towards. In Chapter 5, I show how the GII can be utilized to better understand how selection of the appropriate chemistries can induce particular types of the aforementioned lattice distortions and, in combination with cation ordering (discussed in the next section), change or destroy the presence of certain symmetry operations in perovskites.

3.2 Cation Ordering

The diversity of the perovskite family is further increased by the fact that more than one chemical species can occupy the A-, B-, and X-site.[116] Furthermore, ordering the atoms (as opposed to having a random alloy) can remove the presence of certain symmetry elements from the perovskite crystal structure. Chemical substitution of the A and B cations is an especially fruitful route to obtaining ordered compounds as it often occurs naturally.[117–120] Furthermore, the use of kinetically controlled growth methods such as molecular beam epitaxy has also given a greater degree of control over chemical ordering.[33,35,121–123] I would like to mention here that although anion substitution is a vast field, with a wide variety of oxyhalide, oxynitride, and multihalide perovskites all known to exist, purposeful ordering is difficult to achieve.[98,99,124] In this section I discuss the different types of cation ordering and

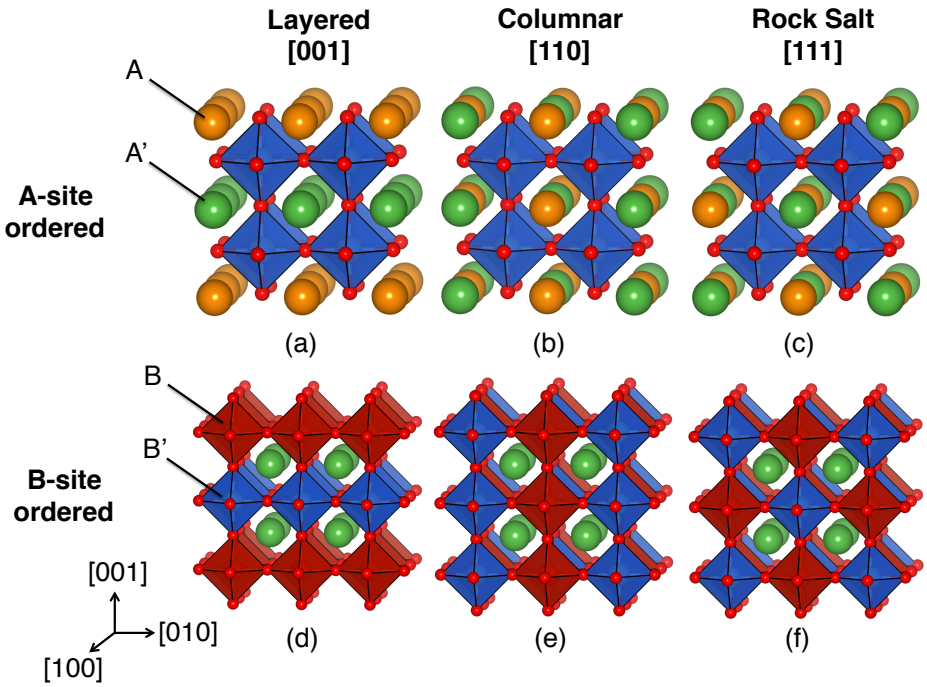

Figure 3.3: Chemical ordering of A and A' (a, b, c) or B and B' (d, e, f) cations along the [001], [110], and [111] crystallographic direction in perovskites. The undistorted $a^0a^0a^0$ phase in combination with layered (a, d) or columnar ordering (b, e) produces space group $P4/mmm$, or $Fm\bar{3}m$ in the presence of rock salt ordering (c, f).

the factors stabilizing them and show how they can be combined with the previously shown octahedral rotation patterns to purposefully change and modify point symmetry operations and induce or enhance physical properties.

The three most common ways that A-site and B-site cations can order in perovskites are colloquially known as "layered", "columnar", and "rock salt" based on how the ordering scheme looks (Figure 3.3). More formally, these orderings are identified by planes which contain "like"-atoms (*i.e.* planes that contain only all A or A' atoms): [001] for layered, [110] for columnar, and [111] for rock salt. As in the case of octahedral rotations, these types of cation ordering modify the point symmetries of different Wyckoff positions, reducing the symmetry from the $Pm\bar{3}m$ space group of the unordered phase; also, similar to rotations, binary cation ordering alone can

not lift inversion symmetry in perovskites. In bulk materials, electrostatic arguments give insight the preference and stability of different ordering patterns for the A and B cations. For A-site ordered compounds, the difference in oxidation state between A and A' is most commonly 0 or 1, and never more than 2; this means that size differential is the more important factor. In terms of this constraint, the layered configuration (Figure 3.3a) is the most favorable type of A-site ordering. Furthermore, layered A-site ordering can be stabilized by both oxygen vacancies and A-site vacancies. A-site columnar (Figure 3.3b) and rock salt (Figure 3.3c) ordering are much less common, and are stabilized by an $a^+a^+c^-$ octahedral rotation pattern or an A/A' charge difference, respectively. In B-site ordered compounds, the valence difference between two different B/B' cations can range anywhere from 0 to 6. Here, layered (Figure 3.3d) and columnar (Figure 3.3e) ordering are often very rare; instead, rock salt ordering (Figure 3.3f) is preferred in order to maximize the separation between highly charged B-sites.[125]

Finally, both the A-sites and B-sites can be cation ordered simultaneously to produce perovskites of the form $(A,A')(B,B')O_6$. Unsurprisingly, the most common configuration is that of "double" perovskites, consisting of layered A-sites with rock salt ordered B-sites (*i.e.*, the most electrostatically preferred configuration for each respective site). However, as eluded to previously, kinetically controlled growth methods such as oxide molecular beam epitaxy allow for layer-by-layer growth of perovskites; in this way, double layered, double columnar, and double rock salt cation ordering patterns may be produced by growth on an [001]-, [110]-, and [111]-terminated substrate. However, this type of growth is still difficult, and realistic control over this level of precision is one of the grand challenges in synthesis science. In Chapter 5, I will explore how the 10 types of cation ordering discussed here can be combined with the 15 octahedral rotation patterns discussed previously to deterministically lift

inversion symmetry and produce polar perovskite oxides.

3.3 Brownmillerites

The family of brownmillerite oxides (general formula $ABO_{2.5}$ or, as I will alternatively refer to them in this thesis, $A_2B_2O_5$) can be derived from ABO_3 perovskites with one-sixth of the oxygen atoms removed (Figure 3.4a), creating parallel rows of ordered anion vacancies along the [110] crystallographic direction; this results in alternating layers of corner-connected BO_4 tetrahedra and BO_6 octahedra (Figure 3.4b). These resulting vacancy channels make these materials very useful for ionic conducting and anion insertion applications.[126–133] While cooperative distortions and octahedral rotations are well understood in perovskites (as discussed in the previous sections), the tetrahedral layers in the brownmillerites add additional structural complexity and possible degrees of freedom for materials design. Both the octahedra and tetrahedra can rotate, with each tetrahedral chain able to 'twist' in a "left-handed" or "right-handed" sense, resulting in two different types of chains related by a mirror plane perpendicular to its direction (Figure 3.5a). Furthermore, these different chains can be ordered relative to each other within the brownmillerite unit cell, resulting in a variety of structures displaying different space group symmetries.

When the tetrahedra and octahedra are not rotated (or have disordered left- and right-handed chains, such as incommensurate ordering or no long range order), the structure displays the *Imma* space group (Figure 3.5b); this aristotype may be used as a high symmetry reference phase for which subsequent structural analyses are made. Some structures, such as Sr_2CoFeO_5 and Sr_2MnGeO_5,[134,135] display this phase at ambient conditions, while others become disordered at high temperature (including $Ca_2Al_2O_5$ and $Ca_2Fe_2O_5$).[136,137] Each of the three low-symmetry bulk hettotypes display two-dimensional sheets of corner-connected octahedra, which rotate out-of-phase

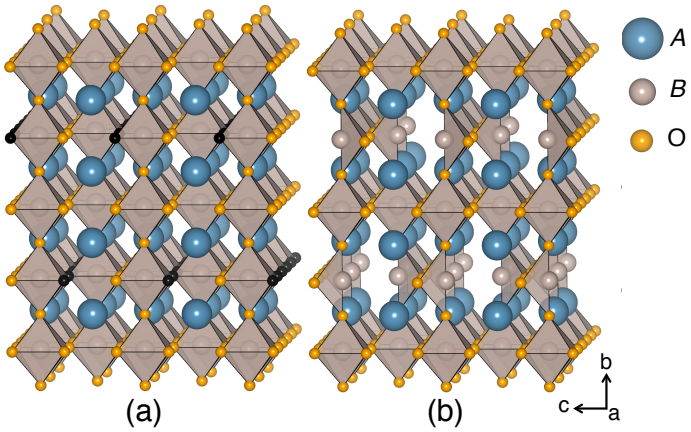

Figure 3.4: The removal of chains of oxygen atoms (colored in black) from the ABO_3 perovskite structure (a) results in the vacancy ordered $ABO_{2.5}$ (or $A_2B_2O_5$) brownmillerite structure (b), which consists of alternating layers of BO_4 tetrahedra and BO_6 octahedra along the b direction. The undistorted rows of BO_4 tetrahedra can then 'twist' (c) to create left- or right-handed chains (colored blue and red, respectively).

along the a and c axes. This rotation transforms like the irreducible representation (irrep) Γ_1^+ of the $Imma$ phase.

Along the b axis, however, the allowed displacements of the oxygen atoms are constrained by the 'handedness' and ordering of the tetrahedral chains, which ultimately control the final symmetry of the brownmillerite structure. The tetrahedral chains can cooperatively rotate in a variety of ways, each described by a different irrep of $Imma$. When the tetrahedra rotate into either all left- or all right-handed chains, the structure displays the polar space group $I2bm$ owing to the Γ_3^- irrep (Figure 3.5b). If there is a racemic mixture of both types of chains, the structure becomes centrosymmetric with different relative orderings generating different symmetries. Alternating chains of different handedness within each tetrahedral layer are described by the Λ_4 irrep and yields the centrosymmetric $Pbcm$ structure (Figure 3.5c), while alternation between layers (given by X_4^+) gives the centric $Pnma$ structure (Figure 3.5d). Because the left- and right-handed chains are related by symmetry and differ

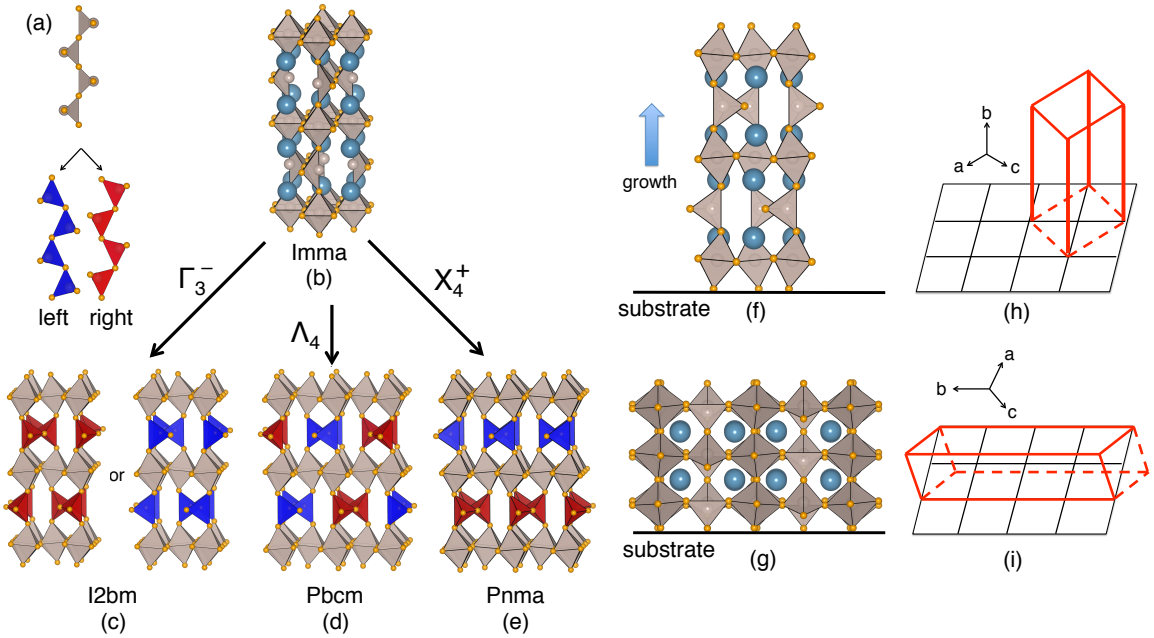

Figure 3.5: (a) Tetrahedral chains can rotate into either a left-handed (blue) or right-handed (red) configuration. The hypothetical high symmetry brownmillerite structure (b) is defined as having no octahedral or tetrahedral rotations and has the *Imma* space group. Relative ordering of tetrahedral chains results in three different low-symmetry structures. If all chains are of the same handedness, the structure is polar *I*2*bm* (c); alternation of left- and right-handed chains within each layer results in centric *Pbcm* (d), while alternation between each layer gives centric *Pnma* (e). The *A*-site cations are omitted from the low-symmetry structures for clarity. When brownmillerite structures are placed under epitaxial strain, the oxygen deficient layers can order (f) parallel or (g) perpendicular to the substrate with the pseudocubic orientations shown in (h) and (i), respectively.

only by small atomic displacements, the formation energies for the different polymorphs are nearly degenerate and should form with equal probability. However, each of the aforementioned ordering types is seen experimentally in various members of the brownmillerite family, and the driving force behind the preferred type in different chemistries is not completely understood.

Another degree of freedom appears for the brownmillerite structures when they are grown as a thin film, *e.g.*, via molecular beam epitaxy or pulsed laser deposition, owing to the constraints imposed by epitaxial strain. In this thin film case, the oxygen-deficient layers can order parallel or perpendicular to the substrate (this is shown in Figure 3.5f and 3.5g, respectively, with the pseudocubic orientation shown in Figure 3.5h and 3.5i). Although different strain states will stabilize one orientation over the other, it is not always clear which will be preferred and why. In (La,Sr)Co_2O_5, for example, tensile strain stabilizes perpendicular ordering while compressive strain stabilizes parallel ordering;[138,139] however, the opposite effect is observed in strained $Ca_2Fe_2O_5$.[140]

What factors lead to and stabilize the preferred ground state in different brownmillerite compounds, both in bulk and under strain? In 2005, Abakumov *et al.* put forth the idea that the twisting of tetrahedral chains away from the undistorted 180° orientation creates local dipole moments with larger rotations producing larger dipoles.[141] Hadermann and Abakumov *et al.* further suggested that the distance between the tetrahedral layers (*i.e.*, the length of the b axis) is also an important factor to consider.[142] Parsons *et al.* then recognized that each tetrahedral ordering scheme distorts the octahedra in different ways; the fact that the octahedra are not connected out-of-plane (along b) causes the apical oxygen atoms to displace more than the equatorial ones, which creates a 'shearing' effect from this non-rigid rotation. Generally, the $I2bm$ phase causes the least octahedral (elastic) distortion, followed

by *Pnma*, with *Pbcm* causing the most. They then rationalized these arguments into a "structure map" relating the observed phase of different brownmillerites to these factors, followed by a classification of several known compounds into this scheme.[143]

In this map, they plot tetrahedral layer separation (*i.e.*, *b*-axis length) against distortion of the tetrahedral chains from 180° (*i.e.*, magnitude of tetrahedral rotations). At high rotation angles, they postulate that the *Pbcm* structure is most stable when the layer separation is high, while *Pnma* is stable at low separation. When the rotation angles are small, they suggest that *I*2*bm* is stable at small layer separation, while *Imma* is stable at large.

Although these observations have been key in building an understanding of structural trends in brownmillerite oxides and are corroborated by some recently synthesized brownmillerite phases (such as $Ca_2Cr_2O_5$),[144] discrepancies in this structure map show there are additional effects which should be considered. Ca_2FeCoO_5 and $Ca_2Co_2O_5$, for example, both display the *Pbcm* rather than the structure-map predicted *Pnma* structure.[145,146] In Chapter 7, I will attempt to resolve these discrepancies by introducing two new structural descriptors and showing how they interact to produce the observed ground state in different brownmillerites.

4. PHYSICS OF ACENTRIC PROPERTIES

In this chapter, I discuss ferroelectricity and piezoelectricity, which arise owing to the lack of inversion symmetry in a material's crystal structure. These properties are immensely important to modern technology and find use in a wide variety of electronic devices, including sensors, actuators, tunnel junctions for non-volatile memory, transducers for medical imaging, tunable dielectrics, and solar cells.[2–13] However, despite these effects being known for well over a hundred years (piezoelectricity was discovered in 1880[147] and ferroelectricity in 1920[148]), new discoveries, insights, and applications are still being made.

A ferroelectric is defined as a material that exhibits a spontaneous electric polarization that is switchable by the application of an electric field.[149] Piezoelectricity, on the other hand, is the appearance of an electric polarization under applied stress; any crystal which is ferroelectric is necessarily also piezoelectric.[150] In this chapter, I first discuss the electric polarization, central to both of these properties. Although this may seem trivial, a proper understanding of it eluded scientists until the early 1990s and the development of the so-called "modern theory".[151–155] I then detail the physics underlying ferroelectric phase transitions and describe how compounds can be divided based on different energetic mechanisms (*i.e.*, proper vs. improper).

4.1 Berry Phases and the Modern Theory of Polarization

The electric dipole is one of the most central properties of interest to dielectric materials, especially ferroelectrics. Despite its importance, however, the modern theory put forth by Resta, King-Smith, and Vanderbilt in 1992 and 1993 was the first truly correct microscopic description of this property in bulk solids.[151–155] My overview

here is based upon two excellent resources: the review by Resta and Vanderbilt (Ref. 156) and the "beginner's guide" by Spaldin (Ref. 157). At the fundamental level, the dipole moment ($\vec{p}$) resulting from the separation (given as the vector $\vec{r}$) of two point charges with charges $+q$ and $-q$ is given by:

$$\vec{p} = q\vec{r}; \tag{4.1}$$

for a collection of charges, the total dipole is simply the sum of each of these individual dipoles. Although this notion of polarized units works well for systems such as small molecules, it falls apart in three dimensional solids with a periodic lattice. In attempting to compute such bulk properties in a crystalline solid, the first approach one can take to is to simply normalize Equation 4.1 to the volume of the unit cell (Ω_{cell}). This is known as the Clausius-Mossotti model and relies on the presence of "polarization centers," which can take the form of many different features in a solid (such as charged ions, bonds, etc.). The main problem with this line of thinking, however, is that in reality the charge density of a solid is continuous and cannot be localized in this way.

As an attempt to rectify this, the presence of polarized units can be removed by replacing the summation of dipoles with an integral over the charge density $n(\vec{r})$, and the polarization ($\vec{P}$) of one unit cell can be computed as:

$$\vec{P}_{cell} = (\frac{1}{\Omega_{cell}}) \int \vec{r}\, n(\vec{r})\, e\, d\vec{r}, \tag{4.2}$$

where e is the fundamental charge of an electron, and the total polarization is the sum over all unit cells. This, however, can still not be a complete picture, as in this formulation the polarization now depends on the size and the shape of the unit cell. For example, consider the unit cells of the one dimensional chain of alternating

charges of $+q$ and $-q$ shown in Figure 4.1a. If we compute the polarization in the standard way, we find that $\vec{P} = \frac{q}{2}$. However, if we simply re-define the unit cell by shifting it half a lattice parameter and compute the polarization of the chain shown in Figure 4.1b, the polarization is reversed and becomes $\vec{P} = \frac{-q}{2}$. This result would imply that the electric polarization is not a bulk effect, but rather depends on details of the surface termination, a thought which does not agree with a thermodynamic description of this property.

Eventually, this discrepancy provided the impetus for the aforementioned "modern theory of polarization," which was developed by Resta, King-Smith, and Vanderbilt in the 1990's. The key insight which led to the reconciliation of polarization as a bulk property is that *changes* in the electric polarization that occur during some process (*e.g.*, switching on an electric field) are more fundamental than absolute magnitudes. Although at first glance this may seem unintuitive, an understanding can be gleaned from considering how ferroelectric polarizations are measured experimentally. One of the oldest methods of measuring ferroelectricity is the Sawyer-Tower circuit, in which a capacitor made from the ferroelectric material of interest is placed in a circuit with a capacitor of a known reference.[158] A voltage is then cycled by a signal generator, and the voltage across the reference is measured. These values are fed into an oscilloscope, which generates a hysteresis loop; the ferroelectric polarization is then defined as one half of the difference between the polarization at the top and bottom of the loop.

The polarization difference $\Delta\vec{P}$ thus requires two states to be completely defined. Switching between these two states involves a reorientation of the electric dipole, causing charge to flow through the sample (*i.e.* a transient current); this is the quantity actually being measured in an experimental setup. The macroscopic electric polarization can then be recast in terms of this current $j(t)$ through the sample over some

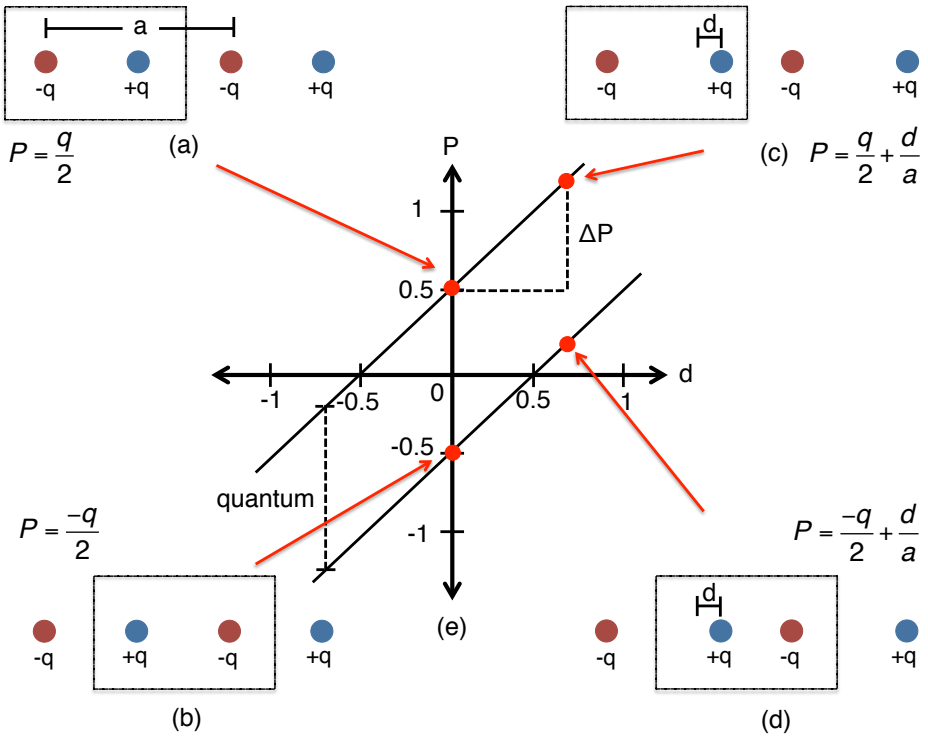

Figure 4.1: (a) In a one dimensional chain of alternating point charges of q and $-q$, computing the "total" polarization results in a value of $\frac{q}{2}$. (b) By shifting the unit cell by half of a lattice parameter, the polarization flips to $\frac{-q}{2}$. If a ferroelectric distortion is applied to the chain (by shifting one point charge by a distance d), we obtain a new polarization of (c) $\frac{q}{2} + \frac{d}{a}$ or (d) $\frac{-q}{2} + \frac{d}{a}$. The polarization of a material, however, should not depend on the definition of the unit cell. (e) The modern theory of polarization put forth the idea that polarization changes (given by ΔP) are more fundamental than magnitudes, and that polarization is actually a multivalued lattice quantity. Computing ΔP for both systems (*i.e.*, a/c and b/d) now results in the same value despite the change in unit cell between them; they fall on different branches of the polarization lattice that are separated by one polarization "quantum".

time t as:

$$\Delta\vec{P} = \int_0^{\Delta t} j(t)dt. \tag{4.3}$$

If we then parameterize this adiabatic change with the parameter λ such that $\lambda = 0$ corresponds to the initial state and $\lambda = 1$ to the final state and take the initial state to be a centrosymmetric reference structure (with $\vec{P} = 0$), we can re-write the spontaneous polarization of a ferroelectric as:

$$\vec{P} = \int_0^1 \frac{d\vec{P}}{d\lambda} d\lambda. \tag{4.4}$$

Now consider the eigenstates ψ_{kn} of a crystal with lattice periodicity with momentum k and quantum number n, which have the form of the Bloch wave function given in Equation 2.15. Assuming that the system remains in its ground state throughout the course of the current flow, we can apply a first-order correction from adiabatic perturbation theory, given by:

$$|\delta\psi_{kn}\rangle = -i\hbar \frac{d\lambda}{dt} \sum \frac{\langle\psi_{km}|\partial_\lambda \psi_{kn}\rangle}{E_{kn} - E_{km}}. \tag{4.5}$$

Summing over all occupied states gives the current as:

$$j(\lambda) = \frac{d\vec{P}}{d\lambda} = \frac{ie}{(2\pi)^3} \int \langle \nabla_k u_{nk} | \partial_\lambda u_{nk} \rangle dk + c^*, \tag{4.6}$$

where c^* is the complex conjugate. After integrating with respect to λ and applying the Born-Oppenhemeier approximation as before to separate the polarization into ionic and electronic parts, we obtain:

$$\Delta\vec{P} = \vec{P}_{ion} + \vec{P}_{elec}(\lambda = 1) - \vec{P}_{elec}(\lambda = 0); \tag{4.7}$$

here the ionic contribution is given by $\vec{P}_{ion} = \frac{e}{\Omega_{cell}} \sum Z^{ion} r$ (where Z^{ion} is the bare nuclear charge of the ion), and the electronic contribution is given by:

$$\vec{P}_{elec}(\lambda) = \frac{e}{(2\pi)^3} \sum \int_{BZ} Im(\langle u_{nk} | \nabla_k | u_{nk} \rangle) dk. \tag{4.8}$$

This equation constitutes a "Berry phase" and is the central result of the modern theory of polarization.

One interesting consequence of casting Equation 4.8 in this way is that the expression is only defined modulo 2π, meaning that the polarization is then defined modulo $\frac{eR}{\Omega_{cell}}$ (where R is the lattice vector). This then implies that polarization is not a vector quantity, but rather a multivalued "lattice." To better understand what this means, reconsider Figure 4.1; if we shift the cations by some distance d (*i.e.*, a ferroelectric displacement) and compute the polarization of the cell in Figure 4.1c, we find that $\vec{P} = \frac{q}{2} + \frac{d}{a}$. Once again, if we shift the unit cell to that shown in Figure 4.1d and compute $\vec{P}$, we find that the polarization is flipped to $\vec{P} = \frac{-q}{2} + \frac{d}{a}$. However, if compute the *change* in polarization between the "non-polar" and "polar" lattice (*i.e.*, Figure 4.1a and 4.1b or 4.1c and 4.1d, respectively) for each choice of lattice, we find that in *both* cases $\Delta\vec{P} = \frac{d}{a}$. We have now removed the unit cell dependence from calculations of the polarization, showing that differences are more fundamental quantities than magnitudes.

Finally, the plot of polarization versus displacement in Figure 4.1e shows how each of these unit cells are related to one another. If a ferroelectric distortion that displaces the atoms by a distance d is induced (going from 4.1a to 4.1c or from 4.1b to 4.1d), there is a corresponding increase in the polarization. Furthermore, if we re-define the unit cell (going from 4.1a to 4.1b or from 4.1c to 4.1d), we move to a different polarization branch; this is what is meant by the fact that the polarization is a "multivalued lattice". Regardless of which branch we are on, the difference between

any two branches (the polarization quantum) does not change. Computationally, this means that after the polarization is computed, the polarization of a higher-symmetry reference phase must also be computed, with the difference being taken as the "true" value; the polarization of a series of a intermediate structures should also be computed to ensure that both the high symmetry and low symmetry phase are on the same branch.

4.2 Ferroelectric Phase Transitions

In most ferroelectrics, there is a phase transition from a high symmetry non-polar paraelectric phase to the ferroelectric phase below some critical temperature T_c.[149] A standard way to categorize ferroelectrics is into either (i) displacive or (ii) order-disorder based upon the details of the high symmetry phase. In *displacive* ferroelectrics, cooperative off-centering of ions from their positions in the high symmetry phase (typically driven by bond formation) breaks inversion symmetry and produces a spontaneous polarization.[159] The prototypical example of this is the perovskite $BaTiO_3$; across the phase transition, the Ti^{4+} cations displace from the center of the oxygen octahedral cage owing to a hybridization between Ti $3d$ and O $2p$ states.[160,161] On the other hand, the symmetry breaking distortions are always present in each unit cell of an *order-disorder* ferroelectric, but are randomly oriented above T_c; it is their cooperative alignment below T_c which then produces the spontaneous polarization.[162] $NaNO_2$ and KH_2PO_4 are two common examples of this, with NO_2 units and hydrogen atoms, respectively, cooperatively selecting a site preference below T_c.[163,164] However, there are very few materials that are purely displacive or purely order-disorder, and most ferroelectrics (including those listed above) have been show to display both types of behavior.[161,165–167]

Ferroelectrics can also be classified by the microscopic mechanism responsible

for the inversion symmetry breaking across the phase transition. For example, a mismatch in the size of the ions can induce lattice distortions across T_c; recall from Chapter 3 that this is what causes octahedral rotations in perovskites (as described by the tolerance factor). These are the so-called "geometric" ferroelectrics, and examples include $BaMnF_4$ and $YMnO_3$.[168,169] There are also "magnetic" ferroelectrics, where inversion symmetry is broken by magnetic ordering, such as that which occurs in rare earth manganites ($GdMnO_3$, $DyMnO_3$, and $TbMnO_3$)[170,171] and $Ni_3V_2O_8$.[172,173] Finally, there is the family of "electronic" ferroelectrics, where a spontaneous polarization is induced by complex ordering of charge (found in $BaBiO_3$)[174] or orbitals (predicted in $SrCrO_3$).[175]

4.3 Ferroelectricity in Perovskites and the Soft Mode

Because perovskites are the focus of this dissertation and one of the most overall studied families of ferroelectric oxides, the physics and chemistry underlying ferroelectricity are presented from the point of view of these materials. The first ferroelectric perovskite was discovered in 1946, when polarization switching was demonstrated in $BaTiO_3$.[176] Up until this point, ferroelectricity had only been found in materials with a hydrogen-bonded network, and the presence of hydrogen was thought to be a necessary condition for a spontaneous polarization. Later work eventually showed that $BaTiO_3$ underwent a series of phase transitions from cubic non-polar $Pm\bar{3}m$ to ferroelectric tetragonal $P4mm$ (393 K, P=33 μC/cm^2), orthorhombic $Amm2$ (278 K, P=36 μC/cm^2), and rhombohedral $R3m$ (183 K, P=27 μC/cm^2). As described previously, the spontaneous polarization is produced by an off-centering of the Ti^{4+} cation from the center of the TiO_6 octahedral cage. Across each phase transition, however, these displacements (and thus the polarization) shift from occurring along the [001] direction to the [110] direction, and finally to the [111] direction as a func-

tion of decreasing temperature. Although there are perovskites whose ferroelectric behavior is much simpler, I use $BaTiO_3$ as an illustrative example because it was the first discovered and most highly studied during the era in which the phenomenological theory was being laid out.

4.4 Landau-Devonshire Theory of Ferroelectricity

Typically in displacive (and order/disorder) phase transitions the space group symmetries of the two phases show a group/subgroup relationship, where the low symmetry phase G approaches the high symmetry G_0 phase continuously. The key concept of Landau theory is to construct an expression for the free energy $\mathcal{F}$ of the system that captures the details of the phase transition near T_c. To describe these phase transitions quantitatively, one can introduce an "order parameter" η as a quantity that captures the reduction in symmetry accompanying the phase transition and usually has a clear microscopic meaning, *e.g.*, collective ionic motion or site-distribution changes. It may also be single or multi-component (this will be covered in more detail in subsequent sections). Ferroelectricity is associated with a crystallographic phase transformation from a centrosymmetric non-polar lattice to a non-centrosymmetric polar lattice, and this change at the critical temperature T_c is always accompanied by a change of crystal symmetry manifesting in a non-zero value of η. This change can be captured as $\mathcal{F}(\eta) = \mathcal{F}_0 + \Delta\mathcal{F}(\eta^i)$, where $\Delta\mathcal{F}$ (being small near the phase transition) can be expanded as a Taylor series in terms of the order parameter η.

In 1949, Devonshire applied Landau's theory of phase transitions to $BaTiO_3$, showing that it accurately predicts the aforementioned phase transitions.[177] In ferroelectrics such as $BaTiO_3$, the primary order parameter in the free energy expansion has the same symmetry elements as the pattern of atomic displacements giving rise to the polarization; that is, the appearance of a spontaneous electric dipole is driving

the phase transition. The simplest second-order phase transition model capturing this transition is:

$$\mathcal{F}(\eta) = \frac{\alpha(T)}{2}\eta^2 + \frac{\beta}{4}\eta^4 + \frac{\gamma}{6}\eta^6 - EP + \dots . \tag{4.9}$$

The form of this equation is such that below some critical temperature T_c at which the polarization condenses, $\alpha(T)$ (which has the form $a(T) = a_0 \times (T - T_c)$) changes sign, resulting in a minimum in the free energy at finite η (Figure 4.2a); there is also a minimum at $-\eta$ corresponding to the opposite sense of the displacements, resulting in the characteristic ferroelectric switching phenomenon. By taking the derivative of this expression with respect to the polarization ($\partial\mathcal{F}/\partial P = 0$), we obtain the electric field in terms of the polarization: $E = a\eta + b\eta^3 + c\eta^5$. We can now solve for the dielectric susceptibility:

$$\chi = \frac{P}{E} = \frac{1}{a} = \frac{1}{a_0(T - T_c)} \tag{4.10}$$

From this, it is easy to see that across the ferroelectric phase transition at T_c, there is a divergence of the dielectric susceptibility; this is analogous to the divergence of the magnetic susceptibility across a ferromagnetic transition as predicted from the Curie-Weiss law.

The divergence can then be connected to the "softening" (*i.e.*, a decrease in the frequency) of a transverse optical phonon through the Lyddane-Sachs-Teller relation.[178] In 1960, Cochran applied this soft mode theory to ferroelectrics and showed that the frequency of the soft phonon becomes zero at T_c and the associated polar displacements obtain a finite amplitude (*i.e.*, "freeze in").[179] We now see that the freezing in of the off-center Ti displacements, which produce the polarization in $BaTiO_3$, are what is driving the ferroelectric phase transition. This is further equivalent to saying that the polarization is the primary order parameter, as was stated previously; materi-

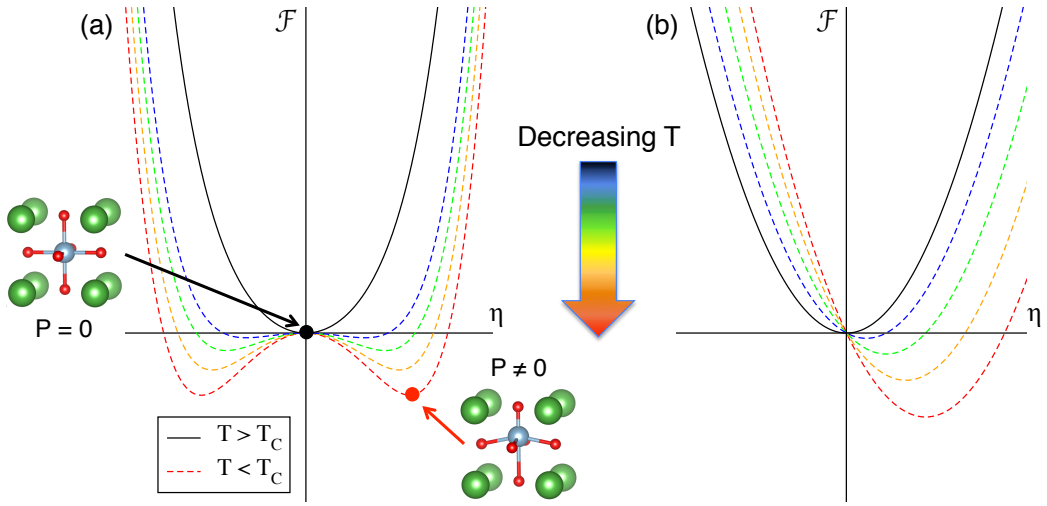

Figure 4.2: The energetics of a paraelectric to ferroelectric phase transition for a (a) proper and (b) improper ferroelectric system.

als which display this type of behavior are known as **proper** ferroelectrics. There are many other perovskites that are proper ferroelectrics, such as $KNbO_3$, which undergoes the same series phase transitions as $BaTiO_3$ (Nb^{5+} displacements).[180] $PbTiO_3$, on the other hand, only transitions to the $P4mm$ tetragonal phase (occurring at 760 K).[181] However, there are Pb^{2+} displacements as well as Ti^{4+} off-centering, giving this material a much larger polarization P=75 μC/cm^2). Similarly, the polarization in $BiFeO_3$ is mainly produced by Bi^{3+} displacements rather than Fe. The chemical mechanisms behind this will be discussed in the next section.

Finally, there are some perovskites which display soft mode behavior, but where the frequency of the polar phonon never reaches zero. Instead, quantum fluctuations stabilize the phonon at low temperatures, and they remain centrosymmetric. Such materials (with $SrTiO_3$ and $KTaO_3$ being the prototypical examples) are called "incipient ferroelectrics" or "quantum paraelectrics" and are often said to be on the cusp of a ferroelectric phase transition. Indeed, recent experiments have shown that $SrTiO_3$, $KTaO_3$, and $CaMnO_3$ can be "nudged" into the ferroelectric state by the

application of epitaxial strain;[182–184] although this same effect has been predicted in $CaTiO_3$, it has not yet been experimentally verified.[185] Furthermore, chemical doping of Pb and introduction of oxygen vacancy defects have also been shown to be able to induce ferroelectricity in $SrTiO_3$, $CaTiO_3$, and $KTaO_3$.[186,187]

4.5 Chemical Mechanisms

While Landau theory and soft mode behavior provide powerful insights into ferroelectric phase transitions, they are, at their heart, phenomenological theories; that is, they are unconcerned with and make no mention of the atomic makeup of a material or chemical mechanisms such as bonding. However, because very few perovskites display ferroelectricity,[188] there clearly must be some chemical criteria for its presence. At it simplest, the appearance of ferroelectricity is a competition between short-range and long-range interactions.[189] Non-polar structures minimize short-range repulsions between electron clouds of adjacent ions and therefore are preferred in most cases. Polar structures are stabilized by long-range Coulomb forces between positive and negative ions (*i.e.*, by dipole-dipole interactions). The ferroelectric distortions (such as Ti^{4+} or Pb^{2+} off-centering) are then stabilized by changes in chemical bonding driven by the second-order (or pseudo-) Jahn-Teller effect.[190–192]

This effect is almost exclusively limited to metals with a d^0 electronic configuration, such as the Ti^{4+} cations in the complex perovskite oxide $BaTiO_3$, or to those with a stereoactive lone-pair, such as Pb^{2+} in $PbTiO_3$.[1,190,193] I note, however, that recent investigations have shown that it *is* in fact possible for atoms with non-zero d^n configurations to undergo proper ferroelectric displacements.[191] The meaning of this becomes clear if we expand the energy of the ground state system as a function

of the Jahn-Teller distortion, quantified by $\mathcal{Q}$:

$$E(\mathcal{Q}) = E_0 + \langle 0|\frac{\partial H}{\partial \mathcal{Q}}|0\rangle \mathcal{Q} + \frac{1}{2}[\langle 0|\frac{\partial^2 H}{\partial \mathcal{Q}^2}|0\rangle - 2\sum_n \frac{|\langle 0|\frac{\partial H}{\partial \mathcal{Q}}|n\rangle|^2}{E_n - E_0}]\mathcal{Q}^2. \tag{4.11}$$

Here, E_0 is the energy of the ground state, while $\langle 0|\frac{\partial H}{\partial \mathcal{Q}}|0\rangle$ is the energy gain or penalty of a first-order Jahn-Teller effect; as expected, this term is only non-zero for degenerate states.

The second-order Jahn-Teller (SOJT) effect is captured by the rest of the expression, and the relative magnitude of term $[i] = (\langle 0|\frac{\partial^2 H}{\partial \mathcal{Q}^2}|0\rangle)$ and term $[ii] = (\frac{|\langle 0|\frac{\partial H}{\partial \mathcal{Q}}|n\rangle|^2}{E_n - E_0})$. By understanding what these terms represent physically, we can gain an understanding of the stabilizing mechanisms behind ferroelectricity. Term $[i]$, which is always positive, describes the energetic penalty for a distortion; or, said another way, this term represents the short-range Coulomb repulsions favoring a centrosymmetric state. On the other hand, term $[ii]$ is always negative and represents the mixing of ground and excited states (*i.e.*, the formation of new bonds). In order to lower the total energy of the system, the magnitude of term $[ii]$ must be larger than term $[i]$, which can be achieved by having low lying excited states and minimizing the denominator $E_n - E_0$. If $[ii] > [i]$, the formation of new bonds is favorable enough to overcome the electrostatic repulsions, and the system distorts.

The reason that the d^0 and ns^2 cations undergo these displacements is because term $[i]$ is smallest for closed shell atoms; without any spatially extended valence electrons, the repulsion represented by this term is minimized. Chemically, these two types of SOJT-active systems are stabilized by slightly different mechanisms. In $BaTiO_3$, for example, the off-centering of Ti^{4+}, a d^0 cation, is stabilized by a hybridization of the empty d states with the $2p$ states of the surrounding oxygen anions. While the off-centering of lone-pair driven ferroelectrics is also driven by a re-hybridization, it is now the p states of the cation interacting with the oxygen $2p$

states, such as the Pb^{2+} $5p$ states in $PbTiO_3$.

4.6 Improper Ferroelectrics

In contrast to proper ferroelectrics, improper ferroelectrics exhibit a transition with an order parameter Q that describes some non-polar (in the sense that it does not alone produce a spontaneous electric polarization) atomic distortion pattern; it thus has a physical meaning other than that of a polar IR-active phonon. The generic Landau functional which describes such transitions takes the form

$$\mathcal{F}(Q,\eta) = \frac{\alpha(T)}{2}Q^2 + \frac{\beta}{4}Q^4 + \frac{\alpha'}{2}\eta^2 + \frac{\beta'}{4}\eta^4 + \xi\eta^m \cdot Q^n + \dots , \tag{4.12}$$

where a macroscopic polarization is induced by the coupling term $\xi\eta^m \cdot Q^n$ when the temperature-dependent α coefficient changes sign. Because the low-order powers of the coupled order parameters are commonly the most important, the coupling term can be truncated[194] to $m = 1$ and $1 \leq n \leq 4$, as well as any biquadratic terms. Consideration of the order of coupling between Q and η then leads to a natural division among displacement patterns active in an improper ferroelectric.

What is Q? Symmetry arguments indicate that Q could be represented as the amplitude of a *zone-boundary* phonon; the Q mode will then occur at or within the Brillouin zone boundary ($k \neq 0$) of the centrosymmetric unit cell and thus is always a multicomponent order parameter (or may represent a combination of different modes). However, routine discovery, let alone design, of improper ferroelectrics which have a suitable coupling between zone-boundary lattice instabilities (that modify the translational symmetry) and polar phonons (which reduce point symmetry) is challenging. Unlike their conventional (proper) counterparts which have well understood stabilization mechanisms for the polar phonon – $dp\sigma$-bond formation and/or stereo-chemical

lone-pair activity – tailoring anharmonic interactions to have a soft Q-related phonon coupled to η need not have an obvious chemical prescription. Despite this complexity, however, there exists a larger class of non-polar modes capable of producing a polarization through anharmonic interactions, which I will review shortly. Determining how to induce this coupling between one or two zone-boundary modes and a set of polar displacements by selecting suitable cations is key to designing new magnetic ferroelectrics.

However, I should make note that there are some forms of order parameter coupling that, while possible, are not examined and fall outside the scope of this thesis. First, the presence of a bilinear coupling of the form ηQ ($m = n = 1$) implies that the ferroelectric transition could occur without a change in the size of the unit cell, in contrast to the zone-boundary origin of Q proposed previously. While this has been observed in magnetic or order-disorder driven ferroelectrics (such as the spiral phase of $TbMnO_3$[170,195] or $Ca_9Fe(PO_4)_7$[196]), I do not consider these 'pseudo-proper' ferroelectrics here. Furthermore, if the lowest order coupling is a (negative) biquadratic $\eta^2 Q^2$ term, the ferroelectric transition is known as "triggered";[197] here, η is not induced solely by Q, but rather Q can be activated, and hence "triggered," by some other instability (for examples and a more detailed treatment of triggered phase transitions, see Refs. 198–200).

The energetics of a paralectric to improper ferroelectric transition are shown in Figure 4.2b. Here, the energy minima shifts to $\eta \neq 0$, losing the double well potential characteristic of a proper transition. This is because the spontaneous polarization is often dynamically stable with respect to the centrosymmetric structure and will only arise as a result of some other distortion. This then means that in order to switch the minima to $-\eta$, the entire sense of the non-polar distortion Q must be reversed. Finally, the presence of a coupling term in the free energy is not sufficient to declare a

material an improper ferroelectric; the energy gain from having both of the distortions present must be greater than either individually.

4.7 Hybrid Improper Ferroelectrics

Recent reports have identified a new type of rotationally-driven mechanism capable of producing polarizations, known as hybrid improper ferroelectricity.[201] In such materials, Equation 4.12 is extended to include multiple, equally important primary Q order parameters. Polarizations arise in these materials from a symmetry allowed trilinear coupling term in the free energy, given by, for example, $\mathcal{F} = \gamma Q_1 Q_2 \eta$, where Q_1 and Q_2 are octahedral rotation modes of different symmetry. Microscopically, the non-polar lattice modes serve to remove inversion centers present in the paraelectric structure, and are often rotations or other structural displacements which distort the polyhedral networks in the crystal structure.

An important note related to the nature of the transition is that it also depends on the critical temperature at which the two non-polar modes responsible for the appearance of P occur. The two modes can condense at the same temperature (an "avalanche" transition[202]), or they can condense at different temperatures (a "staggered" transition[203]). While an avalanche transition would be a true hybrid improper ferroelectric phase transition, a staggered transition may not necessarily be one. When the first mode condenses, a change of the symmetry or size of the unit cell could mix the remaining mode together with the polar mode at the zone-center of the new phase; the onset of this new mode would actually be a *proper* ferroelectric transition following the previously discussed definition. However, because this is somewhat different than the proper ferroelectric transition in $BaTiO_3$, such materials have previously been termed "weakly polar."[204,205] Although in this chapter I have made no distinction between a hybrid improper or weakly polar phase transition when

discussing ferroelectricity arising from a trilinear coupling of modes, the existence of this phenomenon is important to understand during the experimental investigations of these materials as it imposes constraints on the temperature-dependent dielectric response.

5. PREDICTIVE MODELS FOR INVERSION SYMMETRY LIFTING

In this chapter, I put forth two new predictive models for (1) understanding and classifying geometric improper ferroelectrics in terms of structural distortions and (2) designing new non-centrosymmetric perovskites by identifying exactly which combinations of octahedral rotations and cation ordering schemes lift inversion symmetry, and the chemistries that are likely to result in those features. The first model describes a new classification scheme which divides these materials based on how different cooperative anion displacement patterns (divided into "rotational" and "pseudo-rotational" modes) combine to cooperatively lift inversion symmetry. I then provide an overview of the geometric improper ferroelectric literature to show how known compounds fit into this scheme.

In the second model, I detail how the arrangement and control of basic building units (BBUs) and chemical (cation) ordering in a material alters the presence or absence of inversion symmetry. Through consideration of the ordering of centric and acentric BBUs in one- and two-dimensional toy systems, I first review the structural "features" necessary to break spatial parity; I then extend this model into three dimensions and describe how the simultaneous presence of octahedral rotations and cation ordering in perovskite oxides fulfills these criteria. I next apply these guidelines to create the first complete and comprehensive overview of what combinations of these structural distortions and A- and B-site ordering schemes can lift inversion symmetry. Finally, I detail which chemical species have the greatest tendency towards a given rotation pattern through calculation of the global instability index (a quantitative measure of stability based on bond valence arguments) of 137 ABO_3 perovskites. These new models will form the basis upon which the investigations described in the following chapters are based and provide a robust route for the discovery of novel

non-centrosymmetric oxide materials.

5.1 Towards a New Taxonomy for Improper Ferroelectrics

As described in the previous chapter, a structural distortion that is not a polar mode drives the phase transition in improper ferroelectrics. In this section, I review geometric improper ferroelectrics and propose a new classification scheme for their division; as discussed in Chapter 4, these materials' ferroelectric phase transition is driven by atomic size effects rather than electronic degrees of freedom such as spin, charge, or orbital ordering.

I divide the compounds into two variants based on the number and symmetry of modes active in the transition and appearing in the free energy expansion that lead to inversion symmetry lifting. Type I improper ferroelectrics have one primary mode coupled to a polar IR-mode, whereas Type II distinguishes improper ferroelectrics with two active Q modes linked to a polar mode. A literal 'A' or a 'B' is then appended to specify whether the microscopic mode(s) involved in describing the symmetry change are rotational or pseudo-rotational, respectively. This classification method results in five categories of improper ferroelectrics that are summarized in Figure 5.1. In the next sections, I show how previously identified improper ferroelectrics can be classified in this way. I have not intended to be completely exhaustive, but rather choose illustrative examples of how one can apply the classification scheme to understand the atomistic displacements responsible for lifting inversion symmetry.

5.1.1 Type A

Type A compounds contain a single proper rotational mode which couples to a polar mode and stabilizes the ferroelectric state. I first consider the family of boracites, which have the general formula $M_3B_7O_{13}X$; here M is a divalent metal

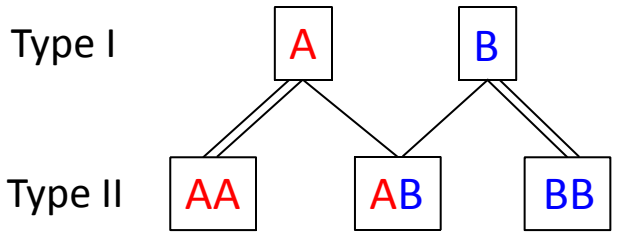

Type	Mode 1	Mode 2
A	Rotation	-
B	Pseudo-rotation	-
AA	Rotation	Rotation
AB	Rotation	Pseudo-rotation
BB	Pseudo-rotation	Pseudo-rotation

Figure 5.1: Geometric improper ferroelectrics can be divided into Type I or II based on whether the polarization is coupled to one or two zone-boundary modes, respectively. Additionally, these modes can be classified as proper (A) or pseudo-rotational (B) modes. The combination of each of these designations results in five distinct classes of geometric improper ferroelectrics.

and X is a halogen. The structure consists of a corner-connected network of BO_4 tetrahedra and BO_3 sheets with highly distorted MO_4X_2 octahedra forming a second network along the [110] direction. This is one of the oldest and most expansive family of ferroelectrics with the mineral boracite ($Mg_3B_7O_{13}Cl$) first discovered in the late 1700s and piezoelectricity found in the late 1800s.[147] Indeed, its low temperature crystal structure was determined to be polar $Pca2_1$ in the 1950s.[206] Eventually, the compound $Ni_3B_7O_{13}Cl$ was shown to be ferroelectric[207] and shortly after $Ni_3B_7O_{13}I$ (which exhibits weak ferromagnetic ordering on the Ni sublattice) became the first identified magnetic ferroelectric.[208,209] Since then, the members of this family have expanded to encompass a range of chemistries, including M=Mg, Cd, Cr, Mn, Fe, Co, Ni, Cu, and Zn and X=F, Cl, Br, I or even OH or NO_3 (see Refs. 210–212 and references therein).

These compounds all display a paraelectric (nonpolar achiral) $F\bar{4}3m$ cubic phase at high temperature and undergo a phase transition to orthorhombic polar $Pca2_1$; certain members also undergo further phase transformations to monoclinic Pb and rhombohedral $R3c$.[213] The microstructure of these materials is often complex with many phases displaying twinning and ferroelectric domains.[214,215] Nonetheless, the primary order parameter driving the transition is clear; at the atomic scale it consists

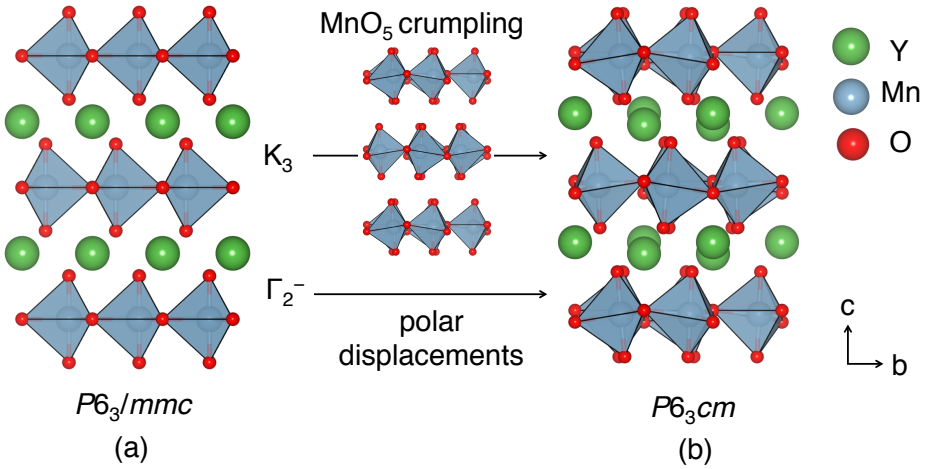

Figure 5.2: The structure of $YMnO_3$ consists of disconnected planes of MnO_5 polyhedra alternating with layers of Y atoms. The ferroelectric transition from (a) $P6_3/mmc$ (b) to $P6_3cm$ occurs via a zone-boundary K_3 mode describing the crumpling of MnF_5 planes and nonpolar Y displacements coupling to a polar Γ_2^- mode.

of a rotation of the B-O framework, which is described as a zone-boundary mode given by the irreducible representation X_5.[216,217] This is coupled to an IR-active Γ_4 mode, which produces a spontaneous polarization via displacements of the M atoms along the [001] direction—the magnitude of which can range from 2×10^{-3} to 5 μC/cm^2.[218] Finally, the boracites display several other interesting properties, including strong magnetoelectric coupling (due to the ferroelectricity and magnetism arising from the same atoms) and ferroelastic effects.[219]

The hexagonal manganites form another well-known family of improper ferroelectrics. The prototypical member, $YMnO_3$, consists of layers of corner-connected MnO_5 bipyramids and exhibits antiferromagnetic ordering of the Mn atoms below 75 K.[220,221] Upon transition from centrosymmetric $P6_3/mmc$ (Figure 5.2a) to polar $P6_3cm$ (Figure 5.2b) at 1260 K, a spontaneous polarization appears owing to a unit cell-doubling tilting of MnO_5 polyhedra (given by irrep K_3) and a "crumpling" of YO planes (irrep Γ_2^-).[169,222] This ferroelectric phase transition has been

extensively studied experimentally, and its exact nature is quite complex and debated.[223–227] First principles calculations and experimental results have shown that while the K_3 mode is soft and the Γ_2^- mode is hard in the phonon band structure of centric $P6_3/mmc$ $YMnO_3$, a coupling of the two modes in the free energy expansion of the form $\mathcal{F} = ... + \alpha_1 Q_{K_3}^3 Q_{\Gamma_2^-} + \beta Q_{K_3}^2 Q_{\Gamma_2^-}^2$ results in a shift of the Γ_2^- mode to a non-zero equilibrium value upon condensation of K_3.[228,229] Based on the scheme presented here, $YMnO_3$ is then classified as a Type A compound.

Although $YMnO_3$ is the prototype of the $R$$MnO_3$ hexagonal manganites, many of the other members display Type A improper ferroelectricity resulting from the same set of atomic distortions, including R = Ho, Er, Tm, Yb, and Lu,[230,231] albeit with different magnitude. The isostructural hexagonal ferrites ($R$$FeO_3$) would also be classified as Type A improper ferroelectrics within this scheme. Several members of this family have been synthesized experimentally, such as R=Eu, Er, Tm, Yb, and Lu.[232] Additionally, recent first principles studies on the hexagonal ferrates have shown that it is theoretically possible to increase the polarization by up to 60% through both chemical pressure (by substituting larger rare earth atoms such as Ce, Pr, and Nd) and epitaxial strain.[233,234]

There are several isomorphic halides that may be classified as Type A owing to the same displacement modes found in the hexagonal transition metal oxides, including $TlFeBr_3$, $RbMnBr_3$, $TlCoCl_3$, and $KNiCl_3$.[235,236] Finally, hexagonal $BaMnO_3$ also undergoes the same $P6_3/mmc$ to $P6_3cm$ transition, despite having a different crystal structure (face sharing rather than corner-sharing polyhedra);[237] indeed, first principles calculations have shown that the same K_3 and Γ_2^- modes are responsible for this transition.[238] This microscopic understanding of the hexagonal manganite structure has led to the design of novel ferroelectric materials, both theoretically ($R$$GaO_3$ and $R$$InO_3$)[239] and experimentally ($YbFeO_3$).[240]

I next turn to the rare earth molybdates with chemical formula $R_2(MoO_4)_3$ (where R=Tb, Gd, or Sm),[241–243] which also exhibit ferroelectricity of this nature.[244] In the paraelectric phase, these oxides exhibit the nonpolar non-centrosymmetric $P\bar{4}2_1m$ space group and consist of R atoms surrounded by completely disconnected MoO_4 tetrahedra (Figure 5.3a). Upon condensation of an unstable phonon mode at the M-point (described as M_2M_4 with respect to the centric $P\bar{4}2_1m$ structure), which manifests as cooperative rotations of the MoO_4 units, the structures reduce to orthorhombic $Pba2$ (Figure 5.3b) with a corresponding appearance of a spontaneous polarization along the c axis (described by the polar mode Γ_3).[236] The polarization arises via displacements of the Gd cations and MoO_4 tetrahedral lattice; the fact that the anti-parallel motions of the Gd atoms mostly cancel, however, means the polarization is only ~ 0.2 μC/cm^2.[245] This symmetry analysis has shown that these compounds can also be considered Type A improper ferroelectrics despite having a completely different crystal structure than the boracites or hexagonal manganates.

A fourth well-known family that can be classified as Type A improper ferroelectrics are those with the chemical formula A_2BX_4. The prototypical member of this family is K_2SeO_4. Like $Gd_2(MoO_4)_3$, the crystal structure consists of disconnected SeO_4 tetrahedra; however, the ratio of A-site atoms to tetrahedra per unit cell is greater than in the molybdates. These compounds are also unique in that the members undergo a phase transition from paraelectric $Pnma$ (Figure 5.3c) to ferroelectric $Pna2_1$ (Figure 5.3d) via an intermediate incommensurate phase[246–248] driven by a nonpolar zone-boundary mode Σ_2 (describing out-of-phase rotations of BO_4 tetrahedra),[249] which is coupled to polar displacements described by Γ_4^-.[250,251] The A_2BX_4 family of improper ferroelectrics includes compounds with vastly different chemistries, including oxides (K_2SeO_4), halides (Rb_2ZnCl_4, Rb_2ZnBr_4, K_2ZnCl_4), and molecular solids ($[N(CH_4)_3]_2ZnCl_4$, $(NH_4)_2BeF_4$).[252–256]

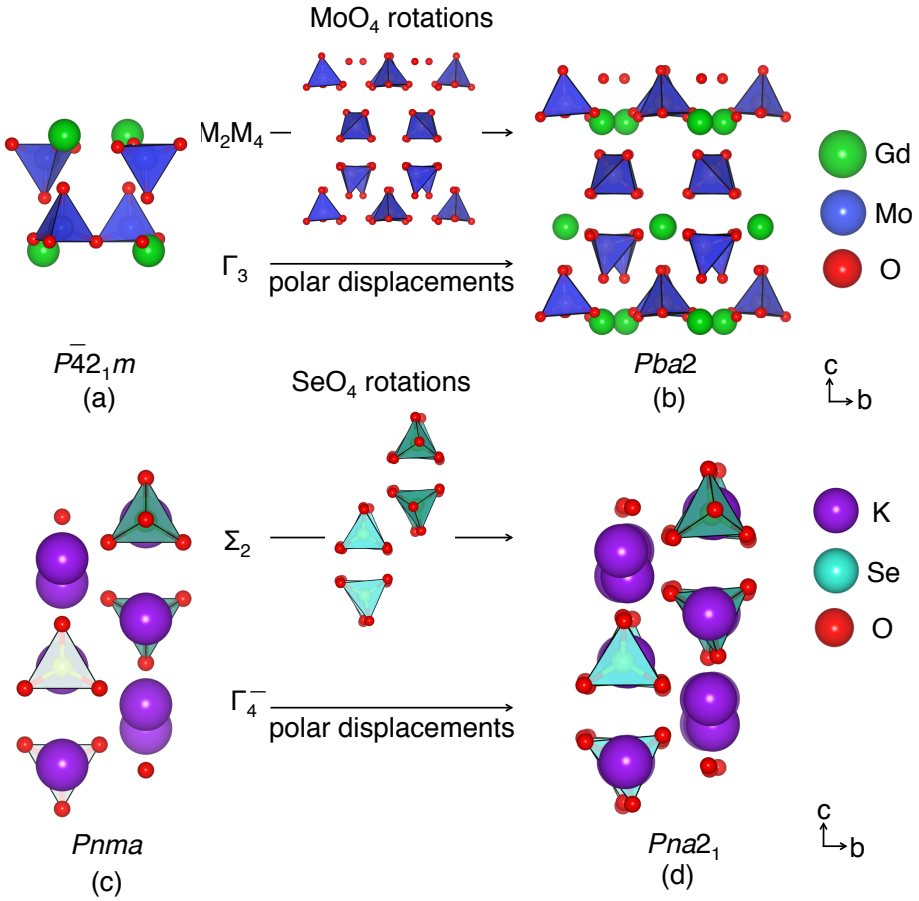

Figure 5.3: The $R_2(MoO_4)_3$ structure consists of disconnected MoO_4 tetrahedra interspersed with R atoms (R = Tb, Gd, Sm). The (a) high symmetry $P\bar{4}2_1m$ structure undergoes a transition to the (b) ferroelectric $Pba2$ phase upon condensation of M_2M_4 and Γ_3 modes via a Type A improper mechanism. The prototypical A_2BX_4 structure is similar, but consists of chains of A-sites and disconnected BX_4 tetrahedra. These compounds undergo a phase transition from (c) high symmetry $Pnma$ to (d) ferroelectric $Pna2_1$ via a Σ_2 mode coupling to a polar Γ_4^- mode, resulting in a spontaneous polarization along c.

Most of the compounds discussed so far undergo a ferroelectric transition into a polar structure from a paraelectric phase containing inversion symmetry. However, this is not a required condition for the appearance of an improper polarization; the paraelectric structure may also be nonpolar non-centrosymmetric. For example, the stuffed tridymite $BaAl_2O_4$ displays a high symmetry $P6_322$ paraelectric phase,[257–259] *i.e.* a space group that is both nonpolar and lacking inversion symmetry.[1] This material consists of corner-connected AlO_4 tetrahedra—the SiO_2 tridymite structure—with Ba cations located in the space between tetrahedra. At 396 K, a soft phonon mode describing tilting of the AlO_4 tetrahedra condenses at the M-point (irrep M_2), driving it to the $P6_3$ ferroelectric phase.[260] The spontaneous polarization in this structure occurs due to coupling of the M_2 mode to a polar Γ_2 mode, producing a small net polarization of 0.08 $\mu C/cm^2$ from an anharmonic interaction.[258,261,262]

A similar series of transitions occurs in the mineral family of sulfate langbeinites, which have the general formula $A_2B_2(SO_4)_3$ and consist of a network of disconnected SO_4 tetrahedra. Most of the compounds, including the specific mineral langbeinite [$K_2Mn_2(SO_4)_3$], undergo a phase transition from a high temperature $P2_13$ phase to a low temperature $P2_12_12_1$ phase, both of which are nonpolar space groups.[263,264] However, several members transition to the intermediate monoclinic $P2_1$, then triclinic P_1 structures, before the $P2_12_12_1$ ground state, including compounds such as $Tl_2Cd_2(SO_4)_3$,[265] $Rb_2Cd_2(SO_4)_3$,[266] and $(NH_4)_2Cd_2(SO_4)_3$.[267,268] Note that both intermediate phases are also ferroelectric. As with the stuffed tridymites, rotations of the SO_4 tetrahedra described by M-point phonons induce the ferroelectric phase transition.

Finally, the compound $RbH_3(SeO_3)_2$ undergoes a similar $P2_12_12_1$ to $P2_1$ ferroelectric transition.[269] The structure consists of SeO_3 units connected through O-H-O bridges. At 158 K, a phonon mode describing twisting of these units condenses at

the Z-point, driving the ferroelectric phase transition.[270] Like the previous two families, the spontaneous polarization is also small in this material, with a magnitude of only $13\,\mathrm{nC/cm^2}$.[271] Interestingly, the Rb member of this family is the only improper ferroelectric; the Li member is a proper ferroelectric, while the Na member is always centrosymmetric.

5.1.2 Type B

The Type B compounds are similar in nature to Type A in that one unstable mode drives the symmetry lowering transition; rather than being a rotational mode, however, it is *pseudo*-rotational. Our search reveals that it is difficult to locate materials which contain only one pseudo-rotational mode coupled to a polar mode that induces an electric polarization. This likely occurs for a variety of reasons. While a first-order Jahn Teller (FOJT) effect is in principle "simple" to achieve through selection of the appropriate transition metal chemistry, this type of distortion alone is insufficient to lift inversion symmetry in a three-dimensional crystal with corner-connected octahedra.[272,273] Additionally, while Berry pseudo-rotations are relatively common in organic compounds[274] and molecules such as PF_5[275] or pentacoordinate silicates,[276] they are extremely rare, if they occur at all, in crystalline solids with polyhedral networks.

Although our search of the literature revealed no Type B ferroelectrics, I offer some suggestions as how to locate or purposefully engineer polar phases of this nature. First, control over the topology of a material could be utilized in combination with the FOJT effect to produce a polar structure. For example, if polyhedra exhibiting FOJT distortions were ordered in such a way that their relative positions cooperatively lift inversion, ferroelectricity could be induced despite the site symmetry of the metal center within the polyhedra itself maintaining inversion symmetry. Second, crystalline

solids containing organic networks (such as metal-organic frameworks discussed in Section 5.1.4) could be a promising avenue for Type B ferroelectrics induced by Berry pseudo-rotations. Finally, compounds which contain molecular rotations are also viable candidate materials. The compound lawsonite ($CaAl_2Si_2O_7(OH)_2{\cdot}H_2O$), for example, displays 'crumpling' of the H_2O and OH molecules (described by Y_2^- mode and driven by steric instabilities) in addition to ferroelectricity;[277] the polarization, however, is actually induced via an order-disorder mechanism. Despite the rarity of these distortions in crystalline solids, their discovery and investigation could open a whole new area of geometric improper ferroelectrics.

5.1.3 Type AA

In Type AA improper ferroelectrics, the polarization arises as a result of two rotational modes. This mechanism was first predicted by density functional theory calculations in the Aurivillius compound $SrBi_2Nb_2O_9$, where it was found that the ferroelectric $A2_1am$ ground state is a result of a coupling between three displacive modes: an octahedral tilting mode, a mode consisting of oxygen movements in the Bi_2O_2 layers, and a polar mode.[278] This result was followed by the discovery of ferroelectricity in 1:1 layered artificial superlattices of the perovskite oxides $PbTiO_3/SrTiO_3$, in which an in-phase and an out-of-phase rotational mode couple to a polar mode to produce an additional contribution to the total spontaneous polarization.[279] Further first principles investigations revealed that, similarly, two rotational modes can also lead to a ferroelectric polarization in Ruddlesden-Popper phases via coupling to a polar mode;[201] because of this, the phenomenon was first dubbed "hybrid improper." Since then, this type of ferroelectricity has been predicted and found in a wide variety of material families, most predominately *layered* oxides.[30] I first examine the aforementioned ferroelectric $SrBi_2Nb_2O_9$ to show that while a trilinear

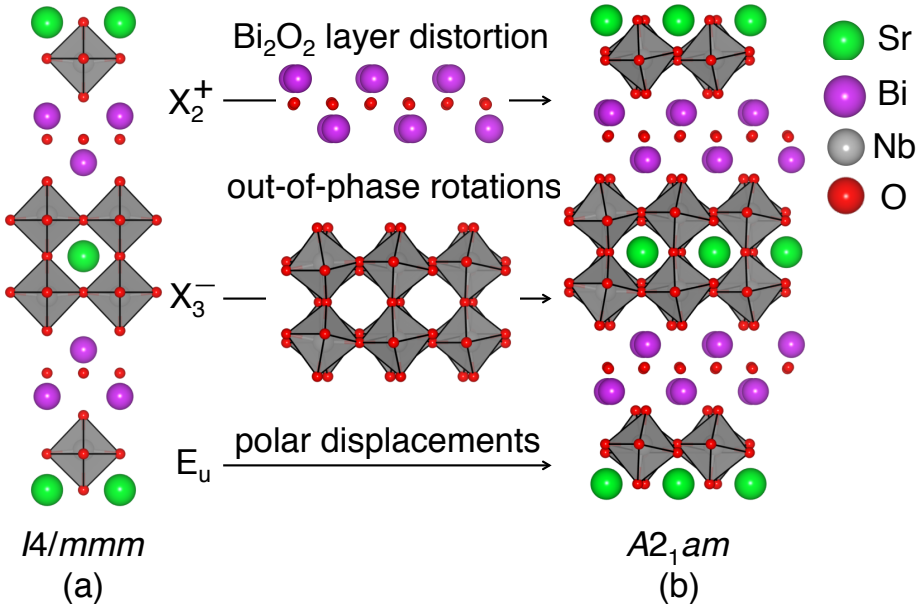

Figure 5.4: Mode decomposition of an $A\mathrm{Bi_2}B_2\mathrm{O_9}$ (a) paraelectric to (b) ferroelectric phase transition. In the $n = 2$ Aurivillius structure, distortions of the $\mathrm{Bi_2O_2}$ layer couple to out-of-phase rotations of the $B\mathrm{O_6}$ octahedra as well as polar displacements to produce a spontaneous polarization. The atoms are colored as follows: A (green), Bi (purple), B (brown), O (red).

coupling may exist in a material, the question of which distortions drive the phase transition is not always immediately apparent, requiring detailed experimental and theoretical study.

$\mathrm{SrBi_2Nb_2O_9}$ is an $n=2$ member of the Aurivillius family[280] with general formula $(\mathrm{Bi_2O_2})(A_{n-1}B_n\mathrm{O}_{3n+1})$; here, a $\mathrm{Bi_2O_2}$ is inserted between every n $AB\mathrm{O_3}$ perovskite blocks.[281] The polar displacements in this material are driven by only one rotational mode (irrep X_3^-), rather than two as in the Ruddlesden-Popper or perovskite families. Interestingly, the rotational mode condenses simultaneously with the E_u polar mode via a proposed avalanche transition with the appearance of a displacement pattern that describes the shifting of the atoms in the $\mathrm{Bi_2O_2}$ layers (irrep X_2^+),[202] which is quite unique. Rather than two nonpolar modes inducing a polarization, the polar mode acts as the primary order parameter with the zone-boundary mode serving as

the secondary order parameter; while this does not make the Aurivillius family a Type AA improper ferroelectric in the strictest sense of our definition, I still find it prudent to include this discussion. It provides an example to illustrate that the form of the coupling requires the condensation of multiple modes; however, knowing the form of the coupling alone is insufficient to identify the displacement mode active in the transition. That understanding comes from a lattice dynamical calculation or through careful experimentation, *e.g.* a temperature-dependent Raman study.[282] Figure 5.4 shows how these distortions take $SrBi_2Nb_2O_9$ from its high symmetry $I4/mmm$ phase (Figure 5.4a) to its ferroelectric $A2_1am$ phase (Figure 5.4b). Other members of the family also display ferroelectricity, such as $n = 1$ Bi_2WO_6[283] and $n = 3$ $Bi_4Ti_3O_{12}$.[284]

In order to understand the features characteristic of the Type AA ferroelectrics within this scheme that can facilitate materials design, I now examine how this phenomenon arises in Ruddlesden-Popper and perovskite compounds in detail. The Ruddlesden-Popper structure has the general formula $(ABO_3)_nAO$; it consists of ABO_3 units ordered along the [001] crystallographic axis with an extra AO layer inserted between every n units.[285,286] The $n = 1$ and $n = 2$ members of this family are illustrated in Figure 5.5a and Figure 5.5b. When $n \to \infty$, the ABO_3 perovskite results (Figure 5.5c). Because these structures are closely related, it should be no surprise that the "improper" polarizations in both compounds can arise from similar structural distortions. As mentioned previously, this requirement is the presence of both in-phase and out-of-phase rotations of the BO_6 octahedral network (an $a^-a^-c^+$ tilt pattern in Glazer notation); the atomic displacement mode producing in-phase rotations transforms like the irreducible representation X_2^+ or M_3^+ for the Ruddlesden-Popper or perovskite structure, respectively, and that for out-of-phase rotations is given by X_3^- or R_4^+ (Figure 5.5d, 5.5e, 5.5f, and 5.5g). These modes then may couple anharmonically to the polar A-site displacement mode Γ_5^- of the

cation ordered perovskite (or equivalently to the nominally antipolar X_5^+ mode of the unordered centrosymmetric ABO_3 structure[287]).

In the case of perovskites, however, odd-period $ABO_3/A'BO_3$ superlattices with layered A-site cation ordering along the [001]-direction is also required to lift the necessary symmetries. Note that ultrashort period 1/1 superlattices are equivalent to $(AA')B_2O_6$ perovskites. The absence of such additional chemical ordering would prohibit the lattice anharmonicities from lifting inversion symmetry.[288] (Other ordering directions for the A and B cations can also yield the same effect, as noted below.) In the Ruddlesden-Popper compounds, this 'topological' requirement is satisfied by the inserted AO layer and spatially disconnected two-dimensional perovskite sheets. The paraelectric Ruddlesden-Popper or layered perovskite structure (Figure 5.5d or 5.5f) is then reduced to its ferroelectric ground state (Figure 5.5e or 5.5g) via this trilinear coupling. In both cases, the materials exhibit anti-polar A cation displacements; the spontaneous polarization then arises as a consequence of two chemically distinct A-sites, preventing a complete cancellation of the oppositely aligned dipoles.

The fact that the 'design rules' summarizing the distortions and cation ordering requirements for lifting inversion and activating an electric polarization in Ruddlesden-Popper and perovskite structures are essentially chemistry-independent[288–290] opens a large discovery space for the creation of new materials. Additionally, cation ordering along alternative directions in perovskites allows different Glazer rotation patterns to lift inversion; tilts consisting of either two modes (such as $a^-a^-c^+$) or one mode (such as $a^0b^-b^-$) can induce improper ferroelectricity.[291] This atomistic understanding has led to a host of new Type AA ferroelectric Ruddlesden-Popper and perovskite compounds. For example, in addition to perovskite oxides, the layered perovskite fluorides $(NaRb)Hg_2F_6$ and $(KRb)Hg_2F_6$ have been predicted to display a spontaneous polarization arising from the anharmonic lattice interaction coupling two rotational

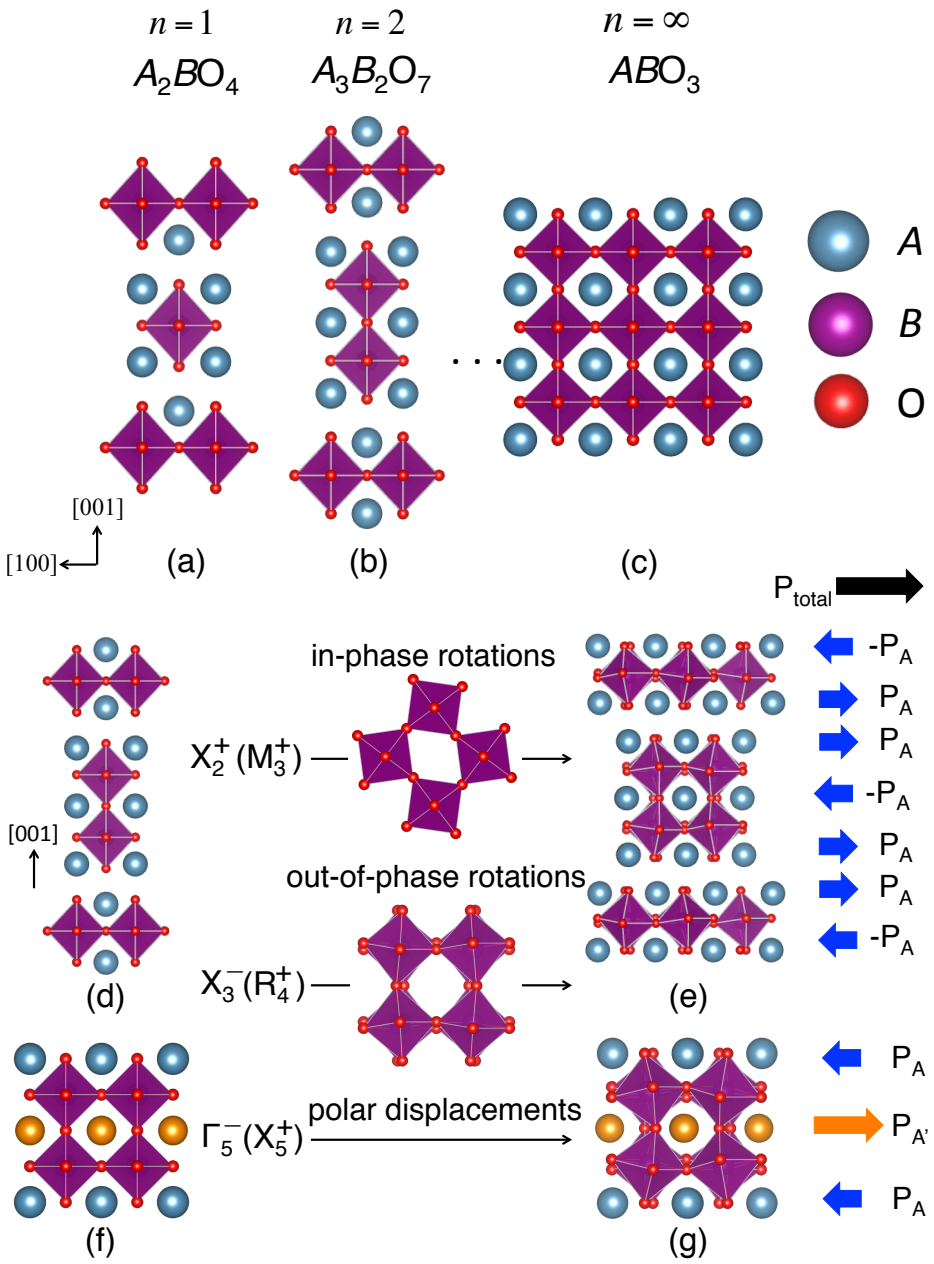

Figure 5.5: Crystal structure of an $(ABO_3)_nAO$ Ruddlesden-Popper phase with (a) $n = 1$, (b) $n = 2$, and (c) $n = \infty$. When $n = \infty$, the ABO_3 perovskite structure is obtained. Both Ruddlesden-Popper and perovskite oxides consist of a corner connected network of 6-fold anion (red) coordinated B-sites (purple) with A-site cations (blue) residing in the interstices.

modes;[292] while fluorides have long been known to be ferroelectric,[293] it is very often due to a proper mechanism (such as in BaMF$_4$ compounds[168]). It is also important to mention that these criteria can be circumvented in some cases when nonpolar ABO$_3$ perovskites are placed under sufficient epitaxial strain, for example in CaTiO$_3$.[294] In the next section, I exhaustively detail all combinations of cation ordering and octahedral rotations which can result in non-centrosymmetric perovskites.

Density functional theory (DFT) calculations provide an especially fruitful route to predict new materials without inversion symmetry, as they allow for high throughput testing of a large numbers of chemistries and the evaluation of relative phase stability from the calculation of formation energies. Recent studies to this end, for example, have predicted several new ferroelectrics in the Ruddlesden-Popper and perovskite families.[21,287] Consider the compound Ca$_3$Ti$_2$O$_7$, which naturally exists as a polar $n = 2$ Ruddlesden-Popper compound[295] and was predicted to be a Type AA ferroelectric with an electric polarization of 20 μC/cm^2.[201] Recently, this was confirmed experimentally in Sr-doped phases of Ca$_3$Ti$_2$O$_7$, where a spontaneous polarization was measured (although slightly smaller than predicted at 8 μC/cm^2) and successfully switched.[296] Substitution of the Ti atoms with Mn results in isostructural Ca$_3$Mn$_2$O$_7$,[297,298] which is also predicted to display a small spontaneous polarization of 5 μC/cm^2.[201,289] Interestingly, it was also found to have a large uniaxial negative thermal expansion.[299] Indeed, these theoretical developments led to synthesis of (Ca$_y$Sr$_{1-y}$)$_{1.15}$Tb$_{1.85}$Fe$_2$O$_7$, an $n = 2$ Ruddlesden-Popper phase displaying coexisting electric polarization and weak ferromagnetism at room temperature.[300] Finally, first principles calculations have predicted ferroelectricity in a series of (LaLn)Fe$_2$O$_6$ ordered perovskite superlattices (where Ln=Ce, Nd, Sm, Gd, Dy, Tm, Lu, Y), showing how this same concept can be applied to a different material family.[301]

The family of $(AA')(BB')$O$_6$ double perovskites, which spontaneously exhibit lay-

ered A-site and rock salt ordered B-sites,[116] are ripe for realizing Type AA ferroelectricity. Similar to the scenario with A-site ordering alone, this type of 'double' cation order lifts inversion symmetry in combination with an $a^-a^-c^+$ tilt pattern. These compounds most often contain an alkali metal (such as Na or K) and a rare earth cation (such as La, Nd, or Tb) on the A and A' site and have been experimentally synthesized with a wide array of different B and B' cations.[117–120,302,303] Additionally, it was recently shown that substitution of smaller rare earth cations on the A'-site can significantly increase the polarization while retaining the B-site magnetic order.[304] Research on these compounds is still ongoing, however, as experimental measurements on polycrystalline samples of (NaLa)(MnW)O_6 and (NaNd)(MnW)O_6 have failed to detect the electric polarization.[305]

Although the previous discussion has focused exclusively on Ruddlesden-Popper and perovskite compounds, other structural families may be classified as Type AA ferroelectrics. The Dion-Jacobson compounds (general formula $A[A'_{n-1}B_nO_{3n+1}]$) have also recently garnered attention as hybrid improper ferroelectrics, as several members are known to be polar, such as $CsBiNb_2O_7$ and $CsNdNb_2O_7$;[306,307] advances in ion-exchange synthesis have also led to the identification of many new phases.[308] While the polarization is also driven by in-phase and out-of-phase rotations (described by the irreps M_2^+/M_3^+ and M_5^-, respectively) as in the perovskites, the A-site atomic displacements comprising the polar mode (Γ_5^-) are ferro- rather than anti-distortive, resulting in much larger electric polarizations. The $n = 2$ compounds $CsBiNb_2O_7$, $RbBiNb_2O_7$, and $RbNdNb_2O_7$, for example, have been predicted to show spontaneous polarizations of 40, 36, and 24 $\mu C/cm^2$, respectively.[309–311] Additionally, the main contribution to the polarization in this family is from the B-site, but is driven by A-site bonding preferences (which provide a somewhat large contribution as well).[312] Recent experimental results have confirmed the presence of ferroelectricity and piezo-

electricity in polar $RbBiNb_2O_7$ and $CsBiNb_2O_7$,[310,313] while theoretical studies have shown the potential for enhancement of the piezoelectric response under strain.[314]

I summarize this section by noting that layered oxides (and halides) provide an open "sand box" for the discovery of new Type AA ("hybrid improper") ferroelectrics with magnetic cations. Although the spontaneous polarizations are produced via different atomic mechanisms, they broadly rely on the anharmonic coupling of two nonpolar distortion modes to a polar mode of the crystal.

5.1.4 Type AB

Materials exhibiting improper ferroelectricity and containing pseudo-rotational modes could also be considered "hybrid." I classify such compounds as Type AB or BB. Here, I will consider pseudo-rotations produced by first-order Jahn-Teller (FOJT) distortions. Like the second-order Jahn-Teller (SOJT) effect discussed previously, the appearance of this phenomenon depends on the d electron configuration of a metal cation; however, the FOTJ theorem applies to a much wider range of d^n configurations. Furthermore, while the SOJT effect itself is responsible for the spontaneous polarization in compounds such as $BaTiO_3$, the FOJT effect cannot drive a ferroelectric phase transition alone, as any distortion of this type preserves inversion symmetry. Finally, although the criteria needed for the appearance of the SOJT effect (*i.e.*, a d^0 transition metal) precludes the appearance of a magnetic moment (with a few exceptions), the FOJT effect has no such restriction. By considering materials in which a spontaneous polarization arises from the coupling of a pseudo-rotation, such as a Jahn-Teller distortion and a proper displacive rotational mode, the space for investigation of novel ferroelectrics is further extended. This type of distortion is especially common in six-fold coordinated transition metal environments, so I return and focus on perovskite-derived structures.

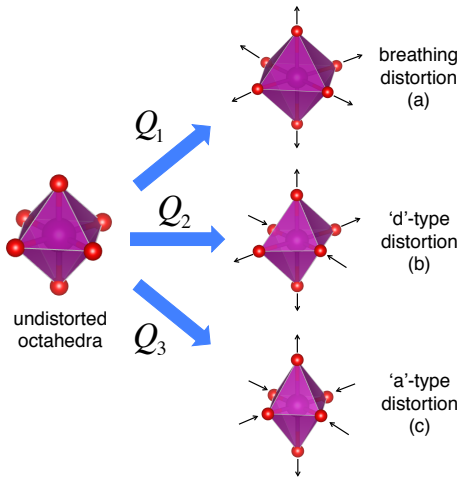

Figure 5.6: Three types of first-order Jahn-Teller distortions that an ideal MO_6 octahedron can undergo. The apical M-O atoms are extended in each case, but the equatorial bonds can either be (a) all elongated and all compressed (also known as a 'breathing' distortion), (b) half elongated and half compressed, or (c) 2/3 compressed and 1/3 elongated and *vice versa*. These are referred to as a Q_1, Q_2, or Q_3 Jahn-Teller distortion, respectively.

The corner-connected BO_6 octahedral network in these structural families can undergo three different types of Jahn-Teller distortions labeled Q_1, Q_2, and Q_3, in which: (1) all B-O bonds can be elongated or compressed (*i.e.*, 'breathing' distortion, Figure 5.6a), (2) the apical oxygens can be elongated while two equatorial oxygens are elongated and two are compressed (*i.e.*, 'd-type' distortion, Figure 5.6b), or (3) all equatorial oxygens can be compressed while the apical oxygens are elongated (*i.e.*, 'a-type' distortion, Figure 5.6c). A symmetry analysis has revealed no combination of the M_2^+ or R_3^+ Jahn-Teller modes with octahedral rotations (described by M_3^+ or R_4^+) lifts inversion in perovskites,[272,273] similar to the fact that no combination of the rotational modes M_3^+ with R_4^+ results in a polar space group. However, cation ordering may be able to provide a route to lift inversion, as in the case of the Type AA hybrid improper ferroelectrics.

Although B-site ordering in combination with Jahn-Teller modes is unable to

lift inversion[315] in perovskites, a recent theoretical crystallographic investigation has shown that it is possible via A-site ordering in $n=1$ Ruddlesden-Popper phases.[290] This is important because while $n=2$ Ruddlesden-Popper phases can display Type AA improper ferroelectricity (such as the aforementioned $Ca_3Mn_2O_7$), polar space groups are exceedingly rare for the $n=1$ RP family; Balachandran et al. showed via data-mining techniques that out of 105 $n=1$ compounds known at the time, only two exhibited a non-centrosymmetric space group.[290] Using the crystal-chemistry guidelines put forth, first principles calculations were used to investigate the A-site ordered $n=1$ Ruddlesden-Popper phase (La,Sr)MnO_4, which is predicted to have a polar $Pca2_1$ ground state displaying a ferroelectric polarization of 1.25 $\mu C/cm^2$.[316] This transition occurs via coupling of a Jahn-Teller distortion of the Mn^{2+} cations (which transforms as the irreducible representation X_2^+) and MnO_6 octahedral rotations (irrep. X_3^+) with polar displacements of the A-sites. The wide variety of first-order Jahn-Teller active cations capable of being substituted on the B-site make this an attractive route to the discovery of more new Type AB ferroelectrics.

The second class of materials which can be classified as Type AB ferroelectrics is the family of metal-organic frameworks (MOFs), especially those with the ABX_3 perovskite architecture. These compounds consist of both organic and inorganic components with transition metal centers coordinated by chains of small organic molecules. Interest in these materials began with the synthesis of a series of formates $[C(NH_2)_3]M[(HCOO)_3]$, where M=Mn, Fe, Co, Ni, Cu, or Zn;[317] each member except M=Zn was found to display spin-canted antiferromagnetic ordering. These structures are similar to perovskites, but rather than the A- and X-sites being occupied by a single cation or anion, they are filled with small organic molecules (here A is the guanidine cation $[C(NH_2)_3]^+$), B is a transition metal, and X is the formate anion ($[COOH]^-$). Out of these six compounds, one (M=Cu) was thought to be a poten-

tial multiferroic due to displaying a polar $Pna2_1$ structure. Indeed, first principles calculations predict the presence of a small polarization of 0.37 μC/cm^2 arising from displacements of the NH_2 groups.[318]

Further investigation of an isostructural Cr MOF (also displaying magnetic order and a small polarization of 0.22 μC/cm^2) then showed that the polarization arises due to a hybrid improper mechanism.[319] However, the transition from centrosymmetric $Pnna$ (Figure 5.7a) to polar $Pna2_1$ (Figure 5.7b) occurs via a trilinear coupling (mediated by hydrogen bonding[320]) between rotations of the organic A-site and a Jahn-Teller distortion of the transition metal B-site to induce the polar displacements. Interestingly, the antiferrodistortive order is produced by a combination of two Q_2 Jahn-Teller distortions on different crystallographic sites; this 'switching' of the short and long bonds is analogous to the Berry pseudo-rotation mechanism operative in PF_5.

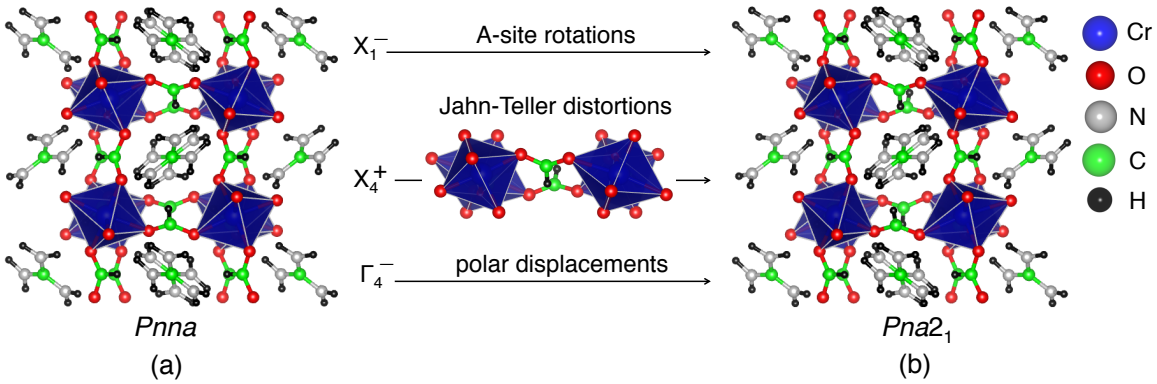

Figure 5.7: Mode decomposition of the paraelectric (a) to ferroelectric (b) phase transition in the $[C(NH_2)_3]Cr[(HCOO)_3]$ metal-organic framework. Here rotations of the A-site molecules and first-order Jahn-Teller distortions of the CrO_6 network couple to polar displacements and drive the structure from centrosymmetric to $Pnna$ to polar $Pna2_1$.

This family of materials offers the potential for a wide variety of novel ferroelectrics, as they are highly tunable via both cation substitution and ligand engineering. Different organic molecules can substitute on the A- and X-sites, while various transition metal cations can occupy the B site. For example, the compound $[(CH_3CH_2NH_3)]Mn[(COOH)_3]$, where the guanidine molecules have been replaced by ethyl-ammonium while maintaining the presence of a first-order Jahn-Teller active transition metal, also displays a $Pna2_1$ space group.[321] First principles calculations have predicted this material to exhibit an electric polarization of $2\,\mu C/cm^2$.[322] Additional substitution of the A-site molecule in this compound with $CH_3CH_2NF_3$ and $PH_3CH_2NF_3$ was predicted to further enhance the polarization to 5 $\mu C/cm^2$ and 6 $\mu C/cm^2$, respectively.

The ABX_3 architecture is not necessarily required for metal-organic frameworks to be Type AB ferroelectrics. For example, the compound $(C_6H_5CH_2CH_2NH_3)_2CuCl_4$ was recently found to exhibit ferromagnetic ordering below 18 K and a small ferroelectric polarization below 4 K on the order of 0.025 $\mu C/cm^2$.[323] Although the structure contains a network of octahedrally coordinated Cu^{2+} atoms corner-connected in the xy plane, they are separated in the z direction by two layers of the phenylethyl amine organic framework. The ferroelectric phase transition in this compound is driven by a tilting or buckling of the $CuCl_4$ complexes, as well as a Jahn-Teller distortion induced by the Cu^{2+} cations, which results in a displacement of the N atoms from their high symmetry positions; this is in contrast to the previously discussed MOFs in which one distortion was a rotation of the organic molecules. As with the previous MOFs, these compounds also offer a high degree of tunability. By replacing the phenylethyl amine molecule with ethyl amine to create $(C_2H_5NH_3)_2CuCl_4$, the polarization increases to 18 $\mu C/cm^2$—an increase of three orders of magnitude.[324]

5.1.5 Type BB

As with Type B improper ferroelectrics, Type BB compounds are fairly difficult to locate as the polarization arises from the coupling of two pseudo-rotational modes. A focus on materials containing Jahn-Teller active cations appears to be a promising way forward for discovering Type BB ferroelectrics. Indeed, this type of mechanism has now been predicted from first principles to arise in the layered vanadate perovskites (LaY)V_2O_6 and (LaPr)V_2O_6.[325] While a proper rotationally induced polarization (*i.e.* a Type AA attribute) also exists in these compounds giving magnitudes of 7.89 (A'=Y) and 2.94 μC/cm^2 (A'=Pr), a second trilinear term of the form $\mathcal{F} \propto \gamma M_{JT} R_{JT} P_z$ coupling a polar mode to two distinct types of Jahn-Teller distortions (given by the irreducible representations M_{JT} and R_{JT}, Figure 5.8) arises in the free energy expansion of (LaPr)V_2O_6. From this, a small additional spontaneous polarization of 0.34 μC/cm^2 is generated perpendicular to the first, due solely to the Jahn-Teller activity of the V^{3+} cations. Although electronic structure calculations show the potential for the existence of Type BB ferroelectrics, confirmation of this effect experimentally remains elusive. As with Type B improper ferroelectrics, exploring materials with either Jahn-Teller active cations or organic frameworks may prove fruitful in finding new Type BB compounds.

5.2 Designing Non-centrosymmetric Perovskites

Because the defining crystallographic feature of all of the ferroelectric materials discussed in the previous section is the lack of inversion centers, simple chemistry-independent models describing how to deterministically remove this parity operation can facilitate the rapid identification and design of new polar compounds. The method of inorganic crystal engineering considers the unit cell of a crystalline solid as being formed by a linkage of "basic building units" (BBUs), which are polyhedra formed by

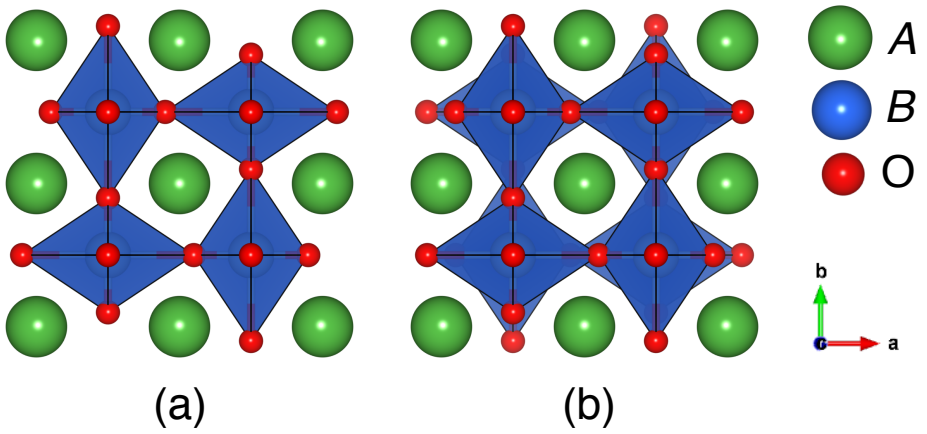

Figure 5.8: Jahn-Teller distortions associated with the (a) M_{JT} and (b) R_{JT} modes.

the cations and anions present on a well defined lattice.[19,326–329] By understanding and manipulating the connectivity among these units, specific acentric properties can be induced from purposefully lifting inversion and then further enhanced through techniques such as chemical substitution and epitaxial strain.[330]

On the other hand, the chemical occupancy of sites among effectively equivalent positions in a crystal can also modify (or remove) inversions centers. Consider the diamond lattice: it is commonly described as a series of corner-sharing carbon tetrahedra and exhibits the nonpolar space group $Fd\bar{3}m$ (no. 227). An examination of this structure reveals that inversion symmetry arises owing to the fact that all of the atoms surrounding the inversion centers (Wykcoff position 16c) are chemically equivalent. Coloring the lattice to transmute diamond into ZnS by substituting half of the carbon atoms with zinc and half with sulfur results in a symmetry reduction to the non-centrosymmetric space group $F\bar{4}3m$ (no. 216).

The identification of similar strategies and their combination into one simple model will allow for the targeted, rational design of new polar materials. In this section, I seek to understand how the arrangement and control of BBUs and chemical (cation) ordering in a material alters the presence or absence of spatial parity. I begin by

identifying the criteria needed to lift "inversion" (in the lower dimensional cases, a 2-fold rotation axis is broken instead) in a one dimensional chain, using basic centric and acentric shapes to draw connections to the crystal engineering approaches I will apply to real materials. This model is next extended to two dimensions to show how the tiling of these units in space can also lead to polar structures.

I then combine these motifs in three dimensional materials using the family of ABX_3 perovskites as a case study; I illustrate how rotations of the BX_6 octahedral network produce the required acentric A-site polyhedral BBUs, while cation ordering cooperatively aligns them so as to break inversion symmetry. By exhaustively examining the space groups produced by all combinations of the 15 distinct BX_6 octahedral rotation patterns in these materials with A-site, B-site, and combined A- and B-site ordering along the [001], [110], and [111] directions, I identify a vast array of new opportunities for non-centrosymmetric phases in the perovskite family. Finally, I discuss the chemical criteria, such as tolerance factor and global instability index (GII), that control the stability of various rotation patterns, while showing how this information can be harnessed for materials design.

5.2.1 Structural Units and Symmetry

First, I consider the simplest case of a BBU that will tile a one dimensional space. The symmetry of a two dimensional pattern repeated in one dimension is given by one of seven *frieze* (line) groups.[331] One can imagine replacing the BBUs in three dimensional systems (*i.e.*, cation-anion polyhedra) with simpler units (triangles and squares) and reducing inversion centers to 2-fold rotation axes. Two different systems can be generated depending on the type of building units chosen: one which contains acentric units (triangles, without a 2-fold rotational symmetry, **case I**), and one which contains centric units (squares, **case II**). Tiling either of these units on a

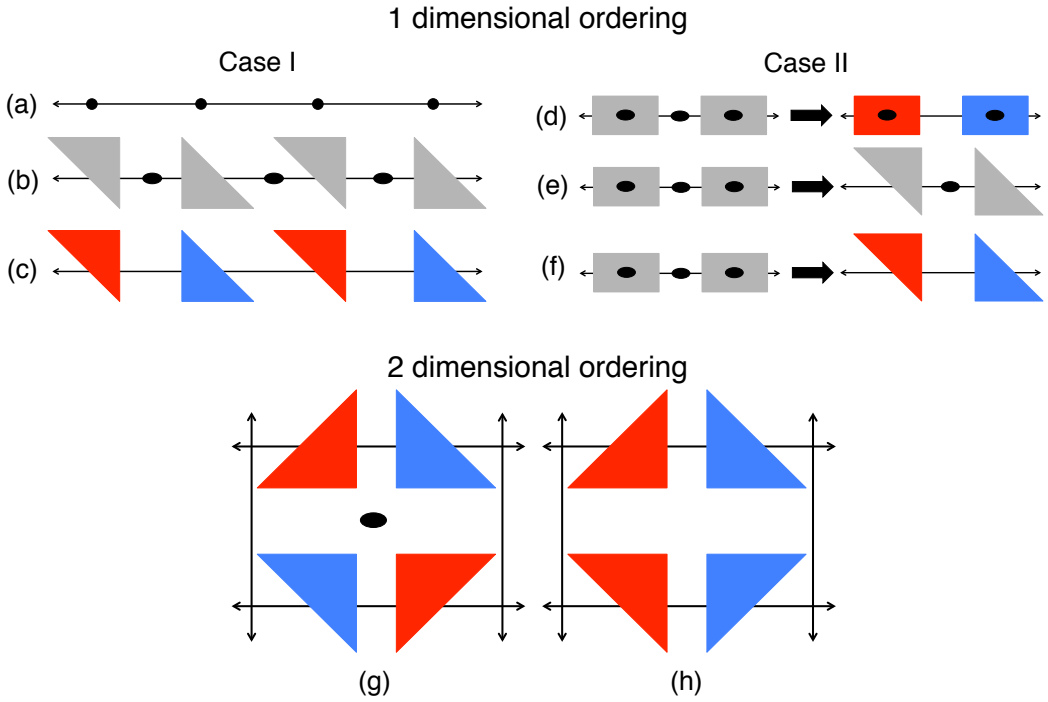

Figure 5.9: (a) A one dimensional lattice is tiled with acentric BBUs on each lattice point, (b) resulting in 2-fold rotation axes between each unit and a $p2$ frieze group. These proper rotations are lifted in (c) by coloring the BBUs, reducing the symmetry of the system to $p1$. Coloring a one dimensional lattice with centric units (d) lifts the rotational symmetry between each unit, while changing the shape of the unit (e) lifts it within each unit. When both actions are combined, all rotation axes present in the system are removed (f). In two dimensions, the difference in spatial tilings of the BBUs results in either a (g) centrosymmetric or (h) non-centrosymmetric lattice despite the fact that both systems contain colored acentric units. The 2-fold rotation can be removed in (g) by rearranging the BBUs into a different ordering configuration (h).

one dimensional lattice (Figure 5.9a) results in a simple one dimensional "crystal." Although the BBU or motif in case I does not contain a 2-fold rotation axis, the way in which they have been tiled generates a two-fold rotation operation between them, resulting in a lattice with frieze group $p2$ (Figure 5.9b). By coloring these units differently (which acts similarly to chemical ordering in a real material as I show later) the 2-fold axis is lifted. The now inequivalent BBUs produce a $p1$ symmetry *i.e.* an acentric "crystal" (Figure 5.9c).

In case II where the one dimensional lattice is tiled with centric BBUs, a two-fold rotation symmetry element will be found within each BBU as well as between them (Figure 5.9d). The frieze group of this unordered lattice is $p2mm$. The consequence of having two rotation elements is that a symmetry reduction requires that *both* of these operations be removed. First, the same 'coloring' technique used in case I may be applied to remove the rotational symmetry between units, leading to a $p11m$ symmetry (Figure 5.9d). In order to lift the 2-fold rotation located *within* each unit, however, the motif must be altered further; reducing the centric squares to acentric triangles produces the previously discussed $p2$ frieze group (Figure 5.9e). In a realistic crystal, this may be accomplished by cooperative displacements of atoms, which destroy the regularity of a polyhedron. By changing the shape and applying the same coloring procedure as before, all rotational symmetries are removed from the system, resulting in a one dimensional lattice exhibiting $p1$ symmetry (Figure 5.9f).

Additional complexities arise when the systems are extended to higher dimensions as there are multiple ways to tile different colored BBUs in space and several new implied symmetries appear owing to group combination rules. Even after following the steps outlined in Figure 5.9, one lattice still exhibits a 2-fold rotation axis (plane group $p2mm$, Figure 5.9g), whereas the other one does not (plane group pm, Figure

5.9h). This difference arises from tiling and ordering the BBUs in more than one dimension, and will become even more important in three dimensions. From these simple one and two dimensional systems, it is clear that in three dimensions the "color" (*i.e.*, chemistry, Figure 5.9a-c), "shape" (*i.e.*, distortions, Figure 5.9d-f), and "arrangement" (*i.e.*, cation ordering, Figure 5.9g-h) of the polyhedral units must be synergistically combined to macroscopically lift inversion symmetry in a crystal.

5.2.2 Extension to Crystalline Perovskites

I now extend these observations and simple principles to crystalline three dimensional materials. Specifically, I focus on how to remove centers of inversion rather than 2-fold rotation axes. I apply these principles to the perovskites, a vast family that exhibits a range of chemistries and a rich variety of physical properties.[31,332–335] The prototypical member has the general chemical formula ABX_3, where A and B are metal cations and X is an anion; although the majority of these materials are oxides (where X=O), there are a wide variety of other types of perovskites, including halides (X=F, Cl, Br, or I),[91–94] sulfides (X=S),[95,96] and nitrides (X=N).[97] Multianion chemistries are also possible.[98–100]

As described in Chapter 3, the crystal structure is constructed from face-sharing AX_{12} cuboctahedra and corner-sharing BX_6 octahedra repeated in space (Figure 3.1b), where the anions are shared among polyhedra. Undistorted cubic ABX_3 perovskites with the $Pm\bar{3}m$ space group (no. 221) have inversion centers located within each centric AX_{12} polyhedra as the A-site cation is found at the $1b$ Wyckoff position $(\frac{1}{2}, \frac{1}{2}, \frac{1}{2})$ with site symmetry $m\bar{3}m$. The octahedra are also centric BBUs with the B-site cation at the $1a$ position $(0, 0, 0)$ with site symmetry $m\bar{3}m$. In addition, there are inversion centers located 'between' polyhedra, *i.e.* similar to the uncolored squares of Figure 5.9d, as the anions which are shared by the BBUs are located at site $3d$

$(\frac{1}{2}, 0, 0)$ with symmetry $(\frac{4}{m}m.m)$.

The question is now: *How can I transform this centrosymmetric $Pm\bar{3}m$ structure into a crystal without inversion symmetry by tiling nominally centric polyhedra?* As was outlined in Figure 5.9, this requires (1) changing the shape of the basic building units and/or (2) "coloring" the polyhedra.

5.2.3 Distorting Basic Building Units Through Octahedral Rotations

Cooperative displacements of the anions are common in perovskites and manifest as nearly rigid "rotations" of the BX_6 network, the magnitude of which directly influences the properties of the material.[336–339] To achieve step (1), I first examine how these displacements lead to changes in the shapes of the BBUs. Because the anions are shared by the two main BBUs in the perovskite structure, I describe the changes to the AX_{12} units as arising indirectly from the various combinations of BX_6 octahedral rotation patterns. (Note that these are also referred to as octahedral tilts in the literature.) The consequence of the nearly rigid BX_6 rotations is that the environment around the A-site will be distorted such that the polyhedron is no longer centric, thus removing the inversion center in the AX_{12} BBUs. As discussed in Chapter 3, the octahedra can either remain unrotated (as in Figure 5.10a), rotate in-phase (Figure 5.10b), or rotate out-of-phase (Figure 5.10c) along each Cartesian axis.

There are 15 distinct combinations of rotations about the various axes that retain the corner-connectivity and rigidity of the BX_6 octahedral network in simple perovskites. Each of these patterns produces a different space group (Table 5.1) and are divided based on whether the tilt pattern exhibits no rotations, only in-phase rotations, only out-of-phase rotations, or a combination of in-phase and/or out-of-phase rotations ("mixed"). The application of these different patterns can locally alter or

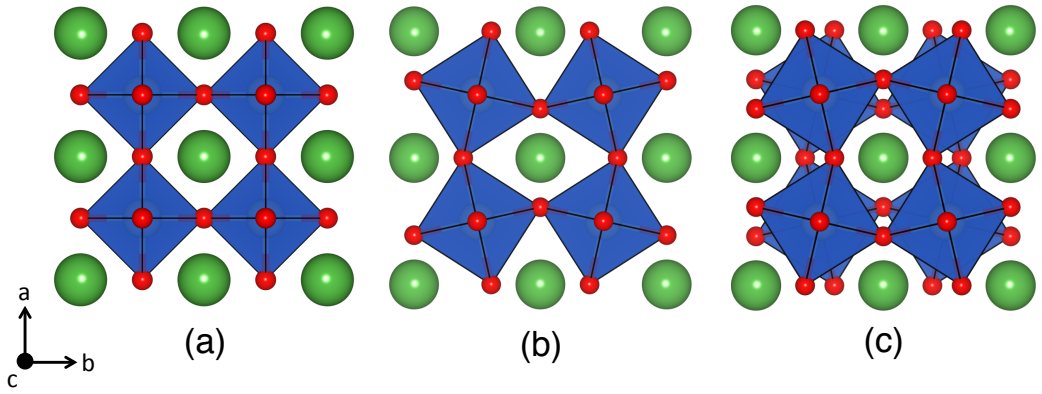

Figure 5.10: Cooperative oxygen displacements can manifest in (a) in-phase or (b) out-of-phase rotations of the extended BX_6 octahedral network.

shift the centers of inversion by distorting the AX_{12} polyhedra since they share the X anions with the BX_6 octahedra. As shown in Table 5.2, the A-X polyhedra created by an in-phase rotation pattern (*e.g.*, $a^0a^0c^+$) are centric rectangular prisms; regardless of how the cations are ordered, in-phase octahedral rotations preserve the inversion centers at the A-site. However, an out-of-phase or mixed rotational pattern is sufficient to generate acentric AX_n building units, which take forms similar to elongated square pyramids. As seen in Table 5.1, the A-site symmetry no longer possesses inversion for these types of rotation patterns.

Nonetheless, there are no non-centrosymmetric space groups in Table 5.1 despite the fact that I have shown it is possible to generate acentric BBUs. This is because the scenario now resembles that shown in Figure 5.9g; although there are acentric units, they are tiled in space in such a way so as to retain the inversion centers between them. In order to remove this remaining inversion center on the B-site, I turn to task (2) and make the BBUs unique by "coloring" the cation sublattice in the perovskite structure through ordered cation substitution.

Table 5.1: The 15 distinct BX_6 rotational pattern can be divided into groups based on whether the pattern contains no rotations (1 variant), in-phase rotations only (4 variants), out-of-phase rotations only (6 variants), or a mixture of in-phase and out-of-phase rotations (4 variants). Each produces a different centrosymmetric space group for the ABX_3 perovskite structure. Although none of the octahedral rotation patterns globally lift inversion, they are able to locally alter the point symmetry of the A-site and B-site cation.

Pattern	Glazer Notation	Space Group	A-Site Sym.	B-Site Sym.
None	$a^0a^0a^0$	$Pm\bar{3}m$ (221)	$m\bar{3}m$	$m\bar{3}m$
In-phase	$a^0a^0c^+$	$P4/mbm$ (127)	$m.mm$	$\frac{4}{m}..$
	$a^0b^+b^+$	$I4/mmm$ (139)	$mmm.$	$..\frac{2}{m}$
			$\frac{4}{m}mm$	$..\frac{2}{m}$
	$a^+a^+a^+$	$Im\bar{3}$ (204)	$m\bar{3}.$	$.\bar{3}.$
			$mmm..$	$.\bar{3}.$
	$a^+b^+c^+$	$Immm$ (71)	mmm	$\bar{1}$
Out-of-phase	$a^0a^0c^-$	$I4/mcm$ (140)	$\bar{4}2m$	$\frac{4}{m}..$
	$a^0b^-b^-$	$Imma$ (74)	$mm2$	$\frac{2}{m}..$
	$a^-a^-a^-$	$R\bar{3}c$ (167)	32	$\bar{3}.$
	$a^0b^-c^-$	$C2/m$ (12)	m	$\bar{1}$
	$a^-b^-b^-$	$C2/c$ (15)	2	$\bar{1}$
	$a^-b^-c^-$	$P\bar{1}$ (2)	1	$\bar{1}$
Mixed	$a^0b^+c^-$	$Cmcm$ (63)	$mm2$	$\bar{1}$
	$a^-a^-c^+$	$Pnma$ (62)	$.m.$	$\bar{1}$
	$a^+b^-c^-$	$P2_1/n$ (11)	m	$\bar{1}$
	$a^+a^+c^-$	$P4_2/nmc$ (37)	$\bar{4}2m$	$\bar{1}$
			$2mm.$	

5.2.4 Lattice Coloring through Cation Order

I now explore the consequence of the combination of A-site, B-site, and mixed A- and B-site ordering with the 15 distinct rotational patterns from Table 5.1 to determine the crystal-chemistry features required to produce non-centrosymmetric perovskites. Each of the ordering types I consider here were discussed in Chapter 3 and summarized in Figure 3.3. Layered ordering of different A and A' cations

Table 5.2: Different BX_6 octahedral rotations distort the AX_{12} environments in perovskites in unqiue ways. In-phase rotations lead to centric polyhedra, while out-of-phase and mixed rotations lead to acentric polyhedra.

Rotations Present	Example	Symmetry	Polyhedra
None	$a^0a^0a^0$	Centric	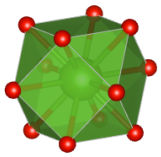
In-phase only	$a^0a^0c^+$	Centric	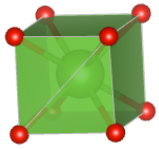
Out-of-phase only	$a^0b^-b^-$	Acentric	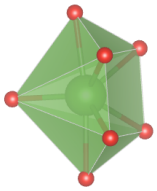
Mixed	$a^-a^-c^+$	Acentric	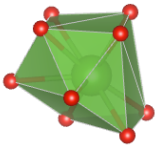

in a cubic perovskite, for example, locally breaks spatial parity on the B-site by reducing the point symmetry of the Wyckoff position from $m\bar{3}m$ to $4mm$ (but retains a centrosymmetric A-site point group of $\frac{4}{m}mm$). Combining this with an appropriate octahedral rotation pattern that produces an acentric A-site environment (Table 5.1) then globally breaks inversion symmetry in the crystal.

A-site Cation Ordering

I first consider replacing half of the A-site cations in an ABX_3 perovskite with chemically distinct A' cations; this is the same as creating an ordered $A_{0.5}A'_{0.5}BX_3$ perovskite [equivalently $(AA')B_2X_6$ compound or an ultrashort period $(ABX_3)_1/(A'BX_3)_1$ superlattice]. Chemical substitution of the A-sites is equivalent to coloring the basic

building units as in Figure 5.9d, while ordering the different cations in the lattice has a similar effect as in Figure 5.9g and 5.9h. The three simple A cation ordering schemes I examine consist of alternating the A and A' cations along the [001], [110], and [111] crystallographic directions (these ordering schemes were discussed in Chapter 3 and shown in Figure 3.3a, 3.3b, and 3.3c, respectively). For simplicity, I differentiate these compounds by using the following labels, with symmetries specified for the ideal undistorted structures:

$$\begin{array}{lcl} [001] & : & \text{Layered}, P4/mmm \\ [110] & : & \text{Columnar}, P4/mmm \\ [111] & : & \text{Rock salt}, Fm\bar{3}m \end{array}$$

An analysis of how each of the 15 rotational patterns distort the A-site environments in these three cation arrangements establishes general rules for designing perovskite compounds without inversion symmetry.

Although some of the A-X BBUs in Table 5.2 are acentric, their relative tiling on the lattice needs to be examined for each ordering scheme. Consider as an example a perovskite with out-of-phase BX_6 rotations about two axes, $a^0b^-b^-$. If the A and A' cations are ordered along [001], each BBU is matched by a corresponding unit that is anti-aligned, preserving inversion symmetry in the material (Figure 5.11a). Ordering along the [111] direction, on the other hand, fully lifts spatial parity owing to the fact that this new cation arrangement provides a cooperative alignment of the acentric units (Figure 5.11b). The alignment or anti-alignment of these distorted A-X polyhedra, which derive from the BX_6 rotations, is due solely to the effect of cation ordering, directly analogous to the BBU coloring in the two dimensional system (Figure 5.9g and 5.9h). However, all inversion centers are lifted in the layered superlattice if both in-phase and out-of-phase rotations are present,[20] as the asymmetry of the A-site unit

produced (Table 5.2) is sufficient to break inversion regardless of alignment. Finally, there is no combination of BX_6 octahedral rotations and [110]-ordering which lifts inversion symmetry, owing to the fact that the BBUs in one chemical homogenous column are always anti-aligned with those in a different one.

I then systematically combined [001], [110], and [111] ordering with the 15 different Glazer rotation patterns of Table 5.1. However, the kind of ordering present must also be taken into account in addition to the direction of the ordering. This means that although alternation of A and A' along the [001]-direction is considered "layered," it is also possible to have layered ordering along [100] or [010]. This can have a direct effect on inversion symmetry in the crystal structure; it may or may not be present depending on how the cation ordering and the rotational pattern are arranged relative to each other. For example, applying the $a^-a^-c^+$ tilt pattern to a layered $(AA')B_2X_6$ superlattice results in a polar space group ($Pmc2_1$) *only* if the direction of the layers is perpendicular to the direction of in-phase rotations. Layering orthogonal to any other crystallographic axis results in a centrosymmetric $P2_1/m$ space group. Taking this caveat into consideration for the [001]- and [110]-ordered structure results in a total of 105 possible combinations of ordering and rotation patterns.

The resulting space groups from each of these combinations is summarized in a heat map (Figure 5.12), with the combination of one ordering type and one rotational pattern shown in a large box (an example is highlighted in blue). This intersection is then divided into four smaller sections, which are colored orange if a given combination produces a centrosymmetric (CS), polar (P), enantiomorphic (E), or second harmonic (SH) active crystal class. The number within a box denotes how many *unique* space groups are produced by that combination (note that a single space group may span more than one of these categories). As an illustrative example, consider layered A-sites (along the [001], [010], and [100] directions) in addition to an $a^-a^-a^-$ rotational

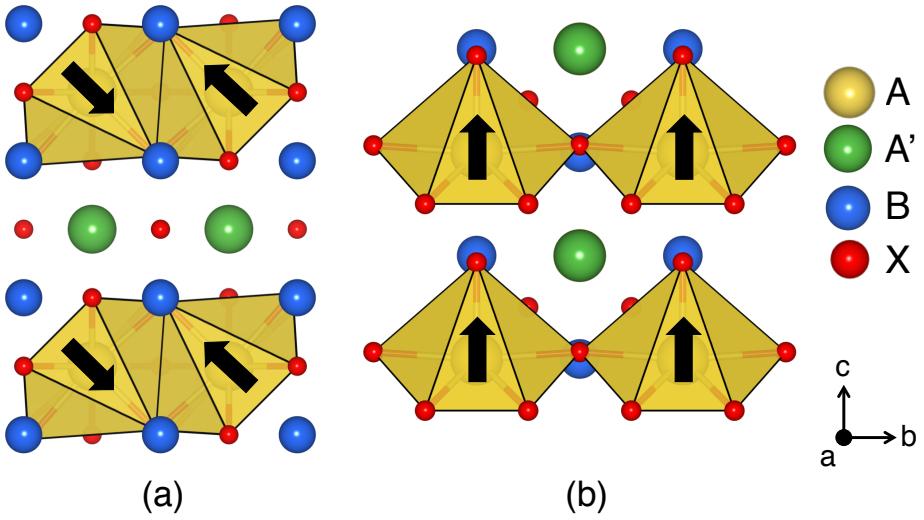

Figure 5.11: The (a) layered and (b) rock salt A-site cation ordering schemes when combined with an out-of-phase only $a^0b^-b^-$ BX_6 octahedral rotation pattern result in different orientations of the acentric BBUs. Only A-X polyhedra are shown for clarity; A'-X polyhedra are not shown, but order in a similar manner. The fact that the A-X polyhedra are cooperatively aligned in the rock salt structure leads to a loss of inversion symmetry.

pattern; this combination only results in one distinct centrosymmetric space group ($R\bar{3}c$), despite the fact that this combination represents three crystal structures. If layered A-sites are combined with the $a^+a^+c^-$ pattern, on the other hand, the three crystal structures produced exhibit two distinct space groups, one which is second harmonic active ($P\bar{4}2m$) and one classified as both polar *and* second harmonic active ($Pmm2$).

A further examination of the phase space shown in Figure 5.12 reveals that this systematic investigation of ordering and rotations is consistent with the analysis of the A-site environment distortions (Table 5.2). To summarize: (1) no octahedral rotation patterns can remove inversion symmetry in columnar ordered structures, (2) mixed rotation patterns can lift inversion symmetry in layered ordered structures, and (3) both out-of-phase and mixed rotation patterns can break inversion symmetry

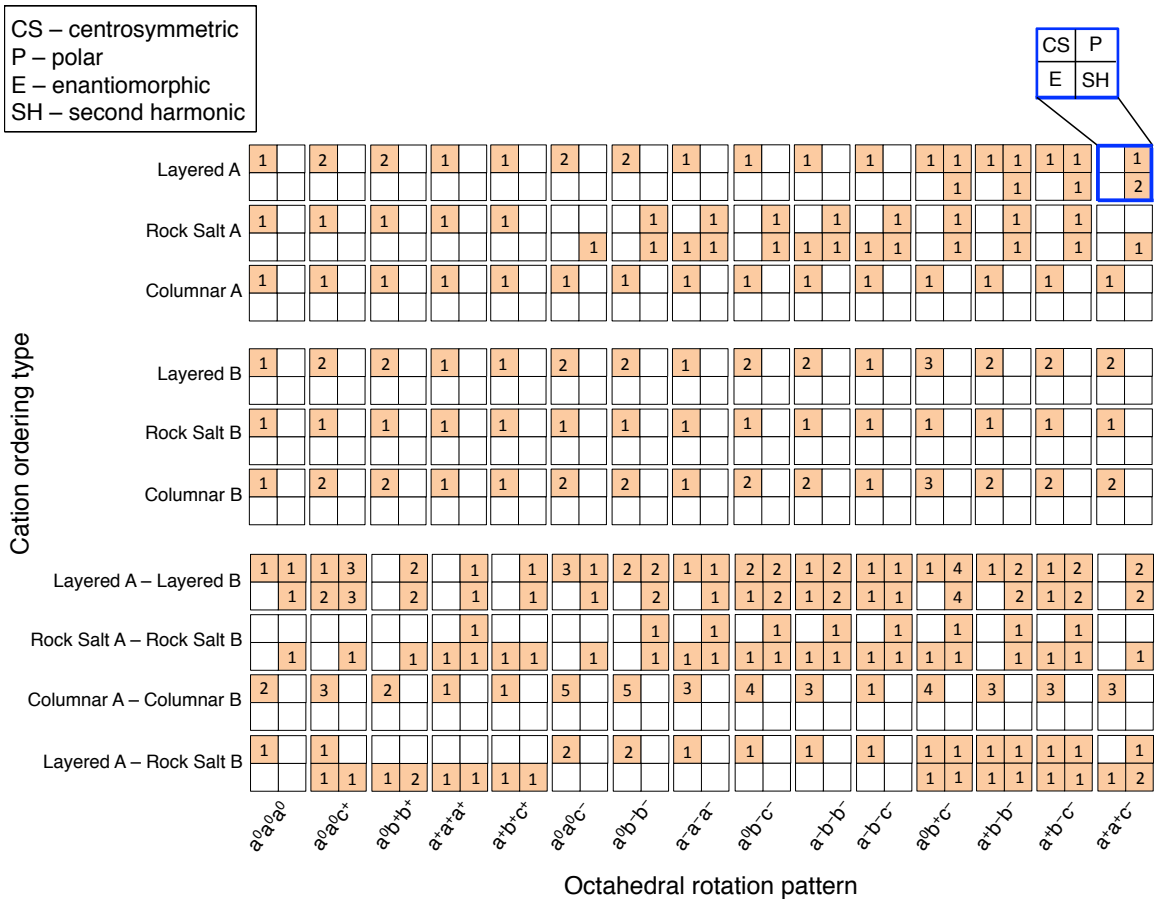

Figure 5.12: Summary of space groups produced when A-, B-, and mixed A- and B-cation order along various directions are combined with the 15 Glazer rotation patterns. Each combination results in a different frequency of occurrence in centrosymmetric (CS), polar (P), enantiomorphic (E), and second harmonic (SH) active structures. The numbers within each box represent the number of distinct space groups of a given type produced by an ordering–rotation combination.

in rock salt ordered structures; these are analogous to the steps taken to remove 2-fold rotation axes in two dimensional systems presented in the previous sections. Furthermore, this analysis is consistent with previous theoretical results on A-site ordered perovskites. For example, it has been shown that an $a^-a^-c^+$ rotational pattern can break inversion symmetry in layered and rock salt ordered compounds, but not in columnar ordered.[20,21,340] Additionally, $a^0b^-b^-$ and $a^-a^-a^-$ tilt patterns have been shown to lift inversion symmetry in rock salt ordered compounds, but not layered or columnar.[291]

B-site Cation Ordering

I next ordered the B-site cations in the same three configurations (Figure 3.3d-f) to produce 105 $A_2(BB')X_6$ superlattices. Although the cubic aristotype structures exhibit the same space groups reported in the previous section, no combination of any octahedral rotation pattern with these simple B-site ordering produces a polar space group (middle section, Figure 5.12). While combining octahedral rotation patterns and A-site ordering breaks two different inversion centers in the crystal (*i.e.* those within and between A-X BBUs, respectively), rotations and B-site ordering both break the same inversion center (those between the polyhedra). Despite appearing as a "negative result," this analysis will become useful in the next section, in which A and B cations are ordered simultaneously. Furthermore, B-site cation ordering is significantly more common than A-site, with each of the [001]-, [111]-, and [110]-B-site ordered compounds having been realized experimentally in a wide variety of materials;[341–344] this understanding of how B-site ordering affects the symmetry of perovskites is therefore helpful in the quest for discovery of new polar double perovskites.

Combined A-site and B-site Cation Ordering

Finally, I examine $(AA')(BB')X_6$ structures with combinations of [001]-, [111]-, and [110]-ordering. I first investigate the combination of like orderings; that is, compounds exhibiting layered A- with layered B-sites, rock salt ordered A- with rock salt ordered B-sites, and columnar ordered A- with columnar ordered B-sites. In this case, not only can the A/A'- and B/B'-site layers and columns be ordered perpendicular to each crystallographic axis, but they can also be aligned perpendicular to each other. Therefore, for each combination of layered and columnar cation ordering and a single octahedral rotation pattern, there are nine possible permutations of A and B cation arrangements. Furthermore, because A-site cations prefer to order in a layered fashion and B-site cations prefer to order in a rock salt fashion,[116] I also examined structures exhibiting this type of mixed ordering; this is the most common type of ordering seen in experimentally synthesized $(AA')(BB')O_6$ compounds.[345–348] The combination of each like-ordered compound with the 15 rotational patterns allows for 285 distinct $(AA')(BB')X_6$ structures. Adding the additional 45 structures resulting from layered A-sites and rock salt B-sites results in a total of 330 combinations, which are summarized in the bottom portion of Figure 5.12.

Every octahedral rotation pattern, when combined with either the double layered or double rock salt ordering scheme, produces at least one non-centrosymmetric perovskite structure owing to the fact that the ordering of the A- and B-sites alone cooperatively lifts the inversion centers within and between BBUs in the crystal structure. Furthermore, as with A-site only cation ordering, every combination of double columnar ordering and octahedral rotations resulted in a nonpolar space group; it is therefore clear that ordering along the [110]-direction is not a worthwhile route to producing polar compounds. A surprising result, however, is that *in-phase* rotations are able to lift inversion with the layered A/rock salt B type of ordering, while

the out-of-phase rotation patterns result in entirely centrosymmetric structures; this is in contrast to the A-site ordering, which displays the opposite phenomenon. Although this may seems counterintuitive, breaking down how each type of ordering lifts inversion gives a more clear indication of what is happening.

First, recall that combining layered A-sites with patterns containing only in-phase or out-of-phase rotations can never break inversion for the reasons mentioned previously; that is, patterns with purely in-phase rotations only produce centric A- and A'-site BBUs. Consider, for example, the cubic A-X environment produced by the $a^0a^0c^+$ tilt pattern in an $(AA')B_2X_6$ compound; these A- and A'-site units are located at Wyckoff positions $2c$ and $2d$, both with point symmetry $m.mm$. However, the fact that this rotation pattern exhibits a handedness means that it fully lifts inversion within the B-site octahedral BBUs (at Wyckoff position $4e$, with point symmetry 4..) in such a compound. Rock salt ordering of the B-sites reduces the point symmetry of the A- and A'-site Wyckoff positions to 2.22, producing a chiral $P42_12$ $(AA')(BB')X_6$ structure. On the other hand, the out-of-phase BX_6 rotations making up the $a^0a^0c^-$ tilt pattern split the Wyckoff position of the B-site in the $(AA')B_2X_6$ crystal structure; one sits at $2b$ with centrosymmetric point symmetry $\bar{4}$.. while one sits at $2c$ with 4.. symmetry (the same is true of the A- and A'-site, which sit at $2a$ [$\bar{4}$..] and $2c$). In this case, rock salt ordering of the B-sites results in no change of the cation site symmetries. This is an interesting example resulting from the fact that in-phase rotations display a handedness (winding sense) while out-of-phase rotations do not. Finally, I point out that each of the non-centrosymmetric structures produced by this cation ordering scheme forms in the second harmonic active and chiral classes (*i.e.*, they have no unique anisotropic axis, and so are not polar). Because this type of ordering is the most conducive to experimental growth, this result could lead to the generation of new nonpolar chiral perovskites if in-phase only rotational patterns can

be stabilized, a relatively rare type of structure.

5.2.5 Chemical Considerations for Non-centrosymmetric Perovskites

So far I have described how different cooperative anion displacements (manifesting as rotations of the BX_6 octahedral BBUs) and cation ordering remove symmetry operations from the perovskite crystal structure with no mention of the chemical makeup. Although the previous section outlines design rules and structural criteria for lifting inversion in an ABX_3-type lattice, designing a real material requires consideration of several other factors such as cation size and valence differences. Of particular importance to perovskites are the octahedral rotations and understanding how the selection of specific chemistries modifies the tendencies to these distortions. To lift inversion using cation ordering, it is sufficient to simply ensure that the A and A' (and/or the B and B') atoms are chemically distinct and that there is a driving force for ordering; achieving the desired octahedral tilt pattern, however, is a more difficult task. Although there are 15 tilt patterns that maintain corner-connectivity, in practice only a few of them are exhibited in nature.[103] In this section, I discuss several chemical factors behind octahedral rotation preferences in perovskites.

One of the most common descriptors used to parameterize the crystal-chemistry of perovskites is the Goldschmidt tolerance factor (τ),[108] which is a measure of how well the A-site cations fit inside the BX_6 octahedral network. I discussed this metric in detail in Chapter 3, and it is given by Equation 3.1. Although the tolerance factor is a simple way to evaluate the stability of a given potential perovskite chemistry and to infer whether it will exhibit octahedral rotations, prediction of the *type* of rotation pattern is much more difficult;[349–353] furthermore, the value of τ below which octahedral rotations appear is not exact and differs greatly across the perovskite family. Typically, one would expect an ordered artificial superlattice of two

different ABX_3 perovskites to exhibit some combination of the octahedral rotation pattern exhibited by the bulk phases,[121,122,338,354,355] allowing for the selection of different chemistries based upon the part of the phase space of Figure 5.12 one is trying to access. For example, octahedral rotation patterns with only out-of-phase rotations occur commonly in the perovskite aluminates, such as $CeAlO_3$ ($a^0a^0c^-$), $PrAlO_3$ ($a^0b^-b^-$), $LaAlO_3$ ($a^-a^-a^-$), and $NdAlO_3$ ($a^-a^-a^-$).[356–359] Indeed, previous work has shown that both solid solutions (made experimentally)[360,361] and ordered heterostructures (investigated using DFT) of these compounds exhibit only out-of-phase rotations.[291] As another example, consider the $a^0a^0c^+$ tilt pattern; although this never occurs in perovskite oxides under standard conditions, it is fairly common in the halides, with $CsSnI_3$, $CsSnBr_3$, $CsDyBr_3$, $RbSnBr_3$, and $CsPbBr_3$ all exhibiting this phase.[362–366] However, while these chemical heuristics are useful for making simple predictions with commonly exhibited tilt patterns, they are of limited help if one is interested in accessing new phases that do not have bulk analogues, such as the $a^0a^0c^+$ tilt pattern in oxides. Furthermore, investigations of this sort have so far been primarily focused on layered heterostructures, such as $(PbTiO_3)_m/(SrTiO_3)_n$[29] (for a more complete review, see Ref. 22); however, as this work shows, expanding to different types of cation arrangements drastically increases the number of potential non-centrosymmetric compounds.

To compare the stability of various tilt patterns to one another, independent of whether they are exhibited in nature, I turn to the global instability index (GII),[114] given by:

$$\mathrm{GII} = \sqrt{\frac{1}{N}\sum_{i=1}^{N} d_i^2}, \tag{5.1}$$

where N is the number of atoms in the asymmetric unit. Here, d_i is known as the "discrepancy factor" and is the difference between the formal oxidation state of an atom and its computed bond valence sum. The closer an atom is to its ideal valence,

the smaller d_i will be, and GII will be minimized; thus, the smaller the value of GII, the more stable a structure is predicted to be. Previous work has shown that the ground state crystal structure of an ABX_3 compound typically has a GII<0.1 and nearly always less than 0.2.[115]

To evaluate the GII, I utilized the computer program SPuDS (Structure Prediction Diagnostic Software) developed by Lufaso and Woodward, who used it to study the stability of a wide variety of tilt patterns in perovskites.[103] By investigating a variety of hypothetical compounds, they showed how this descriptor can be used to predict materials exhibiting rare tilt patterns, such as $a^0b^+b^+$ and $a^0b^+c^-$. In this work, I computed the GII of 137 distinct ABO_3 perovskite oxides in each of 11 tilt patterns (Figure 5.13). These compounds are separated by the element present on the A- and B-site with the magnitude of the GII given by a gradient heat map; the lighter the color, the lower the GII, and the more stable a given octahedral rotation pattern is predicted to be for that perovskite chemistry.

As an example of using this information to search for chemistries capable of accessing new parts of the phase space from Figure 5.12, I look for a perovskite oxide which has a tendency towards the $a^0a^0c^+$ tilt pattern. I found that perovskites containing Ir on the B-site exhibited the smallest average GII for the $a^0a^0c^+$ tilt pattern, while those with B = Ru showed the second smallest. Based on this, I selected $CaIrO_3$, $SrIrO_3$, $CaRuO_3$, and $SrRuO_3$ for further study and computed the GII for each of these compounds (Table 5.3). In all four cases, the GII of the $a^-a^-c^+$ structure was orders of magnitude lower than the $a^0a^0c^+$ phase, indicating a much more stable structure; indeed, each of these compounds displays the orthorhombic $Pnma$ phase in their ground state (although perovskite $CaIrO_3$ is metastable as it thermodynamically adopts a post-perovskite $Cmcm$ phase).[367–369] I next computed the stability of the two tilt patterns in layered $(CaSr)Ir_2O_6$ and $(CaSr)Ru_2O_6$ superlattices using

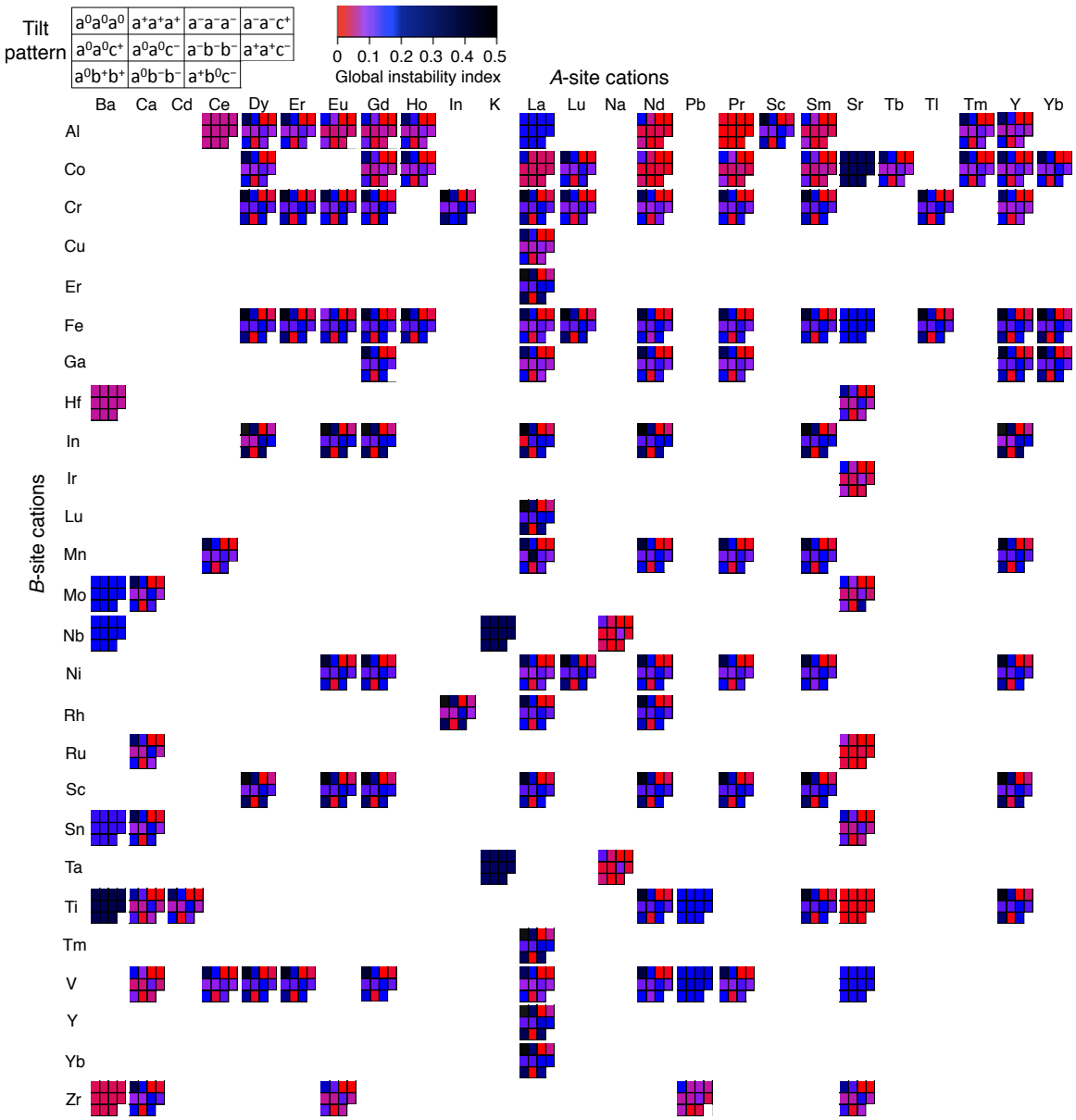

Figure 5.13: The global instability index (GII) of 137 ABO_3 perovskite oxides. The GII of a distinct chemistry in each of 11 octahedral rotation patterns is given by the heat map located at the intersection of a particular A- and B-site cation. Lighter colors indicate a lower GII, and thus a more stable rotation pattern.

Table 5.3: The global instability index (GII) of four bulk ABO_3 perovskites and two layered $(AA')B_2O_6$ superlattices with an $a^0a^0c^+$ and $a^-a^-c^+$ tilt pattern. The energy difference between the two phases for each compound (ΔE, in units of meV per formula unit) was computed using DFT.

Compound	GII, $a^0a^0c^+$ $P4/mbm$	GII, $a^-a^-c^+$ $Pnma$ or $Pmc2_1$	ΔE (meV/f.u.)
$CaIrO_3$	0.0624	0.0073	608.6
$SrIrO_3$	0.0285	0.0001	245.6
$(CaSr)Ir_2O_6$	0.0829	0.0779	277.6
$CaRuO_3$	0.0529	0.0036	400.6
$SrRuO_3$	0.0101	0.0001	156.6
$(CaSr)Ru_2O_6$	0.0791	0.0779	190.9

SPuDS. While the GII of the $a^0a^0c^+$ tilt pattern is not smaller than that of $a^-a^-c^+$ in either of the superlattices, the two values are much closer in the superlattice than in the bulk phases. These values suggest a greater feasibility for the tilts to be stabilized in the cation ordered variants.

To test these predictions, I performed DFT[43] calculations using the Vienna *Ab initio* Simulation Package (`VASP`)[79,80] with projector augmented wave (PAW) pseudopotentials[63] and the PBEsol functional.[54] I used a 5×5×7 and a 7×5×7 Monkhorst-Pack mesh[60] for the $a^0a^0c^+$ and $a^-a^-c^+$ tilt pattern, respectively, and a 650 eV plane-wave cutoff. Finally, I imposed a ferromagnetic ordering of the Ru atoms in $SrRuO_3$ and $(CaSr)Ru_2O_6$, in accordance with their known magnetic properties ($CaRuO_3$ is paramagnetic).[368,370,371] To compare the energetics of the different tilt patterns, I next followed the approach outlined in Ref. 290 by enforcing an $a^0a^0c^+$ and $a^-a^-c^+$ tilt pattern in each of the six compounds and fully relaxing the lattice parameters and internal atomic positions.

In $CaIrO_3$ and $CaRuO_3$, where there is a large difference in the GII of the $a^0a^0c^+$ and $a^-a^-c^+$ phase, the orthorhombic $Pnma$ phase (or $Pmc2_1$ for ordered compounds)

is much more energetically stable (the energy difference between the two phases for each compound is given as ΔE in Table 5.3). When Ca is replaced with Sr, the GII of the two structures become much closer and the energy between them decreases significantly. Finally, when the Ca- and Sr-based compounds are combined into an [001]-ordered superlattice, the GII becomes nearly the same for both tilt patterns. However, their relative energy differences do not decrease; rather, the values are marginally larger than that found for the Sr bulk compounds. These calculations reveal that although the GII is a useful qualitative metric for a structure to favor a given tilt pattern (*i.e.*, it predicts the greater stabilization of the $a^0a^0c^+$ tilt pattern in $SrIrO_3$ and $SrRuO_3$ over $CaIrO_3$ and $CaRuO_3$), using it alone as an absolute predictor for phase stability could be misleading.

Finally, I note that while using this type of design strategy to select a chemistry for an ordered compound may induce the desired tilt pattern, there is no guarantee that the cations will order or the material will remain insulating (a prerequisite for many dielectric applications). In bulk perovskite oxides, the structural and chemical factors required for the stabilization of various ordering patterns are well known.[116] B-site ordering is much more common than A-site ordering in perovskites; it requires a large difference in oxidation state between B and B' (> 2) and typically orders in the rock salt pattern, which provides the maximum separation between the highly charged cations. For A-sites, a size differential is the stabilizing factor; here, the layered ordering is the most common as it is preferred given an A and A' size mismatch. Additionally, layered A-site ordering is stabilized by rock salt B-site ordering, making this combination extremely common in double perovskites. Recent advances in kinetically controlled growth techniques such as molecular beam epitaxy,[33,34] however, have opened the door towards more purposeful cation ordering; various types of ordering can be induced simply by growth on an [001]-, [110]-, or [111]-oriented

substrate. By combining an understanding of the chemical factors stabilizing various octahedral tilt patterns and ways to induce *A*- or *B*-site cation ordering, it is my hope that a wide variety of new non-centrosymmetric perovskite materials can be synthesized and investigated. This will be the focus of the remaining chapters of this thesis.

6. DESIGN AND INVESTIGATION OF NEW FERROELECTRIC MATERIALS

In this chapter, I show how the chemistry-independent models for inversion symmetry breaking put forth in the previous chapter can be applied for the intelligent design of new ferroelectric and piezoelectric materials. As discussed in the previous chapters, earlier efforts on A-site ordered double perovskites of the form $(AA')B_2O_6$ established some design guidelines for the flavors of octahedral rotations[288] that can produce large electric polarizations and small ferroelectric switching barriers when the A and A' cations alternate along the [001]-direction.[287] The [001] ordered arrangement is particularly attractive because (i) it is the one most conducive to layer-by-layer growth methods of artificial oxides,[372] since the geometry is equivalent to an ultra-short period perovskite superlattice, *i.e.* $(ABO_3)/(A'BO_3)$, and (ii) the frequently observed orthorhombic $a^-a^-c^+$ rotation pattern fulfills the necessary symmetry and energetic criteria outlined to produce this type of rotation-induced ferroelectricity. Owing to the directional control of cation order through advanced solid-state synthetic chemistry methods[116,373] and the accessibility of perovskite substrates with [110] and [111] surface terminations, these previous observations lead to the main questions of this chapter: How do the alternative cation ordering schemes and octahedral rotation patterns capable of lifting inversion symmetry identified in Chapter 3 affect the structure and properties, and can they be harnessed to create new non-centrosymmetric materials?

To answer this, I performed three different computational studies on ferroelectric perovskite oxides, which span several different areas of the phase space summarized in Figure 5.12. First, I consider A-site ordering only, combined with three cation ordering schemes and a mixed $a^-a^-c^+$ tilt pattern, allowing for the disentanglement

of the influence of cation ordering while holding the rotation pattern constant. Second, I look at one A-site cation ordering scheme, but two out-of-plane only tilt patterns ($a^0b^-b^-$ and $a^-a^-a^-$) and investigate the effect of changing the octahedral rotation pattern. Finally, I combine both layered A-site and rock salt B-site ordering and a mixed $a^-a^-c^+$ tilt pattern and examine the effect of chemical substitution on the ferroelectric properties. These results, published as Refs. 21, 291 and 348, show how the simple crystallographic and chemical models of the previous chapter can be harnessed to design a wide variety of new materials.

6.1 Computational Methods

All investigations were performed by employing density functional theory[43] using projector augmented-wave potentials[63] within PBEsol[54] as implemented in the Vienna *ab-initio* Simulation Package (`VASP`).[79,80] For the gallate, zirconate, and hafnate bulk compounds, I fully relaxed the lattice parameters and internal atomic positions of the known *Pnma* ground state ($a^-a^-c^+$ Glazer tilt pattern) using a 7×7×7 Monkhorst-Pack k-point mesh and a 600 eV plane wave cutoff. The valence electron configurations used were as follows: $5s^25p^65d^16s^2$ for La, $5s^25p^64f^16s^2$ for Nd, $3p^64s^2$ for Ca, $4s^24p^65s^2$ for Sr, $4s^24p^1$ for Ga, $5s^24d^2$ for Zr, $5p^36s^1$ for Hf, and $2s^22p^4$ for O. I next assembled nine superlattices from these bulk compounds. To ensure the correct ground state, I first computed the force constants of each superlattice using density functional perturbation theory[77] with a plane-wave cutoff of 800 eV; from this, the post-processing tool *phonopy*[374] was used to generate the phonon band structures. I then used linear combinations of the unstable modes found to add atomic displacements, resulting in 15 candidate structures for each ordered superlattice. I then performed a full relaxation using a plane-wave cutoff of 550 eV and a 5×5×5 Monkhorst-Pack k-point mesh, including the lattice and atomic degrees of freedom,

on each to determine the ground state. The total polarization was then calculated using the Berry phase method[153,155] as implemented in `VASP`.

The same procedure was then followed for the aluminate compounds. A plane-wave cutoff of 550 eV and a 5×5×5 Monkhorst-Pack mesh[60] were used during the structural relaxations. The valence electron configurations used were as follows: $5s^2 5p^6 5d^1 6s^2$ for La, $5s^2 5p^6 4f^1 6s^2$ for Nd, $5s^2 5p^6 6s^2 5d^1$ for Pr, $5s^2 5p^6 5d^1 6s^2$ for Ce, $3s^2 3p^1$ for Al, and $2s^2 2p^4$ for O. I note here that DFT calculations on Ce-based compounds often treat the $4f$ electron explicitly, while also including a Hubbard U correction of 6-10 eV on those states. Here I specifically chose a Ce PAW which does not include the $4f$ states, instead placing these electrons in the core to eliminate the need for any adjustable U parameters in the calculations. The piezoelectric, elastic, and Born effective charge tensors of the aluminates were computed within density functional perturbation theory[375,376] using an increased 800 eV plane wave cutoff.

For the double perovskites, all nine compounds were initially fixed to the experimentally determined (NaLa)(MnW)O_6 $P2_1$ structure, followed by a relaxation of the lattice parameters and internal atomic positions. A plane-wave cutoff of 550 eV and a 2×4×1 Monkhorst-Pack mesh was used during the structural relaxations. The valence electron configurations used were as follows: $3s^1$ for Na, $3s^2 3p^6 4s^1$ for K, $4s^2 4p^6 5s^1$ for Rb, $5s^2 5p^6 5d^1 6s^2$ for La, $5s^2 5p^6 4f^1 6s^2$ for Nd, $4s^2 4p^6 4d^2 5s^1$ for Y, $3p^6 4s^1$ for Mn, $5d^5 4s^1$ for W, and $2s^2 2p^4$ for O. I applied a Hubbard U correction of 4 eV using the Dudarev formalism[81] to treat the correlated Mn $3d$ states, as well as an antiferromagnetic collinear spin ordering. The electric polarizations were, as before, computed using the Berry phase method.

All mode decompositions were performed using the ISODISTORT tool of the ISOTROPY software suite,[82] while graphical rendering of the crystal structures was performed using VESTA.[83]

6.2 Effect of Cation Ordering on Ferroelectric Properties

6.2.1 Ground State Structures and Energetics

To address one of the main questions of this chapter and illustrate the design process for realizing new polar oxides based on coupling cation order and octahedral rotations, I first investigated [001]-, [111]-, and [110]-type A-site ordering within an orthorhombic $a^-a^-c^+$ tilt pattern. I first determined the ground state crystal structures of six non-polar perovskite dielectrics (which were selected because they are band insulators and never exhibit polar ground states) from which I will create the ordered double perovskites: $LaGaO_3$, $NdGaO_3$, $SrZrO_3$, $CaZrO_3$, $SrHfO_3$, and $CaHfO_3$. Each adopts the $a^-a^-c^+$ mixed-tilt system (space group $Pnma$) previously determined[288] necessary for the octahedral rotations to break inversion symmetry in the presence of [001] A cation order. The magnitude of out-of-phase $a^-a^-b^0$ (θ_{xy}) and in-phase $a^0a^0c^+$ (θ_z) tilting each compound exhibits are summarized in Table 6.11 as defined in Ref. 36. Consistent with the available experimental results for the gallates,[377,378] these structures exhibit sizable displacements (δ_{xy}) of the A cations from their high symmetry positions in the xy-plane with Nd more so than La due to its smaller size as reflected by its smaller tolerance factor (τ).[108] The same is true in the zirconates and hafnates with Ca displacing more than Sr. These features are critical to rotation-induced ferroelectrics because, as discussed in Chapter 5, the spontaneous polarization largely arises from the non-zero canceling of AO layer dipoles.[287]

I next used these bulk perovskites as components to assemble ordered double perovskites with continuous B cation sublattices as $(LaNd)Ga_2O_6$, $(SrCa)Zr_2O_6$, and $(SrCa)Hf_2O_6$. The A cation ordering is taken along the [001], [111], or [110] crystallographic directions (relative to the pseudocubic perovskite directions) as discussed in Chapter 3 (Figure 3.3a, b, c) without changing the composition.

The lowest energy ground state structures are obtained using density functional

Table 6.1: Summary of calculated structural parameters for the orthorhombically distorted perovskites. The tolerance factor (τ) is calculated using bond lengths obtained from the bond valence model.[103] Tilt and rotation angles are defined following the convention given in Ref. 36. δ_{xy} is a measure of the planar A cation displacements relative to the aristotype cubic perovskite.

Bulk phase	τ	θ_{xy} (deg.)	θ_z (deg.)	δ_{xy}(Å)
$LaGaO_3$	0.956	12.6	6.96	0.168
$NdGaO_3$	0.936	15.5	10.3	0.299
$SrZrO_3$	0.942	13.4	8.59	0.207
$CaZrO_3$	0.891	18.9	11.3	0.317
$SrHfO_3$	0.949	11.7	7.15	0.157
$CaHfO_3$	0.897	17.4	10.7	0.289

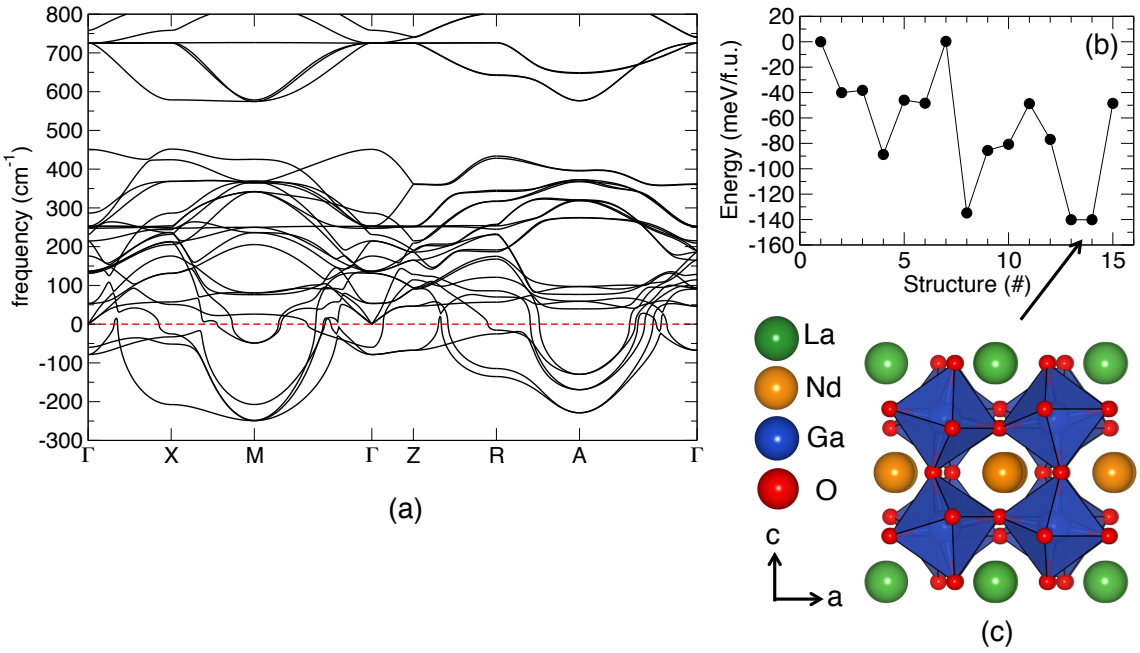

Figure 6.1: (a) The calculated phonon band structure of layered $(LaNd)Ga_2O_6$ along the $\Gamma(0,0,0)$–$X(\frac{1}{2},0,0)$–$M(\frac{1}{2},\frac{1}{2},0)$–$\Gamma(0,0,0)$–$Z(0,0,\frac{1}{2})$–$R(0,\frac{1}{2},\frac{1}{2})$–$A(\frac{1}{2},\frac{1}{2},\frac{1}{2})$–$\Gamma(0,0,0)$ band path throughout the Brillouin zone. (b) Total energy (taken with respect to the cubic undistorted phase, structure 1) for $(LaNd)Ga_2O_6$ with different combinations of unstable modes. (c) Ground state (lowest energy) structure of $(LaNd)Ga_2O_6$.

calculations with the PBEsol exchange-correlation functional through a symmetry-restricted soft-phonon search (*cf.* Computational Methods, Section 6.1). An example of this technique as applied to (LaNd)Ga_2O_6 is shown in Figure 6.1. Unstable modes in the phonon band structure (Figure 6.1a) are combined, and the total energy of that configuration is compared to all others normalized to the number of formula units (meV/f.u., Figure 6.1b); the lowest energy structure is taken to be the ground state (Figure 6.1c). The ground state crystal structures for all nine superlattices are tabulated in Appendix A, Tables A.1 to A.9. For all compositions explored, the space groups adopted by the layered, rock salt, and columnar orderings are the polar $Pmc2_1$ (space group no. 26) and $Pmn2_1$ (31), and non-polar $P2_1/m$ (11), respectively. Each structure contains A cation displacements within the xy-plane and the $a^-a^-c^+$ BO_6 tilt pattern, consistent with the preferred bulk tilt patterns. The low symmetry phases also show substantial energy gains relative to the high-symmetry configurations (Table 6.2), largely from the octahedral rotations.

A group theoretical analysis[82] of the atomic displacements in terms of symmetry-modes involved in the structural transition (referenced relative to a disordered A cation (5-atom) cubic perovskite[287]) reveals three main modes are present in the ground state structure: M_3^+ (describing in-phase rotations), R_4^+ (out-of-phase rotations), and X_5^+ (anti-polar A-site displacements). There is a small secondary, symmetry-allowed distortion for the polar structures (Γ_4^-), which lifts inversion symmetry and produces the ionic contribution to the electric polarizations described later (Table S4). Note that the presence of layered or rock salt cation order and the superposition of $M_3^+ \oplus R_4^+$, which describes the $a^-a^-c^+$ tilt system, are sufficient to lift inversion symmetry in the absence of any polar atomic displacements.

In all configurations, the M_3^+ and R_4^+ modes describing the octahedral rotations significantly lower the energy relative to the high-symmetry paraelectric structure,

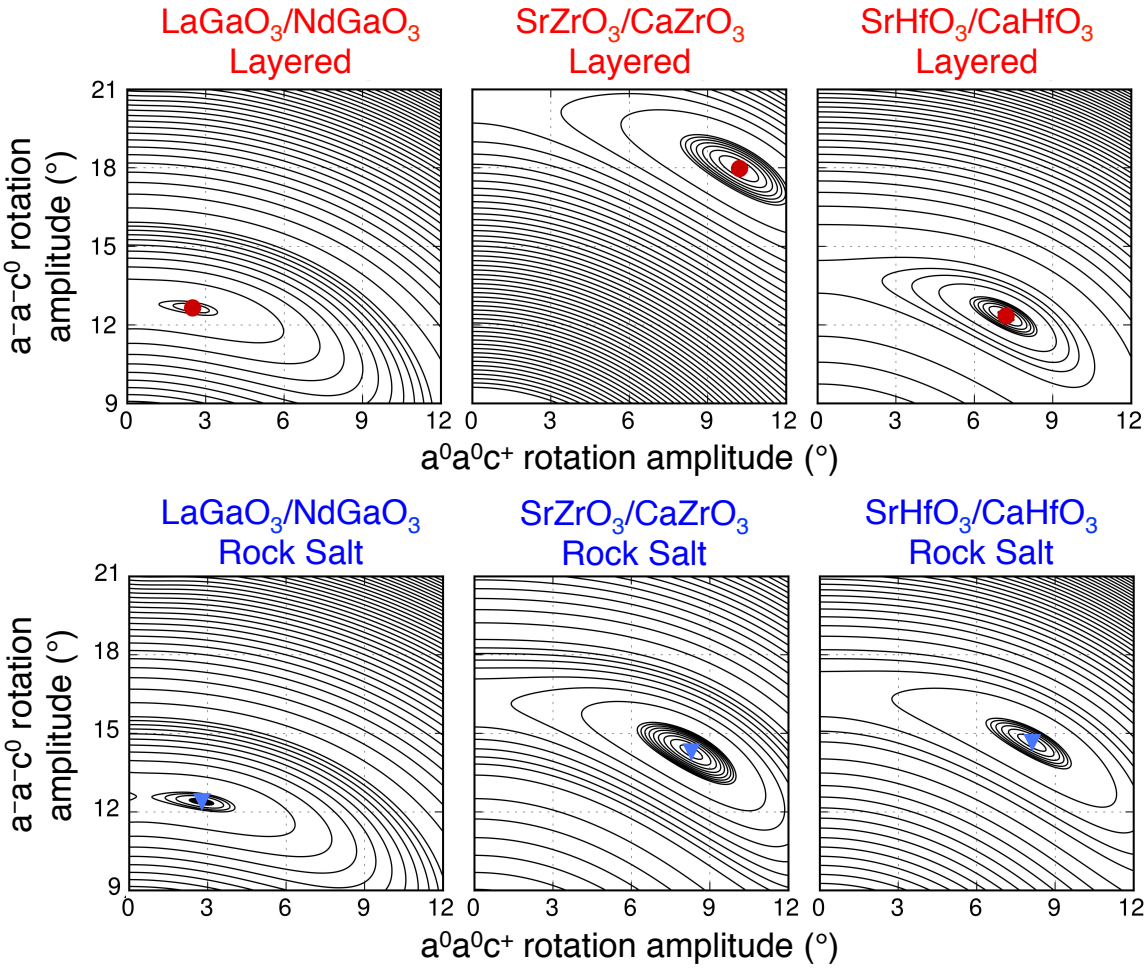

Figure 6.2: The calculated two-dimensional energy surface contours for the $(AA')B_2O_6$ perovskites with respect to the amplitude of the out-of-phase (abscissa) and in-phase (ordinate) rotation angles. For all compositions, the layered and rock salt ordering have energy minima located at non-zero values of the $a^0a^0c^+$ and $a^-a^-c^0$ tilt patterns, indicating the microscopic driving force for inversion symmetry breaking originates from the octahedral rotations.

Table 6.2: Summary of atomic and electronic ground state properties of the ordered $(AA')B_2O_6$ perovskites. The energy stability (ΔE_0) is given relative to the fully relaxed high-symmetry reference phase without octahedral distortions. ΔE_R gives the relative energy difference for the ground state structures within a single composition. Positive values indicate higher energy configurations; energy differences are given in units of meV/f.u. The '—' indicates the polarization P is required to be zero by symmetry.

Structure	Ordering	S.G.	ΔE_0	ΔE_R	P (μC/cm^2)
(LaNd)Ga_2O_6	Layered	$Pmc2_1$	-498.0	0.839	5.22
	Rock Salt	$Pmn2_1$	-951.7	0	1.78
	Columnar	$P2_1/m$	-939.3	6.708	—
(SrCa)Zr_2O_6	Layered	$Pmc2_1$	-1306	6.118	3.61
	Rock Salt	$Pmn2_1$	-1364	0	2.84
	Columnar	$P2_1/m$	-1301	17.05	—
(SrCa)Hf_2O_6	Layered	$Pmc2_1$	-983.0	9.419	3.09
	Rock Salt	$Pmn2_1$	-1025	0	2.29
	Columnar	$P2_1/m$	-1002	19.14	—

e.g., in rock salt (LaNd)Ga_2O_6 the gains are 394 meV/f.u. for M_3^+ and 761 meV/f.u. for R_4^+. The X_5^+ mode marginally lowers or increases the total energy independent of the other modes. Furthermore, the combination of in-phase and out-of-phase rotations is found to *cooperatively* lower the energy of each system—more so than each octahedral rotation mode individually—indicating the phenomenological origin for the polarization is through a hybrid improper ferroelectric mechanism (Figure 6.2).

The energy minima are deeper for (SrCa)Zr_2O_6 and (SrCa)Hf_2O_6 than that for (LaNd)Ga_2O_6 (Figure 6.2). Also, the energy minima in the (SrCa)-ordered compounds appear at larger rotation angles than (LaNd)Ga_2O_6. This is consistent with the tolerance factors presented in Table 6.11; a smaller tolerance factor results in larger octahedral rotations and typically a deeper minimum. From these observations, I infer that (SrCa)Zr_2O_6 and (SrCa)Hf_2O_6 are likely to exhibit higher ferroelectric switching barriers than (LaNd)Ga_2O_6, as changing the direction of the polarization

in these types of materials involves a complete change in sense of one of the BO_6 octahedral rotation patterns. This is also in agreement with previous results showing that the ferroelectric switching barrier decreases with increasing average tolerance factor.[287]

I now examine the stability and energetic trends of each A cation order for a given chemistry. In every case, the rock salt ordering is more stable than the other A cation ordering schemes in the structurally distorted phases containing octahedral rotations, followed by the layered and then columnar arrangements (ΔE_0, Table 6.2). In the paraelectric phases, however, the layered ordering is the lowest in energy, which is followed by columnar and then rock salt (highest energy). To explain this behavior, I examined the Coulombic contribution to the structure stability by calculating lattice sums at a fixed geometric configuration and varying the charge of the cations from A^{3+}/A^{3+} (B^{3+}) to A^{2+}/A^{2+} (B^{4+}). These combinations correspond to the (LaNd)Ga_2O_6 and (SrCa)Zr_2O_6 (or (SrCa)Hf_2O_6) structures, respectively. When calculated in this way, the Madelung energy of the rock salt structure is lower than the layered structure regardless of the valence state of the cations. This is true in both the paraelectric and polar ground state structures, contrary to the DFT results, which only finds this to be the case in the low-symmetry distorted structures.

This discrepancy can be understood using Pauling's fifth rule of parsimony, which states that it is most favorable for each ion to be in similar environments. Because the paraelectric rock salt structure offers slightly more homogeneous surroundings than the layered or columnar structures (as the A and A' atoms coordinate the anions in a *trans* rather than *cis* fashion), it minimizes the energetic penalties of cation order. Once the crystal symmetry is enforced, however, the paraelectric layered and columnar structures ($P4/mmm$) become lower in energy than the rock salt structure ($Fm\bar{3}m$), because the $P4/mmm$ space group allows for oxygen displacements, while

the $Fm\bar{3}m$ does not, *i.e.*, the oxygen atoms lie on inversion centers.[116] Therefore, the oxygen atoms in the layered and columnar structures can shift in response to the A/A' size differential, while the atoms in the rock salt structure cannot, resulting in an energetic cost.

In the polar layered and rock salt structures, there are no inversion centers owing to the combination of octahedral rotations and cation order. As a result, the A-sites and oxygen atoms are free to move to maximize the Coulombic energy and minimize any repulsive interactions, which results in an enhanced covalency of (A/A')–O bonds. For the same reasons mentioned previously, this lowers the energy of the rock salt ordered compound below that of the layered. The columnar structure is now highest in energy because its distorted structure (space group $P2_1/m$) does not allow for these same energy-lowering polar displacements.

6.2.2 Spontaneous Polarization and Ferroelectric Properties

Using the modern theory of polarization,[153,155] I calculated the electric polarization for the six compositions that exhibit a non-zero polarization in their ground state (P, Table 6.2). For each polar structure, the electric polarization is constrained by symmetry to the [100] direction orthogonal to the in-phase rotation axis. At a fixed composition, the layered A cation order always gives the highest electric polarization followed by the rock salt arrangement, which ranges from 30 to 80% lower in magnitude.

To understand this behavior, I examine the local atomic displacements of the A and A' cations that connect the high-symmetry phases to the low-symmetry ground state crystal structures. Indeed, there is a non-trivial influence of the ordering on the magnitude and direction of the cation displacements (Figure 6.3). Each ordered structure can be thought of as having either columns of A and A' atoms (or combinations

thereof) along the [001]-direction parallel to the axis about which the GaO_6 octahedra rotate in-phase [Figure 6.3a-c]. Based on the specific atomic scale ordering, these columns are either mixed (containing both A and A') or chemically homogeneous. Moving along this direction, the A cations are found to alternate their displacements in the perpendicular direction along [001].

The fact that the A and A' atoms in each chemically heterogeneous column displace by different amounts (owing to ionic size, mass, and covalent bond optimization requirements) yields the net macroscopic electric polarizations in the layered and rock salt structures (*cf.* Table 6.2). Thus, the same atomic displacements that stabilize the rock salt and layered structures produce the spontaneous electric polarizations. Using an ionic charge model and layer polarizations only, this estimate is within 85% of the DFT result, indicating there is not a substantial change in the bonding charge density and the polar A cation displacements are not driven by chemical bond formation or SOJT-activity. These features are characteristic of hybrid improper ferroelectrics.[287] Interestingly, in both the layered and rock salt arrangements, the electric dipoles are constrained to planes but oriented in opposite directions, making these cation ordered polar perovskites the electric analogues to ferrimagents, *i.e.* ferr*i*electrics.[379] In the columnar ordering, each column is made up of chemically equivalent atoms; therefore, the displacement amplitudes are identical and there is no net polarization.

In each configuration explored, atoms contained in the $(A/A')O_2$ plane orthogonal to the direction of in-phase rotations displace, regardless of the chemical species that comprise that plane. Critically, if the direction of the [001]-ordering in the layered structure is no longer collinear with the in-phase octahedral rotation axis, the electric polarization goes to zero. If the direction of in-phase rotations lies in the same plane as the ordered layers, then each "column" of A-sites is made up of chemically identical atoms, resulting in zero polarization as in the columnar arrangement. This

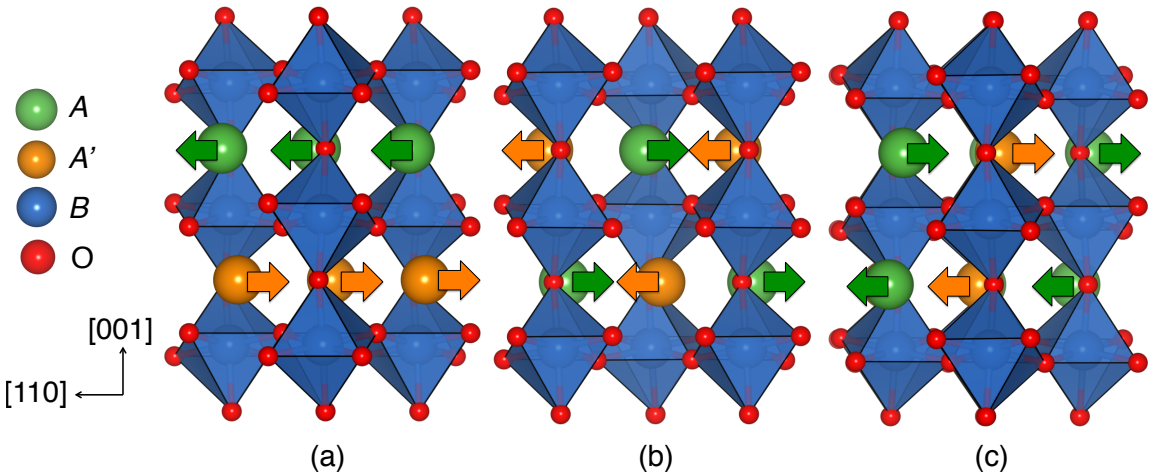

Figure 6.3: Ground state crystal structures of the (a) [001] (layered), (b) [111] (rock salt), and (c) [110] (columnar) atomically ordered $(AA')B_2O_6$ superlattices. The A-site cations displace in the plane orthogonal to the in-phase rotation axis [001].

effect manifests in the crystal symmetry, whereby the polar $Pmc2_1$ would transform to a centrosymmetric $P2_1/m$ space group if the in-phase rotation axis occurs in the [100]-direction, while the layered ordering is maintained along [001]. My calculations on the energetic stability of this layered $P2_1/m$ structure in $(LaNd)Ga_2O_6$ show that the non-polar structure is only ∼0.89 meV/f.u. higher in energy than the polar structure. The fact that these two structures are essentially degenerate could result in the formation of $Pmc2_1$–$P2_1/m$ domains during synthesis, leading to a diminished ferroelectric polarization. Such microstructures have been previously reported in the growth of layered perovskite superlattice thin-films.[380,381]

6.3 Effect of Tilt Pattern on Inversion Symmetry Breaking

The fact that the polarization of the compounds in the previous section arises from a trilinear coupling of two octahedral rotation types ($a^-a^-c^0$ and $a^0a^0c^+$) and a polar mode leads to an often overlooked problem: mode condensation. There is the real possibility that the two rotational modes condense at different temperatures, leading

to a staggered paraelectric to ferroelectric phase transition. Although an avalanche transition (in which the modes condense at the same temperature) is possible in ferroelectric oxides,[202] non-avalanche transitions are also likely to occur.[203] This makes it difficult to predict whether or not there will be two phase transitions from the paraelectric to ferroelectric state in the material without detailed and careful experimental study. However, it is possible to avoid this problem if the spontaneous polarization is induced by only a single rotational mode, making such materials improper (*i.e.* Type A, following the classification introduced in Chapter 5) rather than hybrid improper ferroelectrics (Type AA). Materials of this nature could find use in high-temperature electronic applications such as sensors.[382]

The symmetry analysis-based model I put forth in Chapter 5 reveals that although both in-phase and out-of-phase rotations break inversion symmetry in the layered and rock salt ordered structures, only out-of-phase rotations are required in the rock salt structure. As discussed previously, this is because the ligands comprising the BO_6 octahedron and AO_{12} cuboctahedron in the perovskite structure are formed by the same oxygen atoms; therefore, the rotation of the BO_6 octahedra described by a Glazer tilt system will simultaneously distort the A-site cation coordination topology. The cation ordering scheme must then cooperatively align the now acentric AO_x polyhedra so as to lift inversion symmetry; in the case of tilt patterns with only out-of-phase rotations, the rock salt structure can achieve this while the layered order can not (Figure 5.11). In this section, I investigate materials with a propensity to such tilt patterns and verify that this symmetry analysis holds in real materials.

6.3.1 Bulk Rare Earth Aluminate Ground States

I first determined the ground state structures of four non-polar aluminate dielectrics which contain only out-of-phase AlO_6 octahedral rotations: $LaAlO_3$, $NdAlO_3$,

Table 6.3: Structural details of the bulk aluminate superlattice constituents. Each has a centrosymmetric space group (S.G.) and only out-of-phase rotations about one, two, or three axes; the magnitude of these are given by Θ and determined by measuring the Al-O-Al bond angle θ, $\Theta = (180^\circ - \theta)/2$. The tolerance factor[108] (τ) is computed using bond lengths obtained from the bond valence model.[103] The calculated lattice parameters (in Å) and rotational angle (in degrees) are compared to experimental (Exp.) data (*cf.* text for references).

Compound	S.G.	Tilt	τ	Theory	Exp.
$LaAlO_3$	$R\bar{3}c$	$a^-a^-a^-$	0.995	$a = 5.357$	$a = 5.359$
				$c = 13.22$	c = 13.08
				$\Theta = 5.8$	$\Theta = 5.5$
$NdAlO_3$	$R\bar{3}c$	$a^-a^-a^-$	0.975	$a = 5.325$	$a = 5.333$
				$c = 12.85$	c = 12.98
				$\Theta = 8.4$	$\Theta = 9.4$
$PrAlO_3$	$Imma$	$a^0b^-b^-$	0.982	$a = 5.351$	$a = 5.339$
				$b = 7.504$	$b = 7.494$
				$c = 5.303$	$c = 5.291$
				$\Theta = 8.9$	$\Theta = 9.4$
$CeAlO_3$	$I4/mcm$	$a^0a^0c^-$	0.988	$a = 5.326$	$a = 5.309$
				$c = 7.591$	$c = 7.599$
				$\Theta = 7.2$	$\Theta = 8.1$

$PrAlO_3$, and $CeAlO_3$. The computationally and experimentally determined space groups, lattice constants, and octahedral rotation angles and tilt patterns are summarized in Table 7.1. I find that $LaAlO_3$ and $NdAlO_3$ both exhibit the $a^-a^-a^-$ tilt pattern (space group $R\bar{3}c$), in agreement with experimental results.[356,357] Next, I find that $PrAlO_3$ exhibits the $a^0b^-b^-$ tilt pattern (space group $Imma$) in its ground state. Although this compound is found to exhibit space group $C2/m$ with an $a^0b^-c^-$ tilt pattern at low temperatures experimentally, I find this phase is 10 meV per formula unit (f.u.) higher in energy than the $Imma$ phase; however, $PrAlO_3$ is known to undergo a continuous phase transition to $Imma$ at 150 K.[358] Finally, I find that $CeAlO_3$ displays the $a^0a^0c^-$ tilt pattern (space group $I4/mcm$), which is consistent with the experimentally known low-temperature structure.[383]

6.3.2 *A*-Cation Ordered Ground State Structures

I next ordered $LaAlO_3$ with both $NdAlO_3$ and $PrAlO_3$ along the cubic [111] direction to form two rock salt double perovskites: $(LaNd)Al_2O_6$ and $(LaPr)Al_2O_6$. $CeAlO_3$ and $PrAlO_3$ were ordered in the same way resulting in a third superlattice: $(CePr)Al_2O_6$. By employing the same type of symmetry-restricted soft-phonon search described in the previous section, I determined the ground state structures of each compound, which are summarized in Table 6.4. The full ground state crystal structures are tabulated in Appendix A, Tables A.10 to A.12. Although I found that [001]-ordering is slightly more energetically favorable in these compounds than [111] (between 1 to 6 meV lower in energy), I only considered the rock salt order for further investigation due to the fact that it lifts inversion while the layered structures remain centrosymmetric. All three ordered aluminates exhibit only out-of-phase rotations, which in combination with the [111]-cation ordering results in non-centrosymmetric (chiral or polar) space groups. However, only $(LaPr)Al_2O_6$ and $(CePr)Al_2O_6$ display a spontaneous polarization, as they are polar ($Imm2$), where as $(LaNd)Al_2O_6$ is chiral and non-polar.

I now carry out a detailed examination of each compound's atomic structure to understand the origin for the non-centrosymmetric symmetries, the different space groups adopted, and the microscopic mechanism for the emergence of an electric polarization from the combination of two bulk non-polar dielectrics. In its ground state, $(LaNd)Al_2O_6$ displays an $a^-a^-a^-$ tilt pattern, which is similar to its two bulk ABO_3 constituents, and the $R32$ space group. The distortion relating the undistorted structure to the ground state transforms as a single irreducible representation (irrep), R_4^+, of the undistorted 5-atom $Pm\bar{3}m$, which describes collective oxygen displacements that produce out-of-phase rotations along each Cartesian axis. This may be equivalently described as a single out-of-phase rotation about the trigonal (3-fold) axis of

Table 6.4: Structural details and ferroelectric properties of the [111]-ordered perovskite aluminates computed from DFT-PBEsol. All compounds exhibit out-of-phase rotations in their ground states with the rotation magnitude and electric polarization specified by Θ (degrees) and P (μC/cm^2), respectively.

Compound (τ)	S.G.	Tilt	Lattice Parameters (Å)	Θ	P
$(LaNd)Al_2O_6$ (0.985)	$R32$	$a^-a^-a^-$	$a = 5.338$ $b = 5.338$ $c = 12.96$	7.6	0
$(LaPr)Al_2O_6$ (0.988)	$Imm2$	$a^0b^-b^-$	$a = 7.523$ $b = 5.355$ $c = 5.322$	6.9	1.80
$(CePr)Al_2O_6$ (0.985)	$Imm2$	$a^0b^-b^-$	$a = 7.560$ $b = 5.399$ $c = 5.364$	6.7	1.78

the structure.

As discussed in Chapter 4, the Landau theory of displacive phase transitions allows for the free energy of a system to be expanded in terms of an order parameter; in these superlattices, the order parameter best capturing the symmetry reduction from the cubic to antiferrodistortive phase is the AlO_6 octahedral rotation angle (given by Θ in 6.4), which can be mapped onto the amplitude of the zone-boundary mode R_4^+. This permits me to write a free energy expression for $(LaNd)Al_2O_6$ as

$$\mathcal{F} = \alpha_1 Q_{R_4^+}^2 + \beta_1 Q_{R_4^+}^4 \,, \tag{6.1}$$

with coefficients obtained from fits to the DFT computed mode amplitude–energy plots (Table 6.5).

This compound has a polarization of zero, despite the fact that it exhibits a non-centrosymmetric space group, owing to the chiral structure. The out-of-phase rotations along all three crystallographic axes (in addition to rock salt ordering)

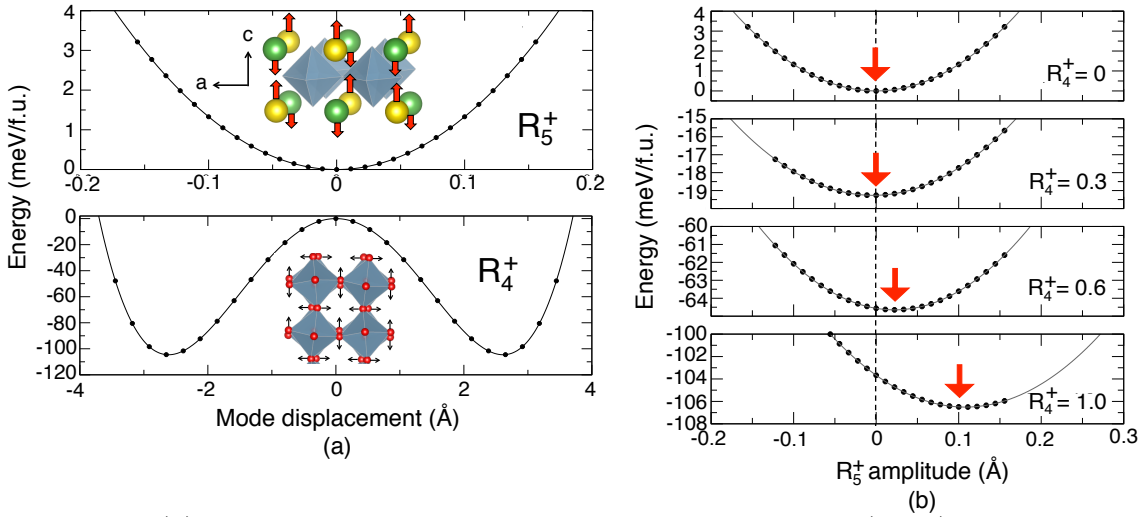

Figure 6.4: (a) Energy as a function of atomic displacements (inset) described by the R_5^+ (upper) and R_4^+ (lower) modes in $(LaPr)Al_2O_6$. (b) The coupling of R_4^+ with R_5^+ results in a cooperative lowering of the total energy, stabilizing the non-centrosymmetric structure (gray lines obtained from a fit of the Landau potential, see text). Note that there exists an equivalent energy minimum at $R_5^+ \simeq -0.1$ for R_4^+ imposed with opposite sense (negative mode amplitude).

removes all possibility for mirror symmetry but is compatible with 3-fold and 2-fold rotation axes. As discussed in the previous section, it is the anti-polar displacements of the different A-site cations which results in the electric polarization (a ferr*i*electric type mechanism) in hybrid improper ferroelectrics.[287] However, although out-of-phase rotations alone can lift inversion symmetry in [111]-ordered superlattices, the A-site atoms cannot displace perpendicular to any direction which contain out-of-phase rotations. These features make the compound chiral and nonpolar. Indeed, in the $R32$ space group, the A and A' cations occupy the $3a$ and $3b$ Wyckoff positions, both of which exhibit site symmetry 32. This symmetry constraint suggests that out-of-phase rotations along one or two directions could be compatible with mirror planes in [111] A-site ordered perovskites since those directions without any rotations would serve as unique anisotropic axes for which a loci of points defining the reflection plane may exist.

I next investigate ordered aluminates which contain out-of-phase rotations along only two crystallographic axes. Because the bulk phases of the constituents in $(LaPr)Al_2O_6$ and $(CePr)Al_2O_6$ superlattices display different octahedral rotation patterns (Table 7.1), there is a competition between having out-of-phase rotations along one, two, or three axes. I find that the ground state structures of both A-site ordered aluminates exhibit the $a^0b^-b^-$ rotational pattern with the polar $Imm2$ space group. This rotation pattern allows for displacements of the A-sites, resulting in small electric polarizations of $1.80\,\mu C/cm^2$ in $(LaPr)Al_2O_6$ and $1.78\,\mu C/cm^2$ in $(CePr)Al_2O_6$.

Unlike $(LaNd)Al_2O_6$, the symmetry of these polar ground state structures requires two irreps for a complete description: Q_1, which describes the out-of-phase rotations and transforms like the irrep R_4^+ (identical to that in $(LaNd)Al_2O_6$), *and* Q_2, which describes A-site displacements and transforms like R_5^+ [see insets in Figure 6.4a]. Both irreps are given relative to the $Pm\bar{3}m$ 5-atom perovskite. Figure 6.4a shows the evolution of the total energy of $(LaNd)Al_2O_6$ with respect to increasing amplitude of these two modes. I find that while R_4^+ is a soft mode (negative quadratic-like curvature about the origin) and results in a large gain, R_5^+ alone leads to an energy penalty (positive curvature). On the other hand, when the two modes coexist [Figure 6.4b], I find that with increasing amplitude of the nominally hard R_5^+ mode any non-zero amplitude of the non-polar out-of-phase rotations (R_4^+) leads to increased stability of the $Imm2$ $(LaNd)Al_2O_6$ structure without a change in curvature of the energy surface. This behavior is similar to that seen in the improper ferroelectric $YMnO_3$,[228] whereby a non-polar mode also stabilizes a hard polar mode with non-zero amplitude. The free energy evolution of $(CePr)Al_2O_6$ exhibits identical behavior.

To understand the anharmonic lattice interactions which provide the stability of

Table 6.5: Free energy expansion coefficients in Equation 6.2 for each [111]-ordered A-site perovskite aluminate.

Coefficient	$(LaNd)Al_2O_6$	$(LaPr)Al_2O_6$	$(CePr)Al_2O_6$
α_1 (meV/Å^2)	-8.130	-30.61	-33.98
α_2 (meV/Å^2)	–	132.9	133.1
β_1 (meV/Å^4)	0.139	2.239	2.433
β_2 (meV/Å^4)	–	1.295	8.967
γ_1 (meV/Å^4)	–	-3.299	-4.085
γ_2 (meV/Å^4)	–	245.2	217.9
δ (meV/Å^4)	–	33.48	33.37

the polar phase, I expand the free energy (with respect to $Pm\bar{3}m$) as

$$\begin{aligned} \mathcal{F} &= \alpha_1 Q_{R_4^+}^2 + \alpha_2 Q_{R_5^+}^2 + \beta_1 Q_{R_4^+}^4 + \beta_2 Q_{R_5^+}^4 \\ &+ \gamma_1 Q_{R_4^+}^3 Q_{R_5^+} + \gamma_2 Q_{R_4^+} Q_{R_5^+}^3 + \delta Q_{R_5^+}^2 Q_{R_4^+}^2 \,. \end{aligned} \tag{6.2}$$

By fitting the free energy expression truncated to quartic order to the calculated total energies in Figure 6.4b, the coefficients in Equation 6.2 are obtained (Table 6.5). I find that the most important anharmonic term coupling $Q_{R_4^+}$ to $Q_{R_5^+}$ is given by $\gamma_1 Q_{R_4^+}^3 Q_{R_5^+}$ with a negative coefficient that leads to the cooperative stability and coexistence of the out-of-phase rotations and polar displacements. The $\gamma_2 Q_{R_4^+} Q_{R_5^+}^3$ term contributes to the asymmetry of the energy surface, but is not the main interaction stabilizing the non-zero polar displacements in the $Imm2$ structure. Similarly, the mixed biquadratic term renormalizes the homogeneous quadratic terms and leads to the decrease in radius of curvature of the free energy curve near the minimum with increasing R_4^+, yet it is not responsible for the minimum. Thus, the requirement of two coupled modes as $\sim Q_{R_4^+}^3 Q_{R_5^+}$ with the primary $Q_{R_4^+}$ octahedral rotation mode reveals that the aluminates behave as conventional improper ferroelectrics and not hybrid-improper ferroelectrics; the latter are susceptible to staggered phase transitions owing to the

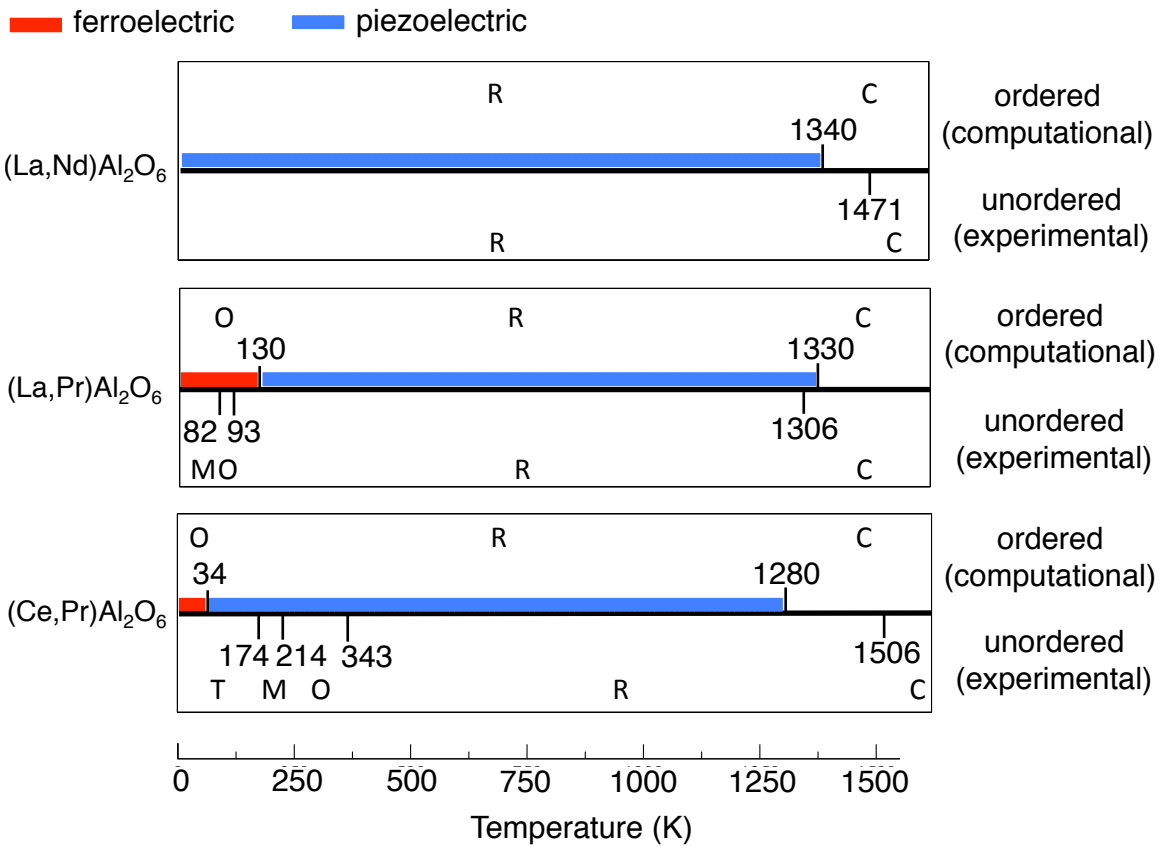

Figure 6.5: The experimentally and computationally determined phase transitions of $(LaNd)Al_2O_6$, $(LaPr)Al_2O_6$, and $(CePr)Al_2O_6$. The phases are defined according to crystal systems with the space group symmetries specified in Table 6.6. Note that the unordered solid solutions for each aluminate are centrosymmetric, whereas the [111] A-cation ordering leads to a non-centrosymmetric structure, which persists to high temperature ($\geq$ 1300 K), allows for ferro- and piezoelectricity (the presence of which is indicated by the red and blue bars, respectively).

necessity of two primary modes.

6.3.3 Structural Phase Transitions

I next investigated the critical temperatures associated with the paraelectric to ferroelectric transitions to explore the potential of these aluminates for high-temperature applications. Recent work has shown that T_c in compounds exhibiting soft-mode driven phase transitions is strongly correlated to the energy difference between the

Table 6.6: The possible crystal systems, octahedral rotation patterns, and space groups (S.G.) that may be found in (LaNd)Al_2O_6, (LaPr)Al_2O_6, or (CePr)Al_2O_6, along with the abbreviations used for each. Note that not every aluminate displays all of the phases tabulated below (see Figure 6.5).

Crystal System	Tilt Pattern	Ordered S.G.	Solid Solution S.G.
(T) Tetragonal	$a^0a^0c^-$	$I\bar{4}2m$ (121)	$I4/mcm$ (140)
(M) Monoclinic	$a^0b^-c^-$	Cm (8)	$C2/m$ (12)
(O) Orthorhombic	$a^0b^-b^-$	$Imm2$ (31)	$Pnma$ (62)
(R) Rhombohedral	$a^-a^-a^-$	$R32$ (155)	$R\bar{3}c$ (167)
(C) Cubic	$a^0a^0a^0$	$Fm\bar{3}m$ (225)	$Pm\bar{3}m$ (221)

two symmetry related structures.[384] By using the fact that $\Delta E = k_B T_c$, where k_B is Boltzmann's constant, I am able to estimate phase transition temperatures using DFT total energies. The phase diagrams of the rare earth aluminate solid solutions (effectively disordered A-site phases) of all compounds investigated have also been experimentally determined[361] and thus will serve as a useful comparison to the predicted critical temperatures of the [111] ordered phases. Because the symmetries of an ordered and disordered compound with the same tilt pattern are different, I refer to the corresponding phases by the crystal system generated by the octahedral rotation pattern to more easily draw comparisons. The abbreviations used for each phase, along with the corresponding tilt pattern and space group, are listed in Table 6.6.

Experimentally, solid solution (LaNd)Al_2O_6 is found to undergo a rhombohedral (R, $a^-a^-a^-$) to cubic (C, $a^0a^0a^0$) phase transition at 1471 K. My calculations of the ordered [111]-system estimate this transition to occur at 1340 K, in close agreement with the experimental results (Figure 6.5, top panel). However, note that other ordered phases (such as [001]) could display different transition temperatures.

Solid solution $(LaPr)Al_2O_6$ displays a more complicated series of phase transitions:

$$\mathrm{M} \xrightarrow{82\,\mathrm{K}} \mathrm{O} \xrightarrow{93\,\mathrm{K}} \mathrm{R} \xrightarrow{1306\,\mathrm{K}} \mathrm{C}.$$

The monoclinic (M) phase exhibits the $a^0b^-c^-$ tilt pattern, while the orthorhombic (O) phase exhibits the $a^0b^-b^-$ pattern. In my calculations of the [111]-ordered phase, however, the monoclinic Cm structure was dynamically unstable compared to the orthorhombic $Imm2$ phase; no local minimum could be found. The experimentally known sequence of phase transitions in the solid solution is therefore not reproduced in the ordered phase (Figure 6.5, center panel). This result may either be a consequence of the cation order or a limitation of the exchange-correlation functional used in the DFT calculations. However, I estimate the O $\rightarrow$ R and R $\rightarrow$ C transitions to occur at 130 K and 1330 K, respectively, again in close agreement with the experimental results of 93 K and 1306 K, which suggests that the monoclinic phase is suppressed by the cation order. Additionally, I found an orthorhombic $Pmc2_1$ ($a^-a^-c^+$) that is $\sim$20 meV higher in energy than the ground state $Imm2$ structure; although this phase is not reported experimentally in the solid solution phase diagram, it could manifest during growth of [111]-ordered $(LaPr)Al_2O_6$.

Finally, solid solution $(CePr)Al_2O_6$ displays the most complicated phase diagram, and has five experimental transitions:[360]

$$\mathrm{T} \xrightarrow{174\,\mathrm{K}} \mathrm{M} \xrightarrow{214\,\mathrm{K}} \mathrm{O} \xrightarrow{343\,\mathrm{K}} \mathrm{R} \xrightarrow{1506\,\mathrm{K}} \mathrm{C}.$$

In contrast, I find the orthorhombic $Imm2$ structure to be the ground state phase, and the tetragonal structure to be unstable (Figure 6.5). Based on energetics, I estimate an O $\rightarrow$ R transition at 34 K and an R $\rightarrow$ C transition at 1280 K.

I conjecture that many of the discrepancies between the ordered aluminates and

the experimental solid solutions, *e.g.* the loss of the tetragonal phase in $(CePr)Al_2O_6$, may be attributed to the *A*-site rock salt ordering pattern and its compatibility with the single antiferrodistortive AlO_6 rotation mode. Because ordering along [111] results in a three dimensional pattern (alternating *A*-sites along each axis), it is more compatible with a three dimensional octahedral rotation pattern ($a^-a^-a^-$, *i.e.*, out-of-phase rotations along each axis), rather than a one- or two-dimensional tilt pattern, which would create a unique axis in the structure. This geometric argument is corroborated by examining rock salt *B*-site ordered perovskites; while rock salt *A*-site ordered perovskite oxides are rare, [111]-type *B*-site ordering is by far the most common.[116,125,385] The three-dimensional $a^-a^-c^+$ tilt system is the most common octahedral rotation pattern adopted by *B*-site ordered perovskites (in addition to being the most common overall). The $a^-a^-a^-$ and $a^0b^-b^-$ patterns are found to be the next most frequently observed, while $a^0a^0c^-$ is the least common.[385,386] By considering this distribution of structures, it seems reasonable that the ground states of the *A*-site ordered aluminates investigated here should also exhibit either the $a^-a^-a^-$ or $a^0b^-b^-$ rotational pattern.

Additionally, it appears that $PrAlO_3$ ($a^0b^-b^-$) influences the tilt pattern of the ordered superlattice more so than the other bulk rare earth aluminates; it turns *off* a rotation about one Cartesian axis in $LaAlO_3$ ($a^-a^-a^-$), stabilizing the $a^0b^-b^-$ rotation pattern. However, it turns *on* a rotation when ordered with $CeAlO_3$ ($a^0a^0c^-$) to also give the $a^0b^-b^-$ rotation pattern. This is due to the fact that the phonon mode that transforms as R_4^+ is much more unstable in $PrAlO_3$ ($\omega = 177.5i$ cm^{-1}) than in $LaAlO_3$ ($\omega = 127.1i$ cm^{-1}) or $CeAlO_3$ ($\omega = 148.4i$ cm^{-1}), leading to control of the superlattice structure by $PrAlO_3$. This suggests that the rotation pattern adopted by the ground state structure could be directly designed by selection of the rotational mode instability strengths (or mismatch) of the bulk ABO_3 perovskite

oxides interleaved to form the superlattice.

6.3.4 Dielectric, Ferroelectric, and Piezoelectric Properties

As discussed previously, I found that the ground state structures of $(LaPr)Al_2O_6$ and $(CePr)Al_2O_6$ are improper ferroelectrics with small electric polarizations of 1.80 and 1.78 $\mu C/cm^2$, respectively, resulting from A-site displacements. My estimate of the critical transition temperatures for each shows that these aluminates would only retain this spontaneous polarization to 93 K and 34 K, at which point they transition from a polar to chiral structure. However, all three compounds retain non-centrosymmetric structures up to high temperatures (>1300 K, see Figure 6.5). To investigate their viability for use in high-temperature applications, I computed the dielectric and piezoelectric tensors for the non-centrosymmetric phases of each ordered compound, as well as the Born effective charges (Table 6.8). Although these properties are all computed at 0 K, they can still be used to draw useful comparisons across different phases.

The total dielectric constant ϵ consists of electronic (frozen-ion) and ionic (relaxed-ion) contributions. I find that the electronic dielectric tensor is approximately isotropic, as well as nearly equivalent across all chemical compositions (a well-known phenomenon in perovskite oxides[387]) and structural phases. The ionic contributions are much larger; I also find that on average they increase when transitioning from the polar $Imm2$ to chiral $R32$ structure. The total dielectric constant of each aluminate also falls well within the known range for perovskite oxides; $(LaNd)Al_2O_6$ in particular displays a dielectric constant near the top of this range.[387]

The relaxed-ion piezoelectric stress (e_{ij}) and strain (d_{ij}) coefficients are related through the compliance tensor C_{ij} (the inverse of the elastic tensor) by $d_{ij} = S_{ik}e_{kj}$. Note that due to symmetry, the $R32$ piezoelectric tensors have 5 components, but

Table 6.7: The computed frozen-ion (ϵ^{elec}), relaxed-ion (ϵ^{ion}), and total (ϵ) dielectric, relaxed-ion piezoelectric stress (e) and strain (d) tensors for (LaNd)Al_2O_6, (LaPr)Al_2O_6, and (CePr)Al_2O_6. Because (LaNd)Al_2O_6 does not exhibit any other phases besides $R32$ and $Fm\bar{3}m$, only the tensor properties of the $R32$ phase are presented. Point group 32 exhibits 3 dielectric and 5 piezoelectric coefficients, but only 2 of which are independent in each case: $\epsilon_{11} = \epsilon_{22} \neq \epsilon_{33}$, and $d_{11} = -d_{12} = -\frac{1}{2}d_{26}$ and $d_{14} = -d_{25}$. The $mm2$ point group exhibits 3 independent dielectric and 5 independent piezoelectric coefficients.

		Dielectric Constant				Piezoelectric Coefficients		
Compound	Phase	Index	ϵ^{elec}	ϵ^{ion}	ϵ	Index	e (C/m^2)	d (pC/N)
(LaNd)Al_2O_6	$R32$	11	4.71	49.7	54.4	11	6.83	13.3
		33	4.61	27.6	32.2	15	4.08	77.7
						26	-6.83	-26.6
(LaPr)Al_2O_6	$Imm2$	11	4.70	23.6	28.3	31	0.11	0.11
		22	4.63	18.8	23.4	32	0.19	0.62
		33	4.78	17.4	22.2	33	0.02	-0.19
						24	0.18	9.05
						15	-0.19	-1.24
	$R32$	11	4.74	36.1	40.8	11	6.83	5.23
		33	4.65	25.9	30.5	15	3.28	54.4
						26	-6.83	-10.5
(CePr)Al_2O_6	$Imm2$	11	4.67	22.4	27.1	31	0.07	0.14
		22	4.58	17.6	22.2	32	0.05	0.04
		33	4.75	16.1	20.8	33	0.06	0.12
						24	0.09	-3.39
						15	-0.11	-0.71
	$R32$	11	4.70	17.3	22.0	11	0.46	2.25
		33	4.61	25.0	29.6	15	0.20	0.26
						26	-0.46	-4.49

Table 6.8: The Born effective charge (Z^*) tensors for $(LaNd)Al_2O_6$, $(LaPr)Al_2O_6$, and $(CePr)Al_2O_6$. Although the Al and O Born effective charge tensors contain small off-diagonal elements, only the main diagonal coefficients are given.

Compound	Phase	Atom	nominal valence	Z^*_{11}	Z^*_{22}	Z^*_{33}
$(LaNd)Al_2O_6$	$R32$	La	+3	+4.47	+4.47	+4.21
		Nd	+3	+4.31	+4.31	+4.14
		Al	+3	+2.95	+2.95	+2.86
		O	−2	−2.42	−2.42	−2.38
$(LaPr)Al_2O_6$	$Imm2$	La	+3	+4.38	+4.25	+4.58
		Pr	+3	+4.30	+4.14	+4.44
		Al	+3	+2.88	+2.94	+2.95
		O	−2	−2.42	−2.42	−2.38
	$R32$	La	+3	+4.72	+4.72	+4.26
		Pr	+3	+4.35	+4.35	+4.20
		Al	+3	+2.95	+2.95	+2.88
		O	−2	−2.44	−2.44	−2.39
$(CePr)Al_2O_6$	$Imm2$	Ce	+3	+4.31	+4.14	+4.47
		Pr	+3	+4.30	+4.13	+4.44
		Al	+3	+2.88	+2.95	+2.96
		O	−2	−2.43	−2.35	−2.47
	$R32$	Ce	+3	+4.36	+4.36	+4.18
		Pr	+3	+4.34	+4.134	+4.18
		Al	+3	+2.96	+2.96	+2.87
		O	−2	−2.44	−2.44	−2.36

only 2 are independent; the $Imm2$ phase has 5 independent coefficients. First, the chiral $R32$ phases of $(LaNd)Al_2O_6$ and $(LaPr)Al_2O_6$ exhibit relatively large piezoelectric coefficients, comparable to those of common lead-free piezoelectric materials such as $BaTiO_3$ and $LiNbO_3$.[388,389] Interestingly, the polar $Imm2$ phase of $(LaPr)Al_2O_6$ has piezoelectric coefficients that are an order of magnitude smaller. Because the chiral phases have no net dipole due to the A-sites sitting on high symmetry positions, an applied stress will generate a much larger induced polarization than in the polar phases (which already have a spontaneous polarization). Additionally, the piezoelectric response of $(CePr)Al_2O_6$ is much smaller than either of the La-based aluminates; it does, however, also show the same increase in response across the $Imm2$-to-$R32$ structural phase boundary (Table 6.8). Thus, while the polarization goes to zero across the $Imm2$-to-$R32$ transition in $(LaPr)Al_2O_6$ and $(CePr)Al_2O_6$, there is a large increase in the piezoelectric response in the chiral structures.

Finally, I computed the Born effective charges for the five phases. Typically, proper ABO_3 ferroelectrics exhibit anomalously large Born effective charges; for example, the nominal charge for Ba, Ti, and O in $BaTiO_3$ are $+2$, $+4$, and -2, respectively, while $Z^*_{\mathrm{Ba}} = +2.56$, $Z^*_{\mathrm{Ti}} = +7.26$, and $Z^*_{\mathrm{O}} = -5.73$.[390] In these ordered aluminates, however, the Born effective charges are close to their nominal values with only the A-site cations displaying any significant deviation. This clearly highlights the difference in mechanism between proper ferroelectrics such as $BaTiO_3$, where polarization arises from B-site displacements due to enhanced covalency with the surrounding oxygen anions, and improper ferroelectrics such as these ordered aluminates, where unequal anti-aligned A-site displacements result in layer dipoles.

6.4 Effect of Chemical Substitution on Hybrid Improper Ferroelectric Properties

In this section, I concentrate on $(AA')(BB')O_6$ double perovskites, which thermodynamically favor simultaneous layering of the A-sites and rock salt patterning of the B-sites (Figure 6.6).[116] This type of chemical ordering, in combination with the common $a^-a^-c^+$ octahedral rotation pattern, is also capable of lifting inversion symmetry through a hybrid improper mechanism.[346] Many double perovskites have been experimentally made with a wide variety of different B cations, including Mg, Mn, Co, Ni, Ti, Fe, W, Sc, Te, and Nb.[117–120,302,303] Here I chose to focus on the series of $(AA')(MnW)O_6$ compounds; in these compounds, the Mn^{2+} atoms are known to order magnetically, and the W^{6+} cations provide the large valance state difference needed for rock salt ordering.[116]

Several of the members of this family have been synthesized experimentally, and many exhibit a polar $P2_1$ ground state at room temperature in addition to magnetic ordering at low temperatures (typically below 15 K);[116] the Néel temperature is so low due to the fact that the B-site rock salt ordering separates the Mn atoms, and the superexchange interaction occurs via a Mn-O-W-O-Mn pathway with non-magnetic W atoms.[391] Furthermore, a large electric polarization of 16 $\mu C/cm^2$ in $(NaLa)(MnW)O_6$ arising via a hybrid improper mechanism is predicted from density functional theory calculations.[346] A recent experimental study, however, found zero spontaneous polarization in samples of $(NaLa)(MnW)O_6$ and $(NaNd)(MnW)O_6$.[305] This discrepancy could be attributed to the polycrystalline samples and difficulties in poling sintered ceramic pellets.

I investigated a series of nine iso-structural compounds with a combination of alkali earth metals on the A-site (A=Na, K, Rb) and rare-earth cations on the A'-site (A'=La, Nd, Y) using first-principles density functional theory calculations. I find

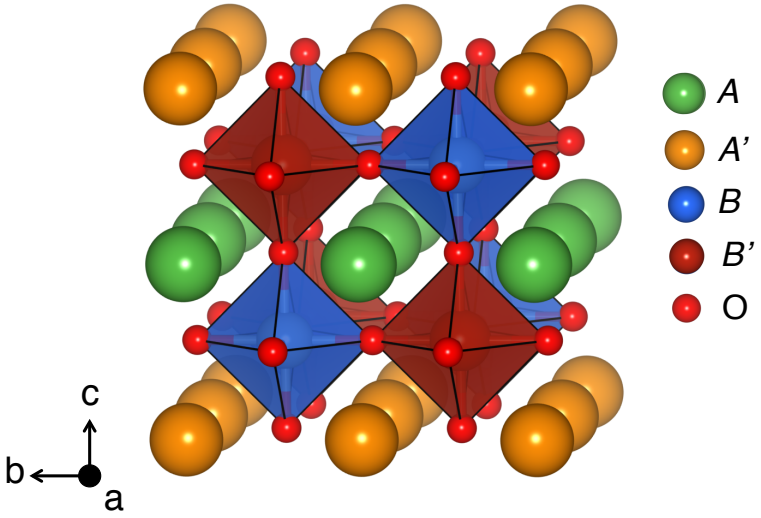

Figure 6.6: The combination of layered A-site and rock salt B-site orderings to create an $(AA')(BB')O_6$ heterostructure produces a $P4/nmm$ crystal structure in the absence of BO_6 octahedral rotations.

all materials in this family display a spontaneous polarization, which is enhanced by up to 150% in those chemistries that maximize the A-A' cation size differential. In order to understand the origin and requirements for the presence of this net dipole, I examined a variety of structural descriptors, including tolerance factors, displacive mode amplitudes, bond valence sums, and layer decomposed dipoles. I found that although the size of the rare earth cation is the largest factor controlling the magnitude of the polarization, consideration of the alkali metal is needed to fully distinguish the compounds with the largest polarization in a single lanthanide family. With this understanding, I then put forth a predictive model based on crystal-chemistry factors to describe other double perovskites, locate new compositions, and determine how to optimize the electric polarization and intrinsic switching barrier. Finally, I observe a small remnant polarization, purely electronic in nature, in the absence of rotations; although this arises due to the nature of the improper mechanism, control over this property could result in 'electronic-only' ferroelectrics, allowing for ultra-fast

Table 6.9: Equilibrium lattice parameters and monoclinic angle (β) of the nine $(AA')(MnW)O_6$ ordered superlattices computed at the DFT+U level. All structures were constrained to the $P2_1$ space group (no. 4).

A	A'	a (Å)	b (Å)	c (Å)	β (deg.)
Na	La	5.572	5.597	8.016	90.225
Na	Nd	5.541	5.667	8.034	90.303
Na	Y	5.438	5.637	7.961	90.270
K	La	5.696	5.722	8.237	90.504
K	Nd	5.634	5.718	8.243	90.587
K	Y	5.519	5.692	8.254	90.729
Rb	La	5.737	5.752	8.337	90.549
Rb	Nd	5.545	5.635	9.492	92.227
Rb	Y	5.407	5.594	9.721	93.131

switching due to unnecessary ionic motion.

6.4.1 Ground State Structures

First, I generated nine double perovskites by occupying alternating A- and B-sites along the [001] and [111] crystallographic directions with monovalent alkali metal (A) and trivalent (A') cations, respectively, to give chemical formula $(AA')(MnW)O_6$. I henceforth refer to each compound according to the A-site chemistry as (AA')MW, where the layered combinations investigated include: (NaLa)MW, (NaNd)MW, (NaY)MW, (KLa)MW, (KNd)MW, (KY)MW, (RbLa)MW, (RbNd)MW, and (RbY)MW. Of these manganese tungstates, (NaLa)MWO_6, (NaNd)MWO_6, and (KLa)MWO_6 have been experimentally realized and ordered in the layered and rock salt configuration.[302,391,392] While (NaLa)MW and (NaNd)MW exhibit the polar $P2_1$ space group and an $a^-a^-c^+$ tilt pattern, (KLa)MW is found to be non-centrosymmetric-nonpolar ($P\bar{4}2m$) and has a complex octahedral tilt pattern ($a^-a^-c^0$, with an in-phase tilt inserted every 5 unit cells).[392] I recognize that synthesis of the unknown compounds may result in many of the complicated structural features exhibited by other members

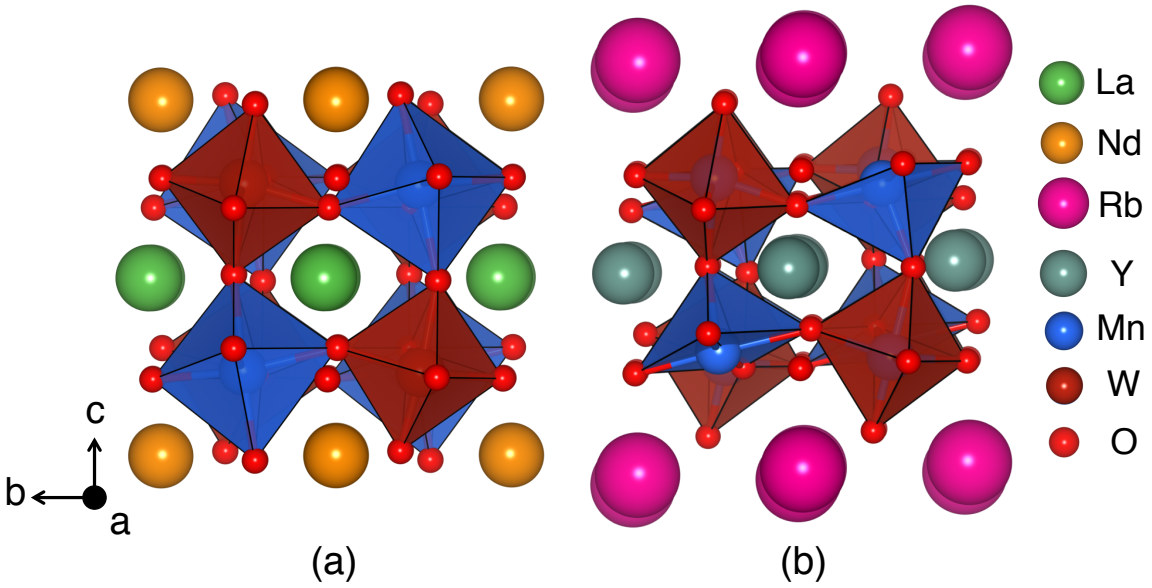

Figure 6.7: The crystal structure of (a) (NaNd)(MnW)O_6 and (b) (RbY)(MnW)O_6. The Na, Rb, and Nd atoms are yellow, pink, and orange, respectively. Each structure exhibits the $P2_1$ space group and contains rock salt ordered Mn (maroon) and W (grey) B-sites as well as layered A and A' sites.

of this family that are not captured in this first-principles modeling, such as incommensurate tilt patterns, twinning, or compositional modulation. However, in order to investigate the magnitude of the spontaneous polarization and make meaningful comparisons between members of this family, I constrained the lattice relaxations of all compounds to be within the $P2_1$ space group and caution synthetic researchers that this phase is unlikely to be the ground state. The ground state crystal structures are tabulated in Appendix A, Tables A.13 to A.21. In each case, the electric polarization is along the in-plane b direction.

The structure of a typical member of this family is shown in Figure 6.7a. I find that while the lattice parameters and monoclinic angles are relatively independent of the A' chemistry, they increase with increasing A cation size (Table 6.9). For seven of the nine compounds, the lattice parameters are relatively similar and the monoclinic angle β deviates from 90° by less than 1°. Interestingly, the (RbNd)MW and (RbY)MW

Table 6.10: Bond valence (BV) sums of A-O, A'-O, Mn-O, and W-O bonds of all nine $AA'(\mathrm{MnW})\mathrm{O}_6$ double perovskites. The values were computed using $BV = \exp[(R_\mathrm{o} - R)/B]$, where R_o is a parameter describing the bond length when atoms have their ideal valence,[393] R is the average bond length determined from DFT calculations, and B is an empirical constant (set to 0.37 for each case here).

A	A'	A-O	A'-O	Mn-O	W-O
Na	La	1.15	3.08	2.33	5.38
Na	Nd	1.13	3.30	2.05	5.42
Na	Y	1.20	3.16	2.05	5.43
K	La	1.19	2.81	2.01	5.48
K	Nd	1.18	3.08	1.97	5.44
K	Y	1.14	3.00	1.91	5.42
Rb	La	1.49	2.82	1.92	5.48
Rb	Nd	0.91	3.11	1.23	5.30
Rb	Y	0.95	3.02	1.07	5.25

compounds are found to have highly elongated c-axes and large monoclinic angles (see the last two rows of Table 6.9). Together these cell distortions also elongate the Mn-O bonds aligned along the c-axis to the point that they are essentially "broken." Figure 6.7b clearly shows this effect, where the Mn coordination transforms to a square pyramidal geometry. Although one might want to attribute this effect solely to the increase in the ionic radius of Rb compared to the other alkali metals, (RbLa)MW does not exhibit this structure type. Instead, I find that the controlling factor is the *difference* in the size of the A-site ionic radii (r) of the cations, *i.e.* $\Delta r = |r_A - r_{A'}|$. Only above a critical Δr ($\sim$ 0.45 Å) do the AA'MW compounds adopt the highly distorted structure.

An examination of the bond valence sums (Table 6.10) also shows that the Mn atoms in (RbNd)MW and (RbY)MW are highly undercoordinated, decreasing from their nominal oxidation state of 2+ to nearly 1+. Although this analysis suggests that these two structures are unlikely to be synthesized in this polymorph, I keep the structures in the hypothetical suite of compounds to evaluate how the electric polar-

Table 6.11: The ionic radii of 12-fold coordinated A (r_A) and A' ($r_{A'}$) atoms, polarization (P), and energy difference between the $P2_1$ ground state and the lowest energy centrosymmetric, supergroup $P2_1/m$, phase (E_B) for all nine AA'(MnW)O_6 compounds.

A	A'	r_A (Å)	$r_{A'}$ (Å)	P (μC/cm^2)	E_B (meV/f.u.)
Na	La	1.39	1.36	16.1	46.0
Na	Nd	1.39	1.27	19.3	224
Na	Y	1.39	1.25	23.6	426
K	La	1.64	1.36	15.5	37.8
K	Nd	1.64	1.27	20.8	109
K	Y	1.64	1.25	26.1	353
Rb	La	1.72	1.36	15.1	20.6
Rb	Nd	1.72	1.27	19.0	193
Rb	Y	1.72	1.25	23.6	243

ization evolves with A cation substitution. Additionally, the A-site bond valence in (RbLa)MW suggests that the Rb atom is over coordinated in this compound. This occurs because Rb and La are the largest alkali and rare earth cations investigated, leading to (RbLa)MW exhibiting the smallest octahedral rotations; this in turn gives a higher coordination number to Rb in comparison to the A-sites of the other compounds. Finally, I find that Nd and Y are always slightly overcoordinated, while La is overcoordinated in (NaLa)MW, but not (KLa)MW or (RbLa)MW. The bond valences of the A' cations also decrease when going from A=Na to K or Rb due to the larger size of these A cations.

6.4.2 Dielectric and Magnetic Properties

Table 6.11 reports the computed electric polarizations for the $P2_1$ equilibrium structures of all nine compounds. The polarization does not show significant variation when changing the alkali cation and keeping the rare-earth chemistry fixed (Figure 6.8a), but it markedly increases upon substitution of the trivalent A' cation with a

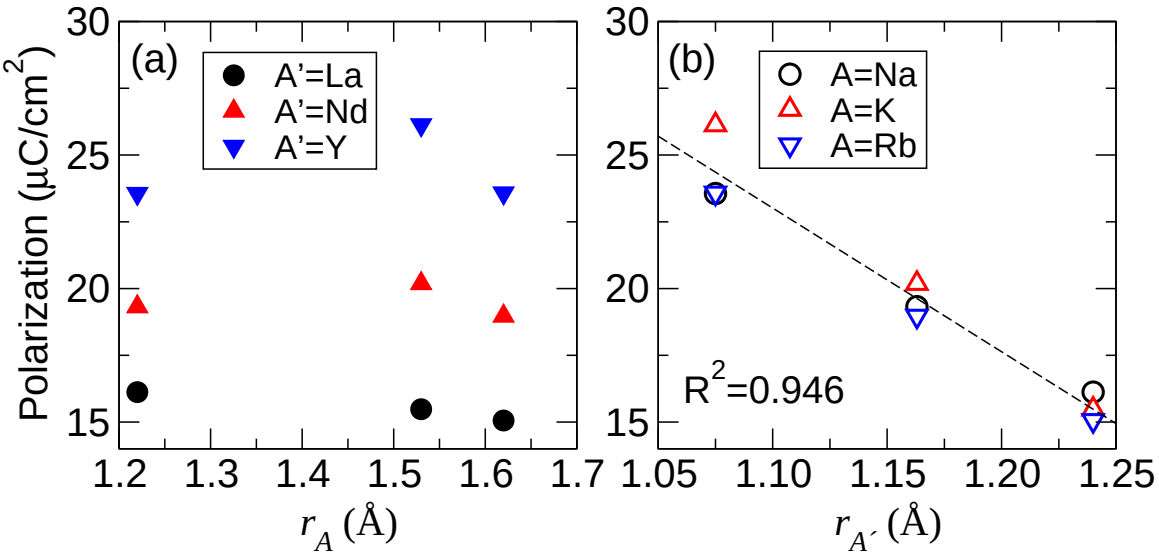

Figure 6.8: The total polarization of each $AA'(\mathrm{MnW})\mathrm{O}_6$ compound as a function of the size of the (a) alkali A cation and (b) rare earth A' cation. Although the polarization remains relatively constant upon substitution of the A site, it is strongly correlated to the size of the rare earth cation. The dashed line shows a linear fit to the data, while R^2 is the coefficient of determination for the fit.

smaller lanthanide element at a fixed alkali metal composition (Figure 6.8b). This suggests that the size of the rare earth cation (Table 6.11) influences the magnitude of the electric polarization to a greater degree than the alkali metal. However, this does not mean that the A-site does not influence the magnitude of the polarization; there are several subtle effects that are not explained by the rare earth chemistry of the A'-site alone and will be explored in more detail in the next section. Additionally, there is a clear trend between the polarization and the energy difference between the $P2_1$ ferroelectric and $P2_1/m$ paraelectric phases (given as E_B in Table 6.11), which can be used as an estimation of the intrinsic ferroelectric switching barrier.

I next investigated how the Mn magnetic moment and band gap evolves with respect to chemical substitution on the A-site. I find that while the band gap matches closely with those experimentally reported,[302] there is no significant correlation in

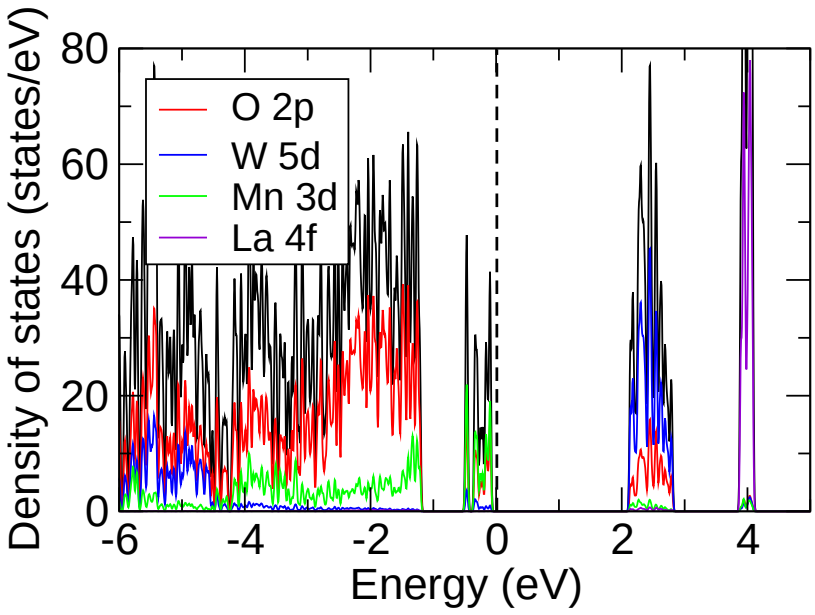

Figure 6.9: Atomically-resolved density of states for (NaLa)(MnW)O_6 with the Fermi level indicated by a broken line at 0 eV. The top of the valence band is made up of O $2p$ states and Mn $3d$ states, while the bottom of the conduction band is primarily W $5d$ states. The A-site cations, Na and La, contribute states far from the band edges.

either of these quantities as a function of polarization. Figure 6.10a and 6.10b show that there is small variation between the magnetic properties and electronic band gap with A-site chemistry—both properties are largely unaffected by the alkali metal and trivalent cations on the A-site. However, the properties are closely clustered for a given A' cation. This is most likely because the magnetic moment only depends on the Mn atoms, and any small changes to it are induced by inductive effects from the A cations that weakly change the length and covalency of the Mn–O bond.[394] The electronic density of states also primarily consists of O $2p$ states and Mn $3d$ states at the top of the valence band and W $5d$ states at the bottom of the conduction band (6.9); the A and A' cations contribute states far from these band edges, and as a result, their chemistry does not significantly impact the band gap. While it is possible that the size of these cations could influence the band gap through alteration

of the Mn-O-W bond angle (by increasing or decreasing orbital overlap), I do not see any large changes.

In order to switch the polarization in these rotationally-induced improper ferroelectrics, the entire sense of the in-phase tilts must be reversed. The $P2_1/m$ structure is the mostly likely intermediate centric phase along a one-step switching path as it contains no in-phase rotations.[346] As the size of the rare earth cation decreases (and thus the polarization increases), the energy difference between these two phases increases by a large amount; this is also reflected in the fact that the compounds with smaller cations have larger octahedral rotations, as mentioned previously. Thus, although an enhancement in the polarization can be achieved through A-site chemical substitution, there is a trade off in the ability of the ferroelectric polarization to be switched. This was reported previously in other rotation-driven ferroelectrics such as layered perovskites and Ruddlesden-Popper phases.[287]

6.4.3 Crystal-Chemistry Descriptors for Electric Polarization

To build a more thorough microscopic understanding of the evolution in the electric polarization with A and A' cation substitution, I explore how structural-chemistry descriptors relate the dielectric properties to the crystal structure. One of the most common descriptors for perovskite oxides is the Goldschmidt tolerance factor,[108] which for the double perovskites examined here can be expressed as

$$\tau_{\text{avg}} = \frac{\bar{r}_A + r_{\text{O}}}{\sqrt{2}\,(\bar{r}_B + r_{\text{O}})}, \tag{6.3}$$

where $\bar{r}_A$ and $\bar{r}_B$ are the average Shannon ionic radii of the A-site and B-site cations of 12-fold coordinated A and A' and 6-fold coordinated B and B' atoms.[109] This quantity gives a simple measure of the distortion of a perovskite oxide; the closer τ_{avg} is to 1, the less distorted (or more cubic) the structure tends to be. If τ_{avg} is less than

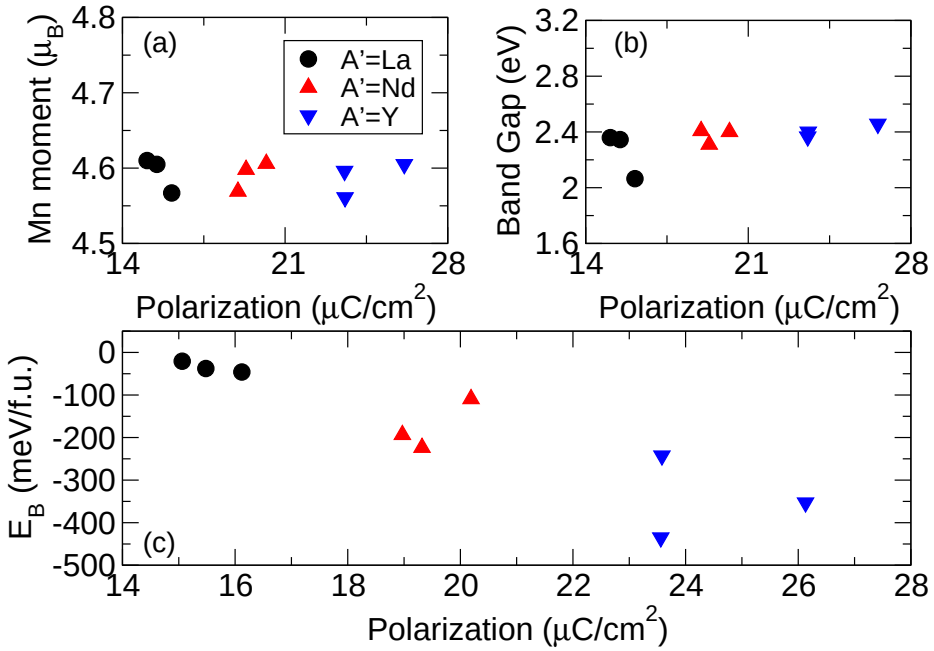

Figure 6.10: The (a) Mn magnetic moment, (b) band gap, and (c) energy difference (E_B) between the $P2_1$ and $P2_1/m$ phases of each compound. While the magnetic moment and band gap remain relatively unchanged upon chemical substitution, the energy difference between the phases increases substantially as the polarization increases.

1, then the A-site cations are too small for the interstices between BO_6 octahedra, and the extended octahedral network rotates in order to alleviate this underbonding of the A-site species.

Because of the ubiquity of this quantity in characterizing perovskites, I first examined the effect of τ_{avg} on the polarization. This parameter alone poorly describes the evolution in the magnitude of the polarization for all compounds and is anti-correlated with the polarization within a given trivalent A' family (Figure 6.11a). Previous work has identified that the difference in tolerance factor ($\Delta\tau$) of the bulk ABO_3 constituents is also an important descriptor of the polarization in perovskites with layered A cation order exhibiting hybrid improper ferroelectricity.[287] Starting from a symmetry analysis, Mulder *et al.* derived a relationship between spontaneous polarization and tolerance factor of the form $P \approx \Delta\tau(1 - \tau_{\text{avg}})$. Here, I consider $\Delta\tau$ to be the difference between the average tolerance factor of the $(AA')MnO_3$ and $(AA')WO_3$ bulk compounds. This quantity improves the correlation among all compounds and the spontaneous polarization (Figure 6.11b) due to information about the difference in atomic radii being included, which will be shown to be an important factor in determining the magnitude of the polarization. Nonetheless, the ionic size of the A' cation alone provides a better predictor of the polarization (Figure 6.8b), albeit is anti-correlated.

I next performed a mode decomposition of the polar structures. Three primary modes relating the low symmetry ground state $P2_1$ structure to the undistorted high symmetry $P4/nmm$ structure have been previously identified and are described by the following irreducible representations (irreps): Γ_5^+ (describing the out-of-phase rotations), Γ_1^- (describing the in-phase rotations), and Γ_5^- (polar mode).[346] (Note the mechanical representations of Γ_1^- and Γ_5^+ are similar to irreps M_3^+ and R_4^+ irreps found in the perovskite literature, which are responsible for reducing a cubic $Pm\bar{3}m$

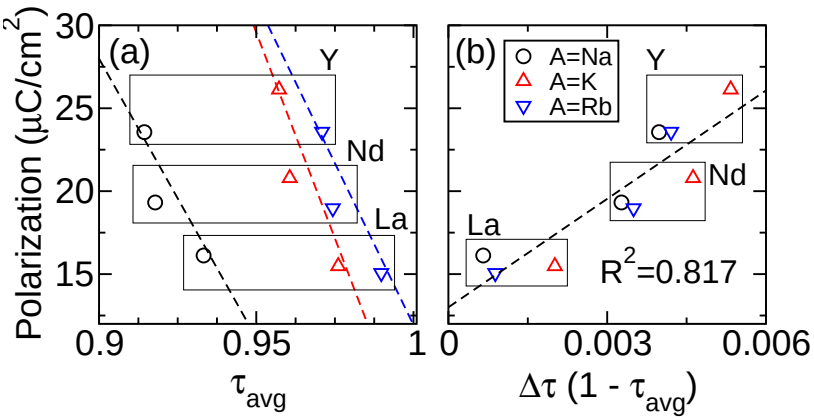

Figure 6.11: (a) Polarization versus tolerance factor of the nine $AA'(\mathrm{MnW})\mathrm{O}_6$ compounds computed using the Shannon ionic radii of 12-fold coordinated A and A' sites. While the tolerance factor by itself is not a good overall predictor of the polarization, it is a good descriptor within each family of constant rare earth A' site (dashed lines are linear fits to the data). (b) Polarization versus tolerance factor renormalized to the tendency of A-sites to displace (see text), $\Delta\tau(1-\tau_{avg})$ provides a much better prediction of the polarization among all compounds.

Table 6.12: Amplitude of the three primary modes relating the nine $P2_1$ $AA'(\mathrm{MnW})\mathrm{O}_6$ ordered superlattices to the undistorted high symmetry $P4/nmm$ phase. Labels of the irreducible representations are generated with respect to the $P4/nmm$ structure.

A	A'	$Q_{\Gamma_5^+}$ (Å)	$Q_{\Gamma_1^-}$ (Å)	$Q_{\Gamma_5^-}$ (Å)
Na	La	1.336	0.897	0.668
Na	Nd	1.486	1.986	0.899
Na	Y	1.589	1.273	1.088
K	La	0.984	0.658	0.449
K	Nd	1.079	0.861	0.625
K	Y	1.251	1.131	0.829
Rb	La	0.868	0.499	0.358
Rb	Nd	1.236	0.882	0.499
Rb	Y	1.503	1.109	0.714

$AB\mathrm{O}_3$ perovskite to the common *Pnma* orthorhombic phase). The mode amplitude Q provides a measure of the degree to which a structure is distorted by these three modes (Table 6.12). I find that the amplitude of Γ_5^+ and Γ_1^- (and thus the $B\mathrm{O}_6$ and $B'\mathrm{O}_6$ octahedral rotations) increases as a function of decreasing atomic size. All three of the main modes show a somewhat clear trend with the polarization, and the amplitude of the Γ_1^- mode is the most strongly correlated (Figure 6). This behavior suggests that the out-of-phase rotations exhibit the largest control over the polarization. Additionally, the polar Γ_5^- mode follows the same trend, indicating that the magnitude of the spontaneous polarization should increase as the A' atomic species get smaller (Fig. 6.12). This is to be expected given the hybrid improper nature of the polarization, as the net dipole in these materials arises due to a non-cancellation of A-site cation displacements; having smaller atoms means they can undergo larger displacements.

By taking all of this structural information into consideration, $(\mathrm{KY})(\mathrm{MnW})\mathrm{O}_6$ appears to be the chemistry best suited for polarization enhancement and experimental investigation in this family of materials. The difference in the atomic size of the K and Y (Δr) is large enough to maximize the polarization, while also small enough to maintain the desired perovskite structure (indicated by the fact that the bond valence of the Mn-O remains close to the nominal value of 2+, Table 6.10). As mentioned previously, however the size of the rotations also increases the ferroelectric switching barrier due to the fact that reversal of the in-phase rotations is required for switching of the polarization (E_B, Table 6.11).

6.4.4 Contributions to the Electric Polarization

The total spontaneous polarization can be decomposed into two parts: an ionic contribution from atomic displacements (P_{ion}) and an electronic contribution arising

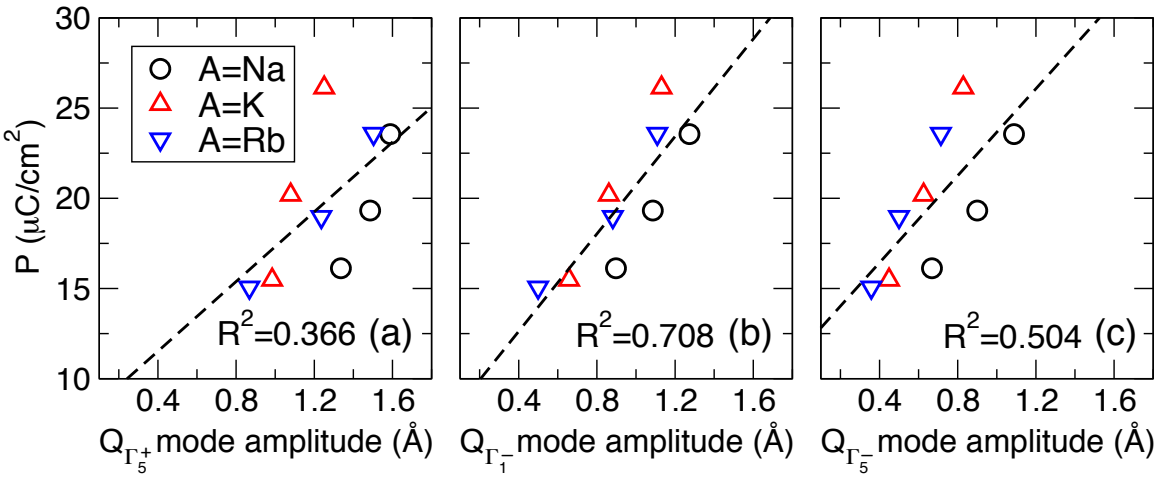

Figure 6.12: Polarization as a function of (a) Γ_5^+ (out-of-phase rotations), (b) Γ_1^- (in-phase rotations), and (c) Γ_5^- (polar mode) mode amplitudes of each AA'MW compound.

from displacement of the electron cloud (P_{elec}). While the size of the rare earth A' cation largely controls the magnitude of the spontaneous polarization, an investigation of the contributions of each atomic species can lead to further insights. Note that while this division is useful for a qualitative discussion and analysis of the polarization, only the sum of the two (*i.e.*, the total polarization $P = P_{ion} + P_{elec}$) has any real physical meaning.

I first examine the ionic contribution. In these hybrid improper ferroelectrics I would anticipate a smaller A' cation to result in a larger polarization due to its ability to displace further. Additionally, a larger alkali atom should also result in a larger polarization, because the A cation displaces less in the direction opposite to the A' cation and cancels less of the A' polarization. One would predict two clear trends by applying these concepts to the manganese tungstates *a priori*: (i) $P_{A\text{LaMW}} < P_{A\text{NdMW}} < P_{A\text{YMW}}$ and (ii) $P_{\text{Na}A'\text{MW}} < P_{\text{K}A'\text{MW}} < P_{\text{Rb}A'\text{MW}}$. (NaLa)(MnW)$O_6$ would therefore have the smallest polarization while (RbY)(MnW)O_6 would have the largest, with the other seven compounds found between these extremes. While this expectation holds

for the rare earth trend (Figure 6.8a), it does not hold for the alkali metal trend (Figure 6.8b). If A'=La, I find that $P_{(\mathrm{RbLa})\mathrm{MW}} < P_{(\mathrm{KLa})\mathrm{MW}} < P_{(\mathrm{NaLa})\mathrm{MW}}$, but when La is replaced with Nd, the trend changes such that $P_{(\mathrm{RbNd})\mathrm{MW}} < P_{(\mathrm{NaNd})\mathrm{MW}} < P_{(\mathrm{KNd})\mathrm{MW}}$.

I next investigate these discrepancies by decomposing the polarization into contributions from each layer (Figure 6.13). As can be seen in Figure 6.7, each compound consists of two AO layers, two (MnW)O_2 layers, and two A'O layers along [001]. The polarization of one of each of these layers in the nine superlattices is plotted as a function of A cation size (Figure 6.13a-c) or A' cation size (Figure 6.13d-f). Figure 6.13a reveals the trend that larger A-site cations result in a lower AO layer polarization (and therefore a smaller cancellation of the A' layer) occurs as expected. Additionally, the (MnW)O_2 layer polarization decreases as a function of increasing A cation size (Figure 6.13b) due to the smaller A-site, which allows for greater B-site displacements; the increase in the layer polarization for the (RbNd) and (RbY) compounds occurs from the Mn–O bond breaking. Also as expected, there is a weak dependence of the rare earth layer polarization on the alkali metal on the size (Figure 6.13c) and *vice versa* (Figure 6.13d). Interestingly, the contribution of the (MnW)O_2 layer to the total polarization switches to become greater in the A=K than in the A=Rb compounds upon substitution of Nd by La (Figure 6.13e). By examining the atomically resolved (MnW)O_2 layers, I find that the contributions of the Mn and W atoms to the polarization is larger in the case of A=K than A=Rb. The contributions of the O atoms are larger in (KLa)MW than (RbLa)MW because the octahedral rotations are also larger in (RbNd)MW and (RbY)MW; however, the octahedral rotations become larger than (KNd)MW and (KY)MW due to the separation of the layers, thus allowing for a larger contribution of its O atoms. As expected, the layer polarization of the A'O layer increases as a function of decreasing atomic size (Figure 6.13f).

Following this analysis, I can now explain the trends in the polarization seen in

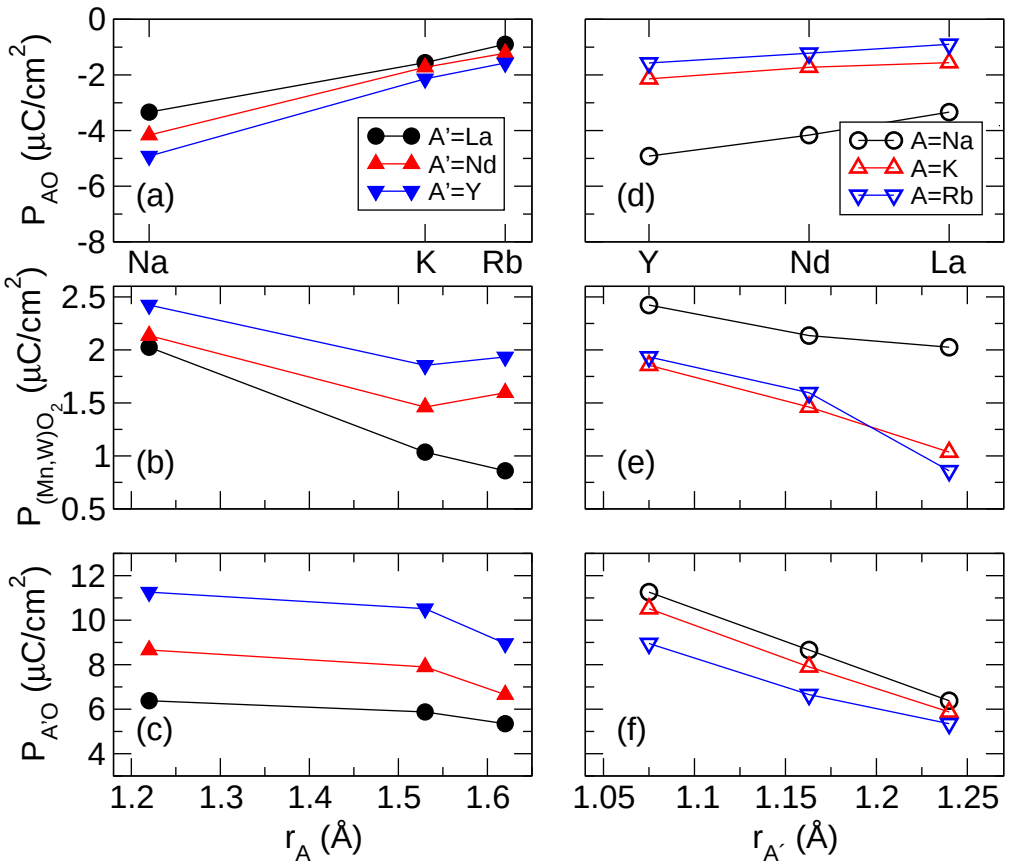

Figure 6.13: Evolution of the ionic contribution to the polarization of the AO, BO$_2$, and A'O layers of each AA'(MnW)O$_6$ compound as a function of the A-site (r_A, a–c) and A'-site ($r_{A'}$, d–f) radius. See text for a detailed discussion.

Figure 6.8b. In the A'=La family, the smaller alkali cation should result in a larger cancellation of the LaO layer polarization, which remains nominally the same in each of the three compounds. The fact that the $(MnW)O_2$ layers contribute more to the total polarization with smaller A-sites overcomes this cancellation, resulting in the calculated trend of $P_{(NaLa)MW} > P_{(KLa)MW} > P_{(RbLa)MW}$. When La is substituted with Nd, the amount that P_{Na} cancels P_{Nd} is much greater than the amount P_K cancels P_{Nd}, even more so than when A'=La. In combination with the trend of the $(MnW)O_2$ layer polarization, this gives $P_{(KNd)MW} > P_{(NaNd)MW} > P_{(RbNd)MW}$. Finally, this same reasoning can rationalize the polarization trend seen in the A'=Y family.

Although the bulk of the total polarization originates from atomic displacements as discussed above (P_{ion}), the *electronic* component provides a non-negligible contribution. In seven of the nine structures, the two contributions are of the same sign with the electronic part providing an enhancement of 2 to 5 $\mu C/cm^2$. In the (NaNd) and (NaY) compounds, however, the electronic polarization is opposite to that of the ionic contribution, resulting in a decrease of the total polarization. Interestingly, these two materials also have the smallest average A-site radius. However, because the magnitude of the electronic polarization in the other compounds are relatively similar, this does not provide a complete explanation and requires further investigation.

An electronic contribution also is present even if the polar displacements are removed from the crystal structures (Fig. 6.14). Because the Γ_1^- and Γ_5^+ modes (in-phase and out-of-phase rotations, respectively) alone are sufficient to lift inversion in the presence of layered A-sites and rock salt ordered B-sites (that is, the space group remains $P2_1$ without the Γ_5^- mode), these materials could theoretically still exhibit a spontaneous polarization without the ionic displacements. To investigate this aspect, I decreased the $Q_{\Gamma_5^-}$ amplitude while keeping the magnitude of $Q_{\Gamma_5^+}$ and $Q_{\Gamma_1^-}$ fixed to the values found in the equilibrium ground state structure. When $Q_{\Gamma_5^-} = 0$, an elec-

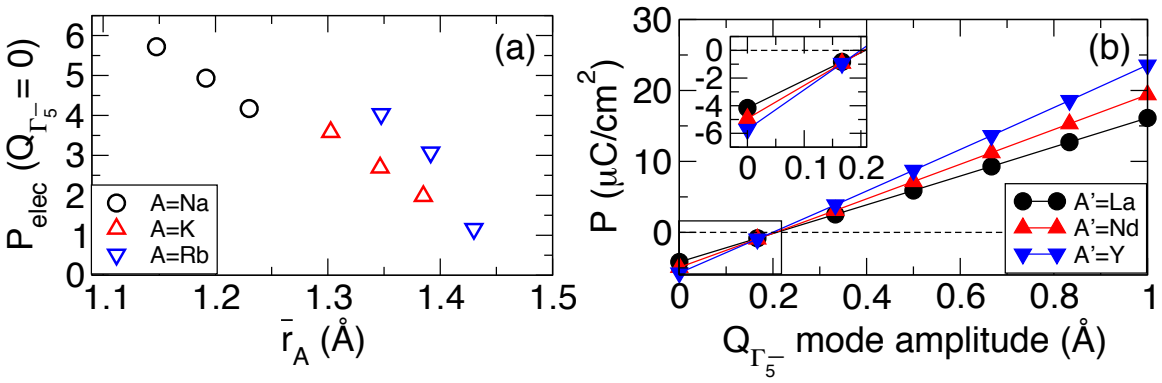

Figure 6.14: (a) The spontaneous electronic polarization remaining when $Q_{\Gamma_5^-} = 0$ (no polar ionic displacements) in all nine $AA'(MnW)O_6$ compounds as a function of average A-site atomic radius. (b) Evolution of the total polarization as a function of $Q_{\Gamma_5^-}$ in the family of $NaA'(MnW)O_6$ compounds. At $Q_{\Gamma_5^-}$=0, the polarization is purely electronic in nature.

tronic polarization (P_{elec}) remained (Figure 6.14a), which was aligned opposite to the total polarization found in the $Q_{\Gamma_5^-} = 1$ ground state. Additionally, as $Q_{\Gamma_5^-}$ increases, the total polarization evolves smoothly to the value obtained in the ground state structures (Figure 6.14b). This result seems counter to what the trilinear coupling term in the free energy previously shown implies, which is that the total polarization should go to zero if the polar mode goes to zero; however, the simplification of the phenomenological invariant disguises the fact that there are both ionic and electronic contributions to this invariant (such a distinction could also allow for a new interpretation of electronically-induced improper ferroelectrics, such as $HoMnO_3$ in terms of generalized spin rotations). This is shown by removing either of the rotational modes (while keeping the polar mode fixed to zero), which destroys this remnant polarization.

A large number of perovskites are cubic with no rotations and disordered A-site cations at high temperatures. I conjecture the electronic only contribution could be observed experimentally if the octahedral rotations can then be maintained at some

temperature above which the A-site cations order in such a way that the Γ_5^- mode causes the layers to cancel the ionic contribution to the polarization. This interesting effect deserves further study as materials displaying purely electronic polarizations could result in entirely new families of ferroelectrics that undergo much less fatigue due to the lack of ionic motion during switching.

7. EFFECT OF EPITAXIAL STRAIN ON BROWNMILLERITE OXIDES

In this chapter, I investigate the effect of strain on the crystal structure and electronic properties of brownmillerite oxides. As discussed in Chapter 3, when brownmillerite oxides are grown as thin films, the oxygen vacant layers can orient themselves parallel or perpendicular to the substrate (Figure 3.5f-i). I use electronic structure calculations to disentangle the complex interactions in two brownmillerite ferrates, $Sr_2Fe_2O_5$ and $Ca_2Fe_2O_5$, relating the stability of the equilibrium (strain-free) and thin film structures to both previously identified and newly herein proposed descriptors. Furthermore, I investigate the effect of compressive and tensile strain on the crystal and electronic structure of these two materials.

7.1 Computational Methods

All investigations were performed using density functional theory as implemented in the Vienna *ab-initio* Simulation Package (`VASP`).[43,79,80] I used projector augmented-wave (PAW) potentials with the PBEsol functional,[54,63] chosen because it is a type of GGA functional adjusted to give better agreement with lattice parameters and bond angles specifically in solids, with valence electron configurations of $3s^2 3p^6 4s^2$ for Ca, $4s^2 4p^6 5s^2$ for Sr, $3d^7 4s^1$ for Fe, and $2s^2 2p^4$ for O. A plane-wave cutoff of 500 eV and a 7×5×7 Monkhorst-Pack mesh was used during the structural relaxations.[60] I applied a Hubbard U correction of 5 eV using the Dudarev formalism to treat the correlated Fe 3d states, a value which provides agreement between the computed and experimental band gap of these materials; I also enforced a G-type anti-ferromagnetic collinear spin ordering on the Fe atoms.[81] Symmetry-adapted mode decompositions

were performed using the ISODISTORT tool, part of the ISOTROPY software suite.[82] Atomic structures were visualized using VESTA.[83]

To simulate the application of epitaxial strain by growth on a cubic [001] terminated perovskite substrate with a square surface net, I fixed the in-plane a and c lattice parameters to be equal and allowed the out-of-plane b axis and ions to fully relax (adopted from the approach of Ref. 36). The $I2bm$, $Pbcm$, and $Pnma$ phases of $Ca_2Fe_2O_5$ and the $I2bm$ and $Pbcm$ phases of $Sr_2Fe_2O_5$ in both the parallel and perpendicular orientation were then strained from -3% to 3% in increments of 1%. Because of the difference in size and equilibrium volume of the $Ca_2Fe_2O_5$ and $Sr_2Fe_2O_5$ unit cells, application of the same percent strain results in different pseudocubic lattice parameters (a_{pc}) for the two structures; for this reason, I report the strain in terms of a_{pc} rather than in terms of percentage.

7.2 Effect of Strain on Anion Vacancy Ordering in Brownmillerite Oxides

7.2.1 Bulk Phases

I first investigated the bulk phases of $Sr_2Fe_2O_5$ and $Ca_2Fe_2O_5$ with the three tetrahedral chain orderings shown in Figure 3.5 using density functional theory calculations. Each compound was frozen into the $I2bm$, $Pbcm$, and $Pnma$ structure to create a total of six phases; the lattice parameters and internal atomic positions were relaxed as described in Section 7.1. The six ground state crystal structures are tabulated in Appendix A, Tables A.22 to A.27. To characterize the brownmillerite structures, I consider three types of rotation angles: the angle between (i) the FeO_4 tetrahedra (Θ_T), (ii) the FeO_6 octahedra (Θ_O), and (iii) the tetrahedra and octahedra (Θ_{OT}). I report these angles as $\Theta_X = (180 - \Phi_X)/2$, where the definition of Φ_X ($X = T$, O, or OT) is shown in Figure 7.1; in this case, a larger angle indicates a larger distortion of the relative bond away from 180°. In the bulk case and the case of par-

allel orientation of vacancies under strain, these three angles are sufficient to describe the structure (Figure 7.1a). In the perpendicular orientation, however, the applied strain and response of the out-of-plane lattice parameter now affect the tetrahedra and octahedra in different ways. To capture this, I divide Φ_O and Φ_T into two unique angles defined by in-plane (i.p.) and out-of-plane (o.o.p.) components (Figure 7.1b). The main structural and energetic results for the two compounds are summarized in Table 7.1.

In the case of $Sr_2Fe_2O_5$, I found that the centrosymmetric *Pbcm* polymorph is the lowest energy structure, followed by *I*2*bm*, with *Pnma* being the highest. In $Ca_2Fe_2O_5$, I found the *Pnma* structure to be lowest in energy, followed by *I*2*bm* and *Pbcm*. Each polymorph is separated from the other two by a small amount of energy (ΔE, Table 7.1), indicating that the formation of a right- or left-handed tetrahedral chain may be equally probable. Furthermore, the lattice parameters, rotation angles, and band gaps vary only slightly between orderings. Between the two chemistries, $Ca_2Fe_2O_5$ has a smaller unit cell and larger rotation angles than $Sr_2Fe_2O_5$, which is due to the smaller size of the Ca^{2+} cation.

Experimentally, the structure of $Sr_2Fe_2O_5$ has been highly contested. Initial structure refinements on powder samples ambiguously supported assignment of both completely disordered tetrahedral chains (space group *Imma*) or pure left- or right-handed ordering (space group *I*2*bm*); this material was thus theorized to display *I*2*bm* symmetry locally, but with random ordering taking place over longer length scales. This was challenged, however, by transmission electron microscopy results showing clear intralayer alternation of tetrahedral chains.[395] Additionally, more recent neutron diffraction experiments on single crystals grown by the floating zone method have indicated that *Pbcm* is indeed the preferred structure type for $Sr_2Fe_2O_5$.[396,397] Furthermore, all of these recent experiments are supported by the aforementioned results

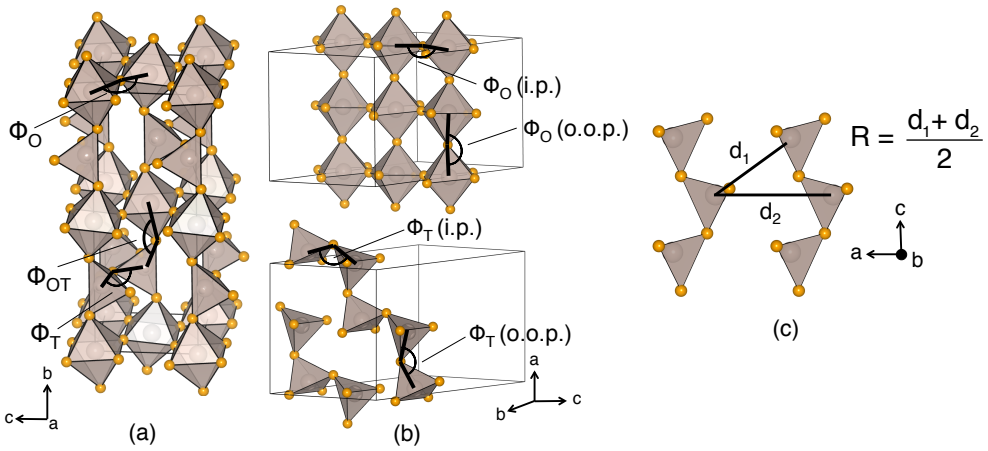

Figure 7.1: (a) The three characteristic angles of the $A_2B_2O_5$ brownmillerite structure. Rotations of the tetrahedral chains, of the octahedral network, and between the tetrahedral and octahedral layers are given by Φ_T, Φ_O, and Φ_{OT}, respectively. These three angles are sufficient to describe the case when the tetrahedral chains order parallel to the substrate. (b) In the perpendicular orientation, the changes in the out-of-plane lattice parameter owing to the strain state splits the octahedral and tetrahedral rotation angles. (c) The average separation distance is given by R, which is defined as the average of the two distances between Fe atoms of different chains (d_1 and d_2).

of our *ab initio* calculations; the small energy difference between the *Pbcm* and *I*2*bm* structures, however, indicate that intergrowths of the phases is not out of the question. In contrast to the ambiguity of $Sr_2Fe_2O_5$, the structure of $Ca_2Fe_2O_5$ is well known to form in the *Pnma* phase,[398] again in agreement with our theoretical results.

I now seek to explain the stability of these materials' preferred ground state phase in terms of local structure. The tetrahedral chain ordering configuration preferred by the ground state can be summarized as a complex competition between two primary energetic factors: (*i*) separation of the tetrahedral chains (*i.e.*, minimization of electrostatic repulsion) and (*ii*) distortion of the nominally regular BO_6 octahedra (minimization of elastic strain energy). The three different ordering schemes shown in Figure 3.5 better maximize either factor (*i*) or (*ii*) at the expense of the other. Following the approach of Zhang *et al.*,[146] I can assign a magnitude to the local dipole

Table 7.1: The energetics and structure of bulk $Sr_2Fe_2O_5$ and $Ca_2Fe_2O_5$. The tolerance factor (τ) is defined by Equation 3.1 in the text. The energy difference between the different tetrahedral chain ordering structures is given as ΔE; each energy is given as the difference in meV between that phase and the lowest energy phase for each compound normalized to the number of formula units. The a, b, and c lattice parameters are given in Angstroms. The rotations of the tetrahedra, octahedra, and between the octahedra and tetrahedra are given in degrees as Θ_T, Θ_O, and Θ_{OT}, respectively; each is defined in Figure 7.1a and 7.1b.

$Sr_2Fe_2O_5$ (P_T = 3.8 D, τ=0.976)							
Symmetry	ΔE (meV/f.u.)	a (Å)	b (Å)	c (Å)	Θ_T (°)	Θ_O (°)	Θ_{OT} (°)
I2bm	12.6	5.501	15.402	5.659	24.48	3.70	15.41
Pbcm	0	5.503	15.407	11.311	24.54	4.43	15.39
Pnma	22.7	5.499	15.413	5.659	24.49	3.64	15.31
$Ca_2Fe_2O_5$ (P_T = 1.7 D, τ=0.923)							
Symmetry	ΔE (meV/f.u.)	a (Å)	b (Å)	c (Å)	Θ_T (°)	Θ_O (°)	Θ_{OT} (°)
I2bm	16.7	5.381	14.617	5.579	27.92	6.538	20.34
Pbcm	23.3	5.386	14.627	11.155	28.16	4.909	19.90
Pnma	0	5.397	14.632	5.561	27.23	8.032	20.45

generated by the tetrahedral rotations (P_T, Table 7.1, given in units of Debye). P_T is calculated based on the Debye equation, $\mu = neR$, where μ is the net dipole moment, n is the number of electrons, e is the elementary charge, and R is the distance between centers of charge; following the approach of Poeppelmeier *et al.*, I estimated the distribution of electrons using bond valence sums.[399] In compounds with large P_T, factor (i) becomes the quantity of interest to maximize; rather than considering the separation along b, however, I quantify this by defining the average *intra*layer separation of the tetrahedral chains as R (shown in Figure 7.1c). Competing with this is factor (ii), *i.e.*, the regularity in the octahedra. I use the average sum-of-squares difference between the measured bond lengths (d_n) and the average bond length (d_{avg}) in the octahedra to quantify this:

$$\Delta = \frac{1}{N}\sum_{i=1}^{n}\left(\frac{d_n - d_{avg}}{d_{avg}}\right)^2. \tag{7.1}$$

Table 7.2: The average intralayer separation of tetrahedral chains (R, defined in Figure 7.1c) and the deviation in the bond lengths of an octahedra (Δ, defined by Equation 7.1) for each phase of $Sr_2Fe_2O_5$ and $Ca_2Fe_2O_5$. The band gap (E_g) of each structure is given in eV.

$Sr_2Fe_2O_5$ (P_T = 3.8 D, τ=0.976)			
Symmetry	R (Å)	Δ ($\times 10^{-4}$)	E_g (eV)
I2bm	5.0977	18.79	2.19
Pbcm	5.0988	19.07	2.15
Pnma	5.0971	19.03	2.09
$Ca_2Fe_2O_5$ (P_T = 1.7 D, τ=0.923)			
Symmetry	R (Å)	Δ ($\times 10^{-4}$)	E_g (eV)
I2bm	5.0173	11.16	2.16
Pbcm	5.0476	10.85	2.13
Pnma	4.9941	10.73	2.07

For small values of P_T, factor (*ii*) becomes the critical quantity to optimize, and minimizing Δ becomes more important than maximizing R.

I computed R and Δ for both of the compounds in all three tetrahedral chain ordering configurations. Interestingly, I found that although $Sr_2Fe_2O_5$ has smaller rotations, it has a larger chain dipole (P_T = 3.8 D) than $Ca_2Fe_2O_5$ (P_T = 1.7 D); generally, one would expect smaller rotations to generate a smaller dipole. This is due to the fact that the electric polarization generated by the apical oxygen atoms tends to cancel that from the equatorial oxygen atoms in the tetrahedra; however, the smaller rotations of the *octahedra* in $Sr_2Fe_2O_5$ means this cancellation happens to a lesser degree, increasing P_T. Again, at large values of P_T, the need to separate the dipoles, factor (*i*), overcomes the need to have regular octahedra, factor (*ii*). $Sr_2Fe_2O_5$ therefore exhibits the *Pbcm* structure, which allows for the best average in-plane separation (R, Table 7.2) of the large dipoles. In $Ca_2Fe_2O_5$, the larger octahedral rotations distort the octahedra more in the presence of tetrahedral chains; in combination with the small chain dipole, this therefore gives more importance to

the phase that keeps the octahedra most regular (Δ, Table 7.2). In this case, that is the *Pnma* structure.

Another approach for understanding these energetic competitions is to consider the the Goldschmidt tolerance factor as given in Equation 3.1.[108] In $Ca_2Fe_2O_5$ (τ=0.923), the *Pnma* phase least distorts the octahedra (as reflected in Δ in Table 7.2) and is therefore the most stable. As τ increases, the need to maximize the separation between dipoles overcomes the steric packing driving force for octahedral rotations and hence they decrease; because *Pbcm* best maximizes this distance (R in Table 7.2), it is the preferred phase for the larger $Sr_2Fe_2O_5$ (τ=0.976).

Finally, despite the structural differences between the bulk $Sr_2Fe_2O_5$ and $Ca_2Fe_2O_5$ phases, the DFT-PBEsol (indirect Γ-X) band gap remains nominally the same ($\sim$ 2.10 eV) across changes in chemistry and tetrahedral ordering. This is due to the fact that O 2*p* states make up the top of the valence band, while the bottom of the conduction band is made up of Fe 3*d* states, making the band gap largely independent of *A*-site chemistry. A more detailed analysis of the changes in the electronic gap is given for the thin film cases below.

7.2.2 Strained Phases

I next investigated the crystal and electronic structure of $Sr_2Fe_2O_5$ and $Ca_2Fe_2O_5$ under epitaxial strain. As mentioned previously, I now consider the orientation of the vacancies as another degree of freedom (*i.e.*, whether the vacancy layers are parallel or perpendicular to the substrate, Figure 3.5f-i), in addition to tetrahedral chain rotation and ordering. First, I find that when $Sr_2Fe_2O_5$ is constrained to a substrate, it retains the *Pbcm* ground state in both parallel (filled symbols) and perpendicular (empty symbols) substrate-vacancy orientations (Figure 7.2a, top), a fact that can be explained using the same arguments presented for the bulk phase. However, I also find

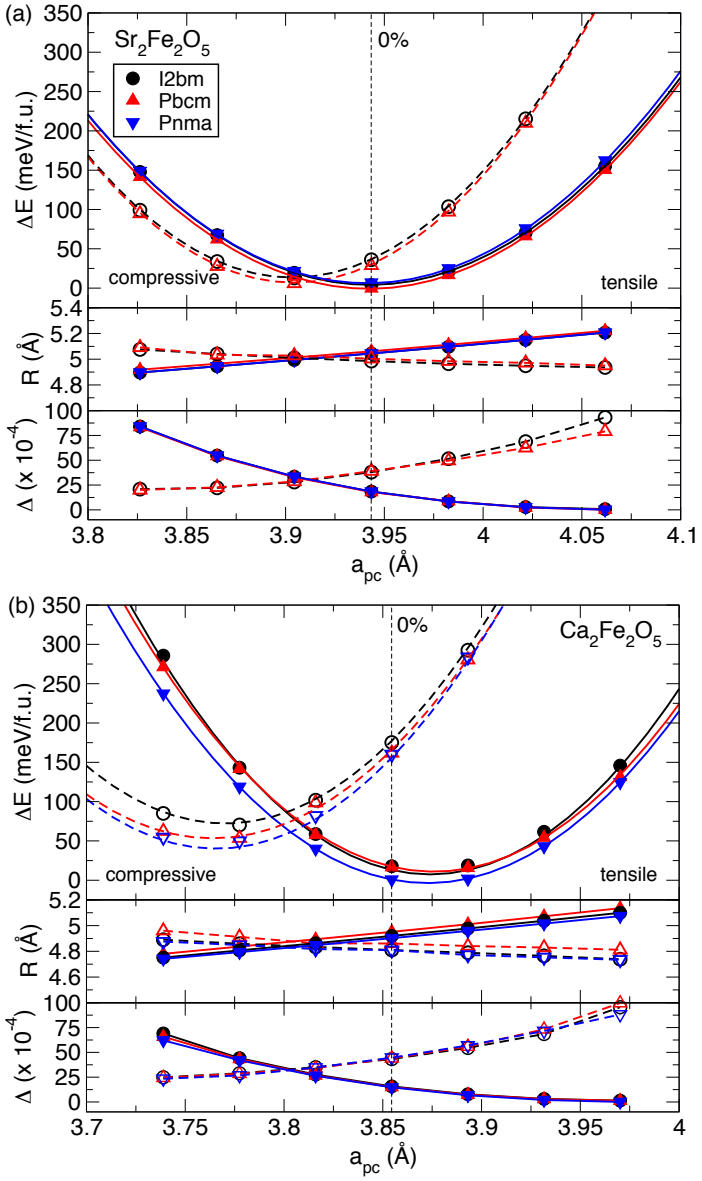

Figure 7.2: Energy of the different tetrahedral chain arrangements in the $Sr_2Fe_2O_5$ (left) and $Ca_2Fe_2O_5$ (right) structures as a function of epitaxial strain (top panels). In both cases, the parallel vacancy ordering (filled symbols) is stabilized under tensile strain, while perpendicular (empty symbols) is stabilized under compressive. This change in stabilization occurs at the point where either the parallel or perpendicular phase maximizes the average intralayer tetrahedral chain separation (R, middle panels) and minimizes the octahedral distortion effect (Δ, bottom panels).

that the perpendicular configuration of oxygen-deficient layers is stabilized over the parallel arrangement under small amounts of compressive strain. This is due to the fact that increasing compressive strain *decreases* the intralayer separation between tetrahedral chains if the vacancies are ordered parallel to the substrate (*i.e.*, becomes more energetically unfavorable), but *increases* R if the vacancies are perpendicular. The strain value at which the perpendicular ordering becomes more stable exactly coincides with the values at which the intralayer separation becomes greater (Figure 7.2a, middle) and the octahedral distortions become smaller (Figure 7.2a, bottom) than that of the parallel ordering.

One important detail to note is that $Sr_2Fe_2O_5$ has a relatively large pseudo-cubic lattice parameter (a_{pc}); only with some of the largest commercially available substrates can it be placed under tensile strain and stabilize the parallel orientation. Many experimental observations agree with our prediction of the energetic stability of vacancy orientation. Growth of $Sr_2Fe_2O_5$ near the transition point, such as on $SrTiO_3$ ($a_{pc} = 3.91$ Å), shows a competition between the two orientations,[400] whereas growth on larger substrates stabilizes the parallel orientation, such as on $KTaO_3$ ($a_{pc} = 3.99$ Å).[401]

When $Ca_2Fe_2O_5$ is placed under epitaxial strain the *Pnma* phase remains lowest in energy, while the *I2bm* and *Pbcm* structures become much closer in energy and strongly compete. As with $Sr_2Fe_2O_5$, the tetrahedral layers in $Ca_2Fe_2O_5$ switch to a perpendicular orientation under compressive strain, and parallel under tensile (Figure 7.2b, top). Once again, this occurs due to the perpendicular orientation maximizing the distance R between intralayer tetrahedral chains and minimizing octahedral distortions, Δ, under compression (Figure 7.2b, middle and bottom). Although the *Pnma* phase minimizes octahedral shearing as in the bulk phase, the very small differences in Δ between the strained phases means that it cannot be the only con-

trolling feature; instead there is a complex interplay between the various structural descriptors that produces the observed ground state. The fact that $Ca_2Fe_2O_5$ has a smaller pseudo-cubic lattice parameter than $Sr_2Fe_2O_5$ means that the parallel phase is experimentally accessible with much more modest strain. Experimental results on thin films of $Ca_2Fe_2O_5$ show that the vacancies order perpendicularly when grown on $LaSrAlO_4$ (LSAO, a_{pc} = 3.75 Å) and $LaAlO_3$ (a_{pc} = 3.79 Å), but order parallel on LSAT (a_{pc} = 3.87 Å) and $SrTiO_3$ (a_{pc} = 3.91 Å), again in agreement with these theoretical results.[140,402] Interestingly, the stabilization of the perpendicular phase under compressive strain and parallel phase under tensile strain does not hold across all brownmillerite oxide chemistries; in the cobaltates, for example, the trend is reversed.

I next investigate the structural evolution of these compounds under strain. For the structures with the parallel orientation, there are only the three bond angles defined previously to consider (Figure 7.1). Under increasing tensile strain, the FeO_4 tetrahedral chains become less distorted (decreasing Fe-O-Fe bond angle), while the octahedral angles and connections between the tetrahedral and octahedral layers become more distorted (increasing Fe-O-Fe bond angle). It should come as no surprise that this trend holds across all three types of ordered phases, as they are all very structurally similar with the exception of the relative orientation of tetrahedral chains (Figure 7.3). Additionally, the chemistry of the *A*-site, although influencing the magnitude of the tilts, does not affect this trend.

When the oxygen-deficient layers reorient to become perpendicular to the substrate, there are now two more angles to consider. In the previous geometries, only one angle of the tetrahedra and octahedra had to be considered owing to the fact that the equatorial oxygen atoms of each were in the plane of epitaxial strain. These same atoms are now oriented such that they are affected by both the plane of epi-

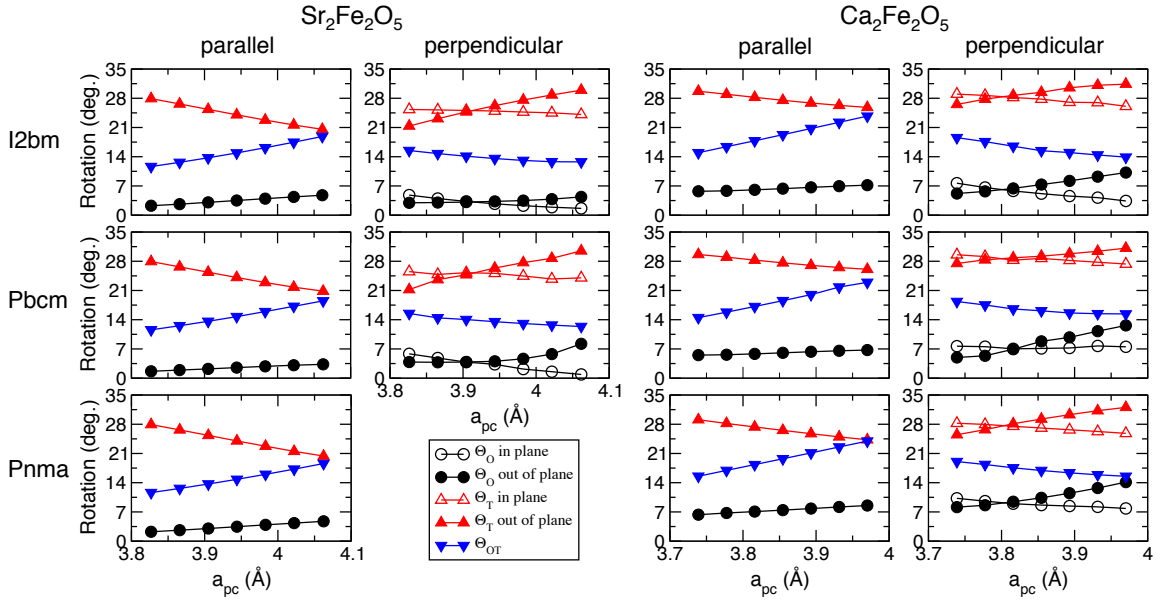

Figure 7.3: The effect of strain on the tilt angles (as defined in Figure 7.1) of the different $Sr_2Fe_2O_5$ (left) and $Ca_2Fe_2O_5$ (right) structures with both parallel and perpendicular vacancy orientation.

taxial strain and the strain-induced changes to the out-of-plane lattice parameter. In order to obtain a full understanding of the structural distortions in this case, I separate the tetrahedral and octahedral angles into in-plane and out-of-plane components. In this perpendicular orientation, increasing tensile strain increases the out-of-plane component of the octahedral and tetrahedral angles, while decreasing the in-plane component, as well as the angle between the layers.

Finally, the band gap of both materials is strongly influenced by strain, ranging from 1.8 eV to 2.6 eV for $Sr_2Fe_2O_5$ (Figure 7.4a) and 1.6 eV to 2.5 eV for $Ca_2Fe_2O_5$ (Figure 7.4b). In both compounds, increasing tensile strain results in an increase of the band gap for the parallel orientation of vacancies, but interestingly, a decrease in the perpendicular orientation. This is due to how an increase in the lattice parameters influences the connectivity of the tetrahedrally and octahedrally coordinated iron atoms (*i.e.*, Θ_{OT}). For the films with the parallel vacancy orientation, Θ_{OT} deviates

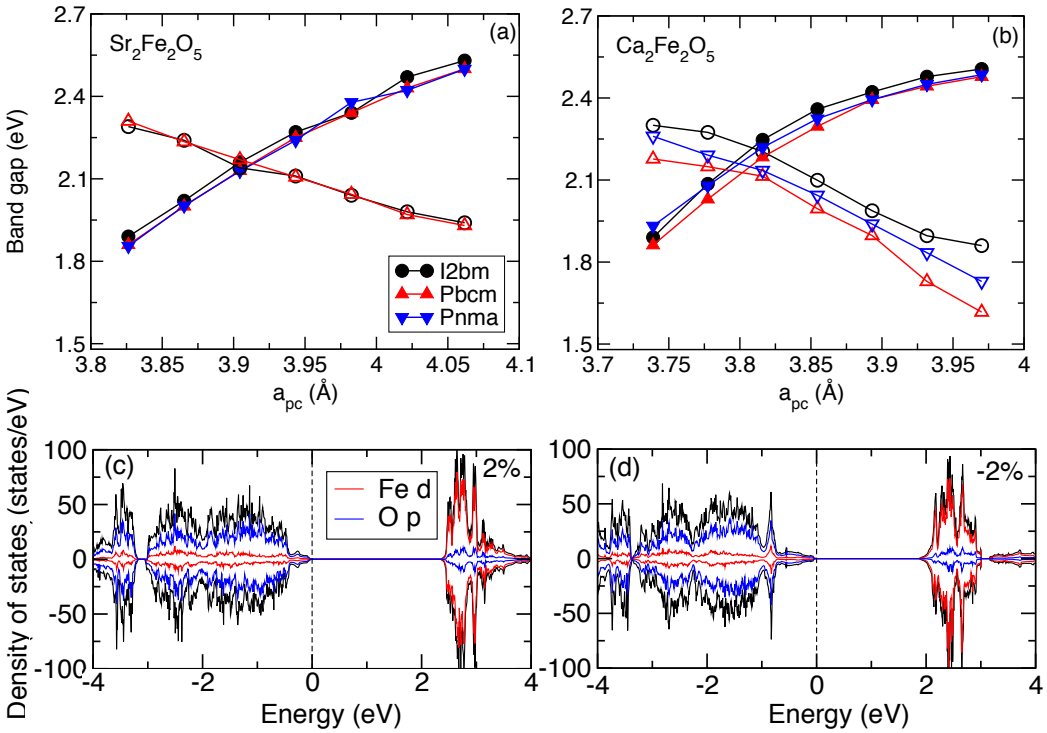

Figure 7.4: The band gap of (a) $Sr_2Fe_2O_5$ and (b) $Ca_2Fe_2O_5$ are strongly influenced by epitaxial strain; the electronic gap for thin film structures with vacancies ordered parallel to the substrate (filled symbols) increases as tensile strain increases, but decreases in the perpendicular orientation (empty symbols). This electronic structure response occurs owing to the manner in which strain affects the angle between the tetrahedral and octahedral layers. The *Pbcm* structure of $Sr_2Fe_2O_5$ with vacancies parallel to the substrate, for example, has a ~ 0.3 eV larger band gap under (c) 2% tensile strain when compared to (d) 2% compressive strain as seen by the change in the atom-resolved densities of states.

further away from 180° as tensile strain increases; this results in decreased overlap of the Fe *d*-orbitals and O *p*-orbitals, giving a higher band gap. Figures 7.4c and 7.4d show, as an example, the difference in the band gap of parallel-oriented $Sr_2Fe_2O_5$ at 2% (2.43 eV) and -2% (2.00 eV). The opposite effect occurs in the perpendicular case, where a decrease in Θ_{OT} provides better overlap and thus a smaller band gap through increased bandwidth.

7.2.3 Comparison to Perovskite Oxides

The fact that BO_6 octahedra in perovskite oxides form a flexible corner-connected network (Figure 3.4a) allows them to easily rotate in space about the different crystallographic axes. The size of these rotations directly affect the magnitude of the B–O–B bond angles, which in turn impacts many electronic and magnetic properties. Although there are 15 distinct ways in which the octahedra can cooperatively rotate while retaining connectivity (as identified by Glazer),[104] the vast majority exhibit either an orthorhombic or rhombohedral tilt pattern (given by $a^-a^-c^+$ or $a^-a^-a^-$ in Glazer notation, respectively). A high degree of control over the electronic structure can be achieved by using epitaxial strain (or chemical substation, as captured by τ) to control these rotations, owing primarily to the strong coupling between the lattice and electronic degrees of freedom in perovskites;[31,338,403,404] as mentioned previously, buckling of the B–O–B bond away from a linear 180° configuration (*i.e.*, increasing the magnitude of the octahedral rotations) decreases the overlap between the O p and metal B d orbitals, thereby increasing the band gap in insulating compounds or inducing bandwidth-driven metal-insulator transitions.[405–410]

As I have shown, the distinct alternating tetrahedral and octahedral layers in brownmillerites allow for many more structural degrees of freedom than perovskites (Figure 7.5a). Application of the same forces (chemical pressure and epitaxial strain) affects the interlayer separation of tetrahedra (*i.e.*, b lattice parameter), as well as the rotations (connectivity) of the different polyhedra (given by Θ_O, Θ_T, and Θ_{OT}); each of these in turn influences the octahedral distortions (Δ), the intralayer dipole separation (R), and the magnitude of the local tetrahedral dipoles (P_T). The balance of these different factors is then what governs the equilibrium structure—the tetrahedral chain ordering and, for the case of thin films, the orientation of the vacancies relative to the substrate (Figure 7.5b).

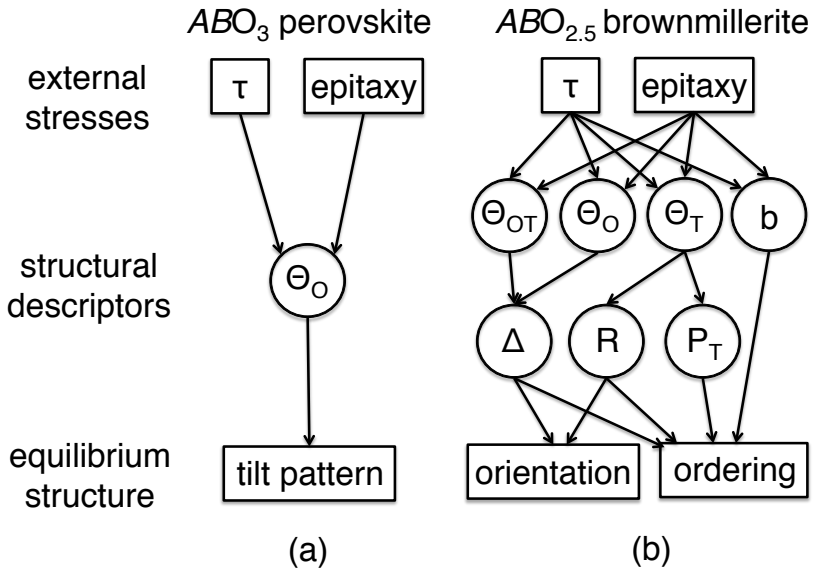

Figure 7.5: The effect of different stress stimuli (ionic size or chemical pressure [captured by τ] and epitaxy) on various structural descriptors, which combine to produce the equilibrium crystal structure in (a) perovskite and (b) brownmillerite oxides.

A feature implied here is that the electronic properties of these oxides are also a structural consequence; hence, control over the structural descriptors makes it possible to control the electronic response. Indeed, the band gaps of the brownmillerites are highly sensitive to rotations of the polyhedra; like the perovskites, the gap opens as the rotations increase owing to a change in orbital overlap. Unlike perovskites, however, it is not solely a single B–O–B bond angle controlling the electronic structure, which is due to the breaking of the structural topology by the oxygen-vacant (tetrahedral) layers. For the brownmillerite oxides, it is the out-of-plane angle between the BO_4 tetrahedra and BO_6 octahedra, given by Θ_{OT} (or, alternatively, B_{tet}–O–B_{oct}), that controls the gap and band edge character. Furthermore, strain affects the band gap of parallel or perpendicularly oriented brownmillerites in completely opposite (asymmetric) ways owing to the response of Θ_{OT} to the biaxial strain state. Although strain has been used to control functional properties in perovskites, it appears to induce even more interesting responses in brownmillerites owing to the additional

structural degrees of freedom present.

8. CONCLUSIONS AND OUTLOOK

In this dissertation, I first developed two new models for describing inversion symmetry breaking *a priori* from basic building units of inorganic compounds and engineering new non-centrosymmetric materials. Although previous work had identified important features necessary for inducing acentric properties from non-polar constituents,[20,287,411] a comprehensive framework was missing. In Chapter 5, I first divided geometric improper ferroelectrics based upon the microscopic mechanism responsible for producing the spontaneous polarization; I then discussed how the basic building units can be assembled to lift inversion symmetry, applied these principles to real materials by systemically establishing what types of distortions and cation ordering schemes are capable of producing non-centrosymmetric perovskites, and then identified the chemistries necessary to induce these distortions.

I next used the information gleaned from this analysis to design novel polar materials, investigate their bulk properties and response under strain, and substantiate the structural and chemical criteria put forth by these models; this comprises Chapters 6 and 7. These results show how an understanding and combined application of crystallography, physics, and chemistry principles can allow for the rapid first-principles discovery of new electronic materials, as well as offer many compounds for experimental investigation.

From a computational standpoint, there is still a wide variety of work that can be continued by starting from these results. The investigation of real materials in Chapters 6 and 7 only scratched the surface of the structural phase space described by Figure 5.12; indeed, much of my recent work has focused on understanding how to access more exotic distortions such as the $a^0a^0c^+$ tilt pattern.[412] Furthermore, the families of materials which exhibit a geometric improper ferroelectric mechanism

(such as those I focused on in Chapter 5) are ripe for magnetic substitution for the creation of new multiferroics or magnetoelectrics. Because the origin of the electric polarization in such systems is not electrostatic or due to SOJT-activity, but rather "geometric" distortions, the polarization can be obtained independent of the magnetic ordering. Finally, all of the density functional theory calculations performed in this thesis were necessarily performed at zero Kelvin. Different types of computational approaches such as model Hamiltonians, molecular dynamics, or Monte Carlo could be applied to study the temperature-dependent properties of these materials. Related scientific questions include:

- strain to control cation ordering
- effects of disorder and interdiffusion in cation ordered materials
- domain microstructure and switching

Although this thesis consists purely of computational work, experimental verification of these theoretical predictions is currently ongoing. One of the most difficult challenges facing researchers is that of synthesis; the schemes proposed in this thesis require the incorporation of multiple cations in a highly ordered fashion. As discussed in Chapter 1, however, non-equilibrium growth methods such as pulsed laser deposition (PLD) or molecular beam epitaxy (MBE) provide an extremely viable route to the realization of these types of materials.[338,413–416] To this end, my experimental collaborators at Drexel University have successfully grown ultrashort 1/1 period superlattices of $SrFeO_{2.5}$ and $CaFeO_{2.5}$ (discussed in Chapter 7) as thin films motivated by my predictions, while microscopy results from Pennsylvania State University have shown that cation ordering of these two centrosymmetric compounds indeed lifts inversion symmetry.

Finally, I would like to discuss the functionality challenge, which includes the op-

timization of properties necessary for integration into electronic devices such as the magnitude of the ferroelectric polarization, Curie temperature, and ease of switching. The multi-mode coupling origin for the electric polarization in these materials begs the question: to what extent can *large* polarizations be achieved, and to what extent can the polarization be reversed (*i.e.* from $+P$ to $-P$), which is required for assigning the 'ferroelectric' designation to these materials? The latter is also critical towards realizing strong magnetoelectric coupling,[301] which is sought to be exploited in a variety of electronic applications, including memory, tunnel junction, spintronic, and microwave devices.[14,15,417,418] Developing a theory for switching in the various improper ferroelectrics is crucial in realizing technologically useful materials. Despite these challenges, the results presented in this thesis provide a useful starting point for the continued discovery and investigation of non-centrosymmetric materials.

Bibliography

[1] P. Shiv Halasyamani and Kenneth R. Poeppelmeier. Noncentrosymmetric oxides. *Chemistry of Materials*, 10(10):2753–2769, 1998.

[2] O. Auciello, J. F. Scott, and R. Ramesh. The physics of ferroelectric memories. *Physics Today*, 51(7):22–27, 1998.

[3] S. T. Lau, K.-H. Lam, H. L. W. Chan, C. L. Choy, H. S. Luo, Q. R. Yin, and Z. W. Yin. High performance relaxor-based ferroelectric single crystals for ultrasonic transducer applications. *Materials Science and Engineering: B*, 111:25–30, 2004.

[4] J. F. Scott. *Ferroelectric Memories*. Springer-Verlag, 2000.

[5] M. Y. Shuravlev, R. F. Rabirianov, S. S. Jaswal, and E. Y. Tsymbal. Giant electroresistance in ferroelectric tunnel junctions. *Physical Review Letters*, 94:246802, 2005.

[6] A. Jamil and T. S. Kalkur. Tunable ferroelectric capacitor-based voltage-controlled oscillator. *IEEE Transactions on Ultrasonics, Ferroelectrics, and Frequency Control*, 54:222–226, 2007.

[7] V. Garcia, S. Fusil, K. Bouzehouane, S. Enouz-Vedrenne, N. D. Mathur, A. Barthélémy, and M. Bibes. Giant tunnel electroresistance for non-destructive readout of ferroelectric states. *Nature*, 460:81–84, 2009.

[8] R. Guo, L. You, Y. Zhou, Z. S. Lim, X. Zou, L. Chen, R. Ramesh, and J. Wang. Non-volatile memory based on the ferroelectric photovoltaic effect. *Nature Communications*, 4:1990, 2013.

[9] E. Defay. *Ferroelectric Tunable Capacitors*, pages 341–378. John Wiley and Sons, Inc., 2013.

[10] V. Garcia, S. Fusil, K. Bouzehouane, S. Enouz-Vedrenne, N. D. Mathur, A. Barthélémy, and M. Bibes. Exploiting dimensionality and defect mitigation to create tunable microwave dielectrics. *Nature*, 502:532–536, 2013.

[11] Y. Chen, K.-H. Lam, D. Zhou, Q. Yue, Y. Yu, J. Wu, W. Qiu, L. Sun, C. Zhang, H. Luo, H. L. W. Chan, and J. Dai. High performance relaxor-based ferroelectric single crystals for ultrasonic transducer applications. *Sensors*, 14:13730–13759, 2014.

[12] K. T. Butler, J. M. Frost, and A. Walsh. Ferroelectric materials for solar energy conversion: photoferroics revisited. *Energy Environmental Science*, 8:838–848, 2015.

[13] T. Kirchartz, J. Bisquert, I. Mora-Sero, and G. Garcia-Belmonte. Classification of solar cells according to mechanisms of charge separation and charge collection. *Physical Chemistry Chemical Physics*, 17:4007–4014, 2015.

[14] M. Bibes and A. Barthélémy. Multiferroics: Towards a magnetoelectric memory. *Nature Materials*, 7:425–426, 2007.

[15] M. Gajek, M. Bibes, S. Fusil, K. Bouzehouane, J. Fontcuberta, A. Barthélémy, and A. Fert. Tunnel junctions with multiferroic barriers. *Nature Materials*, 6:296–302, 2007.

[16] C.-H. Lee, N. D. Orloff, T. Birol, Y. Zhu, V. Goian, E. Rocas, R. Haislmaier, E. Vlahos, J. A. Mundy, L. F. Kourkoutis, Y. Nie, M. D. Biegalski, J. Zhang, M. Bernhagen, N. A. Benedek, Y. Kin, J. D. Brock, R. Uecker, X. X. Xi, V. Gopalan, D. Nuzhnyy, S. Kamba, D. A. Muller, I. Takeuchi, J. C. Booth, C. J. Fennie, and D. G. Schlom. Exploiting dimensionality and defect mitigation to create tunable microwave dielectrics. *Nature*, 502:532–536, 2013.

[17] H. Yu, W. Zhang, J. Young, J. M. Rondinelli, and P. S. Halasyamani. Design and synthesis of the beryllium-free deep-ultraviolet nonlinear optical material $Ba_3(ZnB_5O_{10})PO_4$. *Advanced Materials*, 27:7380–7385, 2015.

[18] X. Dong, Q. Jing, Y. Shi, Z. Yang, S. Pan, K. R. Poeppelmeier, J. Young, and J. M. Rondinelli. $Pb_2Ba_3(BO_3)_3Cl$: A material with large SHG enhancement activated by Pb-chelated BO_3 groups. *Journal of the American Chemical Society*, 137:9417–9422, 2015.

[19] M. D. Donakowski, R. Gautier, J. Yeon, D. T. Moore, J. C. Nino, P. S. Halasyamani, and K. R. Poeppelmeier. The role of polar, lamdba (λ)-shaped building units in noncentrosymmetric inorganic structures. *Journal of the American Chemical Society*, 134:7679–7689, 2012.

[20] J. M. Rondinelli and C. J. Fennie. Octahedral rotation-induced ferroelectricity in cation ordered perovskites. *Advanced Materials*, 24:1961–1968, 2012.

[21] J. Young and J. M. Rondinelli. Atomic scale design of polar perovskite oxides without second-order Jahn-Teller ions. *Chemistry of Materials*, 25:4545–4550, 2013.

[22] J. Young, A. Stroppa, S. Picozzi, and J. M. Rondinelli. Anharmonic lattice interactions in improper ferroelectrics for multiferroic design. *Journal of Physics: Condensed Matter*, 27:283202, 2015.

[23] J. Chakhalian, J. W. Freeland, A. J. Millis, C. Panagopoulos, and J. M. Rondinelli. Emergent properties in plane view: Strong correlations at oxide interfaces. *Reviews of Modern Physics*, 86:1189–1202, 2014.

[24] K. R. Poeppelmeier and J. M. Rondinelli. Mismatched lattices patched up. *Nature Chemistry*, 8:292–294, 2016.

[25] J. Chakhalian, J. W. Freeland, H. U. Habermeier, G. Cristiani, G. Khaliullin, M. van Veenendaal, and B. Keimer. Orbital reconstruction and covalent bonding at an oxide interface. *Science*, 318:1076–1077, 2007.

[26] M. O'Sullivan, J. Hadermann, M. S. Dyer, S. Turner, J. Alaria, T. D. Manning, A. M. Abakumov, J. B. Claridge, and M. J. Rosseinsky. Interface control by chemical and dimensional matching in an oxide heterostructure. *Nature Chemistry*, 8:347–353, 2016.

[27] A. Ohtomo and H. Y. Hwang. A high-mobility electron gas at the $LaAlO_3/SrTiO_3$ heterointerface. *Nature*, 427:423–426, 2004.

[28] J. A. Bert, B. Kalisky, C. Bell, M. Kim, Y. Hikita, H. Y. Hwang, and K. A. Moler. Direct imaging of the coexistence of ferromagnetism and superconductivity at the $LaAlO_3/SrTiO_3$ interface. *Nature Physics*, 7:767–771, 2011.

[29] E. Bousquet, M. Dawber, N. Stucki, C. Lichtensteiger, P. Hermet, S. Gariglio, J.-M. Triscone, and P. Ghosez. Improper ferroelectricity in perovskite oxide artificial superlattices. *Nature*, 452:732–736, 2008.

[30] N. A. Benedek, J. M. Rondinelli, H. Djani, P. Ghosez, and P. Lightfoot. Understanding ferroelectricity in layered perovskites: new ideas and insights from theory and experiments. *Dalton Transactions*, 44:10543–10558, 2015.

[31] J. M. Rondinelli and N. A. Spaldin. Structure and properties of functional oxide thin films: Insights from electronic-structure calculations. *Advanced Materials*, 23:3363–3381, 2011.

[32] D. G. Schlom, L.-Q. Chen, X. Pan, A. Schmehl, and M. A. Zurbuchen. A thin film approach to engineering functionality into oxides. *Journal of the American Ceramics Society*, 91:2429–2454, 2008.

[33] Y. F. Nie, Y. Zhu, C.-H. Lee, L. F. Kourkoutis, J. A. Mundy, J. Junquera, Ph. Ghosez, D. J. Baek, S. Sung, X. X. Xi, K. M. Shen, D. A. Muller, and D. G. Schlom. Atomically precise interfaces from non-stoichiometric deposition. *Nature Communications*, 5:4530, 2014.

[34] J. H. Lee, G. Luo, I. C. Tung, S. H. Chang, Z. Luo, M. Malshe, M. Gadre, A. Bhattacharya, S. M. Nakhmanson, J. A. Eastman, H. Hong, J. Jellinek, D. Morgan, D. D. Fong, and J. W. Freeland. Dynamic layer rearrangement during growth of layered oxide films by molecular beam epitaxy. *Nature Materials*, 13:879–883, 2014.

[35] D. G. Schlom. Perspective: Oxide molecular-beam epitaxy rocks! *APL Materials*, 3:062403, 2015.

[36] A. T. Zayak, X. Huang, J. B. Neaton, and K. M. Rabe. Structural, electronic, and magnetic properties of $SrRuO_3$ under epitaxial strain. *Physical Review B*, 74:094104, 2006.

[37] J. Young and J. M. Rondinelli. Crystal structure and electronic properties of bulk and thin film brownmillerite oxides. *Physical Review B*, 92:174111, 2015.

[38] R. O. Jones and O. Gunnarsson. The density functional formalism, its applications and prospects. *Reviews of Modern Physics*, 61:689–745, 1989.

[39] K. Burke. *The ABC of DFT*. University of California, Irvine, 2007.

[40] R. O. Jones. Density functional theory: Its origins, rise to prominence, and future. *Reviews of Modern Physics*, 87:897–923, 2015.

[41] E. Schrödinger. An undulatory theory of the mechanics of atoms and molecules. *Physical Review*, 28:1049–1070, 1926.

[42] M. Born and R. Oppenheimer. Zur quantentheorie der molekle. *Annalen der Physik*, 84:457–484, 1927.

[43] P. Hohenberg and W. Kohn. Inhomogenous electron gas. *Physical Review*, 136:B864–B871, 1964.

[44] W. Kohn and L. J. Sham. Self-consistent equations including exchange and correlation effects. *Physical Review*, 140:A1133–A1138, 1964.

[45] J. P. Perdew and K. Schmidt. Jacob‘s ladder of density functional approximations for the exchange-correlation energy. *AIP Conference Proceedings*, 577:1–20, 2001.

[46] J. P. Perdew, A. Ruzsinszky, J. Tao, V. N. Staroverov, and G. E. Scuseria. Prescription for the design and selection of density functional approximations: More constraint satisfaction with fewer fits. *Journal of Chemical Physics*, 123:062201, 2005.

[47] J. C. Slater. A simplification of the Hartree-Fock method. *Physical Review*, 81:385–390, 1951.

[48] D. M. Ceperley and B. J. Alder. Ground state of the electron gas by a stochastic method. *Physical Review Letters*, 45:566–569, 1980.

[49] J. P. Perdew and Y. Wang. Accurate and simple analytic representation of the electron-gas correlation energy. *Physical Review B*, 45:13244, 1992.

[50] S. Redner. Citation statistics from 110 years of Physical Review. *Physics Today*, pages 49–54, 2005.

[51] A. van de Walle and G. Ceder. Correcting overbinding in local-density-approximation calculations. *Physical Review B*, 59:14992, 1999.

[52] J. P. Perdew, J. A. Chevary, S. H. Vosko, K. A. Jackson, M. R. Pederson, D. J. Singh, and C. Fiolhais. Atoms, molecules, solids, and surfaces: Applications of the generalized gradient approximation for exchange and correlation. *Physical Review B*, 46:6671, 1992.

[53] J. P. Perdew, K. Burke, and M. Ernzerhof. Generalized gradient approximation made simple. *Physical Review Letters*, 77:3865, 1996.

[54] John P. Perdew, Adrienn Ruzsinszky, Gábor I. Csonka, Oleg A. Vydrov, Gustavo E. Scuseria, Lucian A. Constantin, Xiaolan Zhou, and Kieron Burke. Restoring the density-gradient expansion for exchange in solids and surfaces. *Physical Review Letters*, 100(13):136406, 2008.

[55] A. D. Becke. A new mixing of Hartree-Fock and local density functional theories. *Journal of Chemical Physics*, 98:1372–1377, 1996.

[56] J. P. Perdew, M. Ernzerhof, and K. Burke. Rationale for mixing exact exchange with density functional approximations. *Journal of Chemical Physics*, 105:9982–9985, 1996.

[57] J. Heyd, G. E. Scuseria, and M. Ernzerhof. Hybrid functionals based on a screened Coulomb potential. *Journal of Chemical Physics*, 118:8207, 2003.

[58] D. Koller, P. Blaha, and F. Tran. Hybrid functionals for solids with an optimized Hartree-Fock mixing parameter. *Journal of Physics: Condensed Matter*, 25:435503, 2013.

[59] F. Bloch. Über die quantenmechanik der elektronen in kristallgittern. *Zeitschrift für Physik*, 52:555–600, 1929.

[60] Hendrik J. Monkhorst and James D. Pack. Special points for Brillouin-zone integrations. *Physical Review B*, 13(12):5188–5192, 1976.

[61] U. von Barth and C. D. Gelatt. Validity of the frozen-core approximation and pseudopotential theory for cohesive energy calculations. *Physical Review B*, 21:2222, 1980.

[62] D. R. Hamann, M. Schlüted, and C. Chiang. Norm-conserving pseudopotentials. *Physical Review Letters*, 43:1494–1497, 1979.

[63] P. E. Blöchl. Projector augmented-wave method. *Physical Review B*, 50(24):17953–17979, 1994.

[64] J. P. Perdew. Density functional theory and the band gap problem. *International Journal of Quantum Chemistry*, 19:497–523, 1986.

[65] E. Morosan, D. Natelson, A. H. Nevidomskyy, and Q. Si. Strongly correlated materials. *Advanced Materials*, 24:4896–4923, 2012.

[66] A. Georges, G. Kotliar, W. Krauth, and M. J. Rozenberg. Dynamical mean-field theory of strongly correlated fermion systems and the limit of infinite dimensions. *Reviews of Modern Physics*, 68:13–121, 1996.

[67] W. G. Aulbur, L. Jönsson, and J. W. Wilkins. Quasiparticle calculations in solids. *Solid State Physics*, 54:1–218, 1999.

[68] J. Hubbard. Electron correlations in narrow energy bands. IV. the atomic representation. *Proceedings of the Royal Society of London. Series A. Mathematical and Physical Sciences*, 285:542–560, 1965.

[69] B. Himmetoglu, A. Floris, S. de Gironcoli, and M. Cococcioni. Hubbard-corrected DFT energy functionals: The LDA+U description of correlated systems. *International Journal of Quantum Chemistry*, 114:14–49, 2014.

[70] L. Lindsay, D. A. Broido, and T. L. Reinecke. Thermal conductivity and large isotope effect in GaN from first principles. *Physical Review Letters*, 109:095901, 2012.

[71] I. Errea, M. Calandra, C. J. Pickard, J. Nelson, R. J. Needs, Y. Li, H. Liu, Y. Zhang, Y. Ma, and F. Mauri. High-pressure hydrogen sulfide from first principles: A strongly anharmonic phonon-mediated superconductor. *Physical Review Letters*, 114:157004, 2015.

[72] L.-F. Huang and J. M. Rondinelli. Electrochemical phase diagrams for Ti oxides from density functional calculations. *Physical Review B*, 92:245126, 2015.

[73] T. Morshedloo, M. R. Roknabadi, and M. Behdani. First-principles study of the superconductivity in MgB_2 bulk and in its bilayer thin film based on electron-phonon coupling. *Physica C: Superconductivity and its Applications*, 509:1–4, 2015.

[74] A. Jain and A. J. H. McGaughey. Thermal transport by phonons and electrons in aluminum, silver, and gold from first principles. *Physical Review B*, 93:081206(R), 2016.

[75] N. W. Ashcroft and N. D. Mermin. *Solid State Physics*. Thomson Learning, Inc., 1976.

[76] C. Kittel. *Introduction to Solid State Physics*. John Wiley and Sons, Inc., 2005.

[77] S. Baroni, S. de Gironcoli, A. Dal Corso, and P. Giannozzi. Phonons and related crystal properties from density-functional perturbation theory. *Reviews of Modern Physics*, 73:515–562, 2001.

[78] M. V. Abrashev, A. P. Litvinchuk, M. N. Iliev, R. L. Meng, V. N. Popov, V. G. Ivanov, R. A. Chakalov, and C. Thomsen. Comparative study of optical phonons in the rhombohedrally distorted perovskites $LaAlO_3$ and $LaMnO_3$. *Physical Review B*, 59:4146, 1999.

[79] G. Kresse and J. Hafner. *Ab initio* molecular dynamics for liquid metals. *Physical Review B*, 47(1):558–561, 1993.

[80] G. Kresse and J. Furthmüller. Efficiency of ab-initio total energy calculations for metals and semiconductors using a plane-wave basis set. *Computational Materials Science*, 6:15–50, 1996.

[81] S. L. Dudarev, G. A. Botton, S. Y. Savrasov, C. J. Humphreys, and A. P. Sutton. Electron-energy-loss spectra and the structural stability of nickel oxide: An LSDA+U study. *Physical Review B*, 57:1505, 1998.

[82] B. J. Campbell, H. T. Stokes, D. E. Tanner, and D. M. Hatch. ISODISPLACE: An internet tool for exploring structural distortions. *Journal of Applied Crystallography*, 39:607–614, 2006.

[83] K. Momma and F. Izumi. VESTA 3 for the three-dimensional visualization of crystal, volumetric, and morphology data. *Journal of Applied Crystallography*, 44:1272–1276, 2011.

[84] S. Jin, T. H. Tiefel, M. McCormack, R. A. Fastnacht, R. Ramesh, and L. H. Chen. Thousandfold change in resistivity in magnetoresistive La-Ca-Mn-O films. *Science*, 15:413–415, 1994.

[85] J. G. Bednorz and K. A. Müller. Perovskite-type oxides – the new approach to high-T_c superconductivity. *Reviews of Modern Physics*, 60:585–600, 1988.

[86] B. Yan, M. Jansen, and C. Felser. A large-energy-gap oxide topological insulator based on the superconductor $BaBiO_3$. *Nature Physics*, 9:709–711, 2013.

[87] Y. Saito, H. Takao, T. Tani, T. Nonoyama, K. Takatori, T. Homma, T. Nagaya, and M. Nakamura. Lead-free piezoceramics. *Nature*, 432:84–87, 2004.

[88] M. Li, M. J. Pietrowski, R. A. De Souza, H. Zhang, I. M. Reaney, S. N. Cook, J. A. Kilner, and D. C. Sinclair. A family of oxide ion conductors based on the ferroelectric perovskite $Na_{0.5}Bi_{0.5}TiO_3$. *Nature Materials*, 13:31–35, 2014.

[89] N. C. Bristowe, J. Varignon, D. Fontaine, E. Bousquet, and Ph. Ghosez. Ferromagnetism induced by entangled charge and orbital orderings in ferroelectric titanate perovskites. *Nature Communications*, 6:6677, 2015.

[90] X. Ou, Z. Li, F. Fan, H. Wang, and H. Wu. Long-range magnetic interaction and frustration in double perovskites Sr_2NiIrO_6 and Sr_2ZnIrO_6. *Scientific Reports*, 4:7542, 2014.

[91] V. Luaña, A. Costales, A. M. Pendás, M/ Flórez, and V. M. García Fernández. Structural and chemical stability of halide perovskites. *Solid State Communications*, 104:47–50, 1997.

[92] I. N. Flerov, M. V. Gorev, A. Tressaud, and N. M. Laptash. Perovskite-like fluorides and oxyfluorides: Phase transitions and caloric effects. *Crystallographic Reports*, 56:9–17, 2011.

[93] N. Charles and J. M. Rondinelli. Microscopic origin of pressure-induced isosymmetric transitions in fluoromanganate cryolites. *Physical Review B*, 90:094114, 2014.

[94] N. Charles and J. M. Rondinelli. Ferroelectricity in d^0 double perovskite fluoroscandates. *Physical Review B*, 92:054111, 2015.

[95] R. A. Lelieveld and D. J. W. Ijdo. Sulphides with the $GdFeO_3$ structure. *Acta Crystallographica Section B*, 36:2223–2226, 1980.

[96] J. W. Bennett, I. Grinberg, and A. M. Rappe. Effect of substituting of S for O: The sulfide perovskite $BaZrS_3$ investigated with density functional theory. *Physical Review B*, 79:235115, 2009.

[97] R. Sarmiento-Pèrez, T. F. T. Cerqueira, S. Körbel, S. Botti, and M. A. L. Marques. Prediction of stable nitride perovskites. *Chemistry of Materials*, 27:5957–5963, 2015.

[98] M. Yang, J. Oró-Solé, J. A. Rodgers, A. B. Jorge, A. Fuertes, and J. P. Attfield. Anion order in perovskite oxynitrides. *Nature Chemistry*, 3:47–52, 2011.

[99] E. J. Moon, Y. Xie, E. D. Laird, D. J. Keavney, C. Y. Li, and S. J. May. Fluorination of epitaxial oxides: Synthesis of perovskite oxyfluoride thin films. *Journal of the American Chemical Society*, 136:2224–2227, 2014.

[100] M. Leblanc, V. Maisonneuve, and A. Tressaud. Crystal chemistry and selected physical properties of inorganic fluorides and oxide-fluorides. *Chemical Reviews*, 115:1191–1254, 2015.

[101] P. M. Woodward. Octahedral tilting in perovskites. I. geometrical considerations. *Acta Crystallographica Section B*, 53:32–43, 1997.

[102] P. M. Woodward. Octahedral tilting in perovskites. II. structure stabilizing forces. *Acta Crystallographica Section B*, 53:44–66, 1997.

[103] M. W. Lufaso and P. M. Woodward. Prediction of the crystal structures of perovskites using the software program SPuDS. *Acta Crystallographica Section B*, 57:725–738, 2001.

[104] A. M. Glazer. The classification of tilted octahedra in perovskites. *Acta Crystallographica Section B*, 28:3384–3392, 1972.

[105] A. M. Glazer. Simple ways of determining perovskite structures. *Acta Crystallographica Section A*, 31:756–762, 1975.

[106] K. S. Aleksandrov. The sequences of structural phase transitions in perovskites. *Ferroelectrics*, 14:801–805, 1976.

[107] C. J. Howard and H. T. Stokes. Group-theoretical analysis of octahedral tilting in perovskites. *Acta Crystallographica Section B*, 54:782–789, 1998.

[108] V. M. Goldschmidt. Die gesetze der krystallochemie. *Naturwissenschaften*, 14:477–485, 1926.

[109] R. D. Shannon. Revised effective ionic radii and systematic studies of interatomic distances in halides and chalcogenides. *Acta Crystallographica*, A32:751–767, 1976.

[110] I. D. Brown. Bond valences: a simple structural model for inorganic chemistry. *Chemical Society Reviews*, 7:359–376, 1978.

[111] H. Falcón, A. E. Goeta, G. Punte, and R. E. Carbonio. Crystal structure refinement and stability of $LaFe_xNi_{1-x}O_3$ solid solutions. *Journal of Solid State Chemistry*, 133:379–385, 1997.

[112] H. Yusa, N. Sata, and Y. Ohishi. Rhombohedral (9R) and hexagonal (6H) perovskites in barium silicates under high pressure. *American Mineralogist*, 92:648–654, 2007.

[113] S. A. Larregola, J. Zhou, J. A. Alonso, V. Pomjakushin, and J. B. Goodenough. New routes to synthesizing an ordered perovskite $CaCu_3Fe_2Sb_2O_{12}$ and its magnetic structure by neutron powder diffraction. *Inorganic Chemistry*, 53:4281–4283, 2014.

[114] A. Salinas-Sanchez, J. L. Garcia-Munoz, J. Rodriguez-Carvajal, R. Saez-Puche, and J. L. Martinez. Structural characterization of BaCuO, (R = Y, Lu, Yb, Tm, Er, Ho, Dy, Gd, Eu and Sm) oxides by x-ray and neutron diffraction. *Journal of Solid State Chemistry*, 100:201–211, 1992.

[115] G. H. Rao, K. Bäruer, and I. D. Brown. Bond-valence analysis on the structural effects in magnetoresistive manganese perovskites. *Journal of Physics: Condensed Matter*, 10:L757–L763, 1998.

[116] G. King and P. M. Woodward. Cation ordering in perovskites. *Journal of Materials Chemistry*, 20:5785–5796, 2010.

[117] M. L. López, M. L. Veiga, and C. Pico. Cation ordering in distorted perovskites $(MLa)(MgTe)O_6$, M=Na,K. *Journal of Materials Chemistry*, 4:547–550, 1994.

[118] M. A. Arillo, J. Gómez, M. L. López, C. Pico, and M. L. Veiga. Structural characterization and properties of the perovskite (NaLa)(MW)O_6 (M=Co, Ni): two new members in the group-subgroup relations for the perovskite-type structures. *Journal of Materials Chemistry*, 7:801–806, 1997.

[119] M. C. Knapp and P. M. Woodward. A-site cation ordering in $AA'BB'O_6$ perovskites. *Journal of Solid State Chemistry*, 179:1076–1085, 2006.

[120] G. King, L. M. Wayman, and P. M. Woodward. Magnetic and structural properties of NaLnMnWO_6 and NaLnMgWO_6 perovskites. *Journal of Solid State Chemistry*, 182:1319–1325, 2009.

[121] S. J. May, C. R. Smith, J.-W. Kim, E. Karapetrova, A. Battacharya, and P. J. Ryan. Control of octahedral rotations in $(LaNiO_3)_n/(SrMnO_3)_m$ superlattices. *Physical Review B*, 83:153411, 2011.

[122] E. J. Moon, P. V. Balachandran, B. J. Kirby, D. J. Keavney, R. J. Sichel-Tissot, C. M. Schlepütz, E. Karapetrova, X. M. Cheng, J. M. Rondinelli, and S. J. May. Effect of interfacial octahedral behavior in ultrathin manganite films. *Nano Letters*, 14:2509–2514, 2014.

[123] A. Bhattacharya and S. J. May. Magnetic oxide heterostructures. *Annual Review of Materials Research*, 44:65–90, 2014.

[124] S. A. Kulkarni, T. Baikie, P. P. Boix, N. Yantara, N. Mathews, and S. Mhaisalkar. Band-gap tuning of lead halide perovskites using a sequential deposition process. *Journal of Materials Chemistry A*, 2:9221–9225, 2014.

[125] P. K. Davies, H. Wu, A. Y. Borisevich, I. E. Molodetsky, and L. Farber. Crystal chemistry of complex perovskites: New cation-ordered dielectric oxides. *Annual Review of Materials Reseach*, 38:369–401, 2008.

[126] K. R. Kendall, C. Navas, J. K. Thomas, and H.-C. zur Loye. Recent developments in perovskite-based oxide ion conductors. *Solid State Ionics*, 82:215–223, 1995.

[127] J. C. Boivin and G. Mairesse. Recent material developments in fast oxide ion conductors. *Chemistry of Materials*, 10:2870–2888, 1998.

[128] A. Rolle, R. N. Vannier, N. V. Giridharan, and F. Abraham. Structural and electrochemical characterisation of new oxide ion conductors for oxygen generating systems and fuel cells. *Solid State Ionics*, 176:2095–2103, 2005.

[129] A. L. Shaula, Y. V. Pivak, J. C. Waerenborgh, P. Gaczyñski, A. A. Yaremchenko, and V. V. Karton. Ionic conductivity of brownmillerite-type calcium ferrite under oxidizing conditions. *Solid State Ionics*, 177:2923–2930, 2006.

[130] A. Orera and P. R. Slater. New chemical systems for solid oxide fuel cells. *Chemistry of Materials*, 22:675–690, 2010.

[131] E. V. Antipov, A. M. Abakumov, A. M. Alekseeva, M. G. Rozova, J. Hadermann, O. I. Lebedev, and G. Van Tendeloo. Oxygen and fluorine doping in Sr_2MnGaO_5 brownmillerite. *Physica Status Solidi A*, 201:1403–1409, 2004.

[132] E. Sullivan and C. Greaves. Fluorine insertion reactions of the brownmillerite materials $Sr_2Fe_2O_5$, Sr_2CoFeO_5, and $Sr_2Co_2O_5$. *Materials Research Bulletin*, 47:2541–2546, 2012.

[133] N. A. Tarasova, Ya. V. Filinkova, and I. E. Animitsa. Electric properties of oxyfluorides $Ba_2In_2O_{5-0.5x}F_x$. *Russian Journal of Electrochemistry*, 49:45–51, 2013.

[134] P. D. Battle, T. C. Gibb, and P. Lightfoot. The crystal and magnetic structures of Sr_2CoFeO_5. *Journal of Solid State Chemistry*, 76:334–339, 1988.

[135] A. M. Abakumov, A. M. Alekseeva, M. G. Rozova, E. V. Antipov, O. I. Lebedev, and G. V. Van Tendeloo. Ordering of the tetrahedral chains in the Sr_2MnGaO_5 brownmillerite. *Journal of Solid State Chemistry*, 174:319–328, 2003.

[136] B. Lazic, H. Krüher, V. Kahlenberg, J. Konzett, and R. Kaindl. Incommensurate structure of $Ca_2Al_2O_5$ at high temperatures – structure investigation and Raman spectroscopy. *Acta Crystallographica*, B64:417–425, 2008.

[137] H. Krüher and V. Kahlenberg. Incommensurately modulated ordering of tetrahedral chains in $Ca_2Fe_2O_5$ at elevated temperatures. *Acta Crystallographica*, B61:656–662, 2005.

[138] D. O. Klenov, W. Donner, B. Foran, and S. Stemmer. Impact of stress on oxygen vacancy ordering in epitaxial $La_{0.5}Sr_{0.5}CrO_{3-\delta}$ thin films. *Applied Physics Letters*, 82:3427–3429, 2003.

[139] J. Gazquez, S. Bose, M. Sharma, M. A. Torija, S. J. Pennycook, C. Leighton, and M. Varela. Lattice mismatch accommodation via oxygen vacancy ordering in epitaxial $La_{0.5}Sr_{0.5}CrO_{3-\delta}$ thin films. *APL Materials*, 1:012105, 2013.

[140] S. Inoue, M. Kawai, N. Ichikawa, H. Kageyama, W. Paulus, and Y. Shimakawa. Anisotropic oxygen diffusion at low temperature in perovskite-structure iron oxides. *Nature Chemistry*, 2:213–217, 2010.

[141] A. M. Abakumov, A. S. Kalyuzhnaya, M. G. Rozova, E. V. Antipov, Hadermann. J., and G. V. Van Tendeloo. Compositionally induced phase transition in the $Ca_2MnGa_{1-x}Al_xO_5$ solid solutions: Ordering of tetrahedral chains in the brownmillerite structure. *Solid State Science*, 7:801–811, 2005.

[142] J. Hadermann, A. M. Abakumov, H. D'Hondt, A. S. Kalyuzhnaya, M. G. Rozova, M. M. Markina, M. G. Mikheev, N. Tristan, R. Klingeler, B. Büchner, and E. V. Antipov. Synthesis and crystal structure of the $Sr_2Al_{1.07}Mn_{0.93}O_5$ brownmillerite. *Journal of Materials Chemistry*, 17:692–698, 2007.

[143] T. G. Parsons, H. D'Hondt, J. Hadermann, and Hayward M. A. Synthesis and structural characterization of $La_{1-x}A_xMnO_{2.5}$ (A=Ba,Sr,Ca) phases: Mapping the variants of the brownmillerite structure. *Chemistry of Materials*, 21:5527–5538, 2009.

[144] A. M. Arevalo-Lopez and J. P. Attfield. Crystal and magnetic structures of the brownmillerite $Ca_2Cr_2O_5$. *Dalton Transactions*, 2015.

[145] F. Ramezanipour, J. E. Greedan, A. P. Grosvenor, J. F. Britten, L. M. D. Cranswick, and V. O. Garlea. Intralayer cation ordering in a brownmillerite superstructure: Synthesis, crystal, and magnetic structures of Ca_2FeCoO_5. *Chemistry of Materials*, 22:6008–6020, 2010.

[146] J. Zhang, H. Zheng, C. D. Malliakas, J. M. Allred, Y. Ren, Q. Li, T.-H. Han, and J. F. Mitchell. Brownmillerite $Ca_2Co_2O_5$: Synthesis, stability, and re-entrant single crystal to single crystal structural transitions. *Chemistry of Materials*, 16:7172–7182, 2014.

[147] J. Curie and P. Curie. Developpement par compression de l'electricite polaire dans les cristaux hemiedres a faces inclinees. *Bulletin de la Scoiete Mineralogique de France*, 3:90, 1880.

[148] J. Valasek. Piezo-electric and allied phenomena in rochelle salt. *Physical Review*, 17:475–481, 1920.

[149] M. E. Lines and A. M. Glass. *Principles and Applications of Ferroelectrics and Related Materials*. Oxford University Press, 1977.

[150] R. C. Powell. *Symmetry, Group Theory, and the Physical Properties of Crystals*. Springer, 2010.

[151] R. Resta. Theory of the electric polarization in crystals. *Ferroelectrics*, 136:51–55, 1992.

[152] R. Resta. Macroscopic electric polarization as a geometric quantum phase. *Europhysics Letters*, 22:133–138, 1993.

[153] R. D. King-Smith and D. Vanderbilt. Theory of polarization of crystalline solids. *Physical Review B*, 47:1651(R), 1993.

[154] R. D. King-Smith and D. Vanderbilt. First-principles investigation of ferroelectricity in perovskite compounds. *Physical Review B*, 49:5828, 1994.

[155] R. Resta. Macroscopic polarization in crystalline dielectrics: the geometric phase approach. *Reviews of Modern Physics*, 66:899–915, 1994.

[156] R. Resta and D. Vanderbilt. Theory of polarization: A modern approach. *Topics in Applied Physics*, 105:31–68, 2007.

[157] N. A. Spaldin. A beginners guide to the modern theory of polarization. *Journal of Solid State Chemistry*, 195:2–10, 2012.

[158] C. B. Sawyer and C. H. Tower. Rochelle salt as a dielectric. *Physical Review*, 35:269, 1930.

[159] M. T. Dove. Theory of displacive phase transitions in minerals. *American Mineralogist*, 82:213–244, 1997.

[160] H. F. Kay and P. Vousden. XCV. symmetry changes in barium titanate at low temperatures and their relation to its ferroelectric properties. *Philosophical Magazine*, 40:1019–1040, 1949.

[161] W. Zhong, D. Vanderbilt, and K. M. Rabe. Phase transitions in $BaTiO_3$ from first principles. *Physical Review Letters*, 73:1861–1864, 1994.

[162] V. H. Schmidt. Review of order-disorder models for KDP-family crystals. *Ferroelectrics*, 72:157–173, 1987.

[163] H. M. Lu, R. Qi, and J. R. Hardy. A priori study of the order-disorder phase transition in $NaNO_2$. *Solid State Communications*, 87:1151–1154, 1993.

[164] S. Koval, J. Kohanoff, J. Lasave, G. Colizzi, and R. L. Migoni. First-principles study of ferroelectricity and isotope effects in H-bonded KH_2PO_4 crystals. *Physical Review B*, 71:184102, 2005.

[165] M. Ichikawa, T. Gustafsson, and I. Olovsson. Is $NaNO_2$ a pure order-disorder type ferroelectric? *Solid State Communications*, 87:135–139, 2002.

[166] B. Zalar, V. V. Laguta, and R. Blinc. NMR evidence for the coexistence of order-disorder and displacive components in barium titanate. *Physical Review Letters*, 90:037601, 2003.

[167] S. Horiuchi and Y. Tokura. Organic ferroelectrics. *Nature Materials*, 7:357–366, 2008.

[168] C. Ederer and N. A. Spaldin. Origin of ferroelectricity in the multiferroic barium fluorides $BaMF_4$: A first principles study. *Physical Review B*, 74:024102, 2006.

[169] B. B. Van Aken, T. T. M. Palstra, A. Filippetti, and N. A. Spaldin. The origin of ferroelectricity in magnetoelectric $YMnO_3$. *Nature Materials*, 3:164–170, 2004.

[170] P. Tolédano. Pseudo-proper ferroelectricity and magnetoelectric effects in $TbMnO_3$. *Physical Review B*, 79:094416, 2009.

[171] Andrei Malashevich and David Vanderbilt. First principles study of improper ferroelectricity in $TbMnO_3$. *Physical Review Letters*, 101(3):037210, 2008.

[172] T. Goto, T. Kimura, G. Lawes, A. P. Ramirez, and Y. Tokura. Ferroelectricity and giant magnetocapacitance in perovskite rare-earth manganites. *Physical Review Letters*, 92:257201, 2004.

[173] G. Lawes, A. B. Harris, T. Kimura, N. Rogado, R. J. Cava, A. Aharony, O. Entin-Wohlman, T. Yildirim, M. Kenzelmann, C. Broholm, and A. P. Ramirez. Magnetically driven ferroelectric order in $Ni_3V_2O_8$. *Physical Review Letters*, 95:087205, 2005.

[174] T. Thonhauser and K. M. Rabe. Fcc breathing instability in $BaBiO_3$ from first principles. *Physical Review B*, 73:212106, 2006.

[175] K. Gupta, P. Mahadevan, P. Mavropoulos, and M. Ležaić. Orbital-ordering-induced ferroelectricity in $SrCrO_3$. *Physical Review Letters*, 111:077601, 2013.

[176] A. von Hippel, R. G. Breckenridge, F. G. Chesley, and L. Tisza. High dielectric constant ceramics. *Industrial and Engineering Chemistry*, 38:1097–1109, 1946.

[177] A. F. Devonshire. Theory of barium titanate. *Philosophical Magazine*, 40:1040–1063, 1949.

[178] R. H. Lydanne, R. G. Sachs, and E. Teller. On the polar vibrations of alkali halides. *Physical Review*, 59:673–676, 1941.

[179] W. Cochran. Crystal stability and the theory of ferroelectricity. *Advances in Physics*, 9:387–423, 1960.

[180] G. Shirane, H. Danner, A. Pavlovic, and R. Pepinsky. Phase transitions in ferroelectric $KNbO_3$. *Physical Review*, 93:672, 1954.

[181] H. Sharma, J. Kreisel, and P. Ghosez. First-principles study of $PbTiO_3$ under uniaxial strains and stresses. *Physical Review B*, 90:214102, 2014.

[182] J. H. Haeni, P. Irvin, W. Chang, R. Uecker, P. Reiche, Y. L. Li, S. Choudhury, W. Tian, M. E. Hawley, B. Craigo, A. K. Tagantsev, X. Q. Pan, S. K. Streiffer, L. Q. Chen, S. W. Kirchoefer, J. Levy, and D. G. Schlom. Room-temperature ferroelectricity in strained $SrTiO_3$. *Nature*, 430:758–761, 2004.

[183] M. Tyunina, J. Narkilahti, M. Plekh, R. Oja, R. M. Nieminen, A. Dejneka, and V. Trepakov. Evidence for strain-induced ferroelectric order in epitaxial thin-film $KTaO_3$. *Physical Review Letters*, 104:227601, 2010.

[184] T. Güniter, E. Bousquet, A. David, Ph. Poullay, Ph. Ghosez, W. Prellier, and M. Fiebig. Incipient ferroelectricity in 2.3% tensile-strained $CaMnO_3$ films. *Physical Review B*, 85:214120, 2012.

[185] C.-J. Eklund, C. J. Fennie, and K. M. Rabe. Strain-induced ferroelectricity in orthorhombic $CaTiO_3$ from first principles. *Physical Review B*, 79:220101, 2009.

[186] V. V. Lemanov, A. V. Sotnikov, E. P. Smirnova, and M. Weihnacht. From incipient ferroelectricity in $CaTiO_3$ to real ferroelectricity in $Ca_{1-x}Pb_xTiO_3$ solid solutions. *Applied Physics Letters*, 81:886–888, 2002.

[187] S. M. Yang, S. J. Moon, T. H. Kim, and Y. S. Kim. Observation of ferroelectricity induced by defect dipoles in the strain-free epitaxial $CaTiO_3$ thin film. *Current Applied Physics*, 14:757–760, 2014.

[188] N. A. Benedek and C. J. Fennie. Why are there so few perovskite ferroelectrics? *Journal of Physical Chemistry C*, 117:13339–133349, 2013.

[189] R. E. Cohen. Origin of ferroelectricity in perovskite oxides. *Nature*, 358:136–138, 1992.

[190] Jeremy K. Burdett. Use of the Jahn-Teller theorem in inorganic chemistry. *Inorganic Chemistry*, 20(7):1959–1962, 1981.

[191] I. B. Bersuker. Pseudo Jahn-Teller origin of perovskite multiferroics, magnetic-ferroelectric crossover, and magnetoelectric effects: The $d^0 - d^{10}$ problem. *Physical Review Letters*, 108:137202, 2012.

[192] I. B. Bersuker. Pseudo-Jahn-Teller effect–a two-state paradigm in formation, deformation, and transformation of molecular systems and solids. *Chemical Reviews*, 113:1351–1390, 2013.

[193] I. B. Bersuker. Recent development of the vibronic theory of ferroelectricity. *Ferroelectrics*, 164(1):75–100, 1995.

[194] E. K. H. Salje and M. A. Carpenter. Linear-quadratic order parameter coupling and multiferroic phase transitions. *Journal of Physics: Condensed Matter*, 23:462202, 2011.

[195] A. Cano and A. P. Levanyuk. Pseudoproper ferroelectricity in thin films. *Physical Review B*, 81:172105, 2010.

[196] B. Lazoryak, V. A. Morozov, A. A. Belik, S. Y. Stefanovich, V. V. Grebenev, I. A. Leonidov, E. B. Mitberg, S. A. Davydov, O. I. Lebedev, and G. Van Tendeloo. Ferroelectric phase transition in the whitlockite-type $Ca_9Fe(PO_4)_7$; crystal structure of the paraelectric phase at 923 K. *Solid State Science*, 6:185–195, 2004.

[197] J. Holakovsky. A new type of the ferroelectric phase transition. *Physica Status Solidi B*, 56:615–619, 1973.

[198] Y. Ishibashi. First-order structural phase transition induced by biquadratic coupling of two different modes. *Journal of the Physical Society of Japan*, 63:2082, 1994.

[199] I. N. Flerov, M. V. Gorev, K. S. Aleksandrov, A. Tressaud, J. Grannec, and M. Couzi. Phase transitions in elpasolites (ordered perovskites). *Materials Science and Engineering R: Reports*, 24:81–151, 1998.

[200] I. A. Kornev and L. Bellaiche. Nature of the ferroelectric phase transition in multiferroic $BiFeO_3$ from first principles. *Physical Review B*, 79:100105(R), 2009.

[201] Nicole A. Benedek and Craig J. Fennie. Hybrid improper ferroelectricity: A mechanism for controllable polarization-magnetization coupling. *Physical Review Letters*, 106(10):107204, 2011.

[202] I. Etxebarria, J. M. Perez-Mato, and P. Boullay. The role of trilinear couplings in the phase transitions of aurivillius compounds. *Ferroelectrics*, 401:17, 2010.

[203] R. Machado, M. Sepliarsky, and M. G. Stachiotti. Temperature-driven phase transitions in $SrBi_2Ta_2O_9$ from first-principles calculations. *Applied Physics Letters*, 93:242901, 2008.

[204] G. A. Smolenskii, I. G. Sinii, A. K. Tagantsev, S. D. Prokhorova, V. D. Mikvabiya, and W. Windsch. Acoustic anomaly and nature of the phase transition in the uniaxial weakly polar ferroelectric TSCC. *Journal of Experimental and Theoretical Physics*, 88:1020–1031, 1985.

[205] A. K. Tangantsev. Weakly polar ferroelectricity: dielectric properties and possible nature. *JETP Letters*, 45:447–450, 1987.

[206] T. Ito, N. Morimoto, and R. Sadanaga. Crystal structure of boracite. *Acta Crystallographica*, 4:310, 1951.

[207] E. Ascher, H. Schmid, and D. Tar. Dielectric properties of boracites and evidence for ferroelectricity. *Solid State Communications*, 2:45, 1965.

[208] E. Ascher, H. Rieder, H. Schmid, and H. Stössel. Some properties of ferromagnetoelectric nickel-iodine boracite, $Ni_3B_7O_13I$. *Journal of Applied Physics*, 37:1404–1405, 1966.

[209] H. Schmid. The dice-stone der Würfelstein: Some personal souvenirs around the discovery of the first ferromagnetic ferroelectric. *Ferroelectrics*, 427:1–33, 2012.

[210] R. J. Nelmes. Structural studies of boracites. a review of the properties of boracites. *Journal of Physics C: Solid State Physics*, 7:3840–3854, 1974.

[211] K. Knorr, L. Peters, B. Winkler, V. Milman, and A. G. Castellanos-Guzman. Correlation between composition and structure in boracites. *Journal of Physics: Condensed Matter*, 19:275207, 2007.

[212] M. N. Iliev and H. Schmid. Raman spectroscopy of $M_3B_7O_{13}X$ boracites (M=Cr,Co,Ni,Cu,Zn,Cd; X=Cl,Br,I). *Journal of Raman Spectroscopy*, 45:267–273, 2014.

[213] M. N. Iliev, V. G. Hadjiev, J. Íñiguez, and J. Pascual. Raman imaging approach to the study of ferroelectric domains and raman spectra of multiferroic boracites. *Acta Physica Polonica A*, 116:19–24, 2009.

[214] A. Zimmermann, W. Bollmann, and H. Schmid. Observations of ferroelectric domains in boracites. *Physica Status Solidi A*, 3:707–720, 1970.

[215] Y. Kinoshita, N. Kida, M. Sotome, R. Takeda, N. Abe, M. Saito, T. Arima, and H. Okamoto. Visualization of ferroelectric domains in boracite using emission of terahertz radiation. *Japanese Journal of Applied Physics*, 53:09PD08, 2014.

[216] V. Dvořák. A thermodynamic theory of the cubic-orthorhombic phase transition in boracites. *Czech Journal of Physics B*, 21:1250–1261, 1971.

[217] V. Dvořák and J. Petzelt. Symmetry aspect of the phase transitions in boracites. *Czech Journal of Physics B*, 21:1141–1152, 1971.

[218] M. Clin, J.-P. Rivera, and H. Schmid. Low temperature magnetoelectric effects on $Co_3B_7O_{13}I$. *Ferroelectrics*, 108:213–218, 1990.

[219] P. Tolédano, H. Schmid, M. Clin, and J. P. Rivera. Theory and low-temperature phases in boracites: Latent anitferromagnetism, weak ferromagnetism, and improper magnetostructural couplings. *Physical Review B*, 32:6006–6038, 1985.

[220] H. L. Yakel, W. C. Koehler, E. F. Bertaut, and E. F. Forrat. On the crystal structure of the manganese (iii) trioxides of the heavy lanthanides and yttrium. *Acta Crystallographica*, 16:957–962, 1963.

[221] G. A. Smolenskii and V. A. Bokov. Coexistence of magnetic and electric ordering in crystals. *Journal of Applied Physics*, 35:915, 1964.

[222] T. Katsufuji, M. Masaki, A. Machida, M. Moritomo, K. Kato, E. Nishibori, M. Takata, M. Sakata, K. Ohoyama, K. Kitazawa, and H. Takagi. Crystal structure and magnetic properties of hexagonal $R\mathrm{MnO_3}$ (R=Y, Lu, and Sc) and the effect of doping. *Physical Review B*, 66:134434, 2002.

[223] Th. Lonkai, D. G. Tomuta, U. Amann, J. Ihringer, R. W. A. Hendrikx, D. M. Többens, and J. A. Mydosh. Development of the high-temperature phase of hexagonal manganites. *Physical Review B*, 69:134108, 2004.

[224] I.-K. Jeong, N. Hur, and Th. Proffen. High-temperature structural evolution of hexagonal multiferroic $\mathrm{YMnO_3}$ and $\mathrm{YbMnO_3}$. *Journal of Applied Crystallography*, 40:730–734, 2007.

[225] G. Nebert, M. Pollet, S. Marinel, G. R. Blake, A. Meetsma, and T. T. M. Palstra. Experimental evidence for an intermediate phase in multiferroic $YMnO_3$. *Journal of Physics: Condensed Matter*, 19:466212, 2007.

[226] A. S. Gibbs, K. S. Knight, and P. Lightfoot. High-temperature phase transitions of hexagonal $YMnO_3$. *Physical Review B*, 83:094111, 2011.

[227] B. Lorenz. Hexagonal manganites ($RMnO_3$): Class (I) multiferroics with strong coupling of magnetism and ferroelectricity. *ISRN Condensed Matter Physics*, 2013:497073, 2013.

[228] C. J. Fennie and K. M. Rabe. Ferroelectric transition in $YMnO_3$ from first principles. *Physical Review B*, 72:100103(R), 2005.

[229] C. Kadlec, V. Goian, K. Z. Rushchanskii, P. Kuzel, K. Kohn, R. V. Pisarev, and S. Kamba. Terahertz and infrared spectroscopic evidence of phonon-paramagnon coupling in hexagonal piezomagnetic $YMnO_3$. *Physical Review B*, 84:174120, 2011.

[230] N. Fujimura, T. Ishida, T. Yoshimura, and T. Ito. Expitaxially grown $YMnO_3$ film: New candidate for nonvolatile memory devices. *Applied Physics Letters*, 69(7):1011–1013, 1996.

[231] C.-Y. Ren. Atomic, electronic, and ferroelectric properties of manganite $RMnO_3$ (R=Ho, Er, Tm, Lu) in hexagonal and orthorhombic phases. *Physical Review B*, 79:125113, 2009.

[232] A. A. Bossak, I. E. Graboy, O. Y. Gorbenko, A. R. Kaul, M. S. Kartavtseva, V. L. Svetchnikov, and H. W. Zandbergen. XRD and HREM studies of epitaxially stabilized hexagonal orthoferrites $RFeO_3$ (R=Eu-Lu). *Chemistry of Materials*, 16:1751–1755, 2004.

[233] H. Das, A. L. Wysocki, Y. Geng, W. Wu, and C. J. Fennie. Bulk magnetoelectricity in the hexagonal manganites and ferrites. *Nature Communications*, 5:2998, 2014.

[234] C. Xu, Y. Yang, S. Wang, W. Duan, B. Gu, and L. Bellaiche. Anomalous properties of hexagonal rare-earth ferrites from first principles. *Physical Review B*, 89:205122, 2014.

[235] D. Visser, G. C. Verschoor, and D. J. W. Ijdo. The structure of $KNiCl_3$ at room temperature. *Acta Crystallographica Section B*, 36:28–34, 1980.

[236] J. M. Perez-Mato, D. Orobengoa, and M. I. Aroyo. Mode crystallography of distorted structures. *Acta Crystallographica Section A*, 66(5):558–590, 2010.

[237] E.J. Cusser and P. D. Battle. Crystal and magnetic structures of 2H $BaMnO_3$. *Chemistry of Materials*, 12:831–838, 2000.

[238] J. Varignon and P. Ghosez. Improper ferroelectricity and multiferroism in 2H-$BaMnO_3$. *Physical Review B*, 87:140403(R), 2013.

[239] T. Tohei, H. Moriwake, H. Murata, A. Kuwabara, R. Hashimoto, T. Yamamoto, and I. Tanaka. Geometric ferroelectricity in rare-earth compounds $RGaO_3$ and $RInO_3$. *Physical Review B*, 79:144125, 2009.

[240] Y. K. Jeong, J.-H. Lee, S.-J. Ahn, S.-W. Song, H. M. Jang, H. Choi, and J. F. Scott. Structurally tailored hexagonal ferroelectricity and multiferroism in epitaxial $YbFeO_3$ thin-film heterostructures. *Journal of the American Chemical Society*, 134:1450–1453, 2012.

[241] B. Dorner, J. D. Axe, and G. Shirane. Neutron-scattering study of the ferroelectric phase transformation in $Tb_2(MoO_4)_3$. *Physical Review B*, 6:1950, 1972.

[242] J. Petzelt and V. Dvořak. New type of ferroelectric soft mode in gadolinium molybdate. *Physica Status Solidi B*, 46:413, 1971.

[243] B. K. Ponomarev, B. S. Red'kin, E. Stiep, A. G. Wiegelmann, A. G. M. Jansen, and P. Wyder. Magnetoelectric effect in samarium molybdate. *Physics of the Solid State*, 44:145, 2002.

[244] B. K. Ponomarev and A. Zhukov. Magnetic and magnetoelectric properties of rare earth molybdates. *Physics Research International*, 2012:276348, 2012.

[245] E. T. Keve, S. C. Abrahams, and J. L. Bernstein. Ferroelectric ferroelastic paramagnetic beta $Gd_2(MoO_4)_3$ crystal structure of the transition-metal molybdates and tungstates. VI. *Journal of Chemical Physics*, 54:3185, 1971.

[246] Y. Ishibashi. *Incommensurate Phases in Dielectrics*. North-Holland, 1986.

[247] S. Sawada, M. Takashige, F. Shimizu, H. Suzuki, and T. Yamaguchi. Ferroelectricity in A_2BX_4-type halide compounds. *Ferroelectrics*, 169:207–214, 1995.

[248] J. Leist, H. Gibhardt, K. Hradil, and G. Eckold. Electric field induced anomalies in ferroelectric K_2SeO_4. *Journal of Physics: Condensed Matter*, 20:415209, 2008.

[249] N. Yamada, Y. Ono, and T. Ikeda. A structural study of the incommensurate-to-ferroelectric phase transition in K_2SeO_4. *Journal of the Physical Society of Japan*, 53:2565–2574, 1984.

[250] M. S. Haque and J. R. Hardy. Theoretical lattice-dynamical studies of the incommensurate phase transformation in K_2SeO_4. *Physical Review B*, 21:245–259, 1980.

[251] J. M. Perez-Mato, F. Gaztelua, G. Madariaga, and M. J. Tello. Symmetry-mode analysis of the ferroelectric phase in K_2SeO_4. *Journal of Physics C: Solid State Physics*, 19:1923–1935, 1985.

[252] T. A. Aslanyan. Origin of second-harmonic generation in the incommensurate phase of K_2SeO_4. *Physical Review B*, 70:024102, 2004.

[253] F. Shimizu, M. Takashige, S.-I. Hamazaki, and T. Yamaguchi. Search for new ferroelectrics in Tl_2ZnI_4 group. *Ferroelectrics*, 286:29–42, 2003.

[254] D. Durand, F. Dénoyer, and M. More. Neutron diffraction study of deuterated tetramethylammonium tetrachlorozincate under an applied electric field. *Solid State Communications*, 66:1195, 1988.

[255] P. K. Bajpai. Ferroelectric phase transition in $(NH_4)_2BeF_4$. possibility of molecular distortion type of transition. *Physica Status Solidi B*, 153:101–105, 1989.

[256] B. A. Strukov, J. Kobayashi, and Y. Uesu. Comprehensive study of incommensurate phase transitions in $(NH_4)_2BeF_4$ II. *Ferroelectrics*, 64:57, 1985.

[257] W. Hörkner and H. Müller-Buschbaum. Zur kristallstruktur von $BaAl_2O_4$. *Zeitschrift für anorganische und allgemeine Chemie*, 451:40–44, 1979.

[258] S.-Y. Huang, R. Von Der Mühll, J. Ravez, and P. Hagenmuller. Structural, ferroelectric, and pyroelectric properties of nonstoichiometric ceramics based on $BaAl_2O_4$. *Journal of Physics and Chemistry of Solids*, 55:119–124, 1994.

[259] A. M. Abakumov, O. I. Lebedev, L. Nistor, G. Van Tendeloo, and S. Amelinkx. The ferroelectric phase transition in tridymite type $BaAl_2O_4$ studied by electron microscopy. *Phase Transitions*, 71:143–160, 2000.

[260] H. T. Stokes, C. Sadate, D. M. Hatch, L. L. Boyer, and M. J. Mehl. Analysis of the ferroelectric phase transition in $BaAl_2O_4$ by group theoretical methods and first-principles calculations. *Physical Review B*, 65:064105, 2002.

[261] S.-Y. Huang, R. Von Der Mühll, J. Ravez, and M. Couzi. Phase transition and symmetry in $BaAl_2O_4$. *Ferroelectrics*, 159:127–132, 1994.

[262] S.-Y. Huang, R. Von Der Mühll, J. Ravez, J. P. Chaminade, P. Hagenmuller, and M. Couzi. A propose de la ferroelectricite dans $BaAl_2O_4$. *Journal of Solid State Chemistry*, 109:97–105, 1994.

[263] V. Dvořák. Structural phase transitions in langbeinites. *Physica Status Solidi B*, 52:93–98, 1972.

[264] N. Yamada, M. Maeda, and H. Adachi. Structures of langbeinite-type $K_2(SO_4)_3$ in cubic and orthorhombic phases. *Journal of the Physical Society of Japan*, 50:907–913, 1981.

[265] T. Ikeda and G. Yasuda. The phase transition of ferroelectric $Tl_2Cd_2(SO_4)_3$. *Japanese Journal of Applied Physics*, 14:1287–1290, 1975.

[266] T. Hikita, T. Kudo, Y. Chubachi, and T. Ikeda. Ferroelectric phase transition in $Rb_2Cd_2(SO_4)_3$. *Journal of the Physical Society of Japan*, 41:349–350, 1976.

[267] F. Jona and R. Pepinsky. Ferroelectricity in the langbeinite system. *Physical Review*, 103:1126, 1956.

[268] S. Kreske and V. Devarajan. Vibrational spectra and phase transitions in ferroelectric-ferroelastic langbeinites: $K_2Mn_2(SO_4)_3$, $(NH_4)_2Cd_2(SO_4)_3$, and $Tl_2Cd_2(SO_4)_3$. *Journal of Physics C: Solid State Physics*, 15:7333–7350, 1982.

[269] Y. Goto and E. Sawaguchi. Phase transition in ferroelectric $RbH_3(SeO_3)_2$. *Journal of the Physical Society of Japan*, 49:2255–2262, 1980.

[270] Y. Makita and S. Suzuki. Super-lattice structure of $RbH_3(SeO_3)_2$ below the ferroelectric transition temperature. *Journal of the Physical Society of Japan*, 36:1215, 1974.

[271] H. Grimm and W. J. Fitzgerald. A neutron investigation of the low-temperature structure of $RbH_3(SeO_3)_2$. *Acta Crystallographica Section A*, 34:268–274, 1978.

[272] M. A. Carpenter and C. J. Howard. Symmetry rules and strain/order-parameter relationships for coupling between octahedral tilting and cooperative Jahn-Teller transitions in ABX_3 perovskites. II. Application. *Acta Crystallographica Section B*, 65:147–159, 2009.

[273] M. A. Carpenter and C. J. Howard. Symmetry rules and strain/order-parameter relationships for coupling between octahedral tilting and cooperative Jahn-Teller transitions in ABX_3 perovskites. I. Theory. *Acta Crystallographica Section B*, 65:134–146, 2009.

[274] F. G. Riddell, K. S. Cameron, S. A. Holmes, and J. H. Strange. Five-membered ring rotations, pseudorotations, and hydrogen bond exchange dynamics in the solid state studied by NMR spectroscopy. *Journal of the American Chemical Society*, 119:7555–7560, 1997.

[275] I. Ugi, H. Marquarding, D. Klusacek, P. Gillespie, and F. Ramirez. Berry pseudorotation and turnstile rotation. *Accounts of Chemical Research*, 4:288–296, 1971.

[276] A. R. Bassindale, M. Sohail, P. G. Taylor, A. A. Korlyukov, and D. E. Arkhipov. Four independent structures of a pentacoordinate silicon species at different points on the Berry pseudorotation pathway. *Chemical Communications*, 46:3274–3276, 2010.

[277] E. K. H. Salje, K. Gofryk, D. J. Safarik, and J. C. Lashley. Order-parameter coupling in the the improper ferroelectric lawsonite. *Journal of Physics: Condensed Matter*, 24:255901, 2012.

[278] J. M. Perez-Mato, M. Aroyo, A. García, P. Blaha, K. Schwarz, J. Schweifer, and K. Parlinski. Competing structural instabilities in the ferroelectric Aurivillius compound $SrBi_2Ta_2O_9$. *Physical Review B*, 70:214111, 2004.

[279] E. Bousquet, M. Dawber, N. Stucki, C. Lichtensteiger, P. Hermet, S. Gariglio, J. M. Triscone, and P. Ghosez. Improper ferroelectricity in perovskite oxide artificial superlattices. *Nature*, 452:732, 2008.

[280] B. Aurivillius. *Ark. Kemi.*, 1:463–480, 1949.

[281] A. D. Rae, J. G. Thompson, and R. L. Withers. Structure refinement of commensurately modulated bismuth strontium tantalate, $Bi_2SrTa_2O_9$. *Acta Crystallographica Section B*, 48:418–428, 1992.

[282] Mohammad A. Islam, James M. Rondinelli, and Jonathan E. Spanier. Normal mode determination of perovskite crystal structures with octahedral rotations: theory and applications. *Journal of Physics: Condensed Matter*, 25(17):175902, 2013.

[283] H. Djani, E. Bousquet, A. Kellou, and P. Ghosez. First-principles study of the ferroelectric Aurivillius phase Bi_2WO_6. *Physical Review B*, 86:054107, 2012.

[284] R. L. Withers, J. G. Thompson, and A. D. Rae. The crystal chemistry underlying ferroelectricity in $bi_4ti_3o_{12}$, bi_3tinbo_9, and bi_2wo_6. *Journal of Solid State Chemistry*, 94:404–417, 1991.

[285] S. N. Ruddlesden and P. Popper. New compounds of the K_2NIF_4 type. *Acta Crystallographica*, 10:538–539, 1957.

[286] S. N. Ruddlesden and P. Popper. New compounds of the K_2NIF_4 type. *Acta Crystallographica*, 11:54–55, 1958.

[287] A. T. Mulder, N. A. Benedek, J. M. Rondinelli, and C. J. Fennie. Turning ABO_3 antiferroelectrics into ferroelectrics: Design rules for practical rotation-driven ferroelectricity in double perovskites and $A_3B_2O_7$ ruddlesden-popper compounds. *Advanced Functional Materials*, 23:4810–4820, 2013.

[288] James M. Rondinelli and Craig J. Fennie. Octahedral rotation-induced ferroelectricity in cation ordered perovskites. *Advanced Materials*, 24:1961–1968, 2012.

[289] Nicole A. Benedek, Andrew T. Mulder, and Craig J. Fennie. Polar octahedral rotations: A path to new multifunctional materials. *Journal of Solid State Chemistry*, 195:11 – 20, 2012.

[290] P. V. Balachandran, D. Puggioni, and J. M. Rondinelli. Crystal-chemistry guidelines for noncentrosymmetric A_2BO_4 Ruddlesden-Popper oxides. *Inorganic Chemistry*, 53:336–348, 2014.

[291] J. Young and J. M. Rondinelli. Improper ferroelectricity and piezoelectric responses in rhombohedral (A,A′)B_2O_6 perovskite oxides. *Physical Review B*, 89:174110, 2014.

[292] G. Pilania and T. Lookman. Electronic structure and biaxial strain in $RbHgF_3$ perovskite and hybrid improper ferroelectricity in (Na,Rb)Hg_2F_6 and (K,Rb)Hg_2F_6 superlattices. *Physical Review B*, 90:115121, 2014.

[293] J. F. Scott and R. Blinc. Multiferroic magnetoelectric fluorides: why are there so many magnetic ferroelectrics? *Journal of Physics: Condensed Matter*, 23:113202, 2011.

[294] Q. Zhou and K. Rabe. Strain-induced hybrid improper ferroelectricity in simple perovskites from first principles. *ArXiv e-prints*, 2013.

[295] M. M. Elcombe, E. H. Kisi, K. D. Hawkins, T. J. White, P. Goodman, and S. Matheson. Structure determinations for $Ca_3Ti_2O_7$, $Ca_4Ti_3O_{10}$, $Ca_{3.6}Sr_{0.4}Ti_3o_{10}$, and a refinement of $Sr_3Ti_2O_7$. *Acta Crystallographica Section B*, 47:305–314, 1991.

[296] Y. S. Oh, X. Luo, F.-T. Huang, Y. Wang, and S.-W. Cheong. Experimental demonstration of hybrid improper ferroelectricity and the presence of abundant charged walls in $(Ca,Sr)_3Ti_2O_7$ crystals. *Nature Materials*, 14:407–413, 2015.

[297] N. Guiblin, D. Grebille, H. Leligny, and C. Martin. $Ca_3Mn_2O_7$. *Acta Crystallographica C*, 58:i3–i5, 2002.

[298] M. V. Lobanov, M. Greenblatt, E. N. Caspi, J. D. Jorgenson, D. V. Sheptyakov, B. H. Toby, C. E. Botez, and P. W. Stephens. Crystal and magnetic structure of the $Ca_3Mn_2O_7$ Ruddlesden-Popper phase: neutron and synchrotron x-ray diffraction study. *Journal of Physics: Condensed Matter*, 16:5339, 2004.

[299] S. Senn, M. A. Bombardi, A. Murray, C. C. Vecchini, A. Scherillo, X. Luo, and W. Cheong, S.˙ Negative thermal expansion in hybrid improper ferroelectric Ruddlesden-Popper perovskites by symmetry trapping. *Physical Review Letters*, 114:035701, Jan 2015.

[300] M. J. Pitcher, P. Mandal, M. S. Dyer, J. Alaria, P. Borisov, H. Niu, J. B. Claridge, and M. J. Rosseinsky. Tilt engineering of spontaneous polarization and magnetization above 300 K in a bulk layered perovskite. *Science*, 347:420–424, 2015.

[301] S. Ghosh, H. Das, and C. J. Fennie. Linear magnetoelectricity at room temperature in perovskite superlattices by design. *Physical Review B*, 92:184112, 2015.

[302] G. King, S. Thimmaiah, A. Dwivedi, and P. M. Woodward. Synthesis and characterization of new $AA'BWO_6$ perovskites exhibiting simultaneous ordering of A-site and B-site cations. *Chemistry of Materials*, 19:6451–6458, 2007.

[303] M. A. Arillo, J. Gómez, M. L. López, C. Pico, and M. L. Veiga. Structural and electrical characterization of new materials with perovskite structures. *Solid State Ionics*, 95:241–248, 1997.

[304] J. Young, A. Stroppa, S. Picozzi, and J. M. Rondinelli. Tuning the ferroelectric polarization in $AA'MnWO_6$ double perovskites through A cation substitution. *Dalton Transactions*, 44:10644–10653, 2015.

[305] C. De, T. H. Kim, K. H. Kim, and A. Sundaresan. The absence of ferroelectric polarization in layered and rock-salt ordering $NaLnMnWO_6$ (Ln=La,Nd,Tb) perovskites. *Physical Chemistry Chemical Physics*, 16:5407–5411, 2014.

[306] A. Snedden, K. S. Knight, and P. Lightfoot. Structural distortions in the layered perovskites $CsANb_2O_7$ (A=Nd,Bi). *Journal of Solid State Chemistry*, 173:309–313, 2003.

[307] R. J. Goff, D. Keeble, P. A. Thomas, C. Ritter, F. D. Morrison, and P. Lightfoot. Leakage and proton conductivity in the predicted ferroelectric $CsBiNb_2O_7$. *Chemistry of Materials*, 21:1296–1302, 2009.

[308] Elisha A. Josepha, Sara Farooq, Cinnamon M. Mitchell, and John B. Wiley. Synthesis and thermal stability studies of a series of metastable Dion-Jacobson double-layered neodymium-niobate perovskites. *Journal of Solid State Chemistry*, 216:85–90, 2014.

[309] C. J. Fennie and K. M. Rabe. Ferroelectricity in the Dion-Jacobson $CsBiNb_2O_7$. *Applied Physics Letters*, 88:262902, 2006.

[310] B.-W. Li, M. Osada, T. C. Ozawa, and T. Sasaki. $RbBiNb_2O_7$: A new lead-free high-t_c ferroelectric. *Chemistry of Materials*, 24:3111–3113, 2012.

[311] H. Sim and B. G. Kim. Octahedral tilting and ferroelectricity in $RbANb_2O_7$ (A=Bi,Nd) from first principles. *Physical Review B*, 89:144114, 2014.

[312] N. Benedek. Origin of ferroelectricity in a family of polar oxides: The Dion-Jacobson phases. *Inorganic Chemistry*, 53:3769–3777, 2014.

[313] C. Chen, H. Ning, S. Lepadatu, M. Cain, H. Yan, and M. J. Reece. Ferroelectricity in Dion-Jacobson $ABiNb_2O_7$ (A=Rb, Cs) compounds. *Journal of Materials Chemistry C*, 3:19–22, 2015.

[314] G. Gou and J. Shi. Piezoelectricity enhancement in Dion-Jacobson $RbBiNb_2O_7$ via negative pressure. *Europhysics Lett.*, 108:67006, 2014.

[315] M. W. Lufaso and P. M. Woodward. Jahn-teller distortions, cation ordering and octahedral tilting in perovskites. *Acta Crystallographica Section B*, 60:10–20, 2004.

[316] A. Camaratta and J. M. Rondinelli. *Submitted*, 2015.

[317] K.-L. Hu, M. Kurmoo, Z. Wang, and S. Gao. Metal-organic perovskites: Synthesis, structures, and magnetic properties of $[C(NH_2)_3][MII(HCOO)_3]$ (M=Mn, Fe, Co, Ni, Cu, and Zn; $C(NH_2)_3$ = Guanidinium). *Chemistry - A European Journal*, 15:12050–12064, 2009.

[318] A. Stroppa, P. Jain, P. Barone, M. Marsman, J. M. Perez-Mato, A. Cheetham, H. W. Kroto, and S. Picozzi. Electric control of magnetization and interplay between orbital ordering and ferroelectricity in a multiferroic metal-organic framework. *Angewandte Chemie International Edition*, 50:5847, 2011.

[319] A. Stroppa, P. Jain, P. Barone, J. M. Perez-Mato, and S. Picozzi. Hybrid improper ferroelectricity in a multiferroic and magnetoelectric metal-organic framework. *Advanced Materials*, 25:2284, 2013.

[320] P. Jain, V. Ramachandran, R. J. Clark, H. D. Zhou, B. H. Toby, N. S. Dalal, H. W. Kroto, and A. K. Cheetham. Multiferroic behavior associated with an order-disorder hydrogen bonding transition in metal-organic frameworks (MOFs) with the perovskite ABX_3 architecture. *Journal of the American Chemical Society*, 131:13625–13627, 2009.

[321] Z. Wang, B. Zhang, T. Otsuka, K. Inoue, H. Kobayashi, and M. Kurmoo. Anionic nacl-type frameworks of $[MnII(HCOO)_3]$, templated by alkylammonium, exhibit weak ferromagnetism. *Dalton Transactions*, pages 2209–2216, 2004.

[322] D. Di Sante, A. Stroppa, P. Jain, and S. Picozzi. Tuning the ferroelectric polarization in a multiferroic metal-organic framework. *Journal of the American Chemical Society*, 135:18126–18130, 2013.

[323] A. O. Polyakov, A. H. Arkenbout, J. Baas, G. Blake, A. Meetsma, A. Caretta, P. van Loosdrecht, and T. Palstra. Coexisting ferromagnetic and ferroelectric order in a $CuCl_4$-based organic-inorganic hybrid. *Chemistry of Materials*, 24:133, 2011.

[324] B. Kundys, A. Lappas, M. Viret, V. Kapustianyk, V. Rudyk, S. Semak, Ch. Simon, and I. Bakaimi. Multiferroicity and hydrogen-bond ordering in $(C_2H_5NH_3)_2CuCl_4$. *Physical Review B*, 81:224434, 2010.

[325] J. Varignon, N. C. Bristowe, E. Bousquet, and P. Ghosez. Coupling and electrical control of structural, orbital, and magnetic orders in perovskites. *ArXiv e-prints*, 2014.

[326] L. Brammer. Developments in inorganic crystal engineering. *Chemical Society Reviews*, 33:476–489, 2003.

[327] G. R. Desiraju. Crystal engineering: A holistic view. *Angewandte Chemie International Edition*, 46:8342–8356, 2007.

[328] R. Gautier and K. R. Poeppelmeier. Preservation of chirality and polarity between chiral and polar building units in the solid state. *Inorganic Chemistry*, 51:10613–10618, 2012.

[329] R. Gautier, R. Gautier, K. B. Chang, and K. R. Poeppelmeier. On the origin of the differences in structure directing properties of polar metal oxyfluoride $[MO_xF_{6-x}]^{2-}$ (x = 1, 2) building units. *Inorganic Chemistry*, 54:1712–1719, 2015.

[330] K. J. Choi, M. Biegalski, Y. L. Li, A. Sharan, J. Schubert, R. Uecker, P. Reiche, Y. B. Chen, X. Q. Pan, V. Gopalan, L.-Q. Chen, D. G. Schlom, and C. B. Eom. Enhancement of ferroelectricity in strained $BaTiO_3$ thin films. *Science*, 306:1005–1009, 2004.

[331] International Union of Crystallography. In V. Kopský and D. B. Litvin, editors, *International Tables for Crystallography*, volume E: Subperiodic Groups. Springer, Dordrecht, 2010.

[332] M. A. Peña and J. L. G. Fierro. Chemical structures and performance of perovskite oxides. *Chemical Reviews*, 101:1981–2017, 2001.

[333] M. B. Salamon and M. Jaime. The physics of manganites: Structure and transport. *Reviews of Modern Physics*, 73:583–628, 2001.

[334] J. B. Goodenough. Electronic and ionic transport properties and other physical aspects of perovskites. *Reports on Progress in Physics*, 67:1915–1993, 2004.

[335] G. Pilania, P. V. Balachandran, J. E. Gubernatis, and T. Lookman. Classification of ABO_3 perovskite solids: a machine learning study. *Acta Crystallographica Section B*, 71:507–513, 2015.

[336] J. B. Torrance, P. Lacorre, A. I. Nazzal, E. J. Ansaldo, and Ch. Niedermayer. Systematic study of insulator-metal transitions in perovskites $RNiO_3$ (R =Pr, Nd, Sm, Eu) due to closing of charge-transfer gap. *Physical Review B*, 45:8209, 1992.

[337] T. Kimura, S. Ishihara, H. Shintani, T. Arima, K. T. Takahashi, K. Ishizaka, and Y. Tokura. Distorted perovskite with e_g^1 configuration as a frustrated spin system. *Physical Review B*, 68:060403(R), 2003.

[338] J. M. Rondinelli, S. J. May, and J. W. Freeland. Control of octahedral connectivity in perovskite oxide heterostructures: An emerging route to multifunctional materials discovery. *MRS Bulletin*, 37:261–270, 2012.

[339] E. J. Moon, R. Colby, Q. Wang, E. Karapetrova, C. M. Schlepütz, M. R. Fitzsimmons, and S. J. May. Spatial control of functional properties via octahedral modulations in complex oxide superlattices. *Nature Communications*, 5:5710, 2014.

[340] Nayoung Song, James M. Rondinelli, and Bog G. Kim. Noncentrosymmetric structural transitions in ultrashort ferroelectric $A\mathrm{GaO_3}/A'\mathrm{GaO_3}$ superlattices. *Physical Review B*, 91:134104, 2015.

[341] D. E. Bugaris, J. P. Hodges, A. Huq, A. M. R. Senos, and H.-C. zur Loye. Crystal growth, structures, and optical properties of the cubic double perovskites $\mathrm{Ba_2MgWO_6}$ and $\mathrm{Ba_2ZnWO_6}$. *Journal of Solid State Chemistry*, 184(8):2293–2298, 2011.

[342] P.M. Woodward, T. Vogt, Cox. D.E., A. Arulraj, C.N.R. Rao, P. Karen, and A.K. Cheetham. Influence of cation size on the structural features of $\mathrm{Ln_{1/2}A_{1/2}MnO_3}$ perovskites at room temperature. *Chemistry of Materials*, 10:3652–3665, 1998.

[343] M.T. Anderson and K.R. Poeppelmeier. Lanthanum copper tin oxide ($\mathrm{La_2CuSnO_6}$): a new perovskite-related compound with an unusual arrangement of B cations. *Chemistry of Materials*, 3:476–482, 1991.

[344] D. Serrate, J.M. De Teresa, and M.R. Ibarra. Double perovskites with ferromagnetism above room temperature. *Journal of Physics: Condensed Matter*, 19:023201, 2007.

[345] G. King, S. Thimmaiah, A. Dwivedi, and P.M. Woodward. Synthesis and characterization of new $\mathrm{AA'BWO_6}$ perovskites exhibiting simultaneous ordering of A-site and B-site cations. *Chemistry of Materials*, 19:6451–6458, 2007.

[346] T. Fukushima, A. Stroppa, S. Picozzi, and J. M. Perez-Mato. Large ferroelectric polarization in the new double perovskite $\mathrm{NaLaMnWO_6}$ induced by non-polar instabilities. *Physical Chemistry Chemical Physics*, 13(26):12186–12190, 2011.

[347] W. Dachraoui, Yang T., C. Liu, G. King, J. Hadermann, G. Van Tendeloo, A. Llobet, and M. Greenblatt. Short-range layered a-site ordering in double perovskites $\mathrm{NaLaBB_0O_6}$ (B = Mn, Fe; $\mathrm{B_0}$= Nb, Ta). *Chemistry of Materials*, 23:2398–2406, 2011.

[348] J. Young, A. Stroppa, S. Picozzi, and J. M. Rondinelli. Tuning the ferroelectric polarization in $AA'\mathrm{MnWO_6}$ double perovskites through A cation substitution. *Dalton Transactions*, 44:10644–10653, 2015.

[349] N. W. Thomas. Crystal structure-physical property relationships in perovskites. *Acta Crystallographica Section B*, 45:337–344, 1989.

[350] N. W. Thomas. The compositional dependence of octahedral tilting in orthorhombic and tetragonal perovskites. *Acta Crystallographica Section B*, 52:16–31, 1996.

[351] N. W. Thomas. A re-examination of the relationship between lattice strain, octahedral tilt angle and octahedral strain in rhombohedral perovskites. *Acta Crystallographica Section B*, 52:954–960, 1996.

[352] R. J. Angel, J. Zhao, and N. L. Ross. General rules for predicting phase transitions in perovskites due to octahedral tilting. *Physical Review Letters*, 95:025503, 2005.

[353] M. Ghita, M. Fornari, D. J. Singh, and S. V. Halilov. Interplay between A-site and B-site driven instabilities in perovskites. *Physical Review B*, 72:054114, 2005.

[354] J. He, A. Borisevich, S. V. Kalinin, S. J. Pennycook, and S. T. Pantelides. Control of octahedral tilts and magnetic properties of perovskite oxide heterostructures by substrate symmetry. *Physical Review Letters*, 105:227203, 2010.

[355] R. Aso, D. Kan, Y. Shimakawa, and H. Kurata. Atomic level observation of octahedral distortions at the perovskite oxide heterointerface. *Scientific Reports*, 3:2214, 2013.

[356] H. Lehnert, H. Boysen, P. Dreier, and Y. Yu. Room temperature structure of $LaAlO_3$. *Zeitschrift für Kristallographie*, 215:145–147, 2000.

[357] C. J. Howard, B. J. Kennedy, and B. C. Chakoumakos. Neutron powder diffraction study of rhombohedral rare-earth aluminates and the rhombohedral to cubic phase transition. *Journal of Physics: Condensed Matter*, 12:349–365, 2000.

[358] S. M. Moussa, B. J. Kennedy, B. A. Hunter, C. J. Howard, and T. Vogt. Low temperature structural studies on $PrAlO_3$. *Journal of Physics: Condensed Matter*, 13:L203–L209, 2001.

[359] W. T. Fu and D. J. W. Ijdo. Unusual phase transitions in $CeAlO_3$. *Journal of Solid State Chemistry*, 207:2732 – 2738, 2005.

[360] L. Vasylechko, A. Senyshyn, D. Trots, R. Niewa, W. Schnelle, and M. Knapp. $CeAlO_3$ and $Ce_{1-x}R_xAlO_3$ (R=La, Nd) solid solutions: Crystal structure, thermal expansion and phase transitions. *Journal of Solid State Chemistry*, 180(4):1277 – 1290, 2007.

[361] L. Vasylechko, A. Senyshyn, and U. Bismayer. Chapter 242 perovskite-type aluminates and gallates. In Jean-Claude G. Bnzli Karl A. Gschneidner, Jr. and Vitalij K. Pecharsky, editors, *Perovskite-Type Aluminates and Gallates*, volume 39 of *Handbook on the Physics and Chemistry of Rare Earths*, pages 113 – 295. Elsevier, 2009.

[362] K. Yamada, S. Funabiki, H. Horimoto, T. Matsui, T. Okuda, and S. Ichiba. Structural phase transitions of the polymorphs of $CsSnI_3$ by means of Rietveld analysis of the x-ray diffraction. *Chemistry Letters*, 20:801–804, 1991.

[363] I. Chung, J.-H. Song, J. Im, J. Androulakis, C. D. Malliakas, H. Li, A. J. Freeman, J. T. Kenney, and M. G. Kanatzidis. $CsSnI_3$: Semiconductor or metal? high electrical conductivity and strong near-infrared photoluminescence from a single material. high hole mobility and phase-transitions. *Journal of the American Chemical Society*, 134:8579–8587, 2012.

[364] M. Mori and H. Saito. An x-ray study of successive phase transitions in $CsSnBr_3$. *Journal of Physical Chemistry C*, 19:2391–2401, 1986.

[365] S. Hirotsu, J. Harada, M. Iizumi, and K. Gesi. Structural phase transitions in $CsPbBr_3$. *Journal of the Physical Society of Japan*, 37:1393–1398, 1974.

[366] D. E. Scaife, P. F. Weller, and W. G. Fisher. Crystal preparation and properties of cesium tin(ii) trihalides. *Journal of Solid State Chemistry*, 9:308–314, 1974.

[367] S. Stølen and R. G. Trønines. The perovskite to post-perovskite transition in $CaIrO_3$: Clapeyron slope and changes in bulk and shear moduli by density functional theory. *Physics of the Earth and Planetary Interiors*, 164:50–62, 2007.

[368] A. T. Zayak, X. Huang, J. B. Neaton, and K. M. Rabe. Manipulating magnetic properties of $SrRuO_3$ and $CaRuO_3$ with epitaxial and uniaxial strains. *Physical Review B*, 77:214410, 2008.

[369] Y. F. Nie, P. D. C. King, C. H. Kim, M. Uchida, H. I. Wei, B. D. Faeth, J. P. Ruf, J. P. C. Ruff, L. Xie, X. Pan, C. J. Fennie, D. G. Schlom, and K. M. Shen. Interplay of spin-orbit interactions, dimensionality, and octahedral rotations in semimetallic $SrIrO_3$. *Physical Review Letters*, 114:016401, 2015.

[370] J. M. Rondinelli, N. M. Caffrey, S. Sanvito, and N. A. Spaldin. Electronic properties of bulk and thin film $SrRuO_3$: Search for the metal-insulator transition. *Physical Review B*, 78:155107, 2008.

[371] D. Puggioni and J. M. Rondinelli. Designing a robustly metallic noncenstrosymmetric ruthenate oxide with large thermopower anisotropy. *Nature Communications*, 5:3432, 2014.

[372] P. Zubko, S. Gariglio, M. Gabay, P. Ghosez, and J.-M. Triscone. Interface physics in complex oxide heterostructures. *Annual Review of Condensed Matter Physics*, 2:141–165, 2011.

[373] Walid Dachraoui, Tao Yang, Chang Liu, Graham King, Joke Hadermann, Gustaaf Van Tendeloo, Anna Llobet, and Martha Greenblatt. Short-range layered A-site ordering in double perovskites $NaLaBB'O_6$ B = Mn, Fe; B' = Nb, Ta), journal = Chemistry of Materials, volume = 23, number = , pages = 2398–2406, year = 2011,.

[374] L. Chaput, A. Togo, I. Tanaka, and G. Hug. Phonon-phonon interactions in transition metals. *Physical Review B*, 84:094302, 2011.

[375] S. Baroni and R. Resta. Ab initio calculation of the low-frequency Raman cross section in silicon. *Physical Review B*, 33:5969–5971, 1986.

[376] M. Gajdos, K. Hummer, G. Kresse, J. Furthmuller, and F. Bechstedt. Linear optical properties in the PAW methodology. *Physical Review B*, 73:045112, 2006.

[377] M. Kajitani, M. Matsuda, A. Hoshikawa, K. Oikawa, S. Torii, T. Kamiyama, F. Izumi, and M. Miyake. Neutron diffraction study on lanthanum gallate perovskite compound series. *Chemistry of Materials*, 15:3468, 2003.

[378] A. H. Reshak et al. Effect of U on the electronic properties of neodymium gallate ($NdGaO_3$): Theoretical and experimental studies. *Journal of Physical Chemistry B*, 113:15237, 2009.

[379] G. Gou and J. M. Rondinelli. Piezoelectricity across a strain-induced isosymmetric ferri-to-ferroelectric transition. *Advanced Materials Interfaces*, 1:1400042, 2014.

[380] Y. Ding and D. D. Liang. A model of phase transition induced antiphase boundaries in perovskite and layered perovskite oxides. *Journal of Applied Physics*, 92:5425–5428, 2002.

[381] Y. Ding and Z. L. Wang. Translation and orientation domain boundaries in $La_{2/3}Ca_{1/3}MnO_3$. *Philosophical Magazine*, 86:2329–2342, 2006.

[382] A. Shaulov, W. A. Smith, G. M. Loiacono, M. I. Bell, and Y. H. Tsuo. Improper ferroelectrics for pyroelectric detection of infrared radiation. *Ferroelectrics*, 27:117–121, 1980.

[383] W. T. Fu and D. J. W. Ijdo. Unusual phase transitions in $CeAlO_3$. *Journal of Solid State Chemistry*, 207:2732 – 2738, 2005.

[384] J. C. Wojdel and J. Íñiguez. Testing simple predictors for the temperature of a structural phase transition. *Physical Review B*, 90:014105, 2014.

[385] M. T. Anderson, K. B. Greenwood, G. A. Talyor, and K. R. Poeppelmeier. B-cation arrangements in double perovskites. *Progress in Solid State Chemistry*, 22:197–233, 1993.

[386] C. J. Howard, B. J. Kennedy, and P. M. Woodward. Ordered double perovskites - a group theoretical analysis. *Acta Crystallographica Section B*, 59:463–471, 2003.

[387] S. Coh, T. Heeg, J. H. Haeni, M. D. Biegalski, J. Lettieri, L. F. Edge, K. E. O'Brien, M. Bernhagen, P. Reiche, R. Uecker, S. Trolier-McKinstry, D. G. Schlom, and D. Vanderbilt. Si-compatible candidates for high-κ dielectrics with the Pbnm perovskite structure. *Physical Review B*, 82:064101, 2010.

[388] L. B. Kong, T. S. Zhang, J. Ma, and F. Boey. Progress in synthesis of ferroelectric ceramic materials via high-energy mechanochemical technique. *Progress in Materials Science*, 53:207–322, 2008.

[389] H. Ledbetter, H. Ogi, and N. Nakamura. Elastic, anelastic, piezoelectric coefficients of monocrystal lithium niobate. *Mechanics of Materials*, 36:941 – 947, 2004.

[390] W. Zhong, D. Vanderbilt, and K. M. Rabe. Phase transitions in $BaTiO_3$ from first principles. *Physical Review Letters*, 73:1861–1864, 1994.

[391] G. King, A. S. Wills, and P. M. Woodward. Magnetic structures of NaLMnWO_6 perovskites (L = La, Nd, Tb). *Physical Review B*, 79:224428, 2009.

[392] S. Garcia-Martin, G. King, E. Urones-Garrote, G. Nébert, and P. M. Woodward. Spontaneous superlattice formation in the doubly ordered perovskite $KLaMnWO_6$. *Chemistry of Materials*, 23:163–170, 2011.

[393] D. Altermatt and I. D. Brown. The automatic searching for chemical bonds in inorganic crystal structures. *Acta Crystallographica Section B*, 41:240–244, 1985.

[394] A. Cammarata and J. M. Rondinelli. Covalent dependence of octahedral rotations in orthorhombic perovskite oxides. *Journal of Chemical Physics*, 141:114704, 2014.

[395] H. D'Hondt, A. M. Abakumov, J. Hadermann, A. S. Kalyuzhnaya, M. G. Rozova, E. V. Antipov, and G. V. Van Tendeloo. Tetrahedral chain order in the $Sr_2Fe_2O_5$ brownmillerite. *Chemistry of Materials*, 20:7188–7194, 2008.

[396] J. E. Auckett, A. J. Studer, N. Sharma, and C. D. Ling. Floating-zone growth of brownmillerite $Sr_2Fe_2O_5$ and the observation of a chain-ordered superstructure by single-crystal neutron diffraction. *Solid State Ionics*, 225:432–436, 2012.

[397] J. E. Auckett, A. J. Studer, E. Pellegrini, J. Ollivier, M. R. Johnson, H. Schober, W. Miiller, and C. D. Ling. Combined experimental and computational study of oxide conduction dynamics in $Sr_2Fe_2O_5$ brownmillerite. *Chemistry of Materials*, 25:3080–3087, 2013.

[398] H. Krüger, V. Kahlenberg, V. Petříček, F. Phillipp, and W. Wertl. High-temperature structural phase transition in $Ca_2Fe_2O_5$ studied by in-situ x-ray diffraction and transmission electron microscopy. *Journal of Solid State Chemistry*, 182:1515–1523, 2009.

[399] P. A. Maggard, T. S. Nault, S. L. Stern, and K. R. Poeppelmeier. Alignment of acentric $MoO_3F_3^{3-}$ anions in a polar material $(Ag_3MoO_3F_3)(Ag_3MoO_4)Cl$. *Journal of Solid State Chemistry*, 175:27–33, 2003.

[400] Y. Shimakawa, S. Inoue, M. Haruta, M. Kawai, K. Matsumoto, A. Sakaiguchi, N. Ichikawa, S. Isoda, and H. Kurata. Topotactic changes in thin films of brownmillerite $SrFeO_{2.5}$ grown on $SrTiO_3$ substrates to infinite-layer structure $SrFeO_2$. *Crystal Growth and Design*, 10:4713, 2010.

[401] S. Inoue, M. Kawai, Y. Shimakawa, M. Mizumaki, N. Kawamura, T. Watanabe, Y. Tsujimoto, H. Kageyama, and K. Yoshimura. Single-crystal epitaxial thin films of $SrFeO_2$ with FeO_2 "infinite layers". *Applied Physics Letters*, 92:161911, 2008.

[402] M. D. Rossell, O. I. Lebedev, G. V. Van Tendeloo, N. Hayashi, T. Terashima, and M. Takano. Structure of epitaxial $Ca_2Fe_2O_5$ films deposited on different perovskite-type substrates. *Journal of Applied Physics*, 95:5145–5152, 2004.

[403] A. Vailionis, H. Boschker, W. Siemons, E. P. Houwman, D. H. A. Blank, G. Rijnder, and G. Koster. Misfit strain accommodation in epitaxial ABO_3 perovskites: Lattice rotations and lattice modulations. *Physical Review B*, 88:064101, 2011.

[404] R. L. Johnson-Wilke, D. Marincel, S. Zhu, M. P. Warusawithana, A. Hatt, J. Sayre, K. T. Delaney, R. Engel-Herber, C. M. Schlepütz, J.-W. Kim, V. Gopalan, N. A. Spaldin, D. G. Schlom, P. J. Ryan, and S. Trolier-McKinstry. Quantification of octahedral rotations in strained $LaAlO_3$ films via synchrotron x-ray diffraction. *Physical Review B*, 88:174101, 2013.

[405] H. W. Eng, P. W. Barnes, B. M. Auer, and P. M. Woodward. Investigations of the electronic structure of d^0 transition metal oxides belonging to the perovskite family. *Journal of Solid State Chemistry*, 175:94–109, 2003.

[406] A. Amat, E. Mosconi, E. Ronca, C. Quarti, P. Umari, Md. K. Nazeeruddin, M. Grätael, and F. D. Angelis. Cation-induced band-gap tuning in organohalide perovskites: Interplay of spin-orbit coupling and octahedra tilting. *Nano Letters*, 14:3608–3616, 2014.

[407] M. Filip, G. E. Eperon, H. J. Snaith, and F. Giustino. Steric engineering of metal-halide perovskites with tunable optical band gaps. *Nature Communications*, 5:5757, 2014.

[408] U. Aschauer and N. A. Spaldin. Competition and cooperation between antiferrodistortive and ferroelectric instabilities in the model perovskite $SrTiO_3$. *Journal of Physics: Condensed Matter*, 26:122203, 2014.

[409] H. Li, I. E. Castelli, K. S. Thygesen, and K. W. Jacobsen. Strain sensitivity of band gaps of Sn-containing semiconductors. *Physical Review B*, 91:045204, 2015.

[410] M. Imada, A. Fujimori, and Y. Tokura. Metal-insulator transitions. *Reviews of Modern Physics*, 70(4):1039–1263, 1998.

[411] N. A. Benedek, A. T. Mulder, and C. J. Fennie. Polar octahedral rotations: A path to new multifunctional materials. *Journal of Solid State Chemistry*, 195:11–20, 2012.

[412] J. Young and J. M. Rondinelli. Octahedral rotation preferences in perovskite iodides and bromides. *Journal of Physical Chemistry Letters*, 7(5):918–922, 2016.

[413] F. He, B. O. Wells, Z.-G. Ban, S. P. Alpay, S. Grenier, S. M. Shapiro, W. Si, A. Clark, and X. X. Xi. Structural phase transition in epitaxial perovskite films. *Physical Review B*, 70:235405, 2004.

[414] R. Nechache, C. Harnagea, L.-P. Carignan, O. Gautreau, L. Pintilie, M. P. Singh, D. Ménard, P. Fournier, M. Alexe, and A. Pignolet. Epitaxial thin films of the multiferroic double perovskite Bi_2FeCrO_6 grown on (100)-oriented $SrTiO_3$ substrates: Growth, characterization, and optimization. *Journal of Applied Physics*, 105:061621, 2009.

[415] D. G. Schlom, L.-Q. Chen, C.-B. Eom, K. M. Rabe, S. K. Streiffer, and J.-M. Triscone. Strain tuning of ferroelectric thin films. *Annual Review of Materials Research*, 37:589–626, 2007.

[416] R. Ramesh and N. A. Spaldin. Multiferroics: progress and prospects in thin films. *Nature Materials*, 6:21–29, 2007.

[417] A. S. Tatarenko and M. I. Bichurin. Microwave magnetoelectric devices. *Advances in Condensed Matter Physics*, 2012:286562, 2012.

[418] S. Fusil, V. Garcia, A. Barthélémy, and M. Bibes. Magnetoelectric devices for spintronics. *Annual Review of Materials Research*, 44:91–116, 2014.

Appendix A. CRYSTAL STRUCTURES

The ground state crystal structures for each of the compounds investigated in this thesis are tabulated below.

Table A.1: Calculated crystallographic parameters for the ground state structure of [001]-ordered (LaNd)Ga_2O_6.

$Pmc2_1$ $LaGaO_3/NdGaO_3$, a = 5.539 Å, b = 5.467 Å, c = 7.767 Å				
Atom	Wyckoff Site	x	y	z
La	2a	0.4622	0.2407	0.0000
Nd	2b	0.5473	0.2612	0.5000
Ga	4c	0.2500	0.7515	0.7424
O	4c	0.2098	0.9601	0.7904
O	4c	0.7875	0.5369	0.7026
O	2a	0.0151	0.3268	0.0000
O	2b	0.9784	0.1638	0.5000

Table A.2: Calculated crystallographic parameters for the ground state structure of [111]-ordered (LaNd)Ga_2O_6.

$Pmn2_1$ $LaGaO_3/NdGaO_3$, a = 5.459 Å, b = 5.539 Å, c = 7.764 Å				
Atom	Wyckoff Site	x	y	z
La	2a	0.4917	0.2134	0.0000
Nd	2a	0.0123	0.7023	0.0000
Ga	4b	0.0002	0.2474	0.7495
O	4b	0.2841	0.4652	0.7927
O	4b	0.7086	0.0414	0.7045
O	2a	0.9230	0.2702	0.0000
O	2a	0.5967	0.7666	0.0000

Table A.3: Calculated crystallographic parameters for the ground state structure of [110]-ordered (LaNd)Ga_2O_6.

$P2_1/m$ $LaGaO_3/NdGaO_3$, a = 5.470 Å, b = 5.538 Å, c = 7.765 Å				
Atom	Wyckoff Site	x	y	z
La	2e	0.4905	0.9603	0.2500
Nd	2e	0.0113	0.4549	0.2500
Ga	2a	0.0000	0.0000	0.0000
Ga	2d	0.5000	0.5000	0.0000
O	4f	0.2856	0.2140	0.0445
O	4f	0.7897	0.2901	0.9561
O	2e	0.9214	0.0212	0.2500
O	2e	0.5854	0.5155	0.2500

Table A.4: Calculated crystallographic parameters for the ground state structure of [001]-ordered (SrCa)Zr_2O_6.

$Pmc2_1$ $SrZrO_3/CaZrO_3$, a = 5.817 Å, b = 5.671 Å, c = 8.106 Å				
Atom	Wyckoff Site	x	y	z
Sr	2a	0.2500	0.7368	0.0000
Ca	2b	0.3425	0.7582	0.5000
Zr	4c	0.2936	0.2504	0.7448
O	2a	0.3148	0.1674	0.0000
O	4c	0.5914	0.0497	0.6915
O	4c	0.9983	0.4536	0.7934
O	2b	0.2486	0.3591	0.5000

Table A.5: Calculated crystallographic parameters for the ground state structure of [111]-ordered $(SrCa)Zr_2O_6$.

$Pmn2_1$ $SrZrO_3/CaZrO_3$, a = 5.693 Å, b = 5.807 Å, c = 8.097 Å				
Atom	Wyckoff Site	x	y	z
Sr	2a	0.4935	0.2185	0.0000
Ca	2a	0.0158	0.6992	0.0000
Zr	4b	0.0008	0.2471	0.7492
O	4b	0.2838	0.4653	0.7994
O	4b	0.6976	0.0514	0.6952
O	2a	0.9164	0.2871	0.0000
O	2a	0.6097	0.7759	0.0000

Table A.6: Calculated crystallographic parameters for the ground state structure of [110]-ordered $(SrCa)Zr_2O_6$.

$P2_1/m$ $SrZrO_3/CaZrO_3$, a = 5.677 Å, b = 5.808 Å, c = 8.117 Å				
Atom	Wyckoff Site	x	y	z
Sr	2e	0.5084	0.0441	0.2500
Ca	2e	0.9893	0.5444	0.2500
Zr	2a	0.0000	0.0000	0.0000
Zr	2d	0.5000	0.5000	0.0000
O	4f	0.2980	0.2038	0.5409
O	4f	0.8003	0.2990	0.4419
O	2e	0.0837	0.9490	0.2500
O	2e	0.3962	0.4845	0.2500

Table A.7: Calculated crystallographic parameters for the ground state structure of [001]-ordered $(SrCa)Hf_2O_6$.

$Pmc2_1$ $SrHfO_3/CaHfO_3$, a = 5.803 Å, b = 5.705 Å, c = 8.032 Å				
Atom	Wyckoff Site	x	y	z
Sr	2a	0.4650	0.2395	0.0000
Ca	2b	0.5452	0.2577	0.5000
Hf	4c	0.0010	0.2488	0.7453
O	4c	0.2123	0.9614	0.7890
O	4c	0.7907	0.5408	0.6971
O	2a	0.0177	0.3253	0.0000
O	2b	0.9641	0.1501	0.5000

Table A.8: Calculated crystallographic parameters for the ground state structure of [111]-ordered (SrCa)Hf_2O_6.

$Pmn2_1$ $SrHfO_3/CaHfO_3$, a = 5.469 Å, b = 5.539 Å, c = 7.764 Å				
Atom	Wyckoff Site	x	y	z
Sr	2a	0.4918	0.2135	0.0000
Ca	2a	0.0123	0.7024	0.0000
Hf	4b	0.0002	0.2475	0.7495
O	4b	0.2842	0.4653	0.7927
O	4b	0.7087	0.0414	0.7045
O	2a	0.9230	0.2702	0.0000
O	2a	0.5868	0.7666	0.0000

Table A.9: Calculated crystallographic parameters for all ground state structures of [110]-ordered (SrCa)Hf_2O_6.

$P2_1/m$ $SrHfO_3/CaHfO_3$, a = 5.470 Å, b = 5.538 Å, c = 7.765 Å				
Atom	Wyckoff Site	x	y	z
Sr	2e	0.5094	0.0396	0.2500
Ca	2e	0.9887	0.5451	0.2500
Hf	2a	0.0000	0.0000	0.0000
Hf	2d	0.5000	0.5000	0.0000
O	4f	0.2856	0.2140	0.5446
O	4f	0.7898	0.2902	0.4561
O	2e	0.0785	0.9787	0.2500
O	2e	0.4146	0.4845	0.2500

Table A.10: Calculated crystallographic parameters for the ground state structure of [111]-ordered (LaNd)Al_2O_6.

R32 $LaAlO_3/NdAlO_3$, a = 5.339 Å, b = 5.339 Å, c = 12.96 Å, $\gamma = 120°$				
Atom	Wyckoff Site	x	y	z
La	3a	0.0000	0.0000	0.0000
Nd	3b	0.0000	0.0000	0.5000
Al	6c	0.0000	0.0000	0.7500
O	9e	0.4513	0.0000	0.5000
O	4c	0.5418	0.0000	0.0000

Table A.11: Calculated crystallographic parameters for the ground state structure of [111]-ordered (LaPr)Al_2O_6.

Imm2 $LaAlO_3/PrAlO_3$, a = 5.322 Å, b = 7.523 Å, c = 5.355 Å				
Atom	Wyckoff Site	x	y	z
La	2b	0.0000	0.0000	0.5014
Pr	2a	0.0000	0.0000	0.4966
Al	4d	0.0000	0.7501	0.0000
O	8e	0.7514	0.7763	0.2516
O	2b	0.0000	0.5000	0.0482
O	2a	0.0000	0.0000	-0.0523

Table A.12: Calculated crystallographic parameters for the ground state structure of [111]-ordered (CePr)Al_2O_6.

Imm2 $CeAlO_3/PrAlO_3$, a = 5.318 Å, b = 7.523 Å, c = 5.361 Å				
Atom	Wyckoff Site	x	y	z
Ce	2b	0.0000	0.0000	0.5019
Pr	2a	0.0000	0.0000	0.4966
Al	4d	0.0000	0.7499	0.0000
O	8e	0.7514	0.7767	0.2514
O	2b	0.0000	0.5000	0.0487
O	2a	0.0000	0.0000	-0.0529

Table A.13: Calculated crystallographic parameters for the ground state structure of (NaLa)(MnW)O_6.

$P2_1$ (NaLa)(MnW)O_6, a = 5.572 Å, b = 5.597 Å, c = 8.015 Å, $\beta = 90.225$				
Atom	Wyckoff Site	x	y	z
Na	2a	0.7526	0.2494	-0.0001
La	2a	0.7427	0.3090	0.4997
Mn	2a	0.2482	0.2776	0.7612
W	2a	0.2459	0.2701	0.2335
O	2a	0.4546	0.5358	0.3031
O	2a	0.4782	0.5603	0.6976
O	2a	0.0351	-0.0421	0.7805
O	2a	0.0684	-0.0225	0.2157
O	2a	0.1677	0.2496	0.4909
O	2a	0.3352	0.2962	0.0127

Table A.14: Calculated crystallographic parameters for the ground state structure of (NaNd)(MnW)O_6.

$P2_1$ (NaNd)(MnW)O_6, a = 5.572 Å, b = 5.597 Å, c = 8.015 Å, $\beta = 90.303$				
Atom	Wyckoff Site	x	y	z
Na	2a	0.7485	0.2421	-0.0001
La	2a	0.7370	0.3239	0.4994
Mn	2a	0.2493	0.2776	0.7588
W	2a	0.2408	0.2693	0.2371
O	2a	0.4416	0.5385	0.3107
O	2a	0.4758	0.5385	0.6904
O	2a	0.0469	-0.0565	0.7787
O	2a	0.0805	-0.0266	0.2141
O	2a	0.1549	0.2406	0.4915
O	2a	0.3329	0.3038	0.0183

Table A.15: Calculated crystallographic parameters for the ground state structure of $(NaY)(MnW)O_6$.

$P2_1$ $(NaY)(MnW)O_6$, a = 5.438 Å, b = 5.637 Å, c = 7.961 Å, $\beta = 90.267$				
Atom	Wyckoff Site	x	y	z
Na	2a	0.7466	0.2367	-0.0008
Y	2a	0.7332	0.3362	0.4987
Mn	2a	0.2484	0.2800	0.7561
W	2a	0.2363	0.2698	0.2401
O	2a	0.4305	0.5444	0.3208
O	2a	0.4694	0.5786	0.6806
O	2a	0.0613	-0.0649	0.7771
O	2a	0.0906	-0.0343	0.2135
O	2a	0.1348	0.2272	0.4933
O	2a	0.3312	0.3097	0.0201

Table A.16: Calculated crystallographic parameters for the ground state structure of $(KLa)(MnW)O_6$.

$P2_1$ $(KLa)(MnW)O_6$, a = 5.696 Å, b = 5.722 Å, c = 8.237 Å, $\beta = 90.504$				
Atom	Wyckoff Site	x	y	z
K	2a	0.7565	0.2575	-0.0006
La	2a	0.7503	0.3061	0.5003
Mn	2a	0.2548	0.2753	0.7551
W	2a	0.2419	0.2694	0.2475
O	2a	0.4575	0.5266	0.3052
O	2a	0.4897	0.5592	0.6938
O	2a	0.0194	-0.0278	0.7551
O	2a	0.0504	-0.0049	0.2422
O	2a	0.1749	0.24811	0.4946
O	2a	0.2923	0.2738	0.0254

Table A.17: Calculated crystallographic parameters for the ground state structure of $(KNd)(MnW)O_6$.

$P2_1$ $(KNd)(MnW)O_6$, a = 5.635 Å, b = 5.718 Å, c = 8.243 Å, $\beta = 90.587$				
Atom	Wyckoff Site	x	y	z
K	2a	0.7544	0.2530	-0.0019
Nd	2a	0.7445	0.3211	0.4994
Mn	2a	0.2539	0.2779	0.7533
W	2a	0.2379	0.2693	0.2489
O	2a	0.4479	0.5324	0.3102
O	2a	0.4839	0.5661	0.6883
O	2a	0.0340	-0.0401	0.7556
O	2a	0.0606	-0.0151	0.2412
O	2a	0.1648	0.2422	0.4953
O	2a	0.2912	0.2765	0.0273

Table A.18: Calculated crystallographic parameters for the ground state structure of $(KY)(MnW)O_6$.

$P2_1$ $(KY)(MnW)O_6$, a = 5.519 Å, b = 5.693 Å, c = 8.254 Å, $\beta = 90.729$				
Atom	Wyckoff Site	x	y	z
K	2a	0.7537	0.2477	-0.0034
Y	2a	0.7413	0.3371	0.4987
Mn	2a	0.2524	0.2810	0.7476
W	2a	0.2337	0.2697	0.2531
O	2a	0.4347	0.5411	0.3205
O	2a	0.4741	0.5773	0.6769
O	2a	0.0525	-0.0534	0.7541
O	2a	0.0747	-0.0275	0.2425
O	2a	0.1444	0.2311	0.4964
O	2a	0.2891	0.2793	0.0321

Table A.19: Calculated crystallographic parameters for the ground state structure of (RbLa)(MnW)O_6.

$P2_1$ (RbLa)(MnW)O_6, a = 5.737 Å, b = 5.752 Å, c = 8.337 Å, $\beta = 90.549$				
Atom	Wyckoff Site	x	y	z
Rb	2a	0.7559	0.2620	-0.0005
La	2a	0.7539	0.3022	0.5006
Mn	2a	0.2553	0.2747	0.7509
W	2a	0.2418	0.2693	0.2534
O	2a	0.4637	0.5203	0.3068
O	2a	0.4961	0.5531	0.6924
O	2a	0.0111	-0.0192	0.7449
O	2a	0.0406	0.0028	0.2523
O	2a	0.1795	0.2485	0.4963
O	2a	0.2800	0.2694	0.0326

Table A.20: Calculated crystallographic parameters for the ground state structure of (RbNd)(MnW)O_6.

$P2_1$ (RbNd)(MnW)O_6, a = 5.545 Å, b = 5.635 Å, c = 9.492 Å, $\beta = 92.227$				
Atom	Wyckoff Site	x	y	z
Rb	2a	0.7672	0.2715	-0.0101
Nd	2a	0.7372	0.3155	0.4999
Mn	2a	0.2553	0.2774	0.7047
W	2a	0.2279	0.2686	0.2695
O	2a	0.4426	0.5325	0.3355
O	2a	0.4902	0.5599	0.6637
O	2a	0.0491	-0.0408	0.7378
O	2a	0.0491	-0.0210	0.2593
O	2a	0.1547	0.2391	0.4906
O	2a	0.2968	0.2808	0.0845

Table A.21: Calculated crystallographic parameters for the ground state structure of (RbY)(MnW)O_6.

$P2_1$ (RbY)(MnW)O_6, a = 5.407 Å, b = 5.594 Å, c = 9.721 Å, $\beta = 93.131$				
Atom	Wyckoff Site	x	y	z
Rb	2a	0.7656	0.2778	-0.0127
Nd	2a	0.7292	0.3279	0.4995
Mn	2a	0.2552	0.2791	0.6944
W	2a	0.2182	0.2682	0.2762
O	2a	0.4271	0.5380	0.3505
O	2a	0.4851	0.5668	0.6501
O	2a	0.0720	-0.0522	0.7360
O	2a	0.0579	-0.0322	0.2583
O	2a	0.1288	0.2203	0.4898
O	2a	0.2997	0.2896	0.0984

Table A.22: Calculated crystallographic parameters for the ground state structure of $Sr_2Fe_2O_5$ in the *I2bm* configuration.

Ima2 $Sr_2Fe_2O_5$, a = 15.40 Å, b = 5.659 Å, c = 5.501 Å				
Atom	Wyckoff Site	x	y	z
Sr	8c	0.3915	-0.0164	0.0029
Fe	4a	0.0000	0.0000	0.4984
Fe	4b	0.2500	0.0687	0.5388
O	2a	0.5082	0.7474	0.2503
O	2a	0.3607	-0.0494	0.4849
O	2a	0.2500	0.1393	0.8738

Table A.23: Calculated crystallographic parameters for the ground state structure of $Sr_2Fe_2O_5$ in the *Pbcm* configuration.

Pbcm $Sr_2Fe_2O_5$, a = 5.503 Å, b = 11.31 Å, c = 15.41 Å				
Atom	Wyckoff Site	x	y	z
Sr	8e	-0.0042	0.7418	0.6085
Sr	8e	0.5057	-0.0081	0.1085
Fe	4a	0.0000	0.0000	0.0000
Fe	4c	0.4992	0.2500	0.0000
Fe	4d	0.0401	0.0344	0.2500
Fe	4d	0.5405	0.2155	0.2500
O	8e	0.2505	0.3756	0.5099
O	8e	0.2495	0.8744	-0.0062
O	8e	-0.0151	0.5244	0.6393
O	8e	0.5117	0.7745	0.1392
O	4d	0.8757	0.1807	0.2500
O	4d	0.3752	0.0694	0.2500

Table A.24: Calculated crystallographic parameters for the ground state structure of $Sr_2Fe_2O_5$ in the *Pnma* configuration.

Pnma $Sr_2Fe_2O_5$, a = 5.499 Å, b = 15.41 Å, c = 5.659 Å				
Atom	Wyckoff Site	x	y	z
Sr	8d	0.5037	0.3915	-0.0165
Fe	4a	0.0000	0.0000	0.0000
Fe	4c	0.5412	0.2500	0.4313
O	8d	0.7491	0.0081	0.2489
O	8d	0.5119	0.8607	0.4507
O	4c	0.8763	0.2500	0.3607

Table A.25: Calculated crystallographic parameters for the ground state structure of $Ca_2Fe_2O_5$ in the *I2bm* configuration.

Ima2 $Sr_2Fe_2O_5$, a = 14.78 Å, b = 5.537 Å, c = 5.363 Å				
Atom	Wyckoff Site	x	y	z
Ca	8c	0.3932	-0.0244	0.0074
Fe	4a	0.0000	0.0000	0.4956
Fe	4b	0.2500	0.0668	0.5461
O	2a	0.5145	0.7460	0.2478
O	2a	0.3601	-0.0694	0.4686
O	2a	0.2500	0.1207	0.8978

Table A.26: Calculated crystallographic parameters for the ground state structure of $Ca_2Fe_2O_5$ in the *Pbcm* configuration.

Pbcm $Ca_2Fe_2O_5$, a = 5.386 Å, b = 11.15 Å, c = 14.63 Å				
Atom	Wyckoff Site	x	y	z
Ca	8e	-0.0145	0.7367	0.6067
Ca	8e	0.5163	-0.0127	0.1067
Fe	4a	0.0000	0.0000	0.0000
Fe	4c	0.5030	0.2500	0.0000
Fe	4d	0.0518	0.0346	0.2500
Fe	4d	0.5533	0.2153	0.2500
O	8e	0.2541	0.3766	0.5177
O	8e	0.2455	0.8735	-0.0112
O	8e	-0.0288	0.5345	0.6399
O	8e	0.5186	0.7850	0.1396
O	4d	-0.0958	0.1896	0.2500
O	4d	0.4024	0.0607	0.2500

Table A.27: Calculated crystallographic parameters for the ground state structure of $Ca_2Fe_2O_5$ in the *Pnma* configuration.

Pnma $Ca_2Fe_2O_5$, a = 5.323 Å, b = 14.91 Å, c = 5.529 Å				
Atom	Wyckoff Site	x	y	z
Ca	8d	-0.0192	0.8924	-0.0221
Fe	4a	0.0000	0.0000	0.5000
Fe	4c	0.0531	0.2500	0.5643
O	8d	0.7333	0.5153	0.2663
O	8d	-0.0242	0.3599	0.4302
O	4c	0.4065	0.2500	0.6216